UNIVERSITY OF
LIVERPOOL

Understanding the Molecular Level Structure of Intercalated Materials

Thesis Submitted in accordance with the requirements of the University of Liverpool for the degree of Doctor in Philosophy by

Catherine Cropper.

October 2011

Dedication

This thesis is dedicated to my grandmother, Kathleen Halliwell.
Without her endless love and support this would never have been possible.

Acknowledgements

In the period it has taken to accomplish this research, life has thrown many obstacles in my way, each one of which I have only been able to overcome with support and love of my family and friends. I could write a chapter in acknowledgement of these people and how special they are but the brightest stars are as follows:

Obviously this wouldn't exist without Jon Iggo putting the idea in my head that this was something I could achieve. Many afternoons have been spent shimming magnets and talking over concepts. Jon, you have the patience of a saint!

Neil Winterton has also been a fantastic supervisor, always willing to discuss my ideas and keeping me on the straight and narrow in terms of research. He has always helped me to see the bigger picture while maintaining an eye for detail.

Yaroslav Khimyak, my more primary supervisor has always ruled with a stick. His demands have often been unreasonable and at times I have loathed him but at the same time he has always known best. As much as it pains me to admit, he always knew what he was doing and that I'm not a carrot lead person. He knows how to get the best from me and throughout it all he has provided me with guidance both in science and in life and has moulded me into the person I am today.

To these three, I owe my deepest thanks.

Other characters around the department have also provided me with advice and refuge in times of crisis, Dave Adams, John Warren, Jamie Gould, James Jones and Darren Bradshaw, Rob Dawson, Sam Chong and Abbie Trewin it's over at last!

All the technical and support staff, Tony Ellis, Nadz, Debbie, Sam and Ann the tea lady in particular have provided me with gossip, tea, envelopes and a whole load of laughs throughout, thanks for that!

To my friends in the department, Al, Carly, Pavel, Matt, Babs, Zeyn, Michelle, Robin, big Ne, and Gill. Thank you for providing a distraction and keeping my spirits up during this whole process. Some of my fondest memories have been created in this time and I hope we will have many more.

My NMR family, Laura, Andrea, Lucy and Paul have seen it all. The jumping about because it worked! The tears of frustration. The snapping as the workload piles up. The nights on the town. The hugs and madness. No one knows me better than these four people and I hope we will continue to support each other forever. I wish you nothing but luck and love in everything you do. I would also like to thank Georgie for being a fantastic MChem student and for all her help in the lab.

Laura, Hay, Paul and Gem have picked me up from the pit of tears on many occasions and provided plenty of distractions from nights out, shopping, holidays to weddings. Thanks, you are the best friends I could ever wish for.

The final days were pretty work intensive and for putting up with the moaning, providing a distraction and keeping a smile on my face I have to thank Tony, Millie and the Grays.

A special thanks to my family. Mum and Dad have provided ears for moaning, a refuge for rebuilding myself when it's all got too much, food and water. Anni, thanks for keeping me entertained on my rare trips home. My Liverpool family have also been superb. Always supportive and keeping the faith, thanks especially to Ian, Philly and Hannah, Christine, John and the girls, Robert, Colly and the boys.

Finally, there is one person who deserved a PhD just for putting up with me; my grandma. Having had to live with me for eight years she has seen it all. The hangovers, the break downs, the stress and the excitement. If ever there was an example of unconditional love required to prove a theory this is it. Grandma, I owe you the world, I love you, thank you.

Abstract

Supported ionic liquid phase catalysis is a thriving area of research with many applications. Currently, investigations in this area have focussed on the applications of these systems and there are relatively few reports on the understanding of the interactions of the ionic liquid with the porous support. The aim of this research is observe and analyse these interactions for a number of model systems.

The supported ionic liquid phases (SILPs) discussed herein are made up of an ionic liquid physisorbed onto a mesoporous silica host. The ionic liquids used were chosen because of their ease of handling and similarity in structure. Mesoporous silicas were chosen due to their tunable properties. The potential applications of the systems described here in range from catalysis to gas processing and storage. As the focus of this research is characterisation of the interactions between the ionic liquid and the porous silica support, storage of CO_2 gas is the only application explored herein.

NMR spectroscopy has been extensively used in this research. Not only has it been a versatile tool for elucidation of structures, it has also allowed the measurement of changes in the dynamics of the ionic liquid upon encapsulation.

Combination of high resolution and solid state NMR spectroscopy has also been used to identify the presence of gases in clathrate hydrates. A semi-clathrate hydrate was loaded with methane gas. Solid state NMR experiments were then used to indentify methane molecules present in the cages of the clathrate and quantify the percentage uptake with respect to the semi-clathrate hydrate host.

Navigation

This thesis has been split into two sections. **Section I** details ionic liquids encapsulated in mesoporous silicas and the study of these systems using NMR spectroscopy. This encompasses an overall introduction to ionic liquids and mesoporous silicas (**Chapter 1**), two results chapters, **3** and **4**, and overall conclusions and comparisons between the systems investigated.

Section II (**Chapter 5**) details gas storage in clathrate hydrate systems. This section contains an introduction to clathrate hydrates and the associated results and discussion of the systems investigated.

The common theme throughout this research is NMR spectroscopy. **Chapter 2** gives a detailed introduction to NMR spectroscopy and includes the theory behind NMR spectroscopy as a technique as well as explanations of the experiments performed during the course of the research undertaken.

Publications and Presentations

F. Su, C. L. Bray, B.O. Carter, G. Overend, **C. Cropper,** J. A. Iggo, Y.Z. Khimyak, A. M. Fogg, and A.I. Cooper, "Reversible Hydrogen Storage in Hydrogel Clathrate Hydrates", *Advanced Mater*ials, 2009, 21, 1-5

W. Wang, B. O. Carter, C. L.Bray, A. Steiner, J. Bacsa, J. T. A. Jones, **C. Cropper**, Y. Z. Khimyak, D. J. Adams and A. I. Cooper, "Reversible Methane Storage in a Polymer-Supported Semi-Clathrate Hydrate at Ambient Temperature and Pressure", *Chemistry of Materials*, 2009, 21, 3810-3815

Oral Presentations

Confined Ionic Liquids in Functionalised Mesoporous Silicas", July 2011, MC10, Manchester, UK.

Ionic Liquids Confined in Porous Silicas: An NMR Study", June 2010, NMR-DG Postgraduate Meeting, University of Leeds, UK.

NMR Studies of Ionic Liquids in Mesoporous Silicas", March 2010, British Zeolite Association Conference, University of Southampton, UK.

Poster Presentations

"Caging Methane and Hydrogen Using Natures Blueprints", 2010 SET for BRITAIN, House of Commons, London, UK.

"Hydrogen and Methane Storage: NMR Studies of Clathrate Systems", August 2009, IUPAC/MC9 Conference, Glasgow, UK.

"Hydrogen and Methane Storage: NMR Studies of Clathrate Systems", 2009, Applications of NMR to Materials Chemistry, NMRDG, AstraZeneca, Loughborough, UK.

"Hydrogen and Methane Storage: NMR Studies of Clathrate Systems", 2008, Frontiers of Magnetic Resonance Meeting, BRSG, Warwick, UK.

Abbreviations List

BET	Brauner Emmett Teller
[bmim]	1-butyl-3-methylimidazolium
CP-MAS	Cross polarization magic angle spinning
CSA	Chemical shift anisotropy
CTEABr	Cetyltrimethylammonium bromide
DSC	Differential Scanning Calorimetry
FID	Free induction decay
FSLG	Frequency-switched Lee-Goldberg
FT-IR	Fourier transform infra-red spectroscopy
HETCOR	Heteronuclear correlation
MAS	Magic angle spinning
MCM	Mobil Crystalline Materials
[mmim]	1,3-dimethylimidazolium
[mnim]	1-methyl-3-nonylimidazolium
NMR	Nuclear Magnetic Resonance
NOESY	Nuclear Overhauser Effect Spectroscopy
[omim]	1-octyl-3-methylimidazolium
PEO	poly ethylene oxide
PXRD	Powder X-ray Diffraction
RF	Radiofrequency
RTIL	Room Temperature Ionic Liquid
SFG	Sum frequency generation spectroscopy
SILP	Supported Ionic Liquid Phases
TEOS	tetraethylorthosilicate
Tf	Triflate

T_g	Glass transition temperature
TGA	Thermal Gravametric Analysis
TPPM	Two phase pulse modulation
T_1	Spin lattice/Longitudinal relaxation
T_2	Spin-spin/Transverse relaxation
VOC	Volatile Organic Compound
XPS	X-ray photoelectron Spectroscopy

Contents

List of figures

Section I

Ionic Liquids Encapsulated in Mesoporous Silicas

Chapter 1

Introduction

In order to put the research undertaken into context, the literature included in this chapter covers four main areas. The focus will be on ionic liquids, mesoporous silica materials, supported ionic liquid phases (SILPs) and their characterisation. The section on ionic liquids will include an introduction to the properties of ionic liquids, their numerous applications and more specifically SILP catalysts. The section detailing mesoporous silica materials will focus on the synthesis of mesoporous silica materials and their use as potential supports for SILP catalysts. The characterisation of these materials is one of the main focuses of this research therefore a short overview of the techniques used to characterise the materials mentioned has been included. However, a more in depth technical description is provided in the characterisation techniques chapter.

A brief introduction will be given to clathrates hydrates in **Section II**.

1.1 Ionic liquids

Ionic liquids are broadly defined as salts with a melting temperature below 373 K that are composed of an organic cation and a polyatomic anion.[1] Since there are many known and prospective cations and anions, the potential number of ionic liquids is huge and publications detailing ionic liquids have grown exponentially.[1] Examples of possible combinations are given in **Figure 1.1**.

Most ionic liquids are clear liquids and have a strong potential as solvent media. It has been said that given a material, whether it be plastic or rock, researchers believe that you will be able to find an ionic liquid capable of dissolving it![2]

The earliest material to be classified as an ionic liquid was a "red oil" observed during a Friedel-Crafts reaction in 1914, documented by Walden *et al.*[3] It was later found that the "red oil" was a salt of an alkylated benzenium ion with a chloroaluminate counter anion. The discovery of NMR spectroscopy lead to the characterisation of this material.

a)

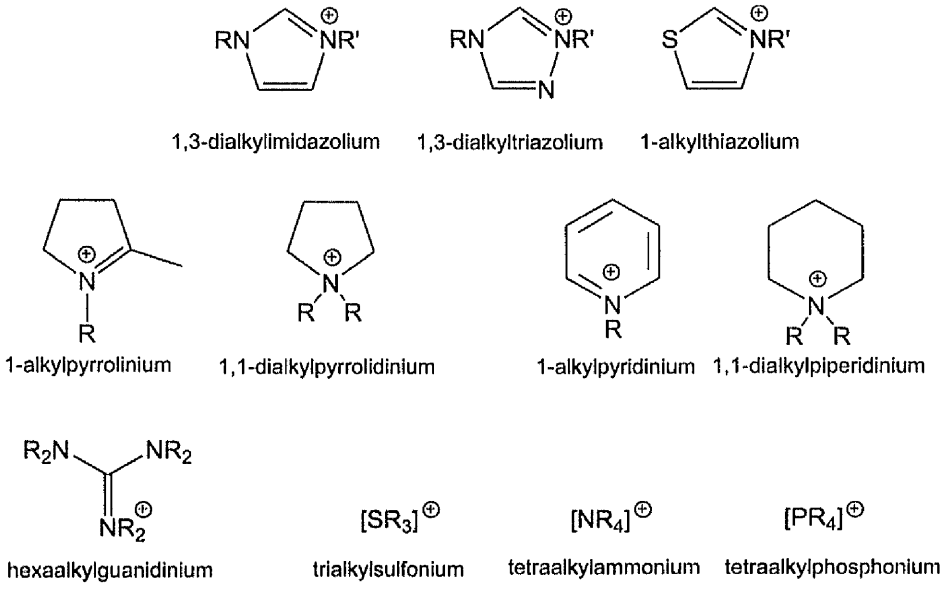

b)

$[AlCl_4]^{\ominus}$ $[Al_2Cl_7]^{\ominus}$ $[Al_3Cl_{10}]^{\ominus}$

$Cl^{\ominus}$ $Br^{\ominus}$ $[F(HF)_n]^{\ominus}$ $NO_3^{\ominus}$ $N(CN)_2^{\ominus}$ $SCN^{\ominus}$ $N_3^{\ominus}$

$[BF_4]^{\ominus}$ $[B(oxalato)_2]^{\ominus}$

$[PF_6]^{\ominus}$ $[SbF_6]^{\ominus}$ $[PF_3(C_2F_5)_3]^{\ominus}$

$[CH_3CO_2]^{\ominus}$ $[CF_3CO_2]^{\ominus}$ $[CH_3SO_3]^{\ominus}$ $[CF_3SO_3]^{\ominus}$ $[(CF_3SO_2)_2N]^{\ominus}$

$[MeOSO_3]^{\ominus}$ $[(MeO)PO_2]^{\ominus}$

Figure 1.1 Examples of common **a)** cations and **b)** anions

Although this initial finding happened early in the 20th century, it was the development of modern ionic liquids within the last fifty years that really accelerated this area of research[4-5] due to the discovery of favourable properties of ionic liquids and their wide range of applications, which will be discussed in the following section.

1.2 Properties and applications of ionic liquids

The properties of room temperature ionic liquids (RTILs) are dependent on the selection of the cation and anion components. A comparison of RTILs with their prosaic counterparts can be made. Using sodium chloride as an example, this salt has a high melting point (above 1073 K) and is solid at room temperature. It is highly corrosive in the molten state. However, the high melting point can be easily attributed to strong electrostatic interactions present in ionic bonding. As sodium chloride consists of small spherical ions that pack closely together, the electrostatic forces are strong leading to an increased melting point in comparison to ionic liquids. In contrast, RTILs generally consist of large, nonspherical cations combined with various anions (that can also be large). It is generally due to the large, bulky cation that these ions cannot pack closely and the resulting large distance between ion pairs leads to weaker interactions yielding substances whose melting points are often below room temperature.[6]

The large number of possible cation-anion combinations allows RTILs to be designed for specific purposes. This means that ionic liquids possess a wide range of properties that can make them favourable alternatives to volatile organic solvents (VOCs).[5] VOCs easily evaporate into surrounding air leading to air pollution and are often flammable. Ionic liquids are neither volatile nor as flammable as VOCs. Choosing the right ionic liquid can lead to a variety of potential applications, *e.g.* as lubricants,[7-8] electrolytes,[9] non-volatile solvents,[10] in gas processing[1] and as possible reaction media for a wide range of chemical processes, including catalysis.[1] Interest in RTILs as a large, multi-purpose class of compounds has grown rapidly owing to the lack of vapour pressure, wide liquid range, high conductivity and wide electrochemical potential windows exhibited, amongst many examples.[1,11]

Ionic liquids have a high polarity yet often weak coordination and high solvating abilities. In comparison to conventional organic solvents they are thermally stable over wide temperature ranges. Their low volatility allows for volatile organic products to be easily separated by distillation or vacuum. For example, pairing the cation, $[bmim]^+$, with the anion, BF_4^-, a hydrophilic solvent is formed whereas, $[bmim]PF_6$ is a hydrophobic solvent.[5]

Some properties of imidazolium based ionic liquids are summarised in **Table 1.1**. Generally, the melting points are lower for ionic liquids with less symmetrical cations. The melting points of imidazolium based ionic liquids can be reduced by increasing the size of the cation and anion. It has also been reported that methylation at the C(2) position on the imidazolium ring can increase the melting point. This can be attributed to an increased steric bulk leading to reduced hydrogen bonding ability in addition to inefficient packing as described above.

Table 1.1 Some physical properties of imidazolium based ionic liquids[1,5,12-14]

Cation	Anion	Melting Point /K	Glass Transition Temperature /K	Density /gcm^{-3}	Viscosity[a] /cP	Electrochemical Potential Window /V
mmim$^+$	BF_4^-	376				
emim$^+$	BF_4^-	285	313	-	43	4.3
bmim$^+$	BF_4^-	188	192	1.12	233	4.1
emim$^+$	PF_6^-	331				
bmim$^+$	PF_6^-	283	212	1.36	450	4.2
emim$^+$	$CF_3SO_3^-$	537				4.1
bmim$^+$	$CF_3SO_3^-$	316				
bmim$^+$	NTf_2^-	248		1.43	52	
bmim$^+$	Cl^-	314 (dried)	192			

[a] Viscosities measured between 293 and298 K. [b] Platinum working electrode

The glass transition temperature (T_g) of a non-crystalline substance can be described as the temperature at which the physical properties change from a glassy amorphous state to a rubbery flexible state.[15] The transition temperature in silicates is related to the energy required to break and re-form covalent bonds in an amorphous lattice of covalent bonds.[16] For imidazolium ionic liquids containing BF_4^-, the T_g decreases as the alkyl chain length of the cation increases. This is attributed to alkyl chains become increasingly flexible. This lowers the lattice energy and results in glass formation rather than crystals when cooled. In general, ionic liquids containing fluorinated anions possess the lowest T_g.

The thermal properties of ionic liquids can be measured using Differential Scanning Calorimetry (DSC) in order to determine melting points and glass transition temperatures. Thermal Gravimetric Analysis (TGA) can also be used to determine decomposition temperatures. As ionic liquids have no discernable vapour pressure, excessive heating will eventually cause thermal decomposition. Most ionic liquids are stable above their melting points, decomposing between 523-723 K.[17-19] Thermal stability of imidazolium based ionic liquids is enhanced by increasing the extent of substitution of the imidazole ring, increasing the chain length of alkyl substituent and decreasing the nucleophilicity of the anion.

Ionic liquids have similar densities to VOCs but much higher viscosities. This is a disadvantage of replacing VOCs with ionic liquids as reaction media in chemical reactions as there is a decrease in heat and mass transfer. This disadvantage is one which would need to be overcome if ionic liquids were to be used in large scale industrial processes. Ionic liquids are highly viscous due to their strong Coulombic interactions and tendency to hydrogen bond. As the size of the anion increases, the Coulombic interaction with the cation becomes weaker producing a less viscous ionic liquid. On the contrary, decreasing the size of the anion increases the hydrogen bonding producing a more viscous ionic liquid. As indicated in **Table 1.1**, imidazolium based ionic liquids containing a fluorinated anion and longer alkyl chain substituents on the cation have the highest viscosities.

Due to the variety of properties arising from the range of ionic liquids available, numerous applications have been developed. Wasserscheid and Welton[1] summarise a number of applications from their use as solvents in organic synthesis and polymerisation reactions to storage of gases and as cleaning fluids. **Table 1.2** summarises some of the industrial processes in which ionic liquids are currently being used.[1]

Table 1.2 Industrial Applications of Ionic Liquids[1]

Company	Process	IL acting as:	Scale
BASF	Acid scavenging	Auxiliary	Commercial
BASF	Extractive Distillation	Extractant	Pilot
BASF	Chlorination	Solvent	Commercial
IFP	Olefin Dimerization	Solvent	Pilot
Degussa	Hydrosilylation	Solvent	Pilot
Degussa	Compatibilizer	Performance additive	Commercial
Arkema	Fluorination	Solvent	Pilot
Chevron Phillips	Olefin Oligomerisation	Catalyst	Pilot
Scionix	Electroplating (Cr)	Electrolyte	Pilot
Eli Lilly	Cleavage of ether	Catalyst/reagent	Pilot
Air Products	Storage of gases	Liquid support	Pilot
Iolitec/Wandres	Cleaning fluid	Performance additive	Commercial
Linde	Gas Compression	Liquid piston	Pilot

One of the fastest growing areas of ionic liquid research is their use in catalysis.[1,20-23] This is predominantly due to substrates and catalysts being in the same phase when VOCs are used whereas, ionic liquids having negligible vapour pressure and can be designed to be immiscible with the product allowing for easier separation. Alternatively, if the product is a low boiling point liquid, distillation could be used to extract the product. The use of RTILs in this manner also has disadvantages. The extraction of a solid from an ionic liquid cannot be performed using distillation as RTILs are non volatile. Their high viscosity makes filtration difficult and washing with another solvent to extract the solid product defeats their point of use. RTILs are, however, known to dissolve in super critical CO_2 and can be easily removed in an uncontaminated form by simple depressurisation of the system although this is costly to set up.[24-25] To overcome these issues, recent attention has been paid to supported ionic liquid phases in which an ionic liquid is anchored to a support surface either by covalent bonding or adsorption. A catalyst is then incorporated into the ionic liquid film.[1,24,26] This is achieved by numerous methods and gives a number of advantages as described in the following section.

1.3 Supported ionic liquid phases (SILPs)

In comparison to conventional liquid-liquid biphasic catalysis in ionic liquid-organic liquid mixtures, the concept of "supported ionic liquid phase" (SILP) catalysis combines well-defined catalytic complexes, non-volatile ionic liquids and porous solid supports. This offers effective use of the catalyst containing ionic liquid phase since it is dispersed in a high surface area support.[1,24,27] As well as circumventing issues related to the high viscosity of ionic liquids, by dispersing a thin film on a high surface area support significantly reduces the amount of RTIL required, affording more cost effective processes.[20-21,28-30] Depending on their composition, ionic liquids can dissolve or reject organic compounds. Since they are polar, they are also ideal candidates for accommodating charged or polar catalysts such as transition metal complexes.[1,4,21,24,27-32]

1.3.1 Considerations when designing SILPs

Apart from careful selection of catalyst, porous host and ionic liquid, there are many considerations to take into account when designing SILP catalysts. **Section 1.4** details support systems that make viable SILP catalysts. This section aims to deal with the process and engineering aspects when designing SILP-catalysts.

During a catalytic reaction using a SILP, gaseous or vapour-phase reactants diffuse through the residual pore space of the porous host and dissolve in the ionic liquid-catalyst phase. The reactants then react with the catalytic sites within the thin film dispersed on the pore walls of the solid support. The products can then diffuse out of the catalytic phase, into the void and out of the catalytic particle. This is shown schematically in **Figure 1.2**.

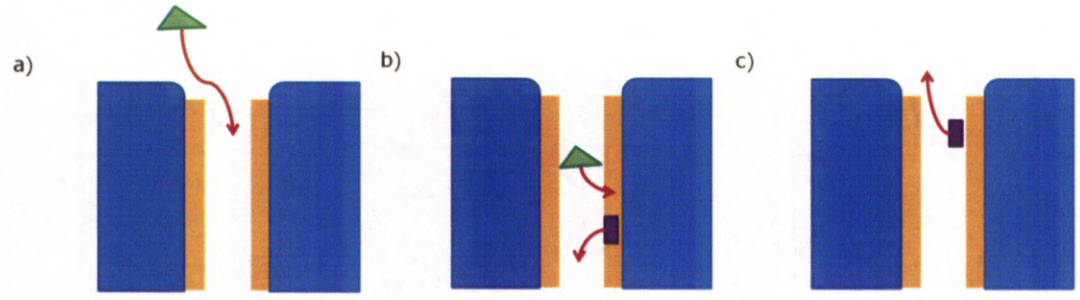

Figure 1.2 Schematic representation of reactions in SILP systems. a) Diffusion of reactant into porous host with ionic liquid-catalyst phase thin film, b) Diffusion of reactant into catalytic layer and diffusion of products out in to pore void, c) Diffusion of products out of SILP system

The catalytic performance of a SILP-catalyst depends on the amount of liquid solvent in the support catalyst, that is, the loading of ionic liquid into the porous host. On one hand it must be enough to constitute a thin film on the catalyst but on the other hand, it must not plug the pore and inhibit the diffusion of reactants. As a consequence, the ionic liquid-catalyst layer is less than 20 Å thick, corresponding to a layer of only a few molecules. This in turn goes some way in enhancing diffusion of reactants.

As well as considering the thickness of the ionic liquid-catalyst layer, careful consideration must be given to the distribution of the film on the porous support. This can be determined by several interacting factors including pore radii and shape, capillary forces, the wetting characteristics of the liquid and possible ionic liquid-support interactions. Often these interactions are difficult to characterise and will be discussed further in **Chapters 3 and 4**.

1.3.2 Various ionic liquid/catalyst/support combinations

RTILs may be immobilized either by physisorption onto the support or *via* covalent bonding to the support surface.[24] However, immobilization not only changes the properties of the RTIL but also constricts its orientation at the support surface.[24,27,33-36] Characterisation of the interactions between the ionic liquid and the support should help in the development of possible applications.[37] An understanding of mass transport and diffusion of substrates through the SILP is also

important for potential catalysis applications.[24] Examples of potential anchoring methods are given in **Figure 1.3.**

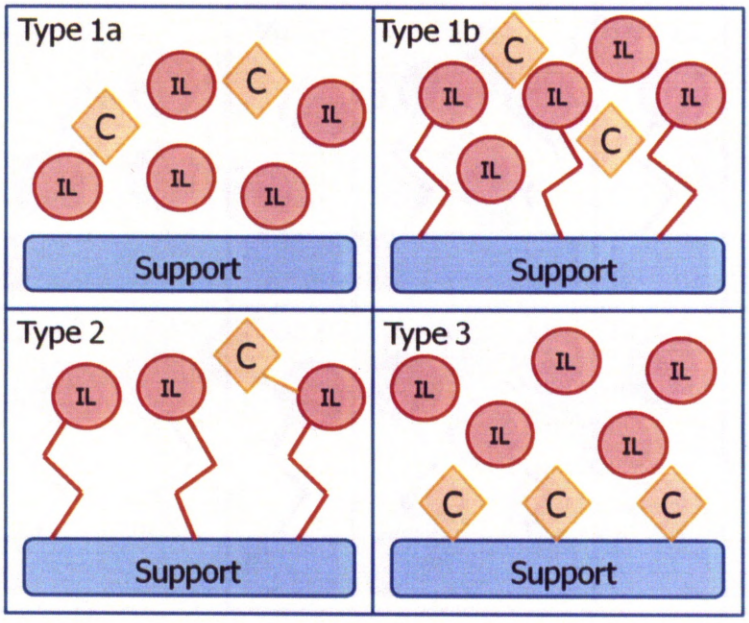

Figure 1.3 Various catalyst-ionic liquid-support combinations

Type 1 consists of a support loaded with a separate ionic liquid phase. The ionic liquid is deposited on the support as a multilayer and acts as an immobilizing medium for the catalyst. The simplest method for preparing this type of system, denoted Type 1a in **Figure 1.3**, is *via* simple impregnation. Before impregnating the ionic liquid into the porous host, the catalyst, for example, a metal and ligand are dissolved in the ionic liquid phase. Another approach, denoted type 1b in **Figure 1.3**, is to first modify the surface of the support with ionic liquid fragments after which, additional ionic liquid and the catalyst are impregnated into the modified support.

Type 2 SILP-catalyst systems are prepared by directly anchoring the ionic liquid to the surface of the support *via* covalent bonding forming a monolayer. The work of Valkenberg *et al.* in the early 21st century made considerable advances in the immobilization of ionic liquids in this manner.[27,34-35,38] Type 2 SILP-catalysts are achieved by post synthetic grafting of the ionic liquid fragments onto a support or by "one-pot" sol-gel synthesis to form a stable solid membrane.[39-43] In these solid materials, the ionic liquid exhibits an almost fluid-like dynamic, despite being confined within a silica network.[40,44] The use of ionic liquids allows us to regard the

gel itself as a stable solid-liquid system termed an "ionogel".[39-40,45-46] Disadvantages of using this technique include the inability to control the concentration of ionic liquid present on the pore surface and the possibility of ionic liquid incorporation in the pore wall. Here, the ionic liquid can be thought of as a ligand, covalently bonded to the support *via* the cation. Part of the anion is then ion-exchanged with anionic catalyst species such as $[WO_4]^{2-}$ or $[PdCl_4]^{2-}$.[36,39,47-49]

Wullen *et al.*[48] were able to produce a composite solid electrolyte *via* one pot synthesis. In this case, [bmim][BF_4], SiO_2 and LiTf were prepared *via* a one-pot sol gel synthesis in which the amorphous SiO_2 network provides the mechanical stability and the ionic liquid/Li salt provide the high ionic conductivity.

Alternatively, the ionic liquid can be covalently anchored to the support *via* the anion. This reduces leaching of the ionic liquid from the support and problems associated with a conventional impregnation route, namely the need to shield the support and ionic liquid from water since any traces of water present during the impregnation step will result in deterioration of the support. This is discussed further in **Section 1.3.4**.

Type 3 SILP-catalysts consist of an ionic liquid impregnated on the surface of a heterogeneous catalyst such as a covalently bonded catalyst[50] or a supported transition metal nanoparticle.[51-57]

1.3.3 Immobilisation *via* the cation

Valkenberg *et al.*[27,34-35,38] have thoroughly explored ionic liquids immobilised *via* an organic cation covalently bonded to the surface of the support. This has a number of advantages over bonding *via* the anion since the functionalised support can be produced in different ways. One option is by reacting an organic compound having suitable reactive groups, such as (ethoxy-alkyl)-silyl groups, with the hydroxyl groups on the surface of the support. Solid covalent bonds are produced as a result of a condensation reaction, with the corresponding alcohol as a by-product. The use of appropriate organic compounds, such as (triethoxysilyl propyl)-alkyl imidazolium chloride, allows the cationic part of the ionic liquids to be applied to a support in large quantities without the structure of the support material being affected.

A second option is the specific incorporation of suitable organic compound in, for example, amorphous silica or mesoporous materials of the MCM-41 type. An organic compound can be incorporated into the support during the synthesis of the support material or via post-synthetic grafting. Thus supports containing the organic bases needed for the ionic liquids can be synthesised by incorporating a suitable amine in the synthesis of the support.[58-64]

An inorganic halide can be added to the functionalised support containing or carrying the organic cation in various ways. The addition method depends on the halide and ionic liquid used. For example, $AlCl_3$ in solution can be added to an imidazolium chloride immobilised on the support. Reaction with the chloride already present produces the chloroaluminate anion. Selection of the suitable solvent is dependant in each case on the halide used. The reaction conditions must also be selected as a function of the halide used; in general the reaction can take place at room temperature.[65-67]

Preferred immobilised ionic liquids *via* the cation are those containing quaternary ammonium, imidazolium, or pyridinium groups, in which one or more of the carbon atoms may be substituted, covalently bonded to the support through a hydrocarbyl or silyl hydrocarbyl linkage. Preferred substituents for the carbon atoms of the quaternary ammonium, imidazolium, or pyridinium groups are alkyl, alkenyl, aralkyl or alkyloxy groups and possibly also containing phosphorus or sulphur as other hetero atoms. The anion is preferably a halide containing aluminium, antimony, gallium, iron, copper, zinc, indium, tin, boron or phosphorus. The anions may also contain transition metal and/or noble metal complexes and ligands which may contain, in addition to carbon and hydrogen, elements such as phosphorus nitrogen, oxygen or sulphur.

1.3.4 Immobilisation *via* the anion

In this case the support is treated with an anion source, *e.g.* inorganic halide, which is selected from inorganic halides suitable for making an ionic liquid. This forms the functionalised support that is then impregnated with the ionic liquid or reagents that react to form the ionic liquid. [65-69]

For the pre-treatment, aluminium, boron, gallium, iron, copper, zinc, indium, and tin halides can be used although aluminium, iron, and tin halides are preferred. Chlorides are the preferred halides, particularly aluminium trichloride.

The treatment step is typically conducted by stirring a slurry of support and a solution of the inorganic halide in a solvent such as dried dichloromethane for approximately one hour at 298 K in an inert atmosphere. The solvent is dried by distillation. The amount of solvent to be used depends on the reaction conditions. Typically, the solvent is used in an amount that allows proper stirring of the mixture. After the treatment, the solvent can be removed by rotary evaporation.

Depending on the support that is used, the ratio of inorganic halide to support in the pretreatment step needs to be optimized. Preferably, the halide reacts with the reactive groups on the surface of the support, typically being hydroxyl groups. Stoichiometric amounts of the inorganic are used, based on the amount and type of reactive groups on the surface. The support is preferably dried prior to contact with the inorganic halide to avoid wasting inorganic halide through the formation of HCl. When using dried supports, the amount of inorganic halide needed to treat the support can be significantly reduced.

The amount of ionic liquid used for impregnating the treated support also depends on the support used and the amount of pretreatment agent on the support. Good results were obtained by Valkenberg *et al.* in processes where an excess of ionic liquid was used, in particular for weight ratio of ionic liquid to support in the range 2:1 to 1:2. Excess ionic liquid after the reaction is removed by Soxhlet extraction with refluxing dichloromethane.[27,34,38]

The impregnation can be conducted by stirring a mixture of the pretreated support and ionic liquid or compounds capable of making an ionic liquid *in situ*. The stirring is usually conducted above the melting temperature of the ionic liquid for at least three hours (often overnight).

It is thought that if a conventional impregnation technique is used, *i.e.* without any pre-treatment to form a functionalized support, the ionic liquid will react with the reactive groups of the support, with formation of HCl. However, if an ionic liquid is present the HCl that is formed will have super-acidic properties, hence, conventional impregnation techniques are expected to result in the formation

of super-acidic HCl, whereas, this is prevented in the method described above. In the case of structured/ordered supports, such as zeolites and MCM-type materials, super-acidic HCl typically was found to destroy the support material.[27]

The inorganic halide is then attached to the support. Upon covalently bonding to the support, it will become part of the ionic liquid that is then absorbed on and into the support. This is thought to be the reason for a decreased leaching of the ionic liquid.[70]

Covalent bonding in SILP systems has been well documented however, physisorption of ionic liquids onto a support has many reported applications and relatively few reports on the analysis of interactions between the ionic liquid and the support. The following sections detail systems in which the ionic liquid is physisorbed onto the support, *i.e.* focussing on types 1a and 1b SILP-catalysts.

1.3.5 Ionic liquids immobilised *via* physisorption

Immobilisation *via* a physisorbed method is common in polymerisation catalysis in which the catalyst is a metal centre with organic ligands. The phyisorption interaction usually occurs between the ligand and the functional groups on the surface of the supporting material.[71-72]

In type 1a and 1b (**Figure 1.3**) the ionic liquid catalyst phase is confined to the supporting material by weak Van der Waals interactions and capillary forces interacting in the pores of the support. In some cases, electrostatic interactions between the ionic liquid and the support can also be applied. Usually, the catalyst is prepared by impregnation, in which a VOC is used initially to reduce viscosity for the impregnation process and is finally removed by evaporation allowing the ionic liquid-catalyst solution to be dispersed on the support.[1,24]

Type 1b systems contain covalently bonded ionic liquid corresponding to monolayer coverage in the hope of avoiding any detrimental surface interactions. This additional treatment is often not necessary when the ionic liquids used are non-acidic and do not undergo reaction with the support surface. Therefore, neutral ionic liquids with inert ions are chosen for SILP-catalysis, eliminating the need for the pre-impregnation covalent grafting.

It should be noted however that 1,3-dialkylimidazolium cations may undergo carbene formation with basic supports. Considering the anion, halogen containing ions are usually avoided as the presence of fluorine can be problematic. This is due to restricted disposal options and the elevated price of hydrolysis stable fluorinated anions such as $[(CF_3SO_2)_2N]^-$ and $[CF_3SO_3]^-$.

The physical entrapment of catalysts in which the active molecule is added during the synthesis of the solid support and the "ship in a bottle" method in which the catalytically active complex is assembled within the pores of the support have both been described previously as physisorbed, immobilised complexes.[73]

The "ship in a bottle" procedure has the advantage that while the complex cannot leave the pores due to steric constraints, it is not restricted in its movement within the pore and can therefore be expected to resemble its homogeneous counterpart. Reactants can diffuse through the pore channels, however, the diameter is too narrow for to allow leaching of the catalyst. This allows the product to be released. The main drawback of this method is steric hinderance due to limited pore sizes, which have so far prevented the use of this group of catalysts in an industrial process. Nevertheless, the catalysts synthesized in this way show enhanced stability.[74]

There are two main methods that are used in the synthesis of physisorbed SILP systems. The first method is to use a volatile cosolvent and is the most common approach as it requires no specialised instrumentation or equipment. In this case, a solution of the ionic liquid is dissolved in a solvent (with a relatively high vapour pressure) that is then coated onto the support. The solvent is then evaporated leaving the RTIL on the surface. This relatively simple method is used to produce thin RTIL films, although the thickness of the physisorbed layer is difficult to control.

Bovio *et al.*[75-76] produced thin [bmim][NTf_2] films on mica by evaporation of a volatile cosolvent (methanol). Using the same method, Du *et al.*[77] deposited [bmim][BF_4] onto single walled carbon nanotubes leading to a series of SILPs. In both examples, X-ray photoelectron Spectroscopy (XPS) was used to analyze the composition of the thin film, and to confirm that there were no side reactions between the pure RTIL, the cosolvent (methanol) and the support materials.

A second method involves direct vaporization deposition of the RTIL under ultra high vacuum (UHV) conditions. Many aprotic RTILs can be successfully vaporized as neutral ion pairs at reduced chamber background pressures ($<10^{-5}$ mbar) and elevated temperatures (>273 K).[78-79] Direct deposition can, in principle, occur *via* the deposition of neutral ion pairs onto the support surface allowing a greater level of control over layer thickness and uniformity.

The preferred method, in terms of sample quality, is direct vapour deposition as the amount of RTIL vaporized onto the support can be varied, giving rise to films of tunable thickness. However, vapour deposition is also the most experimentally challenging, as vaporization without decomposition of aprotic RTILs is best achieved at reduced pressures.[78-79]

1.3.6 Applications of SILPs

RTILs have a known affinity for some gases and recent literature has demonstrated their potential as CO_2 storage media[80-89] and in gas separation.[36] With efficient uptake and release of gas, under controllable conditions, ionic liquids could prove to be a viable storage media for gases. SILP could also be applied to gas storage and investigations into this have appeared recently in the literature.

A recent example of SILP gas processing is the work of Kohler *et al.*[90] in their investigation of continuous gas-phase desulfurisation using SILPs. $[C_{12}mim]Cl/SnCl_2$ was immobilized on a meso-/macroporous alumina support with varying loading levels of 10 and 20 vol% by dissolving in dichloromethane. Thermal stability of the SILP system was tested using TGA and showed the system to be stable up to 473 K. Further TGA testing with varying metal content and Lewis acidity showed that the ionic liquids would be stable under the conditions of the gas-phase desulfurisation at 363 K.

A comparison between $[bmim]Cl/ZnCl_2$, $[bmim]Cl/SnCl_2$, $[C_{12}mim]Cl/SnCl_2$ both neat and supported is made. The presence of $SnCl_2$, longer chains on the cation and the enhanced surface area resulting from being supported on porous alumina was found to increase desulfurisation capabilities. The loading of ionic liquid also affected the desulfurisation performance with 30 vol% being unfeasibly too high. This was attributed to the ionic liquid being too mobile and removal by

gravity and convection under the desulfurisation reaction conditions being a possibility. It was concluded that if extraction of any of the ionic liquid was possible, the properties would be undefined and difficulties would arise when trying to estimate their extraction performance. Finally the stability and regeneration of the $[C_{12}mim]Cl$ SILP with 20 vol% was investigated. Four consecutive loading/unloading cycles were successfully completed. However, due to some formation of dibutyldisulfide (n-butyl mercaptan was used as the adsorber) during the sorption cycles, the capacity of the SILP material was found to decrease from one cycle to the next.

Despite this, there is a clear observation that SILP systems can enhance performance of ionic liquids by offering a high gas/liquid exchange area, efficient use of the ionic liquid and short diffusion distances. These properties have also allowed SILP systems to be used in separation science and a variety of catalytic reactions as previously mentioned. They have been summarised in various reviews[24,26] and books.[1] Examples include:

- Heterogeneous oxidation of pyrimidine and alkyl thioesters using a variety of ionic liquids over mesoporous Ti and Ti/Ge catalysts;[91]
- Acylation of sulfonamines using covalently anchored 1-butyl-3-(3-triethoxysilylpropyl)-4,5,-dihydroimidazolium on silica (a macroporous and mesoporous example were investigated) as catalysts;[92]
- Rhodium-catalysed hydrogenation of propene using $[omim][NTf_2]$ supported on non-porous corrugated polystyrene sheets and porous silica-filled polyethylene composite sheets;[93]
- $[bmim]Cl/AlCl_3$ immobilized on silicon dioxide, and titanium dioxide and zirconium oxide surfaces for alkylation of aromatic compounds with dodecene;[38]
- Suzuki coupling reactions using a palladium catalyst within *N*-3-(3-triethoxysilyl propyl)-3-methyl imidazolium chloride covalently bonded to mesoporous silica, SBA-15;[33]
- Suzuki and Heck reactions catalysed by a SILP system containing a *N*-heterocyclic carbine palladium complex contained in an *N*-3-(3-triethoxysilyl propyl)-3-methyl imidazolium chloride phase covalently anchored to SBA-16;[94]

- Selective hydrogenation of cinnamaldehyde catalysed by a Pd nanoparticle SILP system in which the ionic liquid was again *N*-3-(3-triethoxysilyl propyl)-3-methyl imidazolium based, covalently attached to silica gel.[95]

The focus of research into SILP systems is dominated by their potential applications.[35,38,56,93-94] However, the local structure and changes in molecular motions of the RTIL upon encapsulation are unreported and in-depth studies on the effects of confinement on the physical properties of the RTIL are few.[40,96-97] Since the aim of this research is to focus on the characterisation of interactions between the ionic liquid and the support material, in-depth discussion of applications of SILP systems has been omitted. Characterisation techniques that are currently being used to analyze SILPs are described in **Section 1.5** with other techniques used to characterise the support material and ionic liquids in the bulk.

RTILs have been used for templating mesoporous silicas[98-100] which suggests that there may be significant interaction between the components of the ionic liquid and the structure forming components that template pore formation.[101] Mesoporous silicas are, therefore, ideal candidates for the study of supported RTIL phases as the pore size, volume and surface area can be tailored in a known fashion. Potential support material, their synthesis and properties will now be discussed in the following section.[100,102]

1.4 Potential supporting materials

Support materials for ionic liquids can be microporous (<2.5 nm), mesoporous (2.5-20 nm) or macroporous (>20 nm) (**Figure 1.4**). According to Valkenberg *et al*, it is preferable that supports have BET surface areas of 100 to 1200 m^2/g.[27]

Support materials can range from solid oxide materials such as clays, silica, alumina, aluminosilicates, zeolites, titanium dioxide, boron oxide, to any other metal oxide containing hydroxyl groups on the surface. Such supports include MCM-types of mesoporous materials that have a desirable high surface area for supporting RTILs.

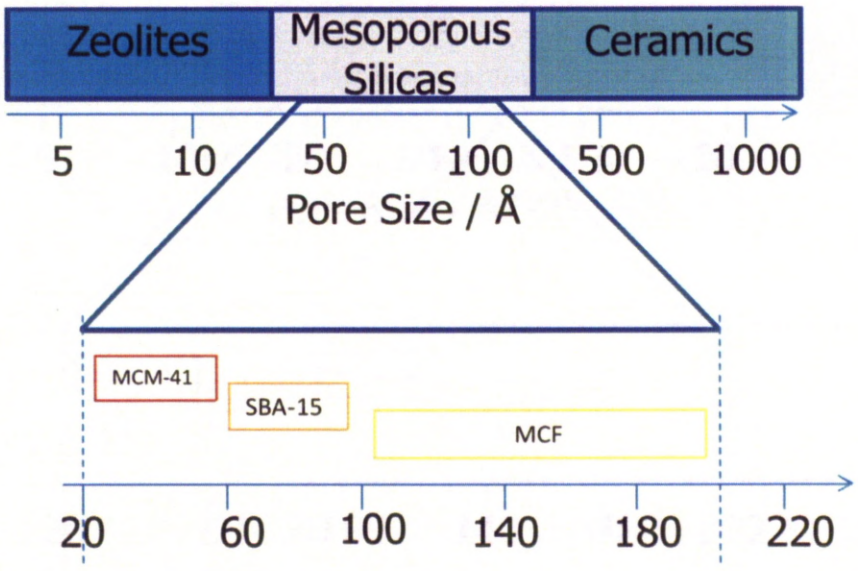

Figure 1.4 Schematic diagram of mesoporous solids and their pore diameters

Depending on the ionic liquid to be supported, treatment of the support material may be necessary. Where the support is contacted with a water-sensitive ionic liquid, the support should be dry. Such dried supports can be obtained by any suitable technique, for example, calcination, desiccation, etc. Depending on the chemical structure of the support, calcining may be the preferred way of drying the support. Supports based on silica, alumina, aluminosilicate, such as zeolite and mesoporous materials of the MCM type, are preferably dried by calcination. The calcination temperature is not critical, and the temperatures applied will be determined by the chemical structure of the support. Typically, calcination is performed at temperatures in the range of 723 to 873 K, for 1 to 6 hours in order to render supports suitable for use in immobilization.

1.4.1 Mesoporous silica materials

Porous silica materials encompass a range of materials from microporous zeolites to macroporous diatoms which are microscopic single-celled algae that inhabit fresh and saltwater bodies throughout the world. Over the last few decades, porous silica-based materials have been used for an increasing amount of applications such as catalysis in the petrochemical industry,[103] as sorbents in gas

separation[104] and in the synthesis of chemical[105-106] and pharmaceutical products.[107-108]

Mesoporous silica materials have a well defined pore size and shape. They have large surface areas (*ca.* 1000 m^2/g) and pore volumes in addition to possessing high thermal and hydrolytic stability. Most examples of mesoporous silica materials also have a high degree of pore order. Due to the increased pore size with respect to microporous zeolites, mesoporous materials are a viable candidate for SILP support materials as the pore dimensions should accommodate layers of ionic liquids without pore blockage.

The first group to synthesise and report ordered silica materials with porosity on the meso scale was the group of Beck *et al.* at Mobil in 1992[109] in their synthesis of Mobil Corporation Material (MCM-41). MCM-41 has high thermal stability and pore diameters in the region of 20-40 Å. The increased pore dimensions of MCM-41 in comparison to its zeolite counterparts has enabled host-guest chemistry with larger molecules *e.g.* metal clusters[110] and proteins.[111] Since the discovery of MCM-41 a significant number of researchers have investigated the formation of various other mesoporous silica phases which has lead to a variety of mesoporous silica materials with differing pore sizes and structural arrangements. Some of these materials are summarised in **Table 1.3**.

1.4.2 Synthesis of mesoporous silica materials

The discovery of MCM-41 opened a new field of research in materials science. Subsequent synthetic routes were developed to produce different structures of mesoporous silicas and non-silicious mesoporous materials.[60,112-115] The discovery of these new materials with their tunable pore dimensions and morphologies motivated several scientific groups to refine their and understand the synthetic conditions. One of the most notable groups is that of Stucky at the University of California, Santa Barbara who synthesised a range of materials denoted SBA-n[116-118] by using different surfactants and reaction conditions. Zhao *et al.* at the University of Fudan, China and Ryoo *et al.* at the Korea Advanced Institute for Technology also produced a range of similar materials denoted FDU-n[119-122] and KIT-n respectively.[123-126]

Mesoporous silicas are commonly synthesized by templating (**Figure 1.5**). This involves formation of micelles during a hydrothermal synthesis (sol-gel process) that is carefully controlled by molar composition, pH, temperature, additives and water content. Upon the removal of the template (usually by calcination), a silica network is maintained creating ordered cavities throughout the network with morphological features in common with those of the absent template. Structures such as MCMs use surfactant templates to form porous networks.[127-131] Micelles formed by surfactants tend to pack in spheres to minimize repulsion which is advantageous to the uniformity of pores determined by the size and shape of the micelle aggregates.

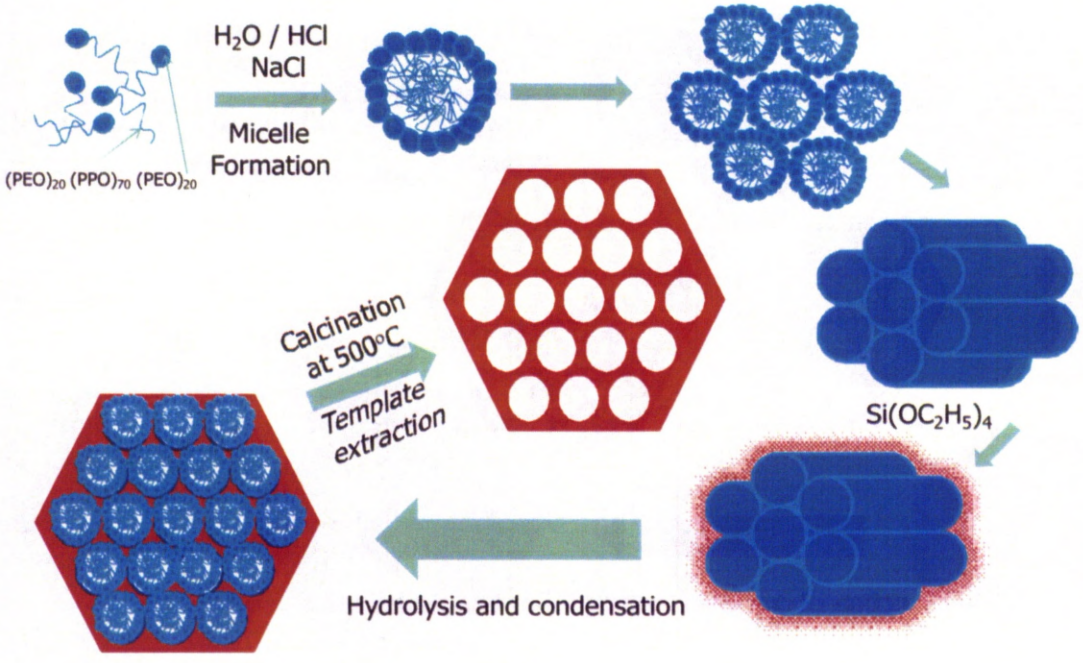

Figure 1.5 Surfactant templating of SBA-15

The surfactant templates used for the synthesis of MCM, SBA, and other mesoporous silicas are detailed in **Table 1.3**. A typical route is to hydrolyse a silica precursor such as tetraethylorthosilicate (TEOS) under controlled pH and temperature in the presence of a surfactant such as P123 ($PEO_{20}PPO_{70}PEO_{20}$), a tri-block copolymer, used in the synthesis of SBA-15 (**Figure 1.5**). P123 forms micelles when dispersed in an acidic solution. The symmetry of the surfactant mesophase, in this case hexagonal, is subsequently replicated on the structure of

the porous solid. Heating the resulting gel during the reaction to a high temperature under static conditions allows condensation of the TEOS precursor around the micelles. The surfactant is then removed by calcination (used for extraction of P123) or an ion exchange process (used if an organic functionality has been added to the network that may be sensitive to high temperatures).[132]

The literature documents two mechanisms explaining the formation of MCM-41 by cationic liquid crystal micellar templating. Here the silica is in the form of a complex mixture of molecular and polymeric anionic species which exhibit control over the template. In the first a liquid crystal phase is present prior to the addition of the silicate species (labelled 1 in **Figure 1.6**) and in the second the addition of the silicate species itself is the driving force behind the aggregation of the subsequent silicate-encased micelles (labelled 2 in **Figure 1.6**). Davis *et al.*[133] used in situ ^{14}N NMR spectroscopy to conclude that the first mechanism is absent in the formation of MCM-41. Further work by Steel *et al*,[134] again with analysis by ^{14}N NMR spectroscopy showed that the second mechanism was correct.

Further work by Stucky *et al.*[135-136] proposed an alternative model in which the formation of the silica mesophase is divided into three steps; multidentate binding of the silicate oligomers to the cationic surfactant; preferential silicate polymerisation; followed by charge density matching of the silicate and surfactant. This was observed using X-ray diffraction which showed the presence of a lamellar phase prior to the formation of the hexagonal structure (labelled 3 in **Figure 1.6**).

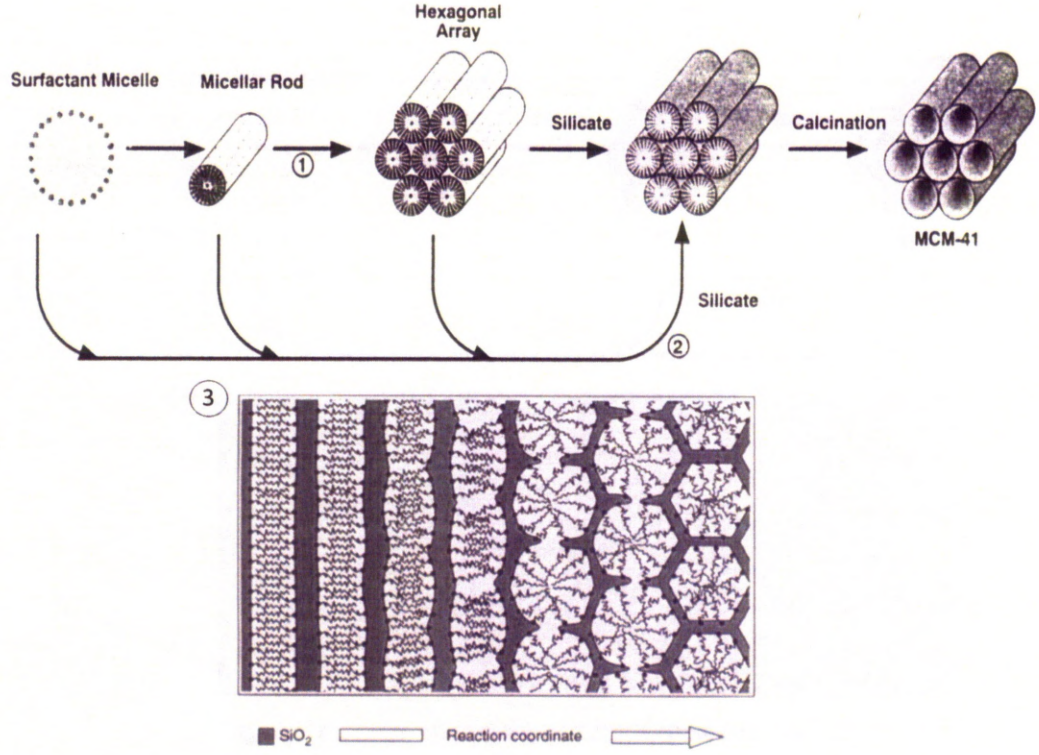

Figure 1.6 Liquid crystal templating mechanism proposed for the synthesis of MCM-41 by Beck *et al.*[109]) liquid crystal phase is present before the addition of the silicate species, 2) shows that the addition of the silicate species itself is the driving force behind silicate encased surfactant micelles, 3) Method proposed by Stucky *et al.*[135] in which a lamellar phase is formed before characteristic hexagonal array of pores is observed.

Table 1.3 Mesoporous structures synthesised using surfactant templating

Mesoporous Material	Surfactant	Mesophase
SBA-1	Cationic (CTEABr) $CH_3(CH)_nNEt_3$	3D Cubic
SBA-2	Gemini C16-3-1	3D Hexagonal
SBA-15	Non-ionic triblock copolymer (P123) $PEO_{20}PPO_{70}PEO_{20}$	Hexagonal planar
SBA-16	Non-ionic triblock copolymer (F127) $PEO_{106}PPO_{70}PEO_{106}$	Cubic
FDU-12	Non-ionic triblock copolymer (F127) $PEO_{106}PPO_{70}PEO_{106}$	Cubic
KIT-6	Non-ionic triblock copolymer (P123) $PEO_{20}PPO_{70}PEO_{20}$	Cubic
MCM-41	Cationic (CTMABr)	Hexagonal planar
MCM-48	Cationic (CTMABr)	Cubic
MCM-50	Cationic (CTMABr)	Lamellar
FSM-16	From Kanemite	Hexagonal planar
HMS	Alkylamines	Hexagonal disordered

SBA-15 and MCM-41 both consist of a hexagonal array of mesopores and differ only by their pore diameters (SBA-15 ranging from 50 – 100 Å compared to *ca.* 20 Å for MCM-41). The increase in wall thickness compared to MCM-type materials gives SBA-15 an enhanced hydrothermal stability. The increased wall thickness may be related to the changes at the inorganic/template interface. With cationic templating the inorganic walls do not entangle with the template and a well defined interface is formed. However, with block co-polymers the PEO blocks are integrated with the inorganic phase which has been confirmed *via* solid-state NMR spin diffusion experiments.[137-138]

Integration of the PEO template components with the inorganic phase also results in the presence of microporosity. However, this can be further controlled by adjusting the temperature (*ca.* 363 K) and time (0 - 48 hours) of ageing. Longer aging times lead to a reduction in microporosity, inferring that

improved segregation of the PEO and inorganic phases must occur with increasing aging time. Temperature and aging time in turn affect the wall thickness and degree of pore wall condensation.[139]

In this study, SBA-15 and MCM-41 materials have been used as support materials. The following section will now discuss the techniques used to characterise these materials, ionic liquids and SILPs.

1.5 Characterisation of RTILs, support materials and SILPs

1.5.1 RTILs

As there is a huge range of RTILs available, their properties vary greatly. The following discussion of characterisation techniques used to investigate structure and properties of RTILs is therefore not exhaustive or comprehensive. For further information the reader is referred to **Chapter 4** of Wasserscheid and Welton.[1]

Until recently, the majority of literature detailing ionic liquids characterisation was focussed on the arrangement of RTILs in molecular solvents. Of late, a variety of techniques have been used to investigate the liquid structure of ionic liquids such as neutron diffraction and X-ray scattering. Properties of ionic liquids, such as their electrochemical properties, viscosity measurements and solubilities, are widely documented. Since the context of this research is to probe molecular level structures, this section will focus on methods used to probe the molecular structure and dynamics of ionic liquids.

Neutron diffraction is one of the most widely used techniques for investigating the structure of ionic liquids. This experiment involves the elastic scattering of neutrons off nuclei in the sample that are then detected at different scattering angles. The resulting scattering profile is then analyzed to yield structural information.

Bowron *et al.* used neutron diffraction to study the structure of [mmim]Cl. The total structure factors, F(Q), for five [mmim]Cl melts were measured, including fully protiated, fully deuterated, a 1:1 mixture, ring only deuterated and chain only

deuterated. The specific local structure showed strong interactions between the chlorine ion and ring hydrogens as well as some interaction with the methyl groups of adjacent imidazolium cations. This was found to be consistent with the crystal structure and implies that the molecular packing and interactions in the first two and three coordination shells is similar in both the liquid and the crystal. The structure of [mmim][PF_6] has also been found to be analogous to this.[1,140]

X-ray diffraction has been used to study both simple molten salts and a wide range of RTIL liquid crystalline phases. The RTIL crystalline phase is normally achieved by increasing the amphiphillic character of the cation through substitution with longer, linear alkyl groups. When alkyl chain lengths are small ($n < 10$) the melting point is relatively low, close to room temperature, whereas, liquid crystal mesomorphism is displayed for $n > 12$.[141-142] Liquid crystalline phases have also been widely investigated using NMR, DSC and single crystal X-ray diffraction. [143-145]

Other techniques include direct recoil spectroscopy[146-148] and metastable atomic electron spectroscopy[149] for investigating the surface structure of ionic liquids X-ray and neutron reflectivity has been used to probe the structure of multilayers both in self supporting films and adsorbed on surfaces. Computational modelling is also becoming more informative and there are many reports of molecular dynamic simulations of ionic liquids in order to understand their structure and dynamics. The reader is again referred to the literature for a more in-depth description.[1,150-151]

NMR spectroscopy has been widely used in the characterisation of ionic liquids as summarised in the recent review by Ananikov[152] and earlier by Giernoth.[153] Both reviews document various NMR techniques that can be employed to investigate the structure, reorientational dynamics, diffusion, interactions with co-solvents and gases and reactions involving ionic liquids. Three main challenges arise when acquiring NMR experiments of ionic liquids; high viscosities, most RTILs not being available in a deuterated form and line broadening caused by salt-containing samples.[153] The scope of this research has extended to elucidation of structures and investigation of the changes in reorientational dynamics of the ionic liquid upon encapsulation discussed in the following sections.

1.5.1.1 Structural determination of RTILs using NMR spectroscopy

The spectra of neat ionic liquids can often be recorded quickly and easily using a single pulse experiment such as ^{1}H, ^{13}C and ^{31}P spectra, on commercially available NMR spectrometers. Issues such as viscosity and line broadening can be overcome by spinning the sample or elevating the temperature. 2D NMR homo- and heteronuclear experiments can also be performed to observe couplings between nuclei that are in close proximity to each other.

Lin *et al.*[154] have studied variations in the chemical shifts for a variety of methylimidazolium salts with different alkyl chain substituents and Br^-, BF_4^-, and PF_6^- anions. They observed a high sensitivity in chemical shift (depending predominantly on the alkyl chain length) for the two protons in the imidazolium ring. The effect was most pronounced for the bromide salts. The change in chemical shift for different imidazolium ILs has also been investigated by Lyčka *et al.*[155] using ^{15}N NMR spectroscopy. They found that the length of the alkyl chain has a much larger effect on the ^{15}N chemical shifts than the choice of anion. Since unsymmetrically substituted RTILs give individual signals for the two nitrogen nuclei, a small asymmetry in the nitrogen charge distribution of the aromatic ring was proposed. The group of Blümel,[156] on the other hand, found very similar electronic surroundings for the two nitrogen atoms when using ^{14}N NMR spectroscopy. Although they also were able to distinguish between the two signals, these showed very similar half-widths. This also proved that the counter anions did not interact preferentially with one of the nitrogen atoms.

To gain more structural insight into neat ILs, 2D homonuclear NMR spectra such as ^{1}H-^{1}H-NOESY NMR has been used for the determination of H–H distances in the liquid state. In the work of Carper *et al*,[157] short mixing times (below 50 ms) the NOESY-distances were in good agreement with theoretical results. Longer mixing times (> 50 ms) resulted in unrealistically short H–H distances due to substantial spin diffusion. Mele *et al.*[158] also investigated cation–cation interactions and distances using NOESY experiments. They compared [bmim][BF_4] with [bdmim][BF_4] and were able to correlate their NMR data with X-ray crystallographic data. It was noted here that even in the liquid state significant interaction of the butyl chains with the polar domains could be detected. The latter two publications

clearly show that neat ionic liquids are supramolecularly ordered in a fashion that mimics the solid state structures.

1.5.1.2 Reorientational dynamics of RTILs determined by NMR spectroscopy

While it is often relatively simple to describe the molecular structure and dynamics of gases and solids, liquids can undergo vibrations, rotations and translations for which a suitable model must be described. The model that is used frequently to describe these motions is the rotational diffusion model, which assumes that molecules rotate by small angular steps about the molecular rotation axes. One quantity that describes the rotational speed of molecules is the reorientational correlation time, τ, which is a measure of average time elapsed when a molecule has rotated through an angle of the order of 1 radian (*ca.* 57^0) and is indirectly proportional to the velocity of rotational motion. A particularly important tool for obtaining information on the reorientational dynamics of molecules is the measurement of spin lattice (T_1) relaxation times using NMR spectroscopy. The relationship between τ and T_1 is described in **Section 2.5.3.2**. There are numerous reports of spin lattice (T_1) relaxation measurements used in combination with NOE experiments to investigate the reorientational dynamics of ionic liquids in solutions and the solid state.[159-166] The data acquired can be used to determine inter-ionic interactions and phase transitions.

Dölle *et al.*[159] examined the reorientational dynamics of [bmim]PF_6 and evaluated the results *via* mathematical fits and comparison to modelling results. They found strong H▪▪▪F bonds *via* quantum-mechanical calculations of ion-pairs and were able to confirm their findings also for the liquid phase. From these results, they assumed that these H-bonds may lead to even higher aggregates with a kind of layer structure. The combination of the hydrogen bonds with strong Coulombic interactions, so they claim, might be the most prominent reason for the relatively high viscosities of many RTILs. In a similar study,[161] the same NMR techniques were employed, this time focussing on [mnim]PF_6[164] and [emim]$BuSO_4$[160] without any significant new findings.

Hayamizu and co-workers[165] have used ^{1}H, ^{19}F and ^{7}Li T_1 relaxation as well as diffusion studies to investigate the reorientational dynamics of *N,N*-diethyl-*N*-methyl-*N*-(2-methoxyethyl) ammonium bis(trifluoromethylsulfonyl)amide. Imanari *et al.*[166] focussed on [bmim]Br for the detection of phase transitions and were able to trace a liquid state as well as super-cooled liquid and a coagulated state by measuring ^{1}H T_1 relaxation times in the temperature range 203 to 393 K. With their data they could also determine the activation energy for rapid reorientational motions. By measurement of spin-spin (T_2) relaxation times they were also able to show that two reorientation motions occur in the vicinity of crystallisation temperature. In a later study by the same authors of the same ionic liquid, ^{13}C T_1 relaxation times were recorded at magnetic field strengths. Discrete segmental motions of the imidazole ring and butyl chain were clearly identified.[167]

The relaxation techniques used in the literature are described in detail in the following chapter.

1.5.2 Support materials

Mesoporous silicas, unlike zeolites that have molecularly ordered repeating units, do not contain any crystalline regions. The amorphous nature of the mesoporous silica network makes detailed analysis of molecular properties more difficult by techniques such as X-ray diffraction. X-ray diffraction can, however, be used to identify pore geometries as described in **Section 2.1.3**. Pore diameters, surface areas and volumes are characterised by N_2 gas sorption isotherm analysis as detailed in **Section 2.2**. Solid-state NMR spectroscopy can be used to identify the degree of condensation of silica within the network by acquiring ^{29}Si NMR spectra. ^{13}C NMR spectra and ^{1}H NMR spectra can be used to identify whether removal of the surfactant template has been successful. Solid-state NMR spectroscopy is commonly used for characterising porous silica products that have had functionalities incorporated onto the surface of pores (such as amines)[62] or into the backbone of the structure to produce periodic mesoporous silicas (PMOs)[168] as the new organic groups would appear in ^{1}H and ^{13}C NMR spectra. T-sites would also be observed in ^{29}Si NMR spectra which correspond to Si bonded to C in different coordination environments. More advanced NMR techniques such as ^{1}H-^{29}Si Heteronuclear Correlation experiments can also be used to determine what

proton environments are associated with silicon.[169] This is detailed further in the following chapter.

1.5.3 SILPs

Recent literature includes investigation of RTILs supported on silica surfaces[34,36,76,92] such as silica monoliths,[170] nano-SiO_x[171] and silica gels,[95,172-173] inside carbon nanotubes,[77,174] between graphite walls,[175-176] on networked polymers[177] and on alumina thin films.[178-180] The characterisation of the surface interface of the RTIL however has proven challenging due to the limited number of techniques available. As well as the aforementioned techniques, sum frequency generation spectroscopy (SFG)[181] is often mentioned and has been used extensively to probe the gas-liquid interface.[182] Photoelectron spectroscopy has also played a key role in characterising ionic liquid interfaces (that is, the interface between an ionic liquid and gas, solid support or a catalyst).[6] Atomic force microscopy has been used to observe layering of RTILs on support surfaces.[75,183-185] Confocal Raman spectroscopy has been used to elucidate interactions between RTILs (based upon the $[bmim]^+$ cation with a fluorinated anion (PF_6^-, BF_4^- and NTf_2^-) and polymer films (Nafion®).[186] Fourier transform infra-red spectroscopy (FT-IR) and Raman spectroscopy have also been used to investigate the vibrational modes of surface molecules at a liquid-gas interface and to deduce the orientation of the cation molecules at the surface.[187] Here it was found that the preferred orientation of the imidazolium cations at the interface can be parallel or perpendicular and depend on factors such as the presence of water, length of alkyl chains in the cation and anion interactions. Direct recoil spectroscopy has also shown that the surface of the ionic liquid is ionic in nature, equally occupied by cations and anions with no segregation.[188]

With respect to the ionic liquid solid-interface, X-ray reflectivity has been used to identify molecular layering and local order in thin liquid crystalline films of $[mmim]PF_6$ and $[omim]PF_6$ (100 - 120 Å in thickness) on polished silicon wafers.[189] In this report initial spin coating of a solution of the ionic liquids in methanol was followed by heating of the samples into an isotropic state and crystallization. The appearance of Bragg diffraction peaks in the reflectivity profiles indicates the presence of an ordered structure. Modelling of the data was then performed and

together it was suggested that the ionic liquid on the silicon support consisted of a multilayer stack of interdigitated amphiphillic bilayers with charged layers at the silicon and air interfaces. This is analogous to the data from direct recoil spectroscopy and suggests a predominantly ionic character at the surfaces.[188]

NMR spectroscopy has a variety of techniques that can be used not only to deduce the structure of an ionic liquid but also changes to dynamics upon encapsulation. Some specific examples detailing NMR characterisation of SILPs are given in the introduction to **Chapters 3** and **4**.

Previously NMR spectroscopy has suffered from low concentration of catalyst in the ionic liquid and has therefore been an unpopular choice of analysis for SILP catalysts. Viscosity is also an issue when recording high resolution NMR spectra due to the broadening of resonances. However, previous studies have been able to combine the results for the reorientational dynamics with viscosity data to compare experimental correlation times with correlation times calculated from hydrodynamic models.[160] By combining experimental and theoretical methods it is possible to make statements about the intermolecular structure and the interactions present in ionic liquids that give rise to specific properties.[157,190-191]

Sensitivity improvements have been attempted, with most approaches using deuterated ionic liquids in order to minimize the number of proton environments thus improving the resolution of the protons on the catalyst. Hardacre *et al.*[192] describe a synthesis and application of fully deuterated ionic liquids while Giernoth *et al.* describe the transition metal free deuteration of imidazolium ionic liquid cations.[193] Giernoth also describes a way to separate ionic liquid signals from reactant (or catalyst) by making use of their relative mobilites and using a pulse field gradient NMR experiment.[194] The aim of the research documented herein is to display how combination of a variety of NMR techniques can be used to gain an understanding of the structure of both the support material and the ionic liquid, the location of the ionic liquid with respect to the support and the interactions between them.

1.6 Aims of the project

This chapter has described how supported ionic liquids can be used for a range of applications from catalysis to gas storage and processing media. This is due to the combination of ionic liquids with their wide range of tunable properties and a support material that can also be tailored. Thus far, investigations have been dominated by the potential applications of SILP systems with less attention being paid to the characterisation of the interaction between catalyst-ionic liquid, support-catalyst and ionic liquid-support. To this end, the aims of this project are to bridge this deficit in the literature.

Due to the broad nature of this task, this research will focus on the interaction between the ionic liquid phase and the support material by using a combination of analytical techniques. Two model systems have been selected. In the first, [bmim]OTf is supported on mesoporous silica, SBA-15. In the second, [bmim]CH_3SO_3, which is solid at room temperature, is supported on SBA-15 and MCM-41. The ionic liquids used were chosen because of their ease of handling and similarity in structure. The loading of ionic liquid onto the support materials will be investigated in both cases. Techniques used in these investigations will include PXRD and N_2 adsorption isotherms to characterise the silica supports and monitor any changes to the support materials that might occur upon loading of the ionic liquids. Solid state NMR experiments such as T_1 inversion recovery, CP-MAS, kinetics and heteronuclear correlations will be used with the aim of monitoring changes to structure and dynamics of the ionic liquid upon impregnation into the support. More specifically, T_1 and kinetic experiments will be used to observe different ionic liquid environments within the pores of the silica supports. The orientation of the ionic liquid with respect to the pore walls will also be investigated using heteronuclear correlation experiments.

Additionally, NMR spectroscopy has also been used to characterise gas uptake by clathrate hydrates. The ability to obtain high resolution ^{13}C CP-MAS and $^{13}C\{^1H\}$ MAS NMR spectra has allowed not only full characterisation of the clathrate hydrate but also a quantitative measure of methane gas present in the clathrate hydrate structure.

Chapter 2

Characterisation Techniques

This chapter summarises the various techniques used to characterise materials made in the course of the research documented in this thesis. This chapter will describe the principles behind each technique, set up of the instruments and other details that are important to consider when analysing materials such as ionic liquids, mesoporous silicas and clathrates. The techniques detailed herein are common to both **Sections I** and **II** and will be referred to in the following chapters accordingly.

2.1 X-Ray diffraction

X-ray diffraction[195-198] is a technique used to characterise a material with an ordered array of scattering centres. These scattering centres are generally a repeating array of atoms in a crystal. A beam of X-rays impinging on a material will be scattered radially by the atomic electrons. If the scattering centres are separated by a distance comparable to the wavelength of the X-rays (typically a few Angstroms) then interference between the X-rays scattered from particular electron centres can occur. If the array of electron centres is ordered, interference maxima and minima occur giving rise to a diffraction pattern. Mesoporous silicas contain an ordered array of pores with a separation that fulfils this criterion therefore diffraction can occur.

2.1.1 X-ray production

Seventeen years after the discovery of X-rays by Wilhelm Rőntgen in 1901,[199] Max von Laue suggested that they may diffract if passed through a crystal.[200] X-rays are electromagnetic radiation that can be generated by bombarding a metal with high energy electrons. The electrons are "boiled off" from a heated cathode by thermionic emission and accelerated by a large applied electrical potential, through a vacuum towards an anode target (**Figure 2.1**). The anode is usually a Co, Cu or Mo target.

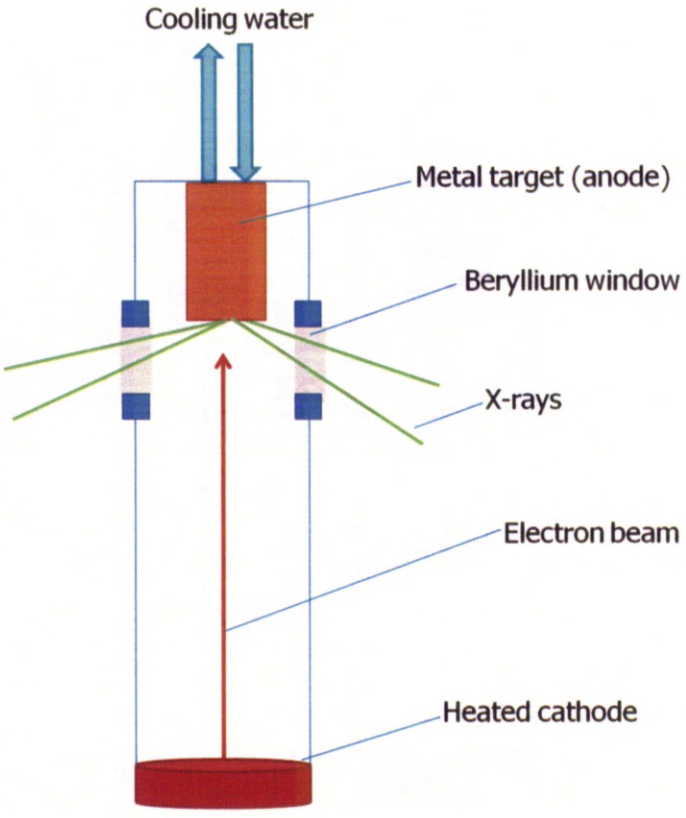

Figure 2.1 X-rays are generated by directing a beam of electrons onto a cooled target

Two distinct processes are involved in the emission of X-rays. In the first process, some electrons are slowed down or stopped by the target and some or all of their kinetic energy is converted to a continuous spectrum of photons, including X-rays. This process is known as *Bremsstrahlung*, german for "breaking radiation" and does not depend on the target material. The continuous *Bremsstrahlung* background radiation is shown in **Figure 2.2.**

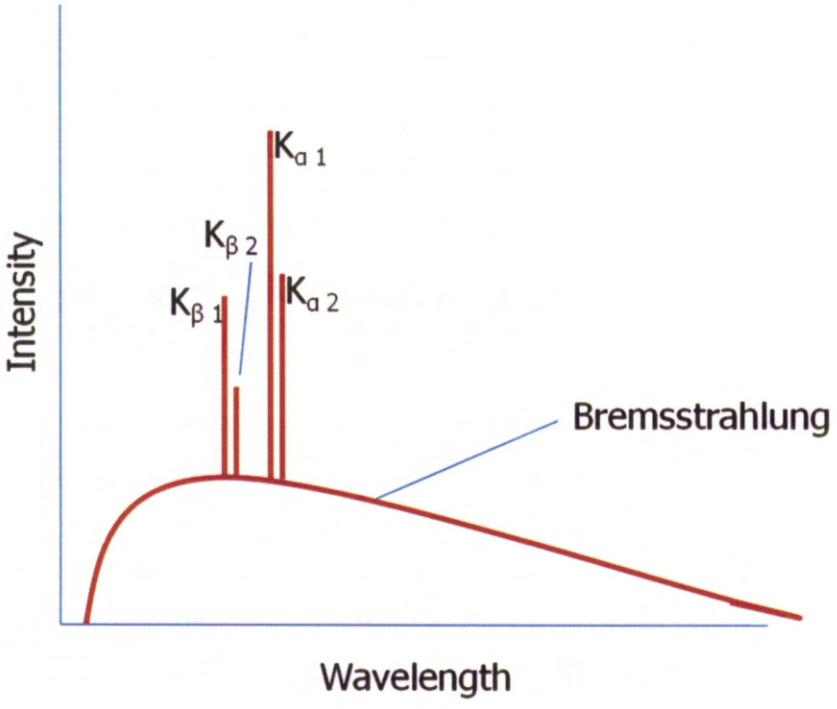

Figure 2.2 X-ray spectrum produced by a metal anode

The second process that gives rise to X-ray radiation does depend on the target material. These X-rays are produced when an electron with enough kinetic energy collides with the electrons in the inner shells of the target's atoms. The collision can expel an electron or excite it to a higher state causing a vacancy. An electron of higher energy then drops into the vacancy emitting energy in the form of an X-ray photon (**Figure 2.3**). As X-ray photons are quanta of energy (equal to the energy drop of the electron), they appear as intense sharp peaks superimposed on the *Bramsstrahlung* continuum (**Figure 2.2**). These peaks correspond to the electron shells involved in producing the X-ray, for example, if the 1s orbital is filled, and this has quantum number 1, it is given the symbol K. This is common for copper targets where electrons drop from 3p→1s or 2p→1s and are denoted K_α and K_β, respectively. Both lines are doublets due to the spin multiplicity in p shells. In copper, the K_α peak in the spectrum consists of two lines at 1.5406 Å and 1.5444 Å for $K_{\alpha 1}$ and $K_{\alpha 2}$ respectively.[198]

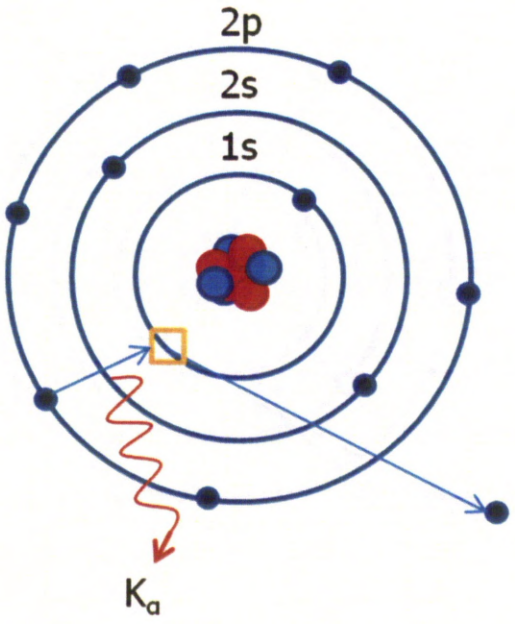

Figure 2.3 Electron vacancy filling and X-ray photon emission

In order to carry out a diffraction experiment, often a single X-ray wavelength is desired. This can be achieved by using a crystal monochromator in which, the X-ray beam coming from the X-ray tube impinges on a single crystal, positioned in a fixed orientation. For a particular angle, θ, and by implementing Bragg's Law, only one wavelength can be diffracted from the single crystal. A filter can also be used to eliminate unwanted wavelengths.

X-ray filters consist of a foil of a metal that has an atomic number two below that of the target used to generate the X-rays. In the foil, transitions between energy levels require less energy due to reduced nuclear charge. This leads to a high absorption coefficient of the X-rays generated. For example, for an X-ray beam generated at a copper target, a nickel filter will absorb X-rays with wavelengths less than 1.5 Å. Therefore, most of the *Bremsstrahlung* radiation will be absorbed as well as peaks from K_β. The X-rays that exit the filter are monochromatic K_α radiation. Since K_α radiation occurs as double peaks that have close wavelengths, diffraction experiments produce close doublets in the diffraction patterns. There are two ways in which to use the monochromatic X-rays produced; single crystal X-ray diffraction and powder X-ray diffraction (PXRD).

2.1.2 Diffraction techniques for powdered samples

This section focuses on PXRD as this is the predominant diffraction technique used for the research contained in this thesis. In single crystal X-ray diffraction, developed initially by Von Laue,[200] a broad beam of monochromatic radiation is passed into a single crystal and the diffraction pattern is often recorded photographically. In comparison, powder X-ray diffraction, developed by Debye, Scherrer and independently, Albert Hull, the monochromatic radiation is exposed to a powder sample. A powder in this context refers to a large number of crystallites that are randomly oriented wherein at least some crystallites are oriented such that diffraction can occur. This diffraction is in the directions governed by the Bragg equation (see **Section 2.1.3**).

The diffractometer uses an X-ray detector to measure the position of the diffracted beams. Scanning the detector around the sample, along the circumference of a circle cuts through Bragg peaks allowing the intensity of the X-rays detected to be collected as a function of the detector angle, 2θ, as depicted in **Figures 2.4 and 2.5.** In a θ-2θ scan, the X-ray tube (source) moves through an angle, θ, with respect to the sample (**Figures 2.4 and 2.5**).

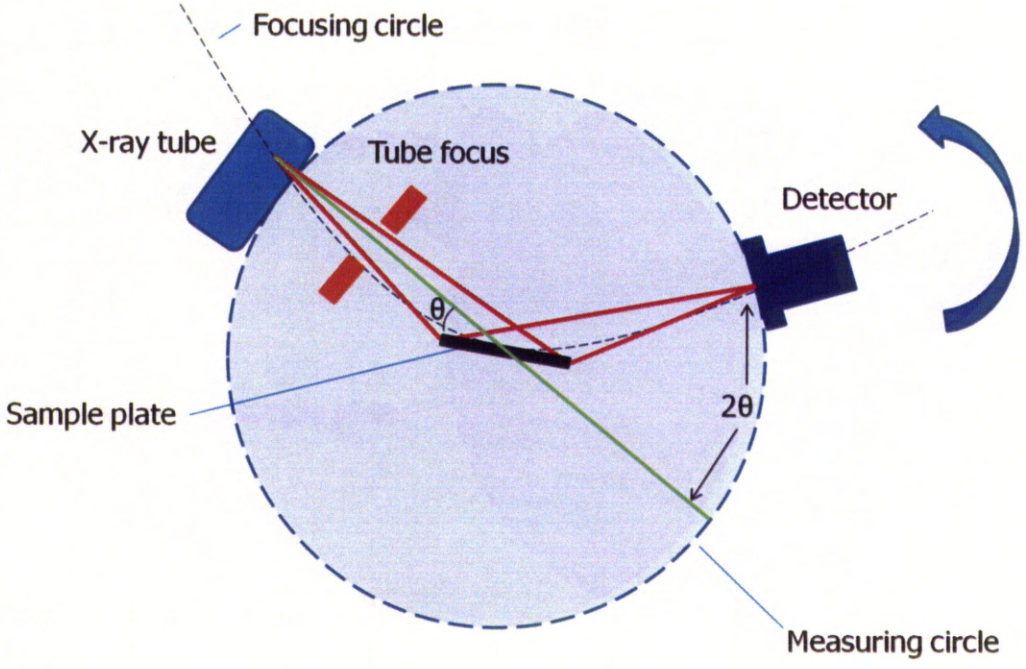

Figure 2.4 Schematic of a powder diffractometer

Powder X-ray diffraction (PXRD) can be used to identify a solid substance by the positions of the diffraction peaks and their intensities. By comparison with diffraction patterns stored in large data banks, such as the Cambridge Structural Database,[201] PXRD patterns can be used to identify known phases, since different solid phases yield different diffraction patterns. They can also be used to determine the relative amounts of each solid phase present in a mixture and for the initial identification of dimensions and symmetries of unit cells.

2.1.3 Bragg's law

By treating a plane of atoms as a semitransparent mirror[196,198,202] and modelling the crystal as stacks of reflecting planes which are separated by a distance, *d*, it is possible to calculate the angle at which incoming X-rays and the crystal must make in order for constructive interference (a 'reflection') to occur (**Figure 2.5**).

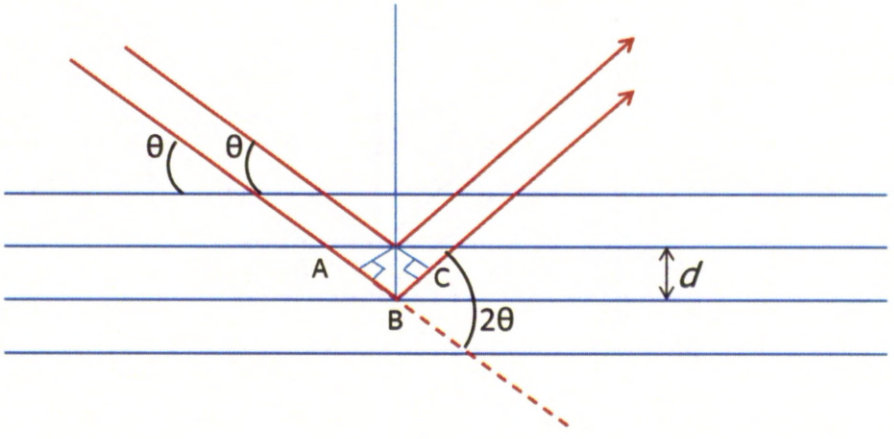

Figure 2.5 Simplified example of X-ray diffraction resulting in reflections at a particular angle, θ

The derivation of the Bragg law treats each lattice plane as if it were reflecting the incident radiation. The path lengths differ by AB+BC, which depend on the glancing angle, θ. Constructive interference occurs when AB+BC is equal to

an integer number of wavelengths, *n* (AB+BC=*n*λ). The path-length difference of the two X-rays shown in **Figure 2.5** is:

$$AB + BC = 2d \sin\theta \qquad \textit{eqn. 2.1}$$

It therefore follows that a reflection should be observed when the glancing angle satisfies the Bragg Law[202] (*eqn. 2.2):*

$$n\lambda = 2d \sin\theta \qquad \textit{eqn. 2.2}$$

The primary use of the Bragg law is to determine the spacing between the layers of atoms, d, as once the angle, θ, has been determined, d-spacing can be easily calculated. Bragg angles for real crystal systems with thousands of parallel planes are accurate to within a few tenths of a degree. The reflections observed on X-ray patterns are generally indexed according to the plane at which they diffract. These planes are labelled using Miller indices.

Depending on the crystal structure, some geometries have systematic absences of reflections caused by destructive interference along a particular plane. Systematic absences occur for lattices such as body centred or face centred in which, contain lattice restrictions on the values that *h*, *k* and *l* may take if the reflections are to have any intensity.[198,203] This results in certain peaks being absent from the diffraction pattern. Systematic absences are governed by the structure factor:

$$S = \sum_p f_p \, e^{-i2\pi(xh+yk+zl)} \qquad \textit{eqn. 2.3}^{203}$$

Where *f* is the scattering power of the atom, *h k* and *l* are the Miller indices and *x, y* and *z* are the coordinates of atom p in the unit cell.[203]

In order to identify different silica mesophases, these systematic absences can be used to our advantage. MCM-41 has a hexagonal array of pores which are identifiable by PXRD. The powder pattern contains characteristic (100), (110) and (200) reflections (**Figure 2.6a**). In contrast, MCM-48 (**Figure 2.6b**) has a cubic centred arrangement of pores. In this case, the powder pattern contains (211) and

(220) reflections with an absence of a (100) reflection due to destructive interference.[109]

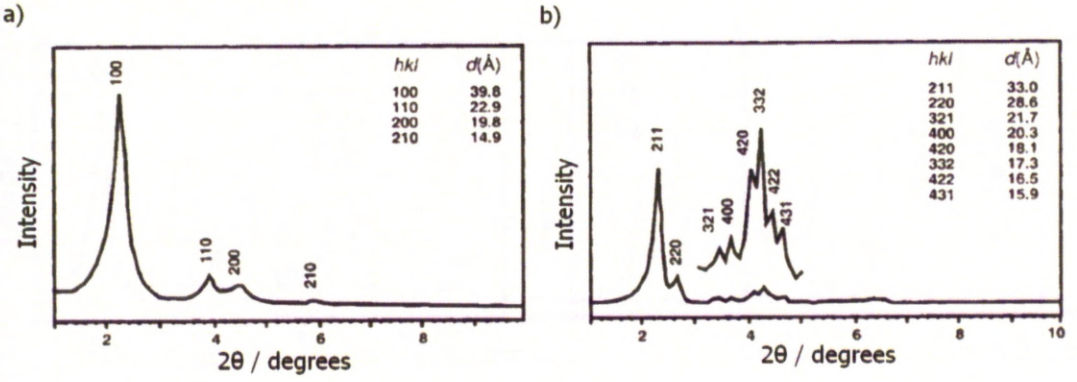

Figure 2.6 Powder X-ray diffraction patters for **a**) MCM-41 and **b)** MCM-48[109]

2.2 Gas sorption isotherm analysis

Nitrogen adsorption at 77 K is an invaluable technique used to measure pore volumes, texture and surface area of porous solids. This information is vital for the design of catalysts and gas storage materials. When a gas comes into contact with a porous solid it may be taken up by the solid or remain on the external surface area. For a porous solid, the internal volume is considered an internal surface and adsorption is the term used to describe the uptake of gas.

Adsorption isotherms are obtained by adsorbing nitrogen onto a solid surface and measuring the adsorbed volume against relative pressure. The shape of the isotherm depends on the solid porous texture. According to IUPAC classification, six types of isotherm can be distinguished (**Figure 2.7**). Of these, only four are usually found in catalyst characterisation (**Figure 2.7**, highlighted in red).[204-208]

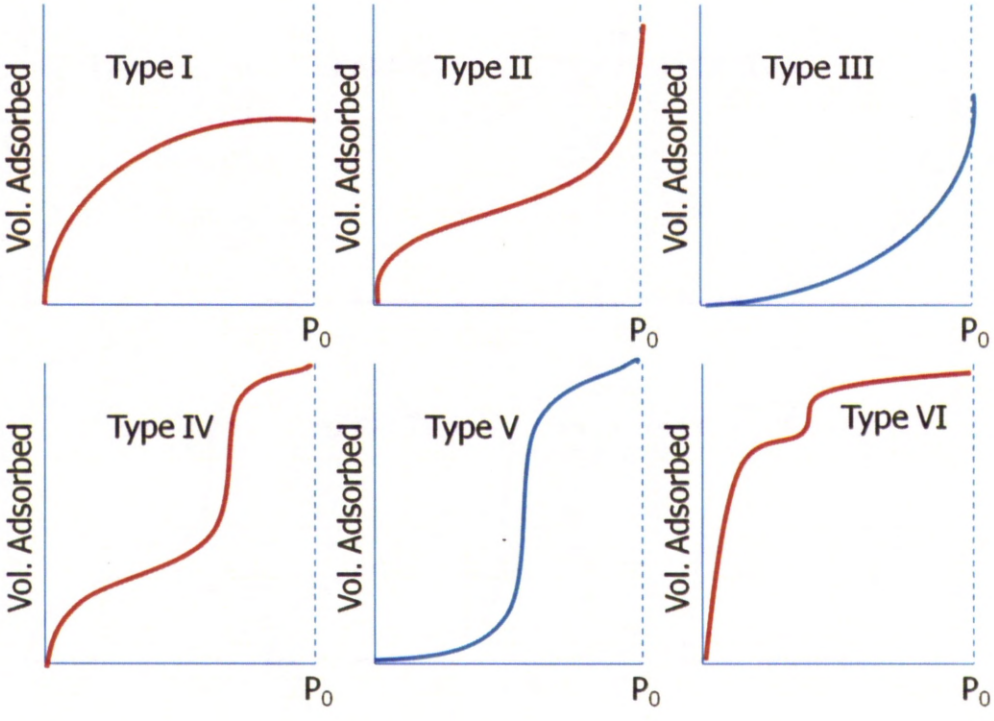

Figure 2.7 Six types of adsorption isotherm usually found by nitrogen adsorption as exhibited by real surfaces. Highlighted in red are four types usually found in catalyst characterisation[204]

Type I isotherms maybe interpreted as closely resembling 'Langmuir' behaviour but also correspond to filling of micropores within a solid rather than monolayer adsorption.[209] The adsorption takes place at low relative pressures because of strong interactions between pore walls and adsorbate. The filling of the pores is completed at slightly higher pressure due interactions between adsorbed molecules. In this case, pore filling takes place without capillary condensation in the low relative pressure region (below 0.3). Upon complete filling of the micropores, adsorption continues on the external surface similarly to mesoporous materials. Examples of microporous type I materials include; silica gels, zeolites and activated charcoals.[204]

Type II isotherms arise from macroporous solids. At low relative pressures a monolayer of nitrogen is formed on the surface while at higher relative pressures a multilayer is formed. The thickness of the adsorbed nitrogen increases until condensation pressure is reached. The pressure of the monolayer formation is low if the interaction between the adsorbant and the adsorbate is strong however, the formation processes for the mono- and multilayer are always overlapped.[204] Examples of materials exhibiting type II isotherms are non-porous or macroporous (pore diameter > 50 nm) carbons or oxides at 77 K.[209]

Type III isotherms are comparatively rare and arise when the interaction between the adsorbant and the adsorbate are weak. H_2O adsorption on graphitized carbons or polyethylene display type III isotherms.

Type IV isotherms are characteristic of mesoporous solids. At low relative pressures the process of adsorption in a monolayer form is similar to that of macroporous solids (type II). The steepness of the curve at this point (labelled **a** in **Figure 2.8**) determines the surface area. At high relative pressures the adsorption in mesopores (2-50 nm) leads to multilayer adsorption until, at a pressure determined by the size of the mesopores, capillary condensation takes place, shown as a sharp increase in adsorption volume in the isotherm plot (labelled **b** in **Figure 2.8**). The occurrence of this step at relative pressures lower than the normal saturation pressure is due to the formation of a curved liquid meniscus in a group of pores of a particular size and shape. The Kelvin equation (*eqn 2.4*) relates the curvature of the meniscus in a pore to the relative pressure at which condensation occurs:

$$r_k = \frac{2\sigma V_l}{RTIn(p/p_0)} \qquad \textit{eqn. 2.4}$$

where r_k is Kelvin radius (radius of curvature), σ is the surface tension of the liquid condensate and V_l is the molar volume. Most common assessment of mesoporosity is based on the Kelvin equation (for example, Barrett, Joyner and Helenda (BJH) method, **Section 2.2.3**). As the mesopores are flooded with nitrogen, adsorption continues on the low external surface.

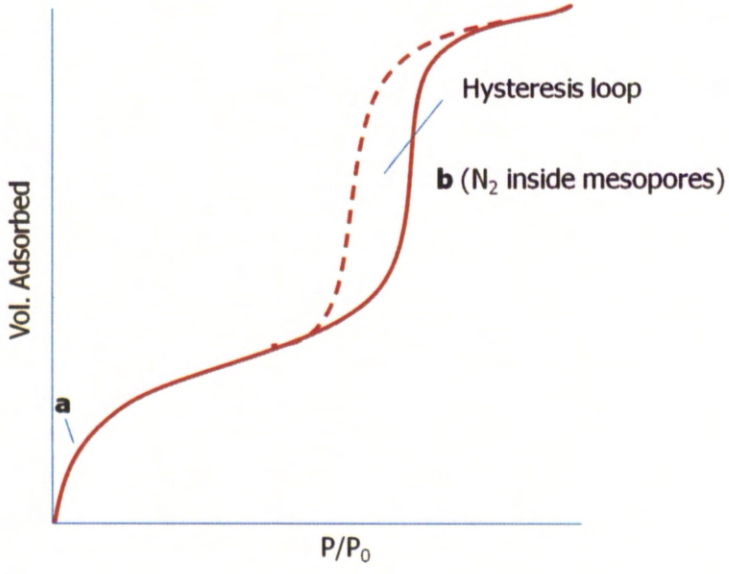

Figure 2.8 Type IV isotherm with H1 hysteresis

Type V isotherms are difficult to interpret and rarely occur.

Type VI isotherms are characteristic of uniform ultramicroporous solids. The pressure at which adsorption occurs depends on the interaction between the surface and adsorbate. If the surface is energetically uniform, the process happens at a well-defined pressure. If the surface contains few groups of energetically uniform sites, a stepped isotherm is observed in which each step corresponds to the completion of the first, second, third, etc. monolayers. Type VI isotherms are observed for materials such as well crystallized zeolites and highly oriented pyrolytic graphite.[209]

2.2.1 Desorption hysteresis in porous solids

Once saturation of the pores is reached, desorption takes place. In mesoporous solids desorption often occurs at a pressure lower than that of capillary condensation giving a hysteresis. The shape of the observed hysteresis depends on the shape of the pore. According to IUPAC classification, four main types of hysteresis are observed (**Figure 2.9**).[204-205,209-211]

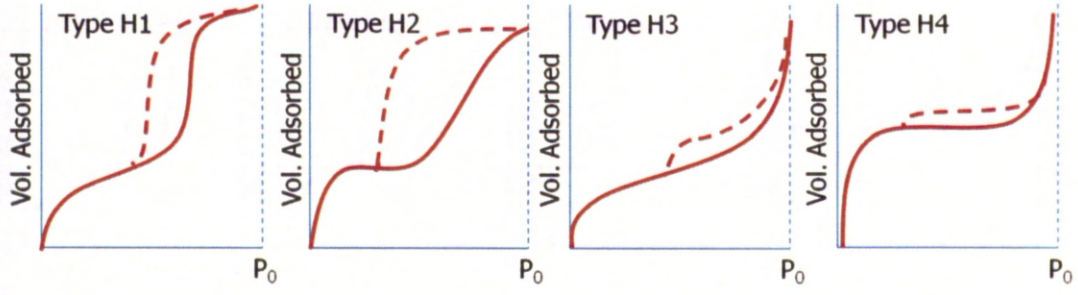

Figure 2.9 Four hysteresis shapes of adsorption-desorption isotherms usually found by nitrogen sorption (desorption is given by dashed lines)

Types H1 (pores of a uniform size and shape, **Figure 2.10b**) and H2 (pores of non-uniform size and shape, **Figure 2.10a**) are observed for materials consisting of crossed, almost cylindrical channels or formed from aggregates (consolidated) or agglomerates (unconsolidated) of spheroidal particles. The shape of the hysteresis loop is dependent on the size of the pore opening and pore body or to the difference in behaviour in adsorption and desorption in near cylindrical pores.

In ink bottle pores (**Figure 2.10a**) the condensation takes place in each section at the relative pressure provided by the Kelvin law (*eqn. 2.4*). In this case the liquid formed at low pressure in the pore opening supplies the vapour for adsorption and condensation in the large pore body. However, evaporation from the pore body cannot occur until the pore opening remains filled.

In the case of near cylindrical pores (**Figure 2.10b**) the meniscus is cylindrical during condensation and hemispherical during evaporation. Most mesoporous materials and catalysts are types H1 and H2. Type H1 is observed

particularly in mesoporous molecular sieves such as MCM-41[125] and periodic mesoporous organosilica (PMO) materials.[168]

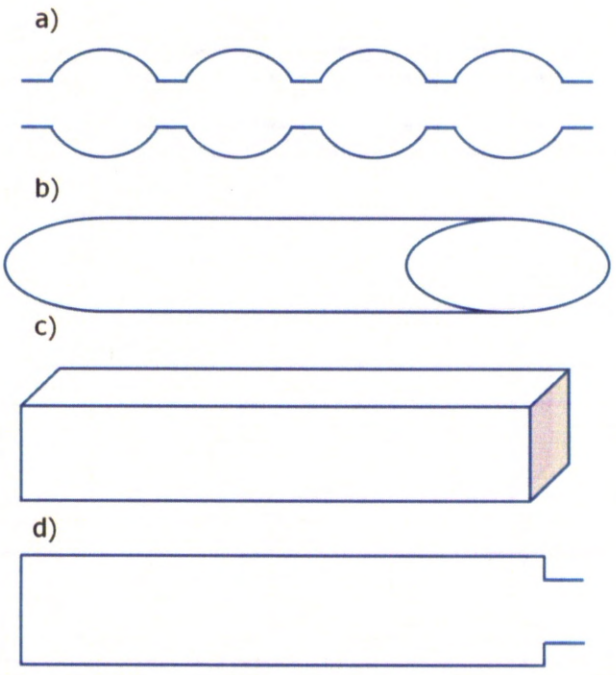

Figure 2.10 a) ink-bottle, **b)** cylindrical **c)** cubic and **d)** edged non-uniform pore shapes

Types H3 (non-uniform size and shape, **Figure 2.10d**) and H4 (uniform size and shape, **Figure 2.10c**) are common for aggregates or agglomerates of particles forming slit shaped pores (plates or edged particles like cubes). In these cases hysteresis is usually due to the different behaviour in adsorption and desorption. For example, in pores formed by parallel plates, the meniscus is flat with an infinite radius during adsorption (condensation does not take place at any relative pressure) and cylindrical with a radius half the distance between the plates during desorption. Examples of materials which exhibit types H3 and H4 hysteresis include active carbons and zeolites.[205,210]

The low pressure closure of the hysteresis loop takes place at a relative pressure of 0.42 for N_2. This is independent of the adsorbent and pore size distribution and is related to the liquid adsorbate properties. This is discussed further in **Section 2.2.4**.

2.2.2 Surface area determination

2.2.2.1 The BET method

The Brunauer, Emmet and Teller (BET)[204,212-214] method for surface area determination, developed in 1940s, is widely used in the characterisation of porous solids such as zeolites, mesoporous silicas and metal organic frameworks (MOFs). This model can be used to determine the monolayer volume (V_m) of the adsorbate and then the surface area (A_s) of a solid using *eqn 2.5*:

$$A_S = \left(\frac{V_m}{22414}\right) N_a \sigma \qquad \textit{eqn. 2.5}$$

Where N_a is Avagadro's number and σ is the area covered by one nitrogen molecule (accepted to be 0.162 nm^2). The molonlayer volume is estimated using the three parameters BET equation. This equation assumes that:

i) The heat of adsorption of the first monolayer is constant (the surface is uniform in terms of adsorption).

ii) Second layer adsorption can only take place on top of the first, third on top of the second, etc. Upon reaching the saturated vapour pressure ($P=P_0$), an infinite number of layers will form.

iii) At equilibrium, the rate of condensation equals that of evaporation for each individual layer.

iv) When the number of adsorbed layers is greater than or equal to two, the equilibrium constants, K^0, are equal and the corresponding value of $\Delta H^0_{AD} = -\Delta H^0_{VAP}$. For the first adsorbed layer, the enthalpy of adsorption is ΔH^0_{AD} as in the Langmuir case.

According to the model the adsorbed volume (V_{ads}) depends on:

i) The relative pressure (P/P_s)

ii) Monolayer volume, V_m

iii) A parameter, *c*, related to the heat of adsorption and liquefaction (high c=strong adsorbate-adsorbant interaction)

iv) A parameter, *n*, formally related to the mean number of layers that can be formed on the solid.

The three parameter BET equation is given by the following:

$$V_{ads} = V_m \frac{cp/p_s}{1-p/p_s} \frac{1-(n+1)(p/p_s)^n+n(p/p_s)^{n+1}}{1+(c-1)(p/p_s)+c(p/p_s)^{n+1}} \quad \textit{eqn. 2.6}$$

If n→∞, the equation can be simplified to the two parameter BET equation (*eqn 2.7*). Practically this equation can be suitably used for n>6 (macroporous and large mesoporous solids).

$$V_{ads} = V_m \frac{cp/p_s}{(1-p/p_s)(1+(c-1)p/p_s)} \quad \textit{eqn. 2.7}$$

The BET method for surface area determination is limited in that reliable results are only obtained within the partial pressure range 0.05 to 0.35 due to the influence of gas sorption at higher pressures. These include capillary condensation and saturation in porous networks.

The BET method cannot be used to measure the surface area of micropores. In this case the monolayer volume given by the BET equation corresponds to the micropore volume plus the monolayer volume on the surface external to the micropores. However, this can be detected using the t-plot method (**Section 2.2.2.2**).[204-205,210]

2.2.2.2 The t-plot method

The t-plot method developed by DeBoer and co-workers[215] takes into account, for a variety of porous solids, the adsorbed volume for a unit surface against pressure and follows a single curve, independent of the solid. The curve is

able to distinguish between meso-, micro- and non-porous materials. **Figure 2.11** shows t-plots of adsorption isotherms for a range of materials.

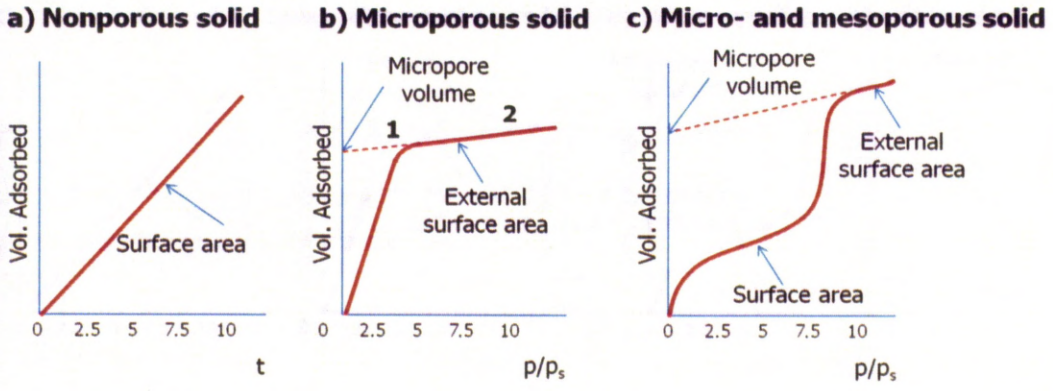

Figure 2.11 Characteristic t-plot adsorption isotherms shapes for a) a nonporous solid, b) a microporous solid and c) a solid containing micro- and mesopores

A straight line is observed for nonporous materials (**Figure 2.11a**). The gradient of the line, *m*, is directly proportional to the surface area, A_s of the solid as given by:

$$A_s = (\frac{m}{22414})t_m N_a \sigma \qquad \textit{eqn. 2.8}$$

In a microporous solid, as the micropores are progressively filled, the adsorption surface decreases giving a decreasing gradient (labelled **1** in **Figure 2.11b**), until, after complete filling, a straight line is observed (labelled **2** in **Figure 2.11b**) with a gradient corresponding to the surface area external to the micropores. At the point where micropores have been filled (labelled **1** in **Figure 2.11b**), it is possible to extrapolate to t=0 to give a y-intercept that corresponds to the adsorbed volume necessary to fill micropores.

For solids possessing meso- and micropores, the adsorption isotherms show a further gradient increase corresponding to filling of the mesopores (**Figure 2.11c**). This is due to capillary condensation as discussed in **Section 2.2**. The t-

plot method can then be used in conjunction with the BET method for full pore surface area determination.

2.2.3 Pore volume and pore size determination

2.2.3.1 BJH method

As discussed in **Section 2.2**, methods for the determination of pore volume are often based on the Kelvin equation (*eqn 2.4*). One of these methods includes that developed by Barrett, Joyner and Halenda (BJH method). This is the most widely used by commercial instruments to perform calculations on mesopores.

The BJH method is as follows; in the capillary condensation step ($p/p_s>0.4$), each pressure increase causes an increase in the thickness of the layer adsorbed on pore walls (*cf.* t-plot method) and capillary condensation in the pores having a core (*i.e.* the empty space of pores) size, r_k, defined by the Kelvin equation (*eqn 2.4*).

By assuming the pore shape (more accurately determined by the hysteresis loop, **Section 2.2.1**), the ratio of the contribution of thickness of the adsorbed film to the total adsorption and then core volume can be calculated. From these results and the assumed pore geometry it is possible to transform the core volume into the pore volume and core size to pore size. In this manner, examination of the isotherm in the range $0.42<p/ps<0.98$, the mesopores volume and size distribution can be obtained.[204,216]

2.2.3.2 DFT method

The density functional theory (DFT) method for pore size and volume determination, first used by Seaton *et al*,[217] consists of the construction of a grand potential functional of the average local density and of a minimization of this with respect to local density. This allows the equilibrium density profile and thermodynamic properties to be obtained.

This method has no theoretical limitations and can be used to determine pore size and volume within the range from untramicroporous to macroporous. The lower size limit is due to the adsorbate molecular size and the upper limit is due to the difficulty in performing precise measurements near saturation.[204]

2.3 Differential scanning calorimetry

Differential scanning calorimetry (DSC) is a technique used to measure the uptake of thermal energy that takes place in a sample during the controlled increase and decrease in temperature. By comparison with a reference sample, thermal transition temperatures can be determined.

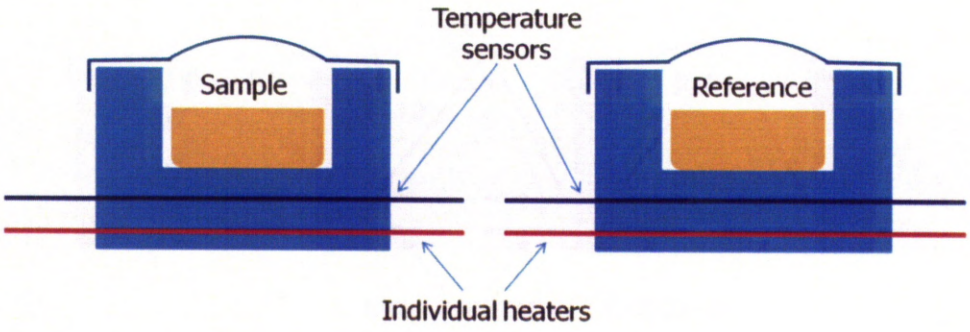

Figure 2.12 Power-compensation DSC

In a power-compensation DSC experiment, the sample and reference (an empty pan) are heated separately according to a defined temperature program (**Figure 2.12**). This program controls the sample and reference heaters in such a way that the two pans are heated at the same linear rate. Depending on the contents of the sample pan the input power to heat the two pans will be different. As a result, as the sample and reference are heated individually, the energy absorbed (endothermic process) or released (exothermic process) is electrically equated for the sample *vs.* the reference. After determination of the amount of extra heat required by the sample, addition or subtraction of the equivalent amount of energy to the sample is applied. In this way, the isothermal conditions of the reference and sample are maintained. The energy differential corresponds to the heat content or specific heat of the sample. An example of a DSC thermogram is shown in **Figure 2.13**.

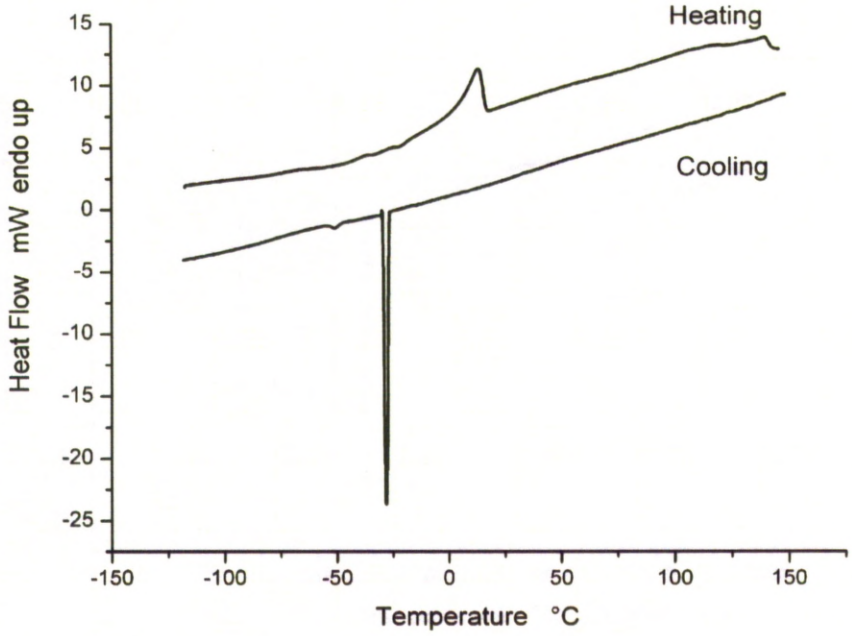

Figure 2.13 Typical DSC thermogram for an ionic liquid ([eim]OTf)[218]

2.4 Nuclear magnetic resonance spectroscopy

Nuclear Magnetic Resonance (NMR) Spectroscopy is a powerful analytical technique that relies on the interaction between an atomic nucleus exhibiting an magnetic moment, $\vec{\mu}$, and an external magnetic field, $\vec{B}$. The magnetic moment, $\vec{\mu}$, is directly proportional to the spin quantum number I, with a proportionality constant, γ, known as the gyromagnetic ratio (a constant for a given type of nucleus). The spin quantum number, I, maybe = 0, ½, 1, 3/2, 2, 5/2 etc. Protons and neutrons have spin number ½. Only nuclei that possess angular momentum are NMR active. For example, ^{12}C has I = 0, therefore no angular momentum, no magnetic moment and no NMR spectrum.[219] Such spin ½ nuclei can therefore be viewed as a tiny bar magnet with a magnet moment (μ) given by:

$$\mu = \gamma \hbar I \qquad \textit{eqn. 2.9}$$

Where γ is the gyromagnetic ratio, $\hbar$ is Planck's constant divided by 2π and I is the spin quantum number of the nucleus. The magnetic moment can align at an angle with or against the external magnetic field. These two states are separated by an energy ΔE (**Figure 2.14**) that depends on the strength of the interaction between the field and the nucleus. Nuclear magnetic resonance is the measurement of ΔE by applying electromagnetic radiation of frequency ν, which causes nuclei to flip from the lower energy level to the higher one and *vice versa*. This causes the resonance condition ΔE = hν to be satisfied.

Not only does ΔE depend on the nucleus under observation, it is also determined by the environment of the nucleus within a molecule, an effect known as chemical shift, which will be discussed in the next section. This allows NMR to be used for studying molecules at an atomistic level.

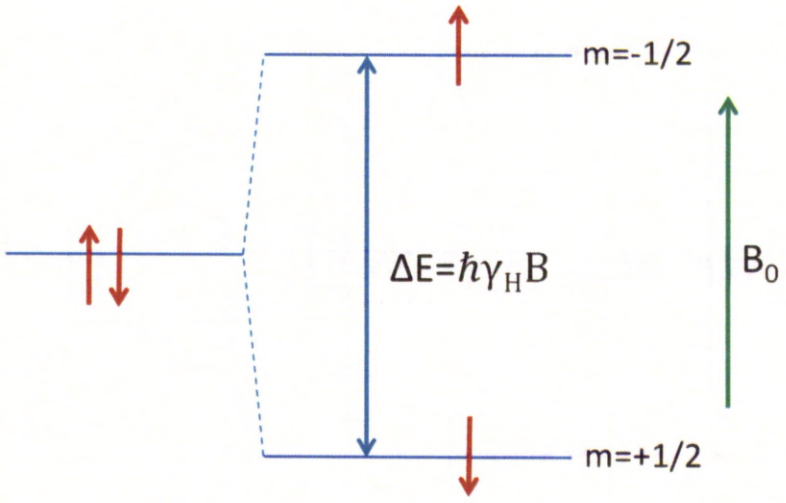

Figure 2.14 Zeeman splitting of a spin I = 1/2 nuclei in a magnetic field

As shown in **Figure 2.14**, the energy of the nucleus is shifted by an amount proportional to the magnetic field strength, the gyromagnetic ratio and the z-component of the angular momentum (the projection of μ on B). This splitting is known as Zeeman splitting. In its simplest form, NMR is the study of the properties of molecules containing magnetic nuclei by applying a magnetic field and observing the frequency of the resonant electromagnetic field. The selection rule for NMR to occur is $\Delta m = \pm 1$; the allowed transitions are therefore between adjacent energy levels. The resonance condition is therefore:

$$\Delta E = h\nu \text{ or } \nu = \frac{\gamma B}{2\pi} \qquad \textit{eqn. 2.10}$$

Where ν is the frequency of electromagnetic radiation. This frequency is also known as the Larmor frequency of nuclei (ω_0) and at a particular magnetic field strength normally lies in the radiofrequency region of the electromagnetic spectrum. For example, in a magnetic field of 12 T, protons ($I = 1/2$) come into resonance at about 500 MHz (the Larmor frequency at that magnetic field).

2.4.1 Chemical shift

As mentioned, the frequency at which nuclei resonate depends on their environment within a molecule, or to be more precise, on the local electron distribution. Chemical shift is a measure of this effect and the reason that NMR is particularly useful to chemists in the characterisation of molecules.

Chemical shift arises because the local field, B, experienced by a nucleus is actually slightly different from the external magnetic field, B_0. This is due to the fluctuation in the local electron distribution. In an atom, B is slightly smaller than B_0 because the external magnetic field causes the electrons to circulate within their atomic orbitals. This induced motion can be thought of as a current passing through a wire generating a small magnetic field in the opposite direction to B_0. This causes the nucleus to be shielded from the external magnetic field by its electrons. This effect is dependent on the electronegativity of the atom and causes the resonance frequency of a nucleus to be slightly lower than a nucleus that has been stripped of its associated electrons.

So far, the situation for a single atom has been described. However, nuclei positioned in molecules are rather more complicated. Within a molecule, the electronic distribution is more complex and depends on neighbouring atoms, the nature of the neighbouring atoms, the position of electron density within polar bonds *etc.* Shielding can occur in molecules however, deshielding can also occur. The effects of shielding cause the resonance frequency to be shifted and hence the chemical shift is characteristic of a particular nuclei's environment. This can be described in mathematical terms by *eqn. 2.11* in which $B_{eff} = B_0+B$:

$$\nu = \frac{\gamma}{2\pi} B_{eff} \qquad \textit{eqn. 2.11}$$

In summary, both the external magnetic field, B_0, and the local magnetic field, B, give rise to the chemical shift observed in NMR spectra, which is characteristic of particular environments within a molecule.

Despite having characteristic chemical shifts for particular environments within a molecule at a given field strength, the appearance of an NMR spectrum for

the same molecule, in the same B_0 field strength, in liquid and solid states would be very different. The difference is that in liquid samples, NMR spectra display narrow, well resolved peaks whereas in the solid state the resonances would be broadened (the causes of which are described in the next section). For these reasons the acquisition of well resolved solid state NMR spectra is more difficult and will now be described.

2.5 Solid state NMR

Various factors can contribute to the linewidths in NMR. These effects can be quantified and are given by the nuclear spin Hamiltonian:

$$\hat{H}_{total} = \hat{H}_z + \hat{H}_{CSA} + \hat{H}_D + \hat{H}_Q + \hat{H}_J \qquad \textit{eqn 2.12}$$

Where $\hat{H}_z$ is the Zeeman interaction, $\hat{H}_{CSA}$ is chemical shift anisotropy, $\hat{H}_D$ is the dipolar interaction, $\hat{H}_Q$ is the quadrupolar interaction and $\hat{H}_J$ is spin-spin interactions (J-coupling).

These factors are orientation dependent (as described in the following sections) and, therefore, depend on the motional freedom of a molecule, *i.e.* whether it is a solid or liquid state as well as the spin quantum number of the nuclei under observation. Often the lines of quadrupolar nuclei are broader than spin ½ nuclei. However, the most common cause of resonance broadening is the amount of molecular tumbling a molecule undergoes. In liquids, molecules tumble quickly and therefore the interactions of the spins are averaged out. In solids, due to their rigid structure, molecular tumbling is significantly reduced which causes a number of additional effects that contribute to resonance broadening.

2.5.1 Nuclear magnetic interactions

The interactions described in *eqn.2.12* contribute to the linewidth observed in solid state NMR spectra. The Zeeman interaction is the same as that for liquids and the spin-spin interaction is small in comparison to other interactions. Also, the nuclei observed in this research are not quadrupolar. For these reasons, only chemical

shift anisotropy and dipolar coupling will be described in the following sections. The magnitude of each interaction is summarised in **Figure 2.15**.[220]

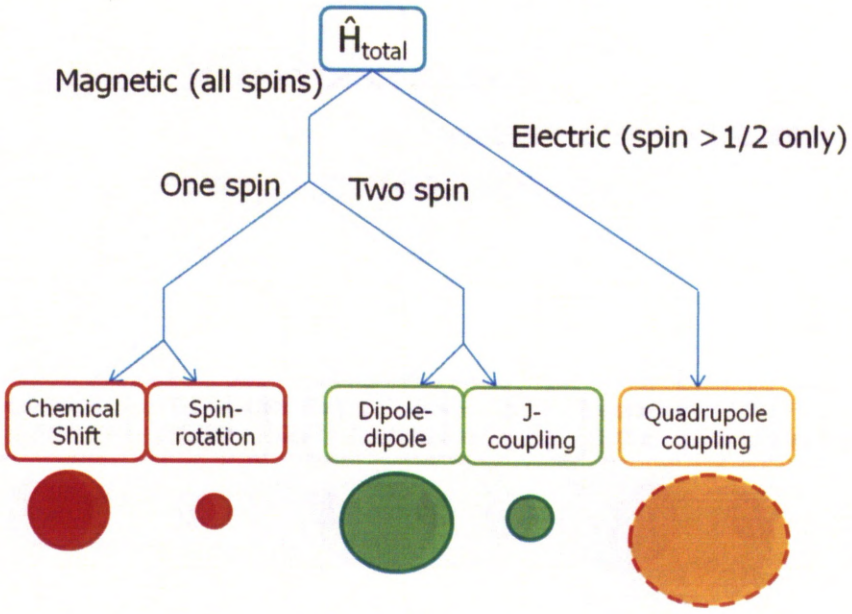

Figure 2.15 Organisation of the spin interaction terms with rough relative magnitudes represented by circles. Quadruploar interaction vanishes for spin ½

2.5.1.1 Chemical shift anisotropy

This term represents the indirect magnetic interaction of the external magnetic field and the nuclear spins, through the involvement of electrons. Often, molecules do not possess a spherical electron distribution and an elongated ellipsoid stretching along the bonds is often assumed. As the molecule can adopt a number of orientations with respect to the B_0 field, the chemical shielding interaction felt by the nucleus is slightly different for each orientation resulting in a slightly different chemical shift (**Figure 2.16**). To further understand this we must first understand the chemical shift Hamiltonian given in *eqn. 2.13*:

$$H_{CSA} = \gamma B_0 I_Z \left[\delta_{iso} - \frac{1}{2}\delta_{CSA}(3cos^2\theta - 1)\right] \qquad \textit{eqn. 2.13}$$

Here, θ represents the orientation of the ellipsoid axis with respect to B_0. The Hamiltonian also describes both the isotropic chemical shift (δ_{iso}), and the magnitude of the CSA (δ_{CSA}), which are described by the following equations:

$$\delta_{iso} = \frac{1}{3}(\delta_{11} + \delta_{22} + \delta_{33}) \qquad \textit{eqn. 2.14}$$

$$\delta_{CSA} = \delta_{iso} - \delta_{33} \qquad \textit{eqn.2.15}$$

The isotropic term, δ_{iso}, is simply the average of all three principal values (shown in **Figure 2.16**). In reality there are not only the three principle values observed due to the random orientation of the molecules giving the powder pattern observed in **Figure 2.17**. The CSA term, δ_{CSA}, is equal to this average minus the chemical shift when the widest part of the electron distribution is aligned with the B_0 field. The geometric term $(3cos^2\theta - 1)$ can be eliminated by spinning at the magic angle (**Section 2.5.2.1**). In order to remove the broadening caused by chemical shift anisotropy, and retain an isotropic chemical shift, various techniques can be applied that are discussed in **Section 2.5.2**.

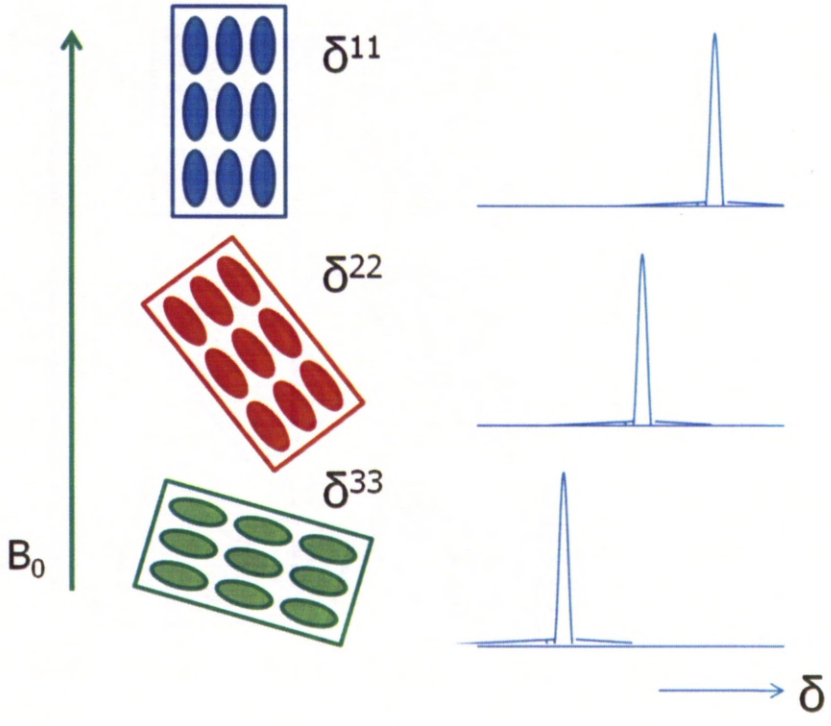

Figure 2.16 Chemical shift dependence on the orientation of the solid with respect to B_0

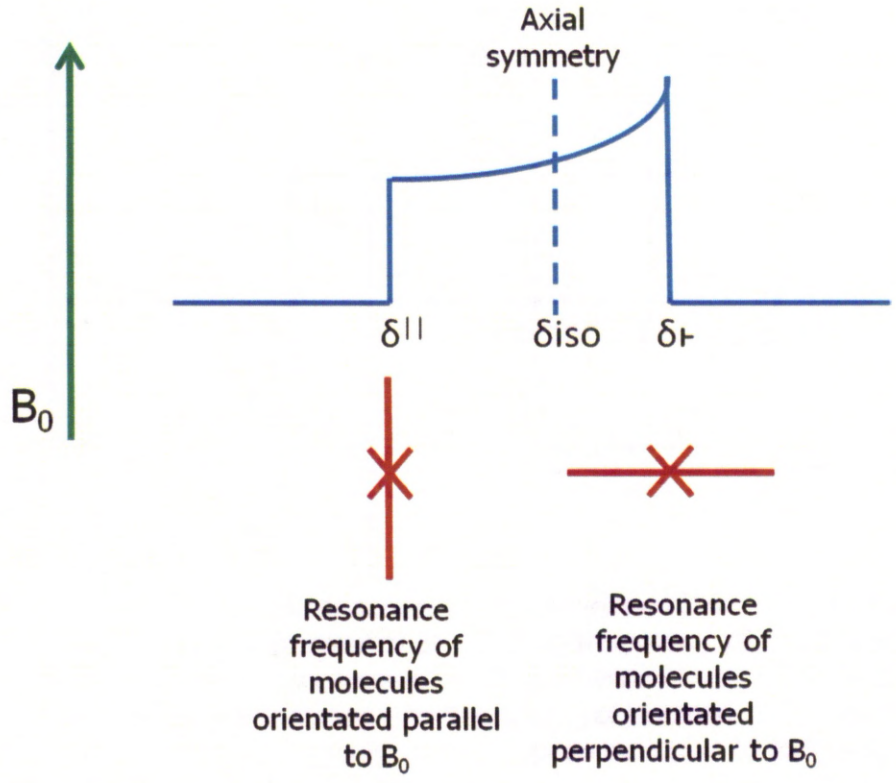

Figure 2.17 Powder pattern of molecule possessing axial symmetry with respect to B_0

2.5.1.2 Dipole-dipole couplings

Dipolar couplings represent the direct magnetic interactions of nuclear spins with eachother. Unlike J-coupling, dipolar coupling is a through-space interaction and exists between nuclei with the same spin (homonuclear) or different spins (heteronuclear).

2.5.1.2.1 Homonuclear dipolar couplings

When same spins, e.g. two ^{1}H spins, are close enough in space they are able to undergo "flip-flop" transitions where one spin flips to a higher energy state and the other flips to a lower energy state in order to conserve energy. The homonuclear dipolar Hamiltonian for a simple two spin system is given by:

$$\hat{H}^{DD,homo}(\theta) = d_{jk}\left(3\hat{I}_{jz}\hat{I}_{kz} - \hat{I}_j.\hat{I}_k\right) \qquad \textit{eqn. 2.16}$$

Where I_j and I_k are spins with the same gyromagnetic ratio (γ) (*i.e.* two protons) and in which:

$$d_{jk} = -\frac{\mu_0}{4\pi}\frac{\gamma_j\gamma_k\hbar}{r_{jk}^3}\frac{1}{2}(3cos^2\theta - 1) \qquad \textit{eqn.2.17}$$

Here γ is the gyromagnetic constant for spins j and k, r_{jk} is the distance between the spins, $\mu_0 = 4\pi \times 10^{-7}\ Hm^{-1}$, the magnetic constant and $\hbar = 1.055 \times 10^{-34}$ Js.

Increasing the magnitude of I_J or I_K operators increase the angular momentum of a spin which causes a change from spin "up" to spin "down". It is important to remember that this interaction only affects spins with chemical shift that are close together. The strength of dipolar Hamiltonian is also reliant on the gyromagnetic ratio. It is for this reason that spin pairs of ^{13}C or ^{29}Si only display weak homonuclear couplings. Also, the chance of two ^{13}C nuclei being in close proximity is rare (natural abundance of ^{13}C is approximately 0.01 %). The gyromagnetic ratio of ^{1}H is large and with 100 % natural abundance the resulting spectra are broad. To combat poor resolution, various techniques are applied to improve the resolution of spectra (particularly ^{1}H) and are described in **Section 2.5.2**.

2.5.1.2.2 Heteronuclear dipolar couplings

Heteronuclear dipolar coupling is the interaction of the magnetic moments of two non-identical spins that are close in space. Often, one spin is more naturally abundant than the other and is labelled I whereas the less abundant spin is labelled S. When placed in a magnetic field, Zeeman splitting occurs and the I and S spins align either parallel or anti parallel with respect to each other. As each spin represents a small bar magnet, the spins "feel" each other's magnetic field if they are in close proximity as well as the larger B_0 field. The strength of the interaction between spins I and S is given by:

$$H_{IS} = -d(3cos^2\theta - 1)I_zS_z \qquad \textit{eqn. 2.18}$$

In which d, the dipolar coupling constant is given by:

$$d = {\left(\frac{\mu_0}{4\pi}\right)\hbar\gamma_I\gamma_S}\Big/{r_{IS}^3} \qquad \textit{eqn. 2.19}$$

where r^3_{IS} is the internuclear distance, $\hbar$ is Plank's constant/2π, γ is the gyromagnetic ratio of spins I and S and I_z and S_z are the Z components of the nuclear spin angular momentum operators I and S. As with homonuclear dipolar coupling, the strength of the coupling is dependent on the gyromagnetic ratio, so the greater the ratio, the stronger the coupling and the broader the resonances observed in the spectrum. The strength of the coupling is also inversely proportional to the distance between the two spins cubed. Therefore, as the distance between the spins increases, the dipolar coupling decreases rapidly. θ represents the angle of the inter-nuclear vector to that of the B_0 field (**Figure 2.18**). For this reason heteronuclear dipolar coupling is orientation dependent, even if the internuclear distance is the same.

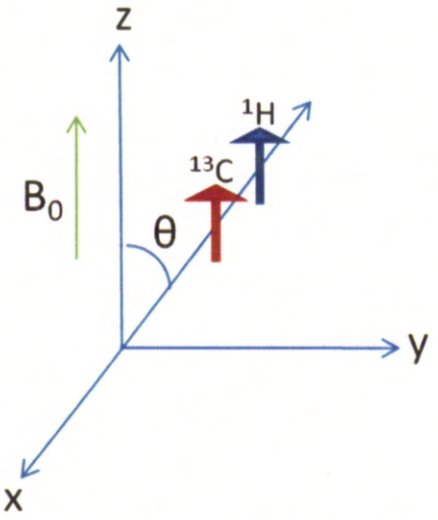

Figure 2.18 The angle between ^{1}H and ^{13}C bond vector within the B_0 field[220]

In a polycrystalline sample, due to the effects of heteronuclear dipolar coupling a "Pake doublet" is observed in the NMR spectrum (**Figure 2.19**). This is a direct result of energy differences arising from H_{IS} depending on the parallel or antiparallel alignment of the I spin with respect to the S spin. The intensities indicate the number of crystallites in a particular orientation with the most intense peaks observed when the inter-nuclear vector is perpendicular to the B_0. When the sample is placed at the "magic angle" (discussed in the following section) the resonance frequency is not altered by heteronuclear dipolar coupling.

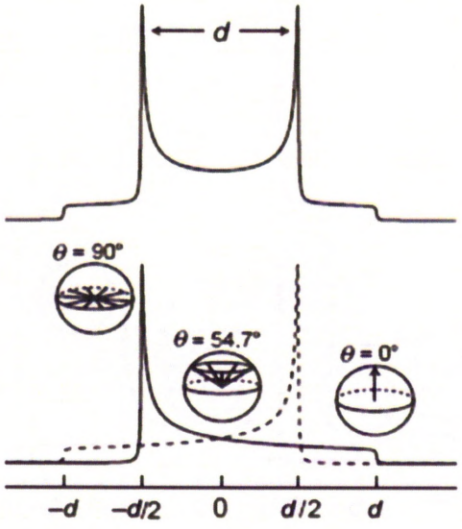

Figure 2.19 Pake pattern resulting from hetero-nuclear dipolar interaction of an I and S spin system[221]

2.5.2 Experimental techniques in solid state NMR

2.5.2.1 Magic Angle Spinning (MAS)

Both CSA and heteronuclear dipolar interactions can be averaged out by spinning the sample at an angle at which the geometric part of the Hamiltonian $(3\cos^2\theta-1) = 0$. This is satisfied when $\theta = 54.74^0$. This angle is equal to the vector given in **Figure 2.18** between the two spins.

By rapidly spinning a polycrystalline powder, the average CSA can be made to resemble an ellipsoid whose long axis is aligned with the spinning axis. This is also true when the CSA is not axially symmetric. When the sample is spun, the CSA values of all crystallites become time-dependent, since the orientation of the crystallites change. **Figure 2.20** shows that an axis inclined at an angle of 54.74^0 represents the direction of the space diagonal of a cube. The x, y, and z axes appear symmetrical when looking down the space diagonal. When we begin to spin the sample, each crystallite experiences the average of the effective chemical shift $\delta_{iso} = (\delta_{xx}+\delta_{yy}+\delta_{zz})/3 = (\delta_{11}+\delta_{22}+\delta_{33})/3$. This results in a resonance in the NMR

spectrum at the isotropic chemical shift. MAS can, therefore, be regarded as a dynamic implementation of cubic symmetry[221] which cancels the anisotropic term.

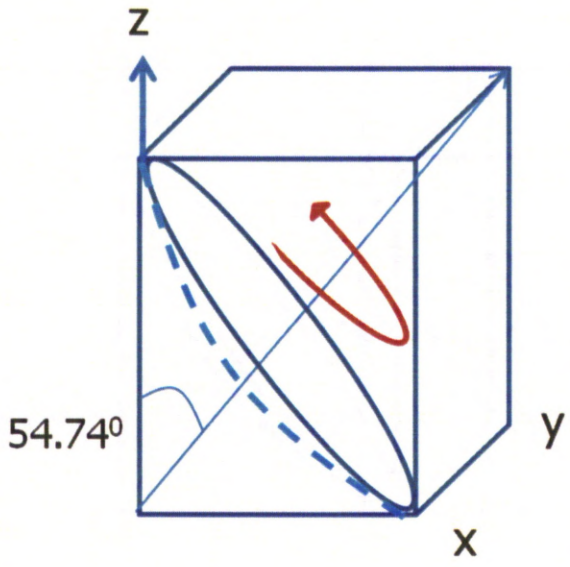

Figure 2.20 The magic angle (54.74^0) is the angle the space diagonal of a cube makes with the z axis. Spinning at a fast rate removes dipolar interactions

In order for MAS to be effective, it needs to be three times greater in magnitude than the interaction it is trying to average out. If these interactions are very strong this can be difficult to achieve. This is particularly the case for hetero- and homonuclear dipolar coupling. To remedy this further, a series of radiofrequency pulses are applied to the sample to eradicate the coupling. This process is known as decoupling.

2.5.2.2 Decoupling

When recording spectra of a dilute spin, S, coupled to an abundant spin, I, significant resonance broadening is observed due to dipolar coupling that exists between them. As this interaction is strong, it cannot be removed by MAS alone but is removed in conjunction with high power radiofrequency (RF) irradiation during acquisition of the free induction decay (FID) of the dilute S spin. This gives much higher spectral resolution. This type of decoupling is known as "high-power

decoupling". The close-to-resonance radiofrequency irradiation causes the I spins to undergo rapid and repeated transitions (α→β) at a rate determined by the power of the irradiation. If the rate of the transition (α→β) is faster relative the S-I coupling strength then the coupling is averaged out to zero due to rapid transitions between +1/2 and -1/2. This method has limited applications because long acquisition times under high-power decoupling can cause sample heating and potentially damage the probehead. To eliminate this problem more sophisticated methods of decoupling have been developed that include; Two Phase Pulse Modulation (TPPM)[222] which uses two high power pulses that differ in phase by 10 to 70°[223-224] and X inverse X (XiX) which uses two pulses differing in phase by 180°.[225]

For nuclei with low gyromagnetic ratios, such as ^{13}C, MAS is sufficient in averaging out homonuclear dipolar interactions. For ^{1}H however, these interactions are much stronger and require very fast MAS to average them (in excess of 30 kHz). Although this is an achievable MAS rate, ^{1}H high resolution solid state NMR relies on multiple pulse sequences to average out ^{1}H-^{1}H dipolar interactions by manipulating the spin part of the Hamiltonian $\left(3\hat{I}_{jz}\hat{I}_{kz} - \hat{I}_j.\hat{I}_k\right)$ (see *eqn.2.18*).

There are two main types of homonuclear decoupling methods, multi-pulse and phase modulated sequences. Multi-pulse sequences, such as Frequency-Switched Lee-Goldburg (FSLG), work by applying the LG condition.[226-229] This is an off resonance RF field with an offset of $\Delta\omega = \omega 1/\tan\theta$ (where ω is the Larmor frequency). An effective RF field inclined at θ (with respect to the z axis) is created in the rotating frame. Therefore, if $\theta = \theta_m = 54.7°$ then the LG offset is defined as $\Delta\omega = \omega 1/\sqrt{2}$ and the effective field acting on the ^{1}H spins is tilted with z" positioned at the magic angle with respect to the laboratory frame (B_0). This leads to homonuclear decoupling during heteronuclear magnetisation transfer (see next section describing CP), allowing more selective magnetisation transfer which is advantageous in 2D correlation experiments (see **Section 2.5.2.5**) in order to measure distances between heteronuclei.[228,230] Switching from positive to negative offsets improves the efficiency of the technique by averaging out pulse imperfections that may be observed when using continuous wave decoupling.[221]

Phase modulated decoupling sequences such as DUMBO[231] use a single pulse of constant amplitude yet the phase is varied at discrete intervals to form a wave by

where the spin component is averaged to zero. The advantage of using phase modulation over pulse modulated sequences is their applicability as windowed decoupling sequences and difficulties when setting up. This has caused the presence of phase modulated pulses to be rare in the literature however, the development of more sophisticated spectrometer hardware has resulted in an increasing popularity of phase modulated decoupling being reported.

Together, MAS and decoupling are useful techniques to obtain high resolution solid state spectra however they eliminate interactions that could be used to probe molecular mobilities, proximities and for obtaining structural information. For this reason, a variety of techniques have been developed to selectively reintroduce the interactions that cause resonance broadening. These techniques will not be discussed in detail here but the reader is referred to the review by Laws, Bitter and Jerschow[221] for further detail. There experiments include REDOR, a heteronuclear recoupling technique and DRAMA, a homonuclear recoupling technique, both used for distance measurements in solids.

2.5.2.3 Cross polarisation

To enhance the signals from rare nuclei such as ^{13}C and ^{29}Si, many solid-state NMR experiments today use a transfer of magnetization from abundant spins (such as ^{1}H) by using a technique called cross polarization (CP). This transfer occurs through the tendancy of magnetization to flow from highly polarized spins to spins with lower polarization when they are brought into contact, analogous to heat flow from a hot object to a cold object when the two are brought into thermal contact. For homonuclear spins, the magnetization can be exchanged through mutual energy conserving spin flips whereas, for heteronuclear pairs such as ^{1}H and ^{13}C, these spin flips are not energy-conserving at high magnetic fields and therefore RF fields need to be applied to drive the transfer of magnetization. The contact condition for heteronuclear magnetization transfer is described by Hartmann and Hahn.[232] This method requires the simultaneous application of two continuous RF fields, one at the resonance frequency of the abundant spin, I and the other at the resonance frequency of the dilute spin, S. The effect of any RF field is to rotate the magnetization about the axis of the applied field. The rotation rate depends on the frequency and amplitude of the RF field. By applying two RF fields, one tuned to

the I spins the other to the S spins, both the I and S spins can be rotated independently around a particular axis at rates determined by the amplitudes of the two applied fields. When the rotation frame frequencies of the I and S spins are equal, an energy conserving dipolar contact between the two spin systems is created analogous to that present in homonuclear systems. The differences in energy are supplied by the two RF fields. It is through this dipolar contact that the polarization is then transferred between the I and S spins. CP-MAS NMR experiments are carried out using the pulse program displayed in **Figure 2.21.**

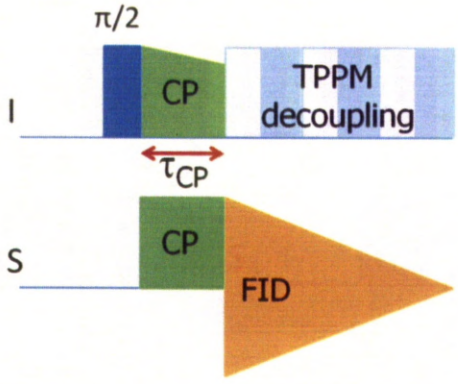

Figure 2.21 I-S CP-MAS pulse sequence with ramped amplitude CP. I refers to the abundant spin ^{1}H and S to dilute spins ^{13}C or ^{29}Si

Initially, proton magnetization is brought into the xy plane by a $\pi/2$ pulse. RF fields are then applied to the I and S spins for a period τ_{CP}, causing the magnetization to be transferred from the I spins to the S spins in their respective rotating frames. Finally, the S spins are detected while the I spins are decoupled using TPPM decoupling described in **Section 2.5.2.2**.

The increase in the S-spin magnetization during the CP mixing period τ_{CP} depends on the strength of the I-S dipolar coupling. The mixing times, τ_{CP}, depend on the nature of the sample but are generally in the range from 100 μs to 10 ms. The polarization build-up curve starts to decay beyond a certain mixing time as a result of relaxation (return to equilibrium as energy is lost to other spins or the surroundings, see **Section 2.5.3.1**).

In a CP spectrum, a direct link between integrated signal intensities and stoichiometric abundances is no longer available due to the many parameters involved such as the magnitude of local I spins available to transfer magnetisation to the S spin. This is also true for liquid-state proton-enhanced or inverse spectroscopy. The maximum enhancement for a CP contact period under Hartmann-Hahn conditions, given by *eqn. 2.20* is γ_I/γ_S:

$$\gamma_I B_I = \gamma_S B_S \qquad \textit{eqn. 2.20}$$

where γ_I and γ_S are the gyromagnetic ratios of spins I and S, respectively. B_I and B_S are the RF fields applied to spins I and S, respectively.

As mentioned, once the Hartmann-Hahn matching condition is satisfied, magnetization can be transferred *via* dipolar coupling. The dipolar coupling Hamiltonian (*eqn. 2.18*) is unaffected when transformed into the rotating frame as the two operators and are unaltered by rotations about the *z*-axis. The energy of the spin system is dependent on the field applied in the rotating frame (B_1) and the magnetization of the spins which are parallel to the z axis. As I and S magnetization have been flipped into the xy plane, and are now perpendicular to the z axis, the dipole operators cannot affect the total energy or the total spin polarization of the systems. When the Hartmann-Hahn matching condition is satisfied, the energy gaps for the I and S spins are equal. Therefore, the dipole operator can now act on the spin system inducing transitions on I which are compensated for by transitions on S or vice-versa. This also means that the net energy and polarization of the system remains constant.[220-221,223,232-233]

2.5.2.4 Dynamics of cross polarisation

Interactions between the porous support and the RTIL can be investigated using cross-polarization MAS NMR spectroscopy. The rate of magnetization transfer in a cross-polarization experiment depends on the strength of dipolar coupling between the abundant spin (I) and the dilute spin (S), the stronger the coupling, the faster the rate of transfer. The coupling, in turn, gets stronger with shorter

internuclear distance (r) and larger gyromagnetic ratios (γ) for the nuclei concerned. The rate of magnetization transfer also depends on how quickly the ^1H magnetization is redistributed amongst the ^1H network of coupled spins through dipolar interactions[223]. Since molecular motion affects the dipolar interactions it will also affect the rate of polarization transfer. This can be monitored by CP kinetics.

CP kinetics measurements are invaluable for studying structure and dynamics of complex solid materials and have been widely used to study periodic mesoporous organosilicas (PMOs),[168] polymer composites,[234] bone apatite[235] and aluminophosphates.[236-237]

The kinetics of CP can be described by a variety of models that depend on the strength of the ^1H–^1H dipolar coupling. The classical I-S model (I being abundant spins and S being dilute spins) is ideal for homogeneous solids where I-S dipolar interactions are weak and I-I interactions are strong enough to provide efficient ^1H – ^1H spin diffusion. For this system the kinetic equation for spin ½ nuclei is:

$$I(t) = I_0\left(1 + \frac{T_{IS}}{T_{1\rho}^S} - \frac{T_{IS}}{T_{1\rho}^I}\right)^{-1}\left[exp\left(-\frac{t}{T_{1\rho}^I}\right) - exp\left(-t\left(\frac{1}{T_{IS}} + \frac{1}{T_{1\rho}^S}\right)\right)\right] \quad \textit{eqn. 2.21}$$

where I_0 is the absolute signal intensity, $T_{1\rho}$ is longitudinal relaxation in the rotating frame and T_{IS} is the CP time constant. For dilute spins, generally, one can assume that $T_{IS}/T_{1\rho} \rightarrow 0$. CP dynamics can therefore be described by the equation:

$$I(t) = I_0\left(1 - \frac{T_{IS}}{T_{1\rho}^I}\right) - exp\left(\frac{t}{T_{IS}}\right) \quad \textit{eqn.2.22}$$

The T_{IS} time constant is related to internuclear distances and molecular mobility. $T_{1\rho}{}^H$ times describe the decay of signal intensity as a function of contact time. The relaxation of protons in the rotating frame is ensured by the presence of ^1H–^1H dipolar interactions. The T_{IS} time is characteristic of individual functional groups whereas $T_{1\rho}{}^H$ relaxation time is a property of the volume of the sample and provides information on the surrounding site.[168]

A second system can be described, which accounts for magnetization transfer not only from directly bound protons but also from those in the surrounding vicinity. This model is the I*I-S model, applicable to non-homogeneous proton

populations. I* denotes protons directly bonded to the S spin and I denotes protons in the surround vicinity that are also able to transfer magnetization to the S spin. The cross polarization in the I*I-S model proceeds in two steps. The first step, which shows a fast increase in signal intensity occurs when I* spins transfer magnetization to the S spin. In the second step, I spins transfer magnetization to I* spins *via* spin-diffusion. This energy exchange between the remote I spins and directly attached I* spins results in additional increase in signal intensity at longer contact times. For isolated SI_n clusters in a powder sample, under magic angle spinning but without significant molecular motion, *eqn. 2.23* describes I*I-S cross polarization dynamics.

$$I(t) = I_0 exp\left(-t/T_{1\rho}^{I}\right)\left[1 - \lambda exp\left(\frac{-t}{T_{df}}\right) - (1-\lambda) exp\left(\frac{-\frac{3}{2}t}{T_{df}}\right) exp\left(-\frac{1}{2}t^2/T_2^2\right)\right]$$

eqn. 2.23

Here, rotating frame relaxation, $T_{1\rho}$, is assumed for protons during cross polarization and $\lambda=1/(n+1)$. T_{df} is the ^1H spin diffusion time constant which describes the strength of the homonuclear dipolar interactions and homogeneity of the I spin pool. T_2 is the spin-spin relaxation time.

2.5.2.5 2D heteronuclear correlation experiments

As described in previous sections, the presence of dipolar couplings can cause unwanted resonance broadening but can also be advantageous in enhancing the spectral resolution of dilute spins. Another application of dipolar couplings is that of heteronuclear correlation (HETCOR) experiments to observe nuclei that are in close proximity to one another. The most commonly used HETCOR experiment in solids correlates ^1H chemical shifts, observed in the indirect dimension, with the chemical shifts of another nucleus, such as ^{13}C or ^{29}Si, observed in the direct dimension.

The pulse sequence (**Figure 2.22**), the ^1H magnetization is first excited with a $\pi/2$ pulse. During t_1, transverse ^1H magnetization is allowed to evolve after which

the remaining ^{1}H magnetization is transferred to ^{13}C *via* CP resulting in a ^{29}Si spectrum in t_2.

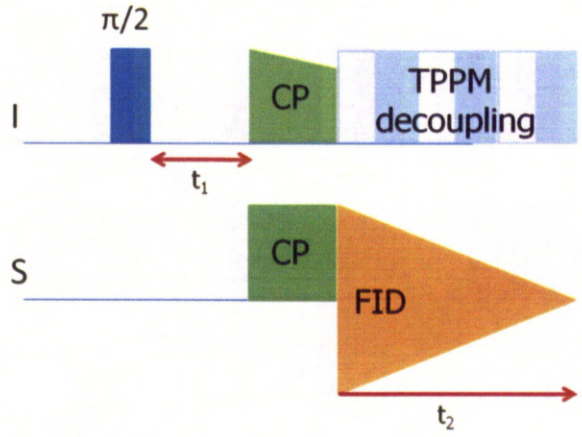

Figure 2.22 Pulse sequence for I-S 2D HETCOR. I refers to abundant spin ^{1}H and S refers to dilute spin ^{29}Si

In the HETCOR experiment, strongly coupled spins transfer polarisation more rapidly than weakly coupled spins, resulting in cross peaks in the spectrum. The distance of magnetization transfer during CP can also therefore be controlled to some extent by varying the CP mixing time. For long CP mixing times, the magnetization will be transported farther away, even to S spin atoms that are not directly bonded. By comparing HETCOR spectra taken at different mixing times, it is possible to gain insight into the local structure and atomic distribution in the sample.

2.5.2.6 Dipolar dephasing

Often the aim in solid-state NMR experiments is to reduce the interactions that cause resonance broadening but as mentioned, these techniques can also be used for advantageous purposes. Dipolar dephasing is one such technique that is used for spectral editing. An explanation of this technique has been included here as it has been helpful in the characterisation of methane clathrate hydrate systems, detailed in **Chapter 5**.

The aim of this experiment is to simplify a high resolution solid-state NMR spectrum by removing signals that originate from nuclei that are directly bonded to

hydrogen. The most common application is in ^{13}C CP-MAS NMR spectroscopy but can, in principle, be applied to any situation in which hydrogen is directly bonded.

The pulse sequence used in the dipolar dephasing experiment (**Figure 2.23**) is initially the same as the CP pulse sequence described in **Figure 2.21**. After polarisation is transferred however, the decoupler is turned off. A dephasing delay is applied after which the decoupler is turned on and the spectrum is acquired. While the decoupling is turned off the time domain signal (FID) from any species strongly coupled to hydrogen will dephase (decay) faster than the signal from species that are weakly coupled to hydrogen.

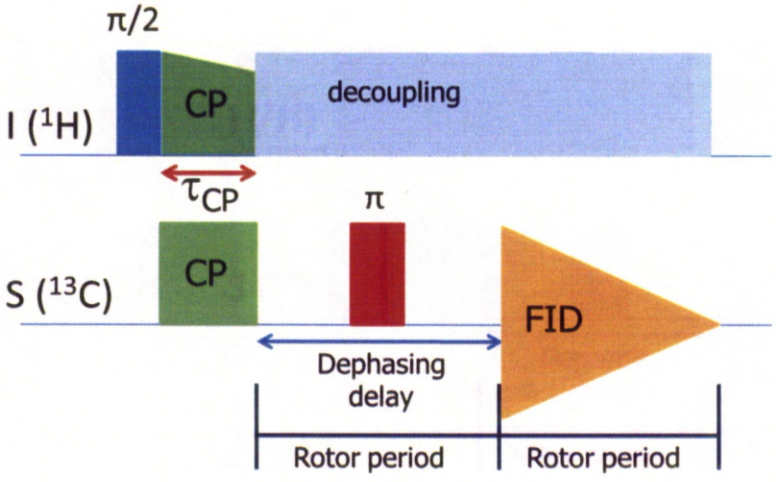

Figure 2.23 Pulse sequence for dipolar dephasing spectral editing

By careful selection of the delay time, it is possible to obtain a spectrum that only displays resonances attributable to species that are not attached to hydrogen. As dephasing relies on dipolar coupling, anything that reduces this (such as spinning the sample) can result in the signal not being suppressed effectively. This is often the case for CH_3 groups in which the internal rotation reduces C-H heteronuclear dipolar coupling resulting in CH_3 resonances rarely being suppressed. This has also been observed for phenyl rings that flip and they are therefore still observable in the spectrum.

The pulse sequence also includes a rotor synchronised refocussing π pulse on the ^{13}C channel. This is because phase distortions that cannot be corrected are

observed in the spectrum in its absence. The precision of the calibration of this pulse and the accuracy of the rotor synchronisation are not critical for this experiment so controlled spinning or rotor triggered pulses are not necessary.

At high spinning rates or in experiments with long dephasing delays it is sometimes necessary to increase the number of rotor periods before and after the refocusing pulse is applied. For ^{13}C, a dephasing delay of 40-50 μs is usually enough to achieve the required discrimination between protonated and non-protonated species. Using a longer delay than necessary can result in a loss of signal from the non-protonated species. [238]

Dipolar dephasing is often used for separating components of a complex mixture of materials. Pharmaceuticals are often delivered in an excipient mix that generally contains a saccharide. Dipolar dephasing can be used to remove the resonances attributable to the saccharide allowing easier elucidation of the active complex.

2.5.3 Probing mobility using solid state NMR

NMR spectroscopy provides a variety of methods for characterisation of molecular mobility and can probe motions within the time scales from picoseconds to seconds (**Figure 2.24**). The effects of these motional processes on nuclear spins depend on their relationship to the three characteristic time-scales of the nuclear spin system; relaxation, spectral and Larmor.

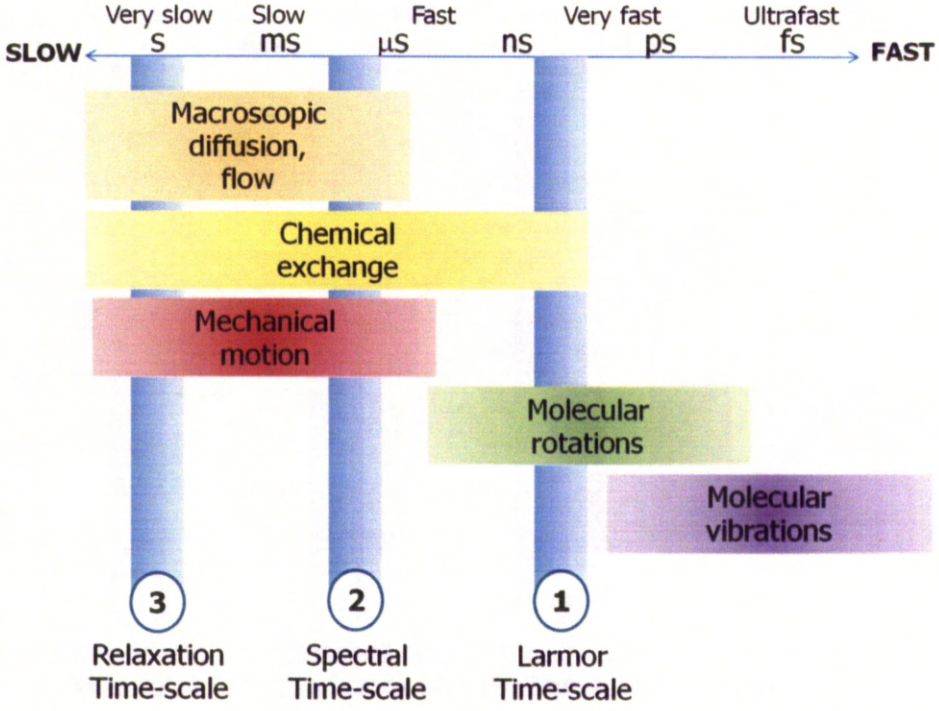

Figure 2.24 Typical motional time-scales for physical processes[220]

The Larmor timescale indicates the time required for the spins to precess through 1 rad in the magnetic field.

The spectral timescale is the inverse width of the NMR spectrum measured in Hz. For example, if two spins with chemical shift frequencies $\Omega^0{}_1$ and $\Omega^0{}_2$ and the chemical shift interactions are dominant, the spectral timescale is given by:

$$\left|(\Omega_1^0 - \Omega_2^0)\tau_{spec}\right| \sim 1 \qquad \textit{eqn. 2.24}$$

If the two spins are both ^{13}C with a chemical shift difference of 100 ppm in a 11.74 T magnetic field, the timescale, $\tau_{spec,}$ is *ca.* 13 µs.

The relaxation time scale indicates the spin-lattice relaxation time constant, T_1. However, the processes that are responsible for spin-lattice relaxation time are on the Larmor timescale. This will be discussed further in the following section.

All of these characteristic timescales depend on the sample, spin isotope and physical parameters such as temperature and the magnetic field strength.[220]

The techniques available for measuring molecular motions using solid-state NMR spectroscopy range from CP based experiments to measurement of various relaxation times. It is the latter that will be described and have been used here. For this reason, the relationship between molecular motions and relaxation times will first be introduced followed by an explanation of the theory behind relaxation and finally the experimental methods used to measure relaxation times.

2.5.3.1 How nuclear relaxation results from molecular motions

Nuclear spin relaxation is the process by which spins return to equilibrium through interaction of the spin system with the thermal molecular environment. Equilibrium in this case is the state in which the populations of the energy levels are predicted by the Boltzmann distribution and at which there is no transverse magnetization. When a RF pulse is applied to an NMR sample in the B_0 field, the equilibrium of the spin system is disturbed. The populations of the energy levels after the pulse deviate from their equilibrium positions and often coherences are created. These coherences depend on the magnitude of the RF pulse, for example, a π pulse inverts the population distribution (180^0 flip where spins are still aligned along the z-axis) whereas a $\pi/2$ pulse equalises spin state population and generates coherences (90^0 flip where spins are transferred into the xy plane allowing them to be observed) (**Figure 2.25**).

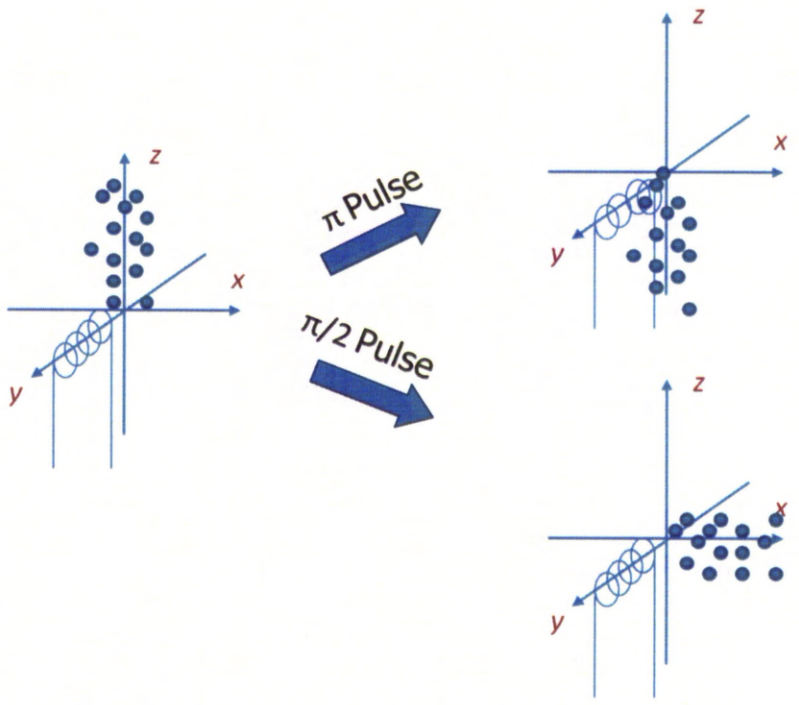

Figure 2.25 Vector diagrams showing distribution of spins after π and π/2 RF pulses are applied

Relaxation processes can be divided into two types, spin-lattice relaxation (T_1) and spin-spin relaxation (T_2). T_1 relaxation is the movement of spins back to their Boltzmann distribution values whereas T_2 is the decay of coherences (**Figure 2.26**).

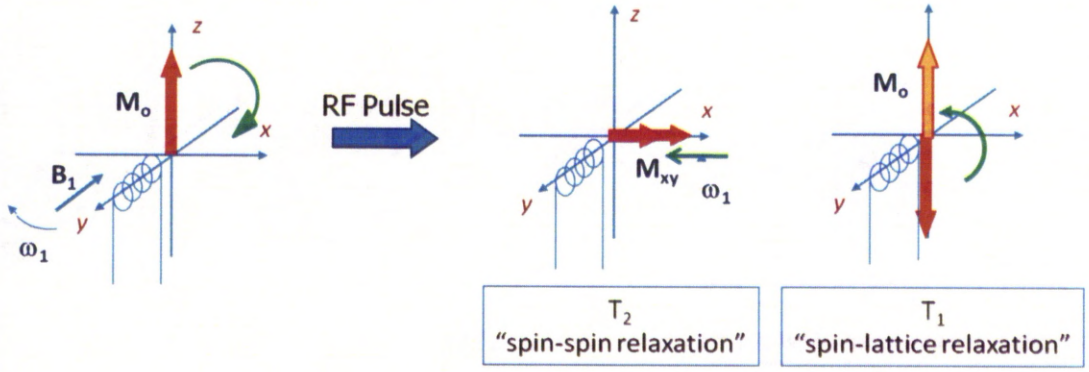

Figure 2.26 Vector diagrams of T_1 and T_2 relaxation

In an isolated spin system T_1 and T_2 are the only two time constants for relaxation whereas in a system that contains coupled spins, more time constants are required to characterise the nature of the relaxation.

For spin ½ nuclei, relaxation is caused by fluctuating magnetic fields at the site of nuclear spins, caused by the thermal motion of molecules. The fluctuating magnetic field, or local environment that the spin is sited will be influenced by other spins that are close in space, *i.e.* dipolar coupling. Chemical shift anisotropy will also influence the local field. This is caused by molecular electron currents induced by the external magnetic field. The total fluctuation of the local magnetic field, although much smaller in magnitude than the external magnetic field, are enough to cause spin-lattice relaxation. Generally, for spin ½ nuclei, the order of influence is dipole-dipole>CSA>spin-rotation.

2.5.3.2 Spin lattice relaxation time (T_1)

T_1 relaxation, as described above is the recovery of z-magnetization (M_z) to the Boltzmann distribution. Bloch theory of NMR describes this recovery as an exponential decay governed by *eqn. 2.25*:

$$\frac{dM_z}{dt} = \frac{(M_0 - M_z)}{T_1} \qquad \textit{eqn.2.25}$$

where M_0 is the magnetization at thermal equilibrium and T_1 is the first order time constant for the process. After the application of a $\pi/2$ pulse, the T_1 time at time, t, is given by:

$$M_z = M_0\left(1 - e^{-t/T_1}\right) \qquad \textit{eqn. 2.26}$$

Longitudinal relaxation (T_1) times are sensitive to motions that fall in the frequency regime of the NMR spectrometer (external magnetic field (B_0), MHz region)[239]. Typical motional contributors to the longitudinal relaxation are diffusion, chemical exchange and mechanical motion.[220] Since the processes responsible for longitudinal relaxation (T_1) are on the Larmor time scale (see **Section 2.5.3**), it is possible to measure the changes in mobility of the RTIL upon encapsulation.

T_1 relaxation can be described as a resonance phenomenon that depends on the number of fluctuating fields that are on resonance. For a highly mobile system, the fluctuations of the oscillating magnetic field have a high frequency and therefore T_1 times are long, greater than the Larmor frequency, ω_0. This behavior is typical of gases and solutions (labeled a in **Figure 2.27b**). As the frequency of the oscillating magnetic field decreases, they become on resonance with NMR transitions. At this point (labeled b in **Figure 2.27b**), the relaxing field and the nucleus being studied are equal. As the frequency of the oscillating magnetic field decreases further due to less molecular tumbling, the relaxing field again becomes off resonance with the NMR transition and T_1 relaxation times begin to increase (labeled c in **Figure 2.27b**). This behaviour is typical of the motion observed in solids.

The random motions described above give rise to a variety of frequencies that can be characterised by a rotational correlation time, *etc*. This is the average time taken for the molecule to rotate through one radian. Short correlation times therefore correspond to rapid tumbling and *vice versa*. The frequency distribution of the fluctuating magnetic fields associated with this motion is termed the spectral density, $J(\omega)$, and can be described as being proportional to the probability of finding a component of the motion at a given frequency, ω(rad s^{-1}). Only when a suitable component exists at the Larmor frequency of a spin, can T_1 relaxation occur. Spectral density is, therefore, given by:

$$J(\omega) = 2\frac{\tau_c}{1+\omega^2\tau^2} \qquad \textit{eqn.2.27}$$

Spectral density can also be represented in graphical form as shown in **Figure 2.27** for fast, intermediate and slow molecular tumbling rates. For a given Larmor frequency, ω_0, as indicated in **Figure 2.27a**, the corresponding T_1 can be measured as a function of molecular tumbling rate. From this it translates that fast molecular motion has a relatively small component at the Larmor frequency, so relaxation is slow (T_1 is long), as might be described for a fluid like motion. This is the region occupied by small molecules in low viscosity solvents, known as the extreme narrowing limit.

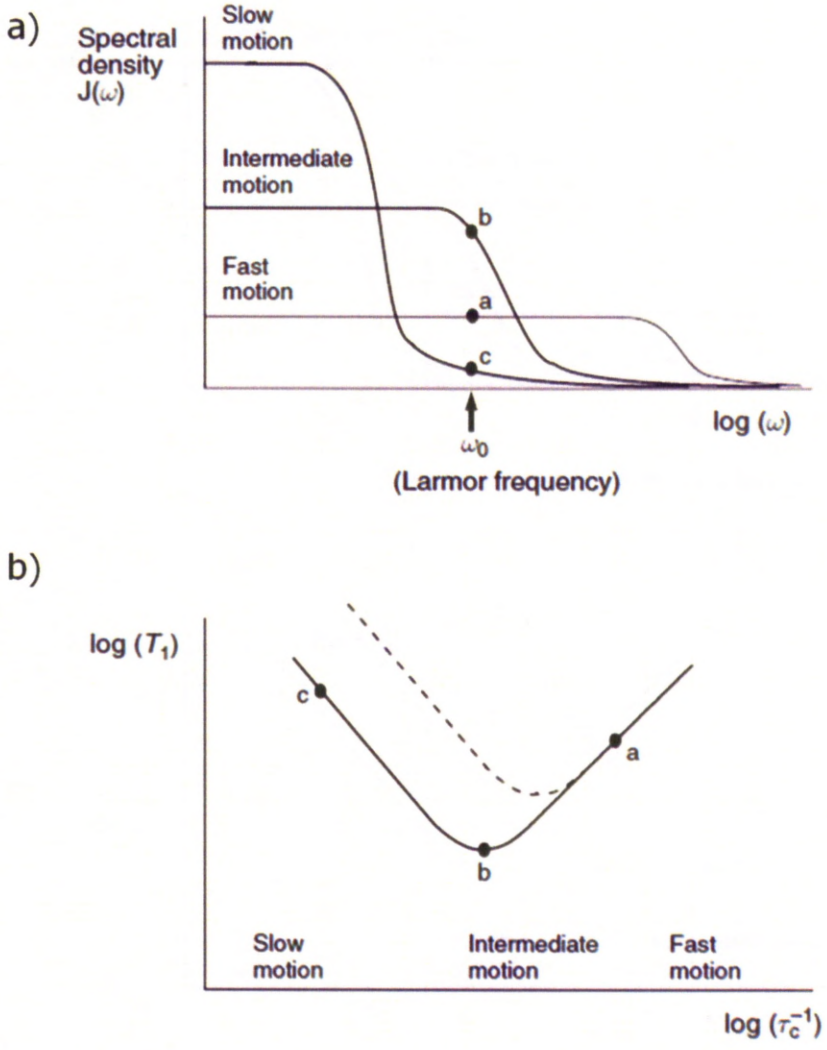

Figure 2.27 a) Schematic representation of spectral density, J(ω), as a function of frequency shown for molecules exhibiting fast, intermediate and slow motions. For spins with Larmor frequency, ω_0, corresponding T_1 curve is given in **b)** as a function of molecular tumbling rate (inverse correlation time, τ_c). Note that the T_1 curve is field dependent as the Larmor frequency is different for spins in different fields and the T_1 minimum will occur at higher fields for faster motions, indicated by dashed line.[240]

As the tumbling rates decrease, the spectral density at ω_0 initially increases but then falls away again as slow tumbling is present. Therefore, the T_1 curve has a minimum at intermediate rates. So, for small rapidly tumbling molecules, faster motion corresponds to slower relaxation and hence narrower linewidths, since longitudinal and transverse relaxation rates are identical ($T_2 = T_1$) under these conditions.[240]

A reduction in tumbling rate, such as by an increase in viscosity or reduction in sample temperature, reduces the relaxation times and broadens the NMR resonance. The point at which the minimum is encountered and the slow motion regime approached is field dependent because ω_0 itself is field dependent (**Figure 2.27**). The behaviour in the slow motion regime is slightly more complex because the energy-conserving flip-flop processes that lead to transverse relaxation are also stimulated by very low frequency fluctuations, and the T_2 curve differs markedly from that for T_1 (**Figure 2.28**). For slow tumbling molecules such as polymers and biological macromolecules, T_1 relaxation times can again be quite long but linewidths become rather broad as a result of short T_2. From this it can be said that T_1 are less sensitive to very slow motions whereas T_2 may still be stimulated by slower motions. Another measure of slow motions that is particularly useful in solids is T_1 relaxation in the rotating frame as described in **Section 2.5.3.3**. Molecular motion is, therefore, fundamental to the process of relaxation, but its analysis of the relationship between specific motions and the relaxation rate is extremely complex.

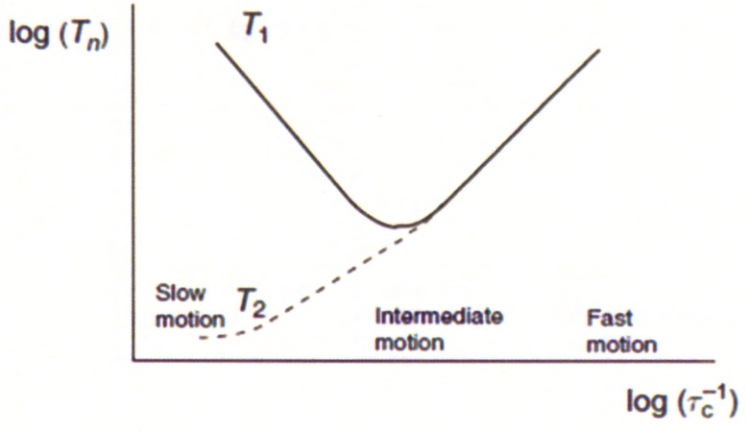

Figure 2.28 Dependence of T_1 and T_2 on the rate of molecular tumbling[240]

Molecular mobility changes with temperature. Therefore, the random field fluctuations originating in the molecular environment and the correlation time, τ_c, will be temperature dependent. Increasing the temperature makes the fluctuations faster and reduces the correlation time. The effect of temperature on T_1 time depends on the location of τ_c with respect to the T_1 minimum.[220] This relationship is given by:[220]

$$T_1^{-1} = \gamma^2 \langle B_x^2 \rangle J(\omega_0) = \gamma^2 \langle B_x^2 \rangle \frac{\tau_c}{1+(\omega_0 \tau_c)^2} \qquad \textit{eqn. 2.28}$$

where γ is the gyromagnetic ratio and $J(\omega_0)$ is the normalized spectral density. B_x is the local magnetic field and ω_0 is the Larmor frequency. The correlation time obeys an Arrhenius relationship:[241]

$$\tau_c = \tau_A e^{(E_A/RT)} \qquad \textit{eqn.2.29}$$

Variable temperature T_1 relaxation measurements are therefore key in analyzing molecular motions.

For spin ½ nuclei the most important relaxation mechanism is through space dipolar coupling between the spins. In viscous liquids and solids this is particularly important as the system is anisotropic. Dipole-dipole relaxation is orientation dependent and is, therefore, influenced by the rotational correlation time which in turn is affected by viscosity and temperature. [220]

2.5.3.2.1 Dipole dipole relaxation

The most important relaxation mechanism for many spin ½ nuclei is from the dipolar interaction between spins. As previously described, dipolar interactions influence the local magnetic field that a spin "feels". As a molecule tumbles, the local magnetic field will fluctuate in turn inducing relaxation.

Dipolar relaxation is often the most dominant relaxation mechanism for protons that rely on their neighbours as a source of magnetic dipoles. Therefore, protons that lack near neighbours relax more slowly. The most obvious consequence of this is lower than expected integrals in routine high resolution ^1H NMR spectra due to the partial saturation of the slower relaxing spins that are unable to recover sufficiently between each scan. If T_1 data are available, then protons with long relaxation times are predicted to be remote from others in the molecule. ^{13}C nuclei are also relaxed primarily by dipolar interactions, either through interactions with directly bound protons or, in the absence of these, by more distant ones. This is analogous to the dipolar coupling responsible for magnetization

transfer in CP-MAS NMR described earlier. In very large molecules and at high field, the CSA mechanism, described in the following section, can also play a role, especially for sp and sp^2 centres or for spin ½ nuclei that exhibit large chemical shift ranges.

Dipolar relaxation can also arise from the interaction of a nuclear spin with an unpaired electron, the magnetic moment of which is over 600 times that of the proton and so provides a very efficient relaxation source. This is sometimes referred to as the paramagnetic relaxation mechanism.

2.5.3.2.2 CSA relaxation

Another, less effective, mechanism of relaxation is CSA. Since the electron distribution in chemical bonds is inherently unsymmetrical or anisotropic, the local field experienced by a nucleus, and hence its chemical shift, will depend on the orientation of the bond relative to the B_0 field. In solution, the rapid tumbling of a molecule averages this CSA so that only a single frequency is observed for each site. This was earlier referred to as the isotropic chemical shift. The fluctuating field caused by CSA is still adequately strong to induce relaxation. This is particularly prominent in solids and for nuclei that exhibit a large chemical shift range as these possess the greatest shift anisotropy, for example, ^{19}F, ^{31}P and many metals.

The characteristic feature of CSA relaxation is its dependence on the square of the applied field, meaning it has greater significance at higher B_0. Nuclei whose relaxation is dominated by the CSA mechanism may show significantly larger linewidths at higher fields if they possess large shift anisotropy, and any potential benefits of greater dispersion and sensitivity may be lost by line broadening. It is for this reason, the study of some metal nuclei may be more successful at lower fields. Reducing the correlation time, by warming the sample, may attenuate the broadening effect, although this approach clearly has rather limited application. In some cases, enhanced CSA relaxation at higher fields can be advantageous. A moderately enhanced relaxation rate can allow more rapid data collection, providing an improvement in sensitivity (per unit time) above that expected from the increase in magnetic field alone.

2.5.3.2.3 Spin rotation relaxation

The smallest contribution to relaxation that will be discussed here is through spin rotation. Molecules or groups that rotate rapidly have an associated molecular magnetic moment that is generated by the rotating electronic and nuclear charges. In solids this type of rotation is restricted due to reduced molecular tumbling and so the contributions from spin rotation are further reduced. The field due to the rotation fluctuates as the molecule or group changes its rotational state as a result of, for example, molecular collisions, and this provides a further mechanism for nuclear relaxation. This is most effective for small, symmetrical molecules or for freely rotating methyl groups, and its efficiency increases as tumbling rates increase. This is in contrast to the previously described mechanisms. Heating a sample enhances spin-rotation relaxation, this temperature dependence being characteristic of this mechanism and allowing its presence to be established.

2.5.3.2.4 Measuring T_1 relaxation times by inversion recovery

T_1 relaxation time measurement can be performed by using an inversion recovery, saturation recovery or progressive saturation pulse sequence. Often, inversion recovery is favored due to its simplicity. As shown in **Figure 2.29**, a π pulse is applied to invert the magnetization. A delay, τ, is then allowed for magnetization to relax after which a $\pi/2$ pulse is applied so that the size of the z-magnetization that is remaining after the delay can be measured.

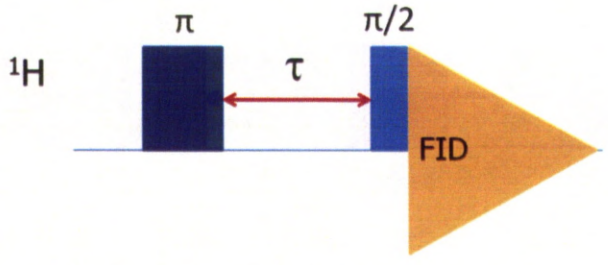

Figure 2.29 T_1 inversion recovery pulse program

The τ times are varied and the peak intensities as a function of delay time, τ, are then measured. The change in intensities can then be fitted according to *eqn. 2.30.*

$$M_z(t) = M_0\left(1 - 2e^{\left(-\frac{\tau}{T_1^H}\right)}\right) \qquad \textit{eqn.2.30}$$

where M_0 is the equilibrium magnetization as would be recorded at τ_∞. Note here that the additional factor of two has been added to *eqn. 2.30* compared to *eqn. 2.26* as the recovery starts from inverted magnetization. The peak intensity will be negative for small values of τ but goes through zero and becomes positive for large values of τ as shown in **Figure 2.30.**

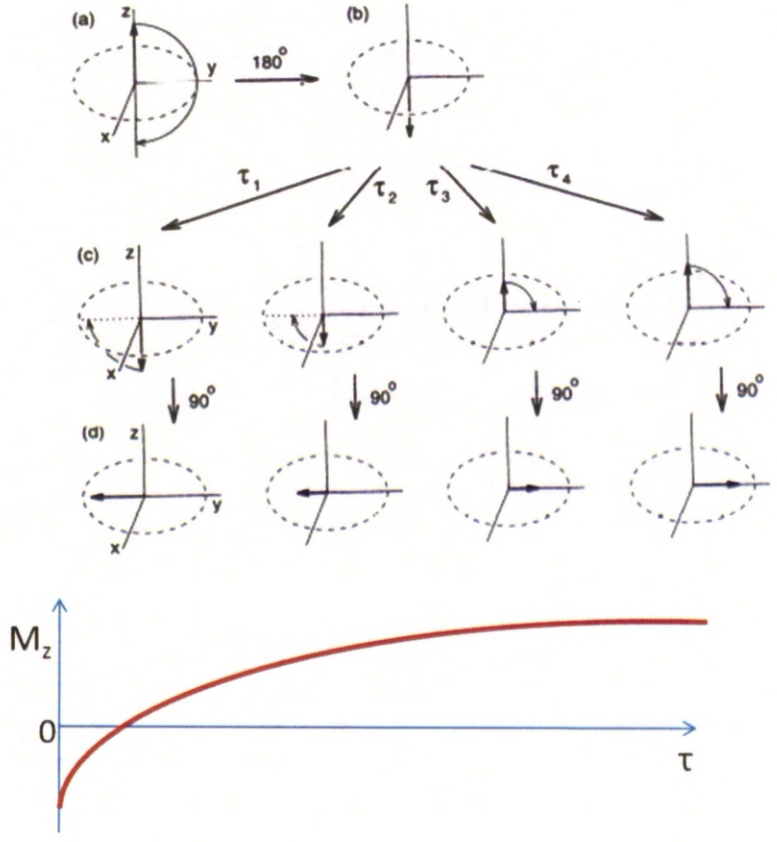

Figure 2.30 Peak intensity (M_z) as a function of delay time, τ. As the delay time increases peaks turn from negative to positive in intensity[220]

The peak intensity has an exponential dependence on the delay time as this rate is dictated by T_1. Measuring the T_1 relaxation times with varying temperature

affords a plot similar to those given in **Figure 2.28** from which interpretation of the motional regime can be extracted.[220]

2.5.3.3 Spin lattice in the rotating frame ($T_1\rho$)

T_1 relaxation in the rotating frame ($T_{1\rho}$) times are sensitive to slower molecular motions in the kHz region (RF field (B_1)). Additional information on the mobility of different parts of the $[bmim]^+$ cation can therefore be obtained by determining $T_{1\rho}$ times.

Spin diffusion can be a problem when measuring $T_{1\rho}{}^H$. However, ^{13}C spins are of low natural abundance, it ensures physical separation between them and therefore low spin diffusion.[242]

In order to eliminate transverse (T_2) contributions the *spin-locking* method devised by Schaefer *et al.*[243] has been used to measure $T_{1\rho}$ relaxation. This method is advantageous over the Carr-Purcell method which allows the T_2 magnetization to precess freely before reversing its evolution using a π pulse.[220]

2.5.3.3.1 Measuring $T_1\rho$

The ^{13}C magnetisation is allowed to relax in the rotating frame during the time τ. The peak intensity is dependent on the amount of magnetization that has relaxed during τ. The contact time for the CP pulse was fixed to 2.0 ms and the recycle delay was 8.0 s.

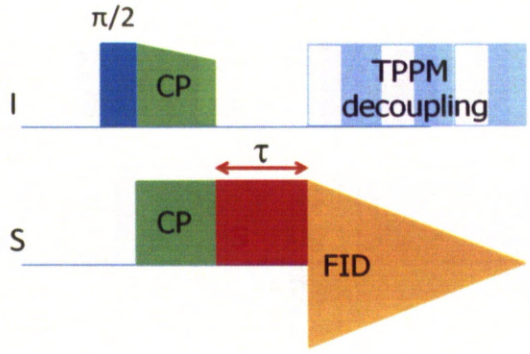

Figure 2.31 Pulse sequence for $T_{1\rho}{}^{S}$ time measurement. I refers to abundant spin ^{1}H and S refers to dilute spin ^{13}C

The peak intensities as a function of spin-lock time can be fitted as a sum of the exponentials in a similar way to T_1:

$$M(t) = \sum_i M_{0i} exp\left(-\frac{t}{T_{1\rho i}^{C}}\right) \qquad \textit{eqn. 2.31}$$

Chapter 3

NMR Spectroscopic Studies of 1-Butyl-3-methylimidazolium Trifluoromethanesulfonate Encapsulated in SBA-15

3.1 Introduction

NMR spectroscopic analysis is frequently used for elucidation of RTIL structures,[244] assessing the reorientational dynamics of RTILs[166] with varying temperature, and observing hydrogen bonding. NMR has previously been used to study solvents encapsulated in porous media[245-255] as well as to probe the effect of confinement on ionic liquid dynamics in monolithic silica ionogels.[40,256] NMR spectroscopy is advantageous over other analytical techniques since it allows changes in molecular motion on a variety of time scales to be probed using various relaxation times.

Le Bideau *et al.*[40] were the first to report temperature dependent relaxation time measurements of ionic liquids confined in monolithic silica matrices. The aim of their research was to investigate whether the properties of the ionic liquid were retained upon encapsulation and covalent bonding to the silica surface. It was found that the pore size affects the reorientational dynamics of the ionic liquid. Above 270 K, the encapsulated and neat RTIL display similar properties. However, below 270 K, confined ionic liquid displayed liquid like behaviour whereas the neat ionic liquid crystallized.

Since then there have been few reports of the use of NMR spectroscopy for characterization of SILPs. However, NMR spectroscopy has been employed to investigate multiscale dynamics of ^{1}H and ^{19}F in ionogels,[257] and to observe the bulk ionic liquid-like mobility of silica bound ionic liquids.[170] Taubert *et al.*[170] have studied 1-ethyl-3-methyl imidazolium [emim]-X ionic liquids (X = dicyanamide [$N(CN)_2$], ethyl sulfate [$EtSO_4$], thiocyanate [SCN] and triflate [CF_3SO_3]) inside silica monoliths using X-ray scattering, nitrogen sorption isotherms, FT-IR spectroscopy, solid-state NMR spectroscopy and DSC. They found that their ionic liquids exhibit bulk like behavior upon impregnation to the silica monolith, similar to the findings of Neouze *et al.*[42] The study of Le Bideau *et al.* showed T_1 relaxation time measurements that were absent in the work of Taubert and Neouze. The conclusions made in these papers were from the appearance of the ^{1}H NMR spectra and are limited to analysis of chemical shift and line shape.

More recently, ^{2}H and ^{19}F solid-state NMR spectroscopy has been used to compare a neat ionic liquid

perdeutero-*N*-(ethylpyridiniumbis(trifluoromethanesulfonyl)amide ($C_2Py][NTf_2]$-d_{10})) and the same ionic liquid confined in mesoporous silica.[96] Changes in the NMR spectra with varying temperature are consistent with phase transitions observed by differential scanning calorimetry (DSC). Upon immobilization of the ionic liquid, the phase transitions observed are absent from where they would be expected for the neat ionic liquid, inferring that the properties of the ionic liquid are altered upon impregnation.

Computational modelling of ionic liquids is well documented in the literature and has taken a variety of approaches *e.g.* clustering of RTIL molecules,[258] interactions between RTILs and water[259] and gas solubilities in RTILs.[81] RTILs encapsulated in porous hosts such as carbon nanotubes[81] or immobilized on graphite surfaces[260] have also been extensively investigated using computational modelling. Conversely, modelling of porous silicas has also been explored[261] with simulations of various encapsulated guests. For example, Tallarek *et al.* document the changes in properties of a water/acetonitrile mixture upon confinement in a nanoporous silica using molecular dynamics simulations.[262]

A particularly relevant paper from Carper *et al.*[263] describes a semi-empirical molecular modelling of RTIL tribology. They describe a system in which imidazolium based ionic liquids with PF_6^- or BF_4^- anions were brought into contact with a hydroxylated silicon surface. They found that RTILs that interact strongly with the surface provide the best lubricant unless the interaction is so strong that it leads to a chemical reaction. This in turn implies that the RTIL forms a protective coating on the surface while retaining its structural integrity. This has been observed previously by Mo *et al.*[264] and Yu *et al.*[265] However, when RTILs are used as protective coatings for metals, the lubricant properties are no longer useful. The interactions in the paper from Carper *et al.*[263] were investigated using a semi-empirical[266] (CACHE) method.

This chapter describes an investigation of the encapsulation of a well studied ionic liquid, 1-butyl-3-methylimidazolium triflate ([bmim]OTf), in mesoporous silica, SBA-15. The loading of [bmim]OTf was varied in order to examine its mobility and orientation with respect to the support using NMR spectroscopy.

In this work, the interactions of [bmim]OTf with the pore surface of SBA-15 have been investigated using solid-state NMR. T_1 relaxation times have been determined for neat RTIL and encapsulated RTIL using the inversion recovery pulse sequence. For systems with long relaxation times (ms to s), expected for these composites since [bmim]OTf is viscous, warming the sample reduces the T_1 relaxation time.

^1H line shapes and T_1 relaxation times have been studied to understand the change, as a function of loading and temperature, in molecular motions upon encapsulation of [bmim]OTf. We also detail how varying the loading of [bmim]OTf has little effect on the ^1H–^{13}C CP-MAS spectra but a significant effect on the intensity and line shapes in $^{13}C\{^1H\}$ MAS NMR spectra. In addition, we show how [bmim]OTf interacts with the surface of SBA-15 mesopores using ^1H-X CP dynamics. A comparative study between computational modeling and experimental results are also presented to demonstrate the interactions of the ionic liquid and the silica pore wall. To the best of our knowledge, this is the first report of these techniques being used collectively to characterise SILPs.

3.2 Experimental

3.2.1 Materials

Pluronic surfactant, P-123, tetraethylorthosilicate (TEOS) and sodium chloride were purchased from Sigma-Aldrich. 1-Butyl-3-methylimidazolium triflate, [bmim]OTf, was purchased from Io-li-tec, and stored in a dry, nitrogen-filled glove box. [bmim]OTf was characterized by ^{1}H and $^{13}C\{^{1}H\}$ NMR and DSC before use. Dichloromethane was purchased from Fisher Scientific and freshly distilled before use. All preparations were carried out using Schlenk procedures, under N_2.

3.2.2 Synthesis of SBA-15

The mesoporous host, SBA-15, was synthesized by the surfactant templating method detailed by Li *et al.*[267] Pluronic surfactant, P-123 (2.0 g), 2M HCl(aq.) (62.5 ml) and NaCl (5.5 g) were mixed at room temperature in a 100 ml polypropylene bottle until a clear, colourless, homogeneous solution was obtained. Tetraethylorthosilicate, TEOS (4.23 ml) was then added and the mixture stirred at 313 K for 20 hours giving a composition of 1 TEOS: 0.017 P123: 6.16 HCl: 4.6 NaCl: 165 H_2O. This was heated at 363 K for 24 hours, filtered, washed with distilled de-ionised (DDI) water and dried. It was then calcined at 823 K for 6 hours to remove the template. Before further use SBA-15 was dried in a vacuum oven at 373 K for 20 hours.

3.2.3 Impregnation of [bmim]OTf in SBA-15

The requisite amount of [bmim]OTf was dissolved in freshly distilled dichloromethane (12.5 ml) and added to the dry SBA-15 (0.25 g). The suspension was refluxed for 2 hours at 313 K following which a dry white paste remained. In cases where solvent remained after 2 hours, excess was removed using a rotary evaporator. This gave a series of encapsulated samples, B-SBA-1 (1.28 g/g

[bmim]OTf in SBA-15), B-SBA-2 (0.64 g/g), B-SBA-3 (0.32 g/g), B-SBA-4 (0.16 g/g) and B-SBA-5 (0.08 g/g).

3.3 Characterisation conditions

3.3.1 Powder X-ray diffraction

Powder X-ray diffraction (PXRD) patterns were measured using a Panalytical X-pert pro diffractometer with Co-$K_{\alpha 1}$ radiation (wavelength of 1.789 Å). This operates in Bragg-Brentano geometry.

Patterns were measured in the 0.7–5.0 2θ range using a flat bracket sample holder.

3.3.2 Nitrogen sorption isotherms

Nitrogen adsorption/desorption isotherms were measured on a Micromeritics ASAP 2420 system at 77 K. Samples were dried and evacuated at 393 K for 5 hours before analysis.

The specific surface area was calculated using the BET method and a linear plot over a range of p/p_0 = 0.06-0.20. Pore size distributions were calculated using the adsorption branch of an isotherm using the BJH method.[268] The pore volume was calculated from the amount of adsorbed N_2 at p/p_0 = 0.99. Micropore surface area and volume were obtained from the hybrid DFT method.

3.3.3 Differential scanning calorimetry

DSC thermographs were recorded on a Perkin Elmer Diamond Hyper Calorimeter, calibrated using an indium primary standard, with solid-solid transitions for cyclohexane and etylbenzene as supplementary low temperature standards. Liquid nitrogen and helium were used as coolant and purge gas respectively. 50 µL aluminium pans were used as sample holders for both neat [bmim]OTf and

encapsulated samples and sample volumes were in the range 12-18 mg (weighed on a 4 decimal place digital analytical balance). Each sample was heated and cooled in the range of 98 K to 303 K. A typical temperature program used for these measurements is as follows:

1. Heating from 293 K to 303 K at 5 K/min;
2. Hold for 1 min;
3. Cool from 303 K to 98 K at 5 K/min;
4. Hold for 1 min;
5. Heat from 98 K to 303 K

This sequence was repeated three times. All transition temperatures reported herein for neat ionic liquid were calculated from the third temperature cycle. Analysis of the encapsulated samples after the first temperature cycle are unreliable due to the thermal history of the sample, which may have caused some seeping of the encapsulated ionic liquid from the pores.

3.3.4 Solid state NMR

Unless otherwise stated solid-state NMR experiments were conducted at ambient temperature (unless otherwise stated) at 9.4 T using a Bruker Avance DSX-400 spectrometer equipped with a 4 mm ^{1}H/X/Y probe.

3.3.4.1 ^{1}H MAS NMR and T_1 inversion recovery

^{1}H magic angle spinning (MAS) NMR spectra were acquired at 400.13 MHz with a ^{1}H $\pi/2$ pulse length of 3.0 μs at an MAS rate of 10.0 kHz and a recycle delay of 8.0 s. The position of the ^{1}H resonances is quoted in ppm from external tetramethylsilane (TMS).

^{1}H T_1 relaxation times were measured for B-SBA-2 and B-SBA-4 over the temperature range 238-323 K using the conventional inversion recovery pulse sequence as described in **Section 2.5.3.2.4, Figure 2.29**. Nineteen different delay times were sampled in the range from 10 μs to 5.0 s.

A typical temperature cycle used in these experiments was as follows:

1. Cool from room temperature to 233 K over 30 min
2. Allow to equilibrate for 20 min then record spectra
3. Heat by 10 K, allow to equilibrate for 20 min then record spectra
4. Repeat step 3 until 323 K is reached
5. After recording spectra at 323 K cool to room temperature overnight
6. Acquire room temperature spectra the following day

The peak intensities were fitted according to *eqn. 2.30.*

3.3.4.2 ^{1}H-X Cross Polarisation Magic Angle Spinning (CP-MAS) and ^{13}C relaxation time in the rotating frame ($T_{1\rho}^{C}$)

^{1}H–^{13}C cross-polarization (CP) MAS NMR spectra were acquired at 400.13 MHz for ^{1}H and 100.61 MHz for ^{13}C at an MAS rate of 8.0 kHz. A ^{1}H $\pi/2$ pulse length of 3.0 μs and recycle delay of 8 s were used. Two phase pulse modulation (TPPM) decoupling[269-270] was used during acquisition. A contact time of 2.0 ms was used for the ramped pulse. The Hartmann-Hahn matching condition was set using hexamethylbenzene (HMB). ^{13}C chemical shifts are quoted in ppm with respect to TMS.

For ^{1}H-^{13}C CP kinetics experiments, various contact times were used in the range 0.01 ms to 16 ms.

^{1}H-^{29}Si CP-MAS NMR spectra were acquired at 400.13 MHz for ^{1}H and 79.49 MHz for ^{29}Si at an MAS rate of 4.0 kHz. A ^{1}H $\pi/2$ pulse length of 3.6 μs and recycle delay of 8.0 s were used. TPPM decoupling[269] was used during acquisition. A contact time of 2.0 ms was used for the ramped pulse. The Hartmann-Hahn matching condition was set using kaolinite. The ^{29}Si chemical shifts are quoted in ppm with respect to TMS. For ^{1}H-^{29}Si CP kinetics experiments, various contact times were used in the range 0.01 ms to 15 ms.

The data points acquired by the CP kinetics experiments were fitted using a two population model derived from the classical I-S model described in **Section 2.5.2.4.**[271]

^{13}C relaxation times in the rotating frame ($T_{1\rho}^{C}$) were acquired for samples B-SBA-2 and B-SBA-4 at a spinning rate of 10.0 kHz using the pulse sequence depicted in **Figure 2.21.** After CP, the ^{13}C magnetization is locked along the *y*-axis for a variable spin lock (τ) time in the range 20 μs to 16 ms.

3.3.4.3 One dimensional $^{13}C\{^{1}H\}$ MAS NMR

^{13}C $\{^{1}H\}$ MAS NMR spectra were acquired with $\pi/2$ pulse of 2.6 μs and recycle delay of 20 s. TPPM decoupling[269] was used during acquisition.

3.3.4.4 ^{1}H-^{29}Si Hetronuclear Correlation (HETCOR)

^{1}H-^{29}Si HETCOR spectra were acquired at an MAS rate of 4.0 kHz. The ^{1}H $\pi/2$ pulse was 3.2 μs and a CP contact time of 2.0 ms was used. TPPM decoupling was used during acquisition (t_2) at a decoupling strength of 89.3 kHz. States-TPPI was employed for phase sensitive detection in order to suppress image peaks and give only pure adsorption 2D spectra.[220,272-274] The recycle delay was set at 2.0 s. 256 increments were recorded in t_1 to cover the full ^{1}H spectral width of 9980.04 Hz corresponding to a dwell time of 12.53 μs. 648 scans acquired in t_2 per increment.

3.3.5 High Resolution MAS (HR-MAS) NMR

^{19}F HR-MAS NMR spectra were acquired at 376.38 MHz using a Bruker double resonance HR-MAS probe optimized for ^{13}C. This was achieved by tuning the ^{1}H channel to the Larmor frequency of ^{19}F. The ^{19}F $\pi/2$ pulse length was 3.2 μs. A MAS rate of 4.0 kHz and a recycle delay of 1.0 s were used. The position of the ^{19}F resonance is quoted in ppm referenced from external dichlorofluoromethane ($CHCl_2F$).

^{19}F spin lattice (T_1) relaxation time was measured using the conventional inversion recovery pulse sequence using a ^{19}F $\pi/2$ pulse length of 3.2 μs at an MAS rate of 4.0 kHz and a recycle delay of 8.0 s. Nineteen different delay times were sampled in the range from 10.0 μs to 5.0 s.

3.3.6 Computational modelling (Performed by Dr. A. Trewin)

Structural analysis was performed on a silica surface taken from amorphous silica available in the Materials Studio Modelling 5.0 package.[275] Terminal bonds were terminated with hydrogens to create surface hydroxyl groups. Connolly and surface accessible surface areas were calculated using the "Atoms, Volumes and Surface" module in Materials Studio Modelling 5.0. The N_2 and [bmim]OTf accessible surface areas were calculated from a simple Monte Carlo integration technique in which a probe molecule is "rolled" over the surface.[276] A probe size of 1.82 Å was used for N_2 and 3.5 Å for [bmim]OTf (these values correspond to the van der Waals radii of nitrogen and a methyl group respectively). The grid interval was set to 0.25 Å. Geometry of the surface was optimised using the universal force field[277] at a course–quality calculation level.

3.3.7 Data analysis

All powder XRD data were processed using PANalytical High Score plus software. Nitrogen adsorption isotherms were analysed using Micromeretics ASAP2020 software. All solid-state NMR spectra were acquired using XWINNMR 3.5. HR-MAS NMR spectra were acquired using Bruker TOPSPIN 1.3. All NMR spectra were processed using Bruker Topspin 2.1 software.

CP kinetics curves, relaxation curves and deconvolution of spectra were fitted using Origin8.1 software.

3.4 Results and discussion

PXRD and N_2 sorption isotherms were used to characterise the textural properties of the RTIL-mesoporous silica composite.

3.4.1 Characterisation of SBA-15 and incorporation of [bmim]OTf into SBA-15

The rationale for the loading level of [bmim]OTf was based on the available mesopore volume of SBA-15. The highest loading was estimated to fill the mesopores of SBA-15 fully. The loading was then successively reduced by half until approximately monolayer coverage was achieved. The dimensions of one [bmim]OTf ion pair in the unit cell were estimated using its crystal structure given by Choudhury *et al.*[278]

3.4.1.1 Powder X-Ray diffraction

The PXRD patterns of the as-synthesized and calcined SBA-15 show typical 2D hexagonal arrangements of mesopores with a sharp (100) reflection (d_{100} = 102.3 Å) in the as-synthesized product. The value of d_{100} decreased to 85.0 Å after removal of the template. The high intensity of reflections confirms the presence of a highly ordered mesostructure. Upon loading SBA-15 with [bmim]OTf (with varying levels of loading (0.08, 0.16, 0.32, 0.64 and 1.28 g/g)), the intensity of the (100) reflection decreased with increasing loading (**Figure 3.1**). This is attributed to x-ray interference by [bmim]OTf and is typical for encapsulation of guest molecules inside mesoporous silica.[279-281] The value of d_{100} remained constant for all loading levels confirming that no disruption in the hexagonal array of mesopores had occurred.

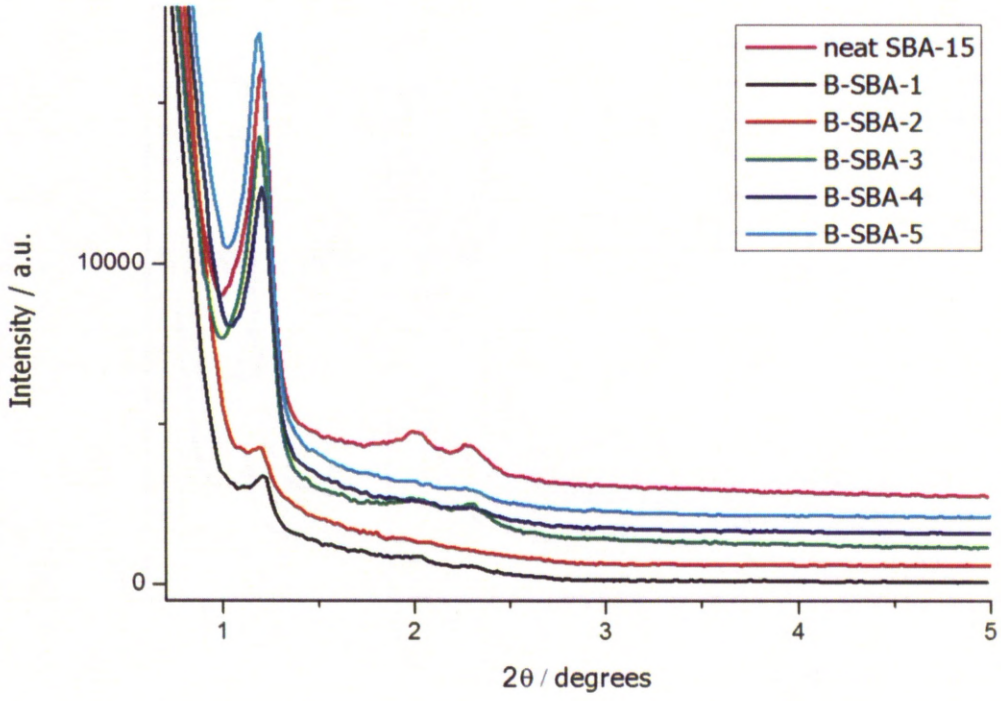

Figure 3.1 PXRD patterns of parent SBA-15 and SBA-15 with varying loading levels of [bmim]OTf

3.4.1.2 Nitrogen adsorption-desorption isotherms

The increasing loading of [bmim]OTf was accompanied by a decrease in pore size, surface area and pore volume as shown in the N_2 adsorption-desorption isotherms (**Figure 3.2**). The parent SBA-15 displays a characteristic type IV adsorption/desorption isotherm with a type H1 hysteresis.[116] Type H1 hysteresis indicates the material possesses cylindrical pores of uniform size and shape.[116] Consistent with the PXRD, SBA-15 shows a high degree of mesoscopic ordering with the sharpest capillary condensation step on the adsorption branch ($p/p_0 \approx 0.70$).

a)

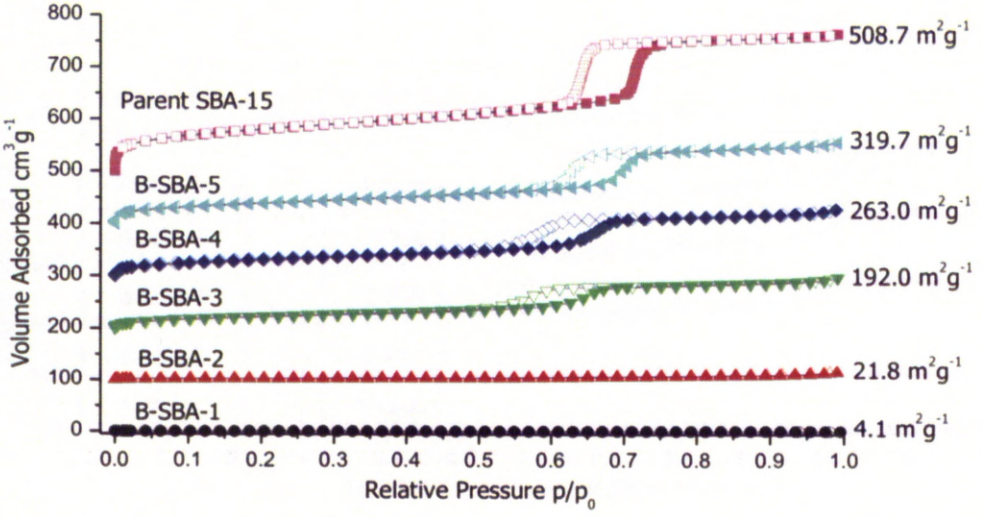

b)

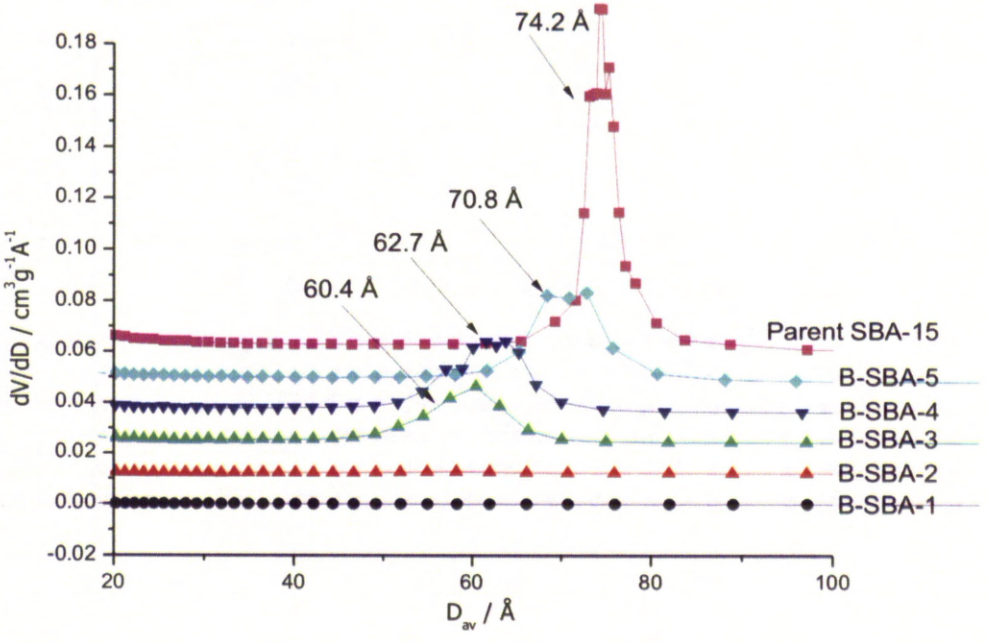

Figure 3.2 a) Nitrogen adsorption–desorption isotherms of parent SBA-15 and SBA-15 with varying loadings of [bmim]OTf (each isotherm is offset by 100 cm^3g^{-1}). **b)** Pore size distribution plots were calculated from the adsorption branch of the N_2 isotherms (each plot is offset by 0.01 $cm^3g^{-1}Å^{-1}$)

The data on textural properties (**Table 3.1**) show that the BET surface areas, total pore volumes and pore size decrease as loading of [bmim]OTf increases. N_2 adsorption–desorption isotherms show similar features upon impregnation of [bmim]OTf suggesting that the ionic liquid does not block the pore opening. The broadening of pore size distribution curves suggests a non-uniform filling of pores. We also observe an increase in pore wall thickness with increasing loading of [bmim]OTf suggesting an interaction between the pore wall and the ionic liquid which results in a surface confined layer. However, the incremental increase in pore wall thickness does not correspond to increasing monolayers of ionic liquid. This could be due to changes in the orientation of the ionic liquid with respect to the pore walls with varying loading levels.

As well as a decrease in mesopore volume and surface area, there is also a decrease in micropore volume and surface area. At the highest loadings of [bmim]OTf (B-SBA-1 and B-SBA-2) no microporosity is displayed due to the ionic liquid being too large to enter the micropore. It is proposed that the surface confined layer of [bmim]OTf in the mesopores blocks the micropore opening, preventing N_2 from penetrating the micropore. This is discussed further in **Section 3.5.4**.

Table 3.1 Textural properties of SBA-15 and [bmim]OTf impregnated SBA-15[a]

Sample	S_{BET} m^2g^{-1}	V_{ads} cm^3g^{-1}	D_{AV}^{ads} Å	d_{100} Å	a^b Å	W Å	mV_{ads} [c] cm^3g^{-1}	mS [c] m^2g^{-1}
Parent SBA-15	509	0.990	74.2	85.0	98	23.8	0.022	44.7
B-SBA-5	320	0.551	70.8	84.8	98	27.2	0.019	43.4
B-SBA-4	263	0.470	62.7	89.1	103	40.3	0.013	29.9
B-SBA-3	192	0.362	60.4	86.0	99	38.6	0.012	27.6
B-SBA-2	21.8	0.059	--	88.8	103	--	--	--
B-SBA-1	4.1	0.006	--	90.4	104	--	--	--

[a]*Pore volumes determined at p/p_0 = 0.9. W is wall thickness determined from $\bar{a}$ - D_{av}.* [b]*Unit cell parameter $\bar{a}$ determined from d_{100} values using $\bar{a} = 2d_{100} / \sqrt{3}$.* [c]*Micropore volume and surface area determined using hybrid density functional theory method.*

The results of N_2 adsorption are in agreement with PXRD data. Whilst PXRD and N_2 adsorption are capable of determining whether the [bmim]OTf has entered the pores of SBA-15, they are limited in probing interactions the ionic liquid with the porous support at the molecular level.

3.4.2 Interaction between $[bmim]^+$ cation and pore surface

3.4.2.1 ^1H MAS NMR and T_1 relaxation time measurements

The ^1H MAS NMR spectra of SBA-15 loaded with [bmim]OTf recorded at ambient temperature (**Figure 3.3**) confirm the presence of [bmim]OTf encapsulated in SBA-15 in all samples. The peaks in the ^1H MAS NMR spectra are relatively broad, which could be associated with the relatively high viscosity of the ionic liquid although this assumes that the ionic liquid remains as a liquid upon encapsulation. The resonance assignment is as follows: δ/ppm = 1.09 C(9), 1.59 C(8), 2.07 C(7), 4.17 C(10), 4.40 C(6), 7,81 C(4), 7.88 C(5) and 9.11 C(2).[244] The spectra are free of resonances associated with residual solvent.

As the loading of [bmim]OTf decreases, the linewidth of each resonance broadens, indicative of a less mobile cation environment. Further inspection of the linewidths as a function of loading, shown in **Figure 3.4**, indicate that above *ca.* 0.3 g/g (B-SBA-1 and B-SBA-2) the lineshape is attributable to bulk ionic liquid inside the pores. Below *ca.* 0.25 g/g (B-SBA-3, 4 and 5) the lines are significantly broadened consistent with an increasing the contribution of a surface confined layer. The resonances corresponding to the butyl chain remain narrow when compared with those of the imidazolium ring and N-methyl protons, suggesting that the butyl chain is more mobile than the imidazolium ring. We do not observe a resonance with a shoulder for surface confined and bulk material, as suggested by Lin *et al.*[282] in their study of confinement of butan-1-ol in SBA-15. The absence of a shoulder is believed to have arisen from inherent broadening of the resonances. The ^{1}H line widths of neat [bmim]OTf have been omitted in **Figure 3.4** as MAS was not applied during acquisition of the NMR spectra.

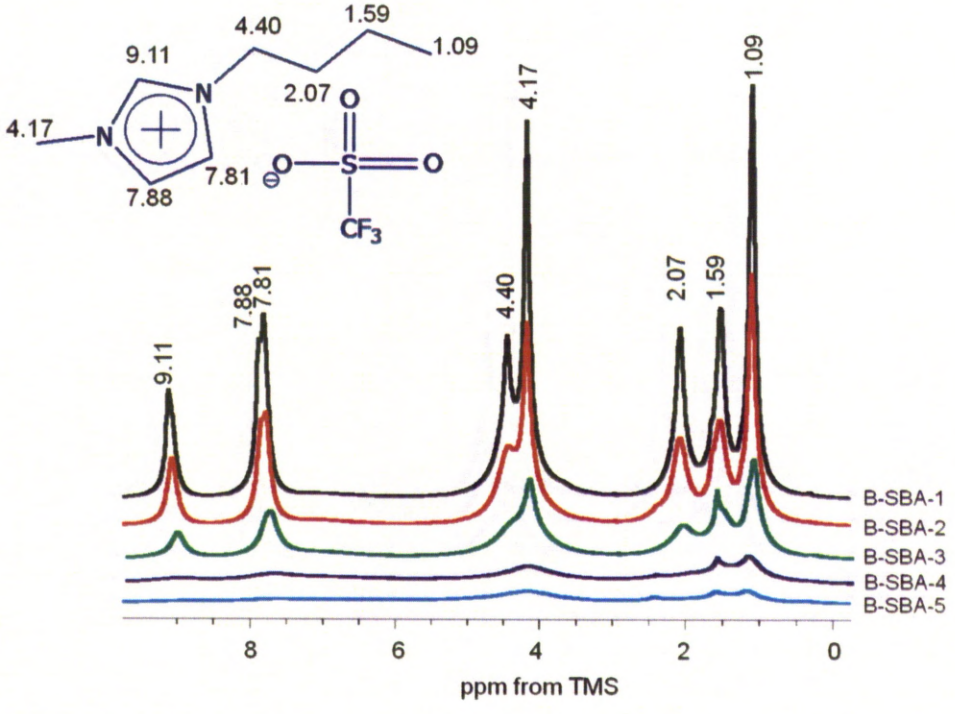

Figure 3.3 ^{1}H MAS NMR spectra of B-SBA-1, B-SBA-2, B-SBA-3, B-SBA-4 and B-SBA-5 recorded at ambient temperature. MAS rate was 10.0 kHz

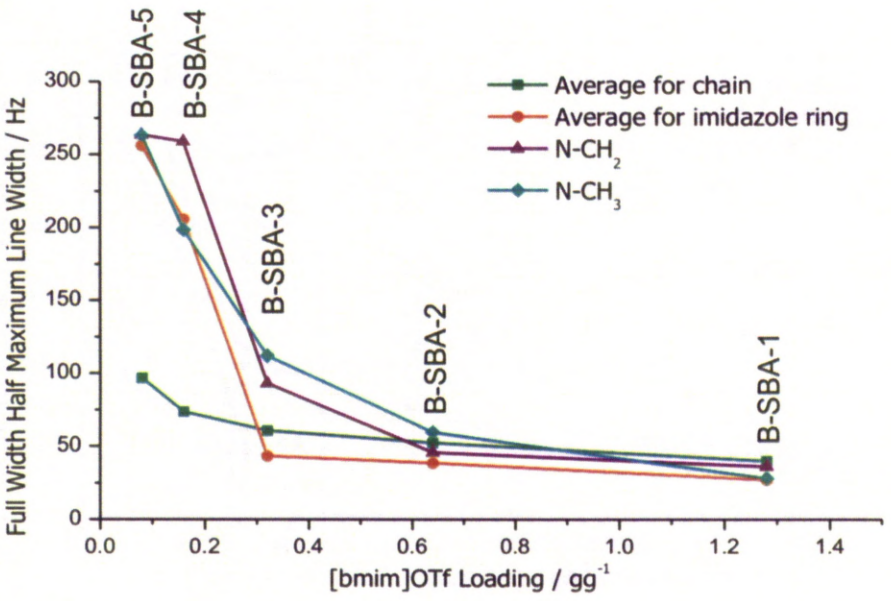

Figure 3.4 Effect of loading on the broadening of resonances

T_1 relaxation times for [bmim]OTf encapsulated in SBA-15 as a function of loading are presented in **Figure 3.5** (along with relevant data for neat ionic liquid) and the temperature dependence of the T_1 relaxation times is shown in **Figure 3.6**.

T_1 relaxation times for neat [bmim]OTf are longer for the protons of the imidazolium ring and shorter for the protons of the butyl chain as expected: the butyl chain has greater internal rotational molecular motion. The range of T_1 relaxation times for neat [bmim]OTf is 517 ms compared to 29 ms for [bmim]OTf loaded into SBA-15, B-SBA-1. Upon encapsulation of [bmim]OTf with higher loadings (B-SBA-1, 1.28 g/g and B-SBA-2, 0.64 g/g), the T_1 relaxation times are found to be similar for both butyl chain and imidazolium ring protons. We ascribe this to restricted molecular motion causing an increase in ^1H-^1H dipolar coupling for the whole cation, which results in the T_1 relaxation times being similar.

At lower loadings, *e.g.* B-SBA-4, 0.16 g/g where the linewidth data suggest that a surface confined layer may be present, the range of T_1 relaxation times is greater. Pore filling at low loading would allow the ions in the surface confined layer to rotate more freely compared with bulk ionic liquid inside the pore. This

increase in molecular mobility compared to B-SBA-1 and B-SBA-2 would result in less effective ^1H-^1H dipolar coupling and hence the T_1 relaxation times of the imidazolium ring and chain protons begin to diverge (**Figures 3.5 and 3.6a**). Similar observations of changes in T_1 relaxation times for neat and encapsulated ionic liquid have been reported by Lin *et al.*[282] when comparing the organic solvent, butan-1-ol confined in SBA-15 to bulk butan-1-ol. They observed a decrease in T_1 relaxation time of up to 893 ms upon loading for H(1) and a decrease in the range of T_1 relaxation times from 711 ms for bulk butan-1-ol to 133 ms for encapsulated butan-1-ol.[282]

A greater degree of restricted motion is shown by a decrease in T_1 relaxation time as the amount of bulk IL is reduced (**Figure 3.5**). At loadings lower than 0.3 g/g, the T_1 relaxation times begin to increase. This could be due restricted molecular motions, below the T_1 minimum, characteristic of a surface confined layer.

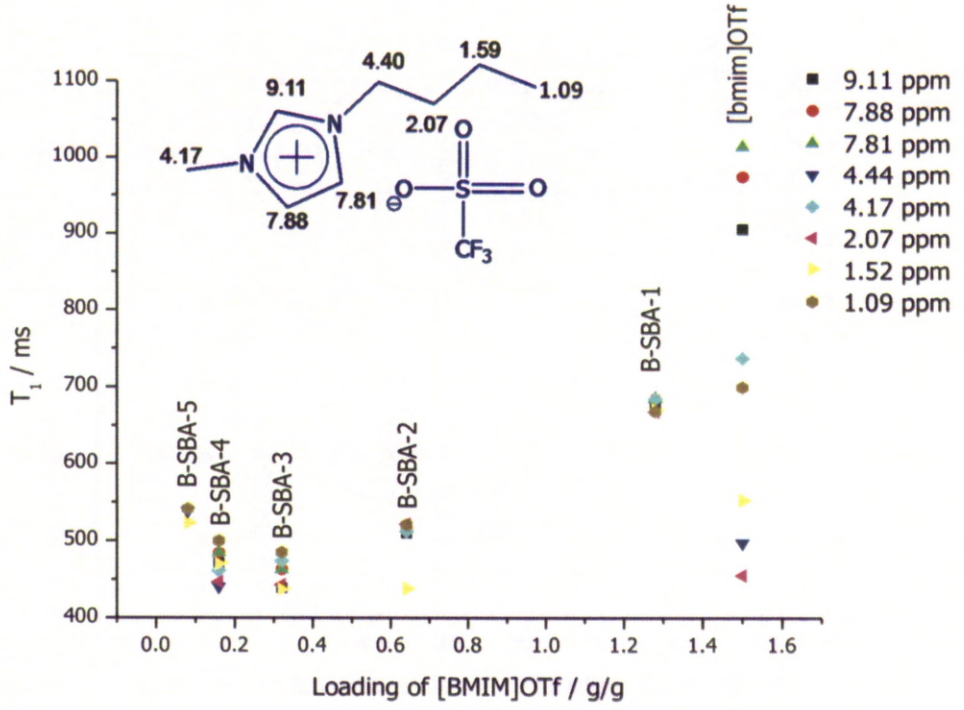

Figure 3.5 ^1H T_1 relaxation time versus loading of [bmim]OTf in SBA-15 at ambient temperature. T_1 minimum is at loading of approximately 0.30 g/g [bmim]OTf

Figure 3.6 shows ^{1}H T_1 relaxation time *vs* temperature for both 0.64 g/g (B-SBA-2 and 0.16 g/g (B-SBA-4)) loadings. Spectra were recorded by cooling from room temperature to 243 K and heating at 10 K intervals to 323 K. This heating cycle was chosen in order to give a true representation of the interactions between the pore wall and [bmim]OTf upon impregnation, *i.e.* the location of the ionic liquid upon encapsulation is maintained during analysis before any possible redistribution or further diffusion of the ionic liquid into the pores could occur by heating the sample. Both curves display a minimum T_1 time at room temperature. This means when recording T_1 relaxation times *vs* loading, we are at a border between the regions where $1>> \omega_0^2\tau_C^2$ and $1<< \omega_0^2\tau_C^2$. These regions correspond, respectively, to fast and slow molecular motions on the frequency scale of NMR.[283]

The T_1 values are higher for B-SBA-2 (0.64 g/g loading of [bmim]OTf) indicating a more mobile environment, *i.e.* the bulk [bmim]OTf is the dominant contributor to the T_1 relaxation time. Also at higher loading, ^{1}H–^{1}H dipolar coupling can be assumed to be the dominant mechanism of relaxation. This is evidenced by the small range of T_1 times for the protons and at temperatures above *ca.* 313 K the range of values begins to increase indicating the motion of the ion is increased.

Figure 3.6a also shows T_1 relaxation times of *ca.* 450 ms at 295 K. These relaxation times were recorded after the temperature cycle (cooling to 233 K and then heating to 323 K at 10 K intervals before cooling to room temperature overnight) and could be attributed to reorientation at high temperatures.

Comparison of the T_1 relaxation times displayed *vs.* loading (**Figure 3.5**) and *vs.* temperature (**Figure 3.6**) show slightly different times that are due to the implementation of a cooling and heating cycle during the NMR experiment.

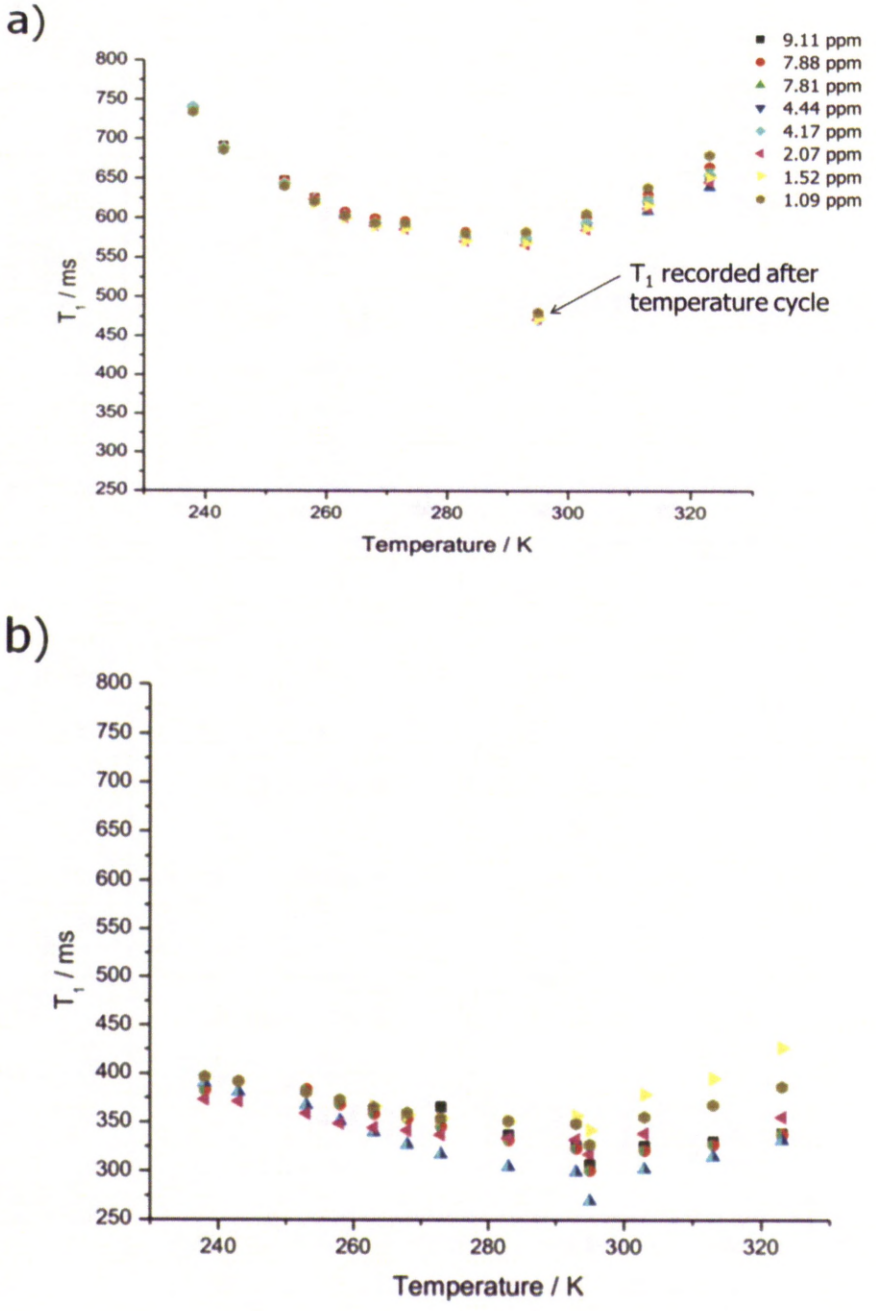

Figure 3.6 ^{1}H T_1 relaxation curves for **a)** B-SBA-2 and **b)** B-SBA-4 [bmim]OTf in SBA-15 at varying temperatures

Combination of the textural information gained from PXRD and N_2 sorption isotherms with the NMR characterisation of the interactions between the IL and the porous support indicates the presence of a surface confined layer and bulk RTIL in the pores.

3.4.2.2 ^{1}H-^{13}C CP and $^{13}C\{^{1}H\}$ MAS NMR spectra

^{1}H-^{13}C CP-MAS and $^{13}C\{^{1}H\}$ MAS NMR, **Figure 3.7,** give complementary information to the T_1 measurements above about mobility and hence about the nature of the surface confined layer. Assignment of the resonances in these spectra is as follows: δ/ppm = 13.4 C(9), 19.7 C(8), 32.3 C(7), 50.0 C(10), 36.4 C(6), 123.1 C(4), 124.3 C(5) and 137.2 C(2).[244] A quartet is also observed in the $^{13}C\{^{1}H\}$ MAS NMR at 122.0 ppm corresponding to the CF_3 group on the anion.[284]

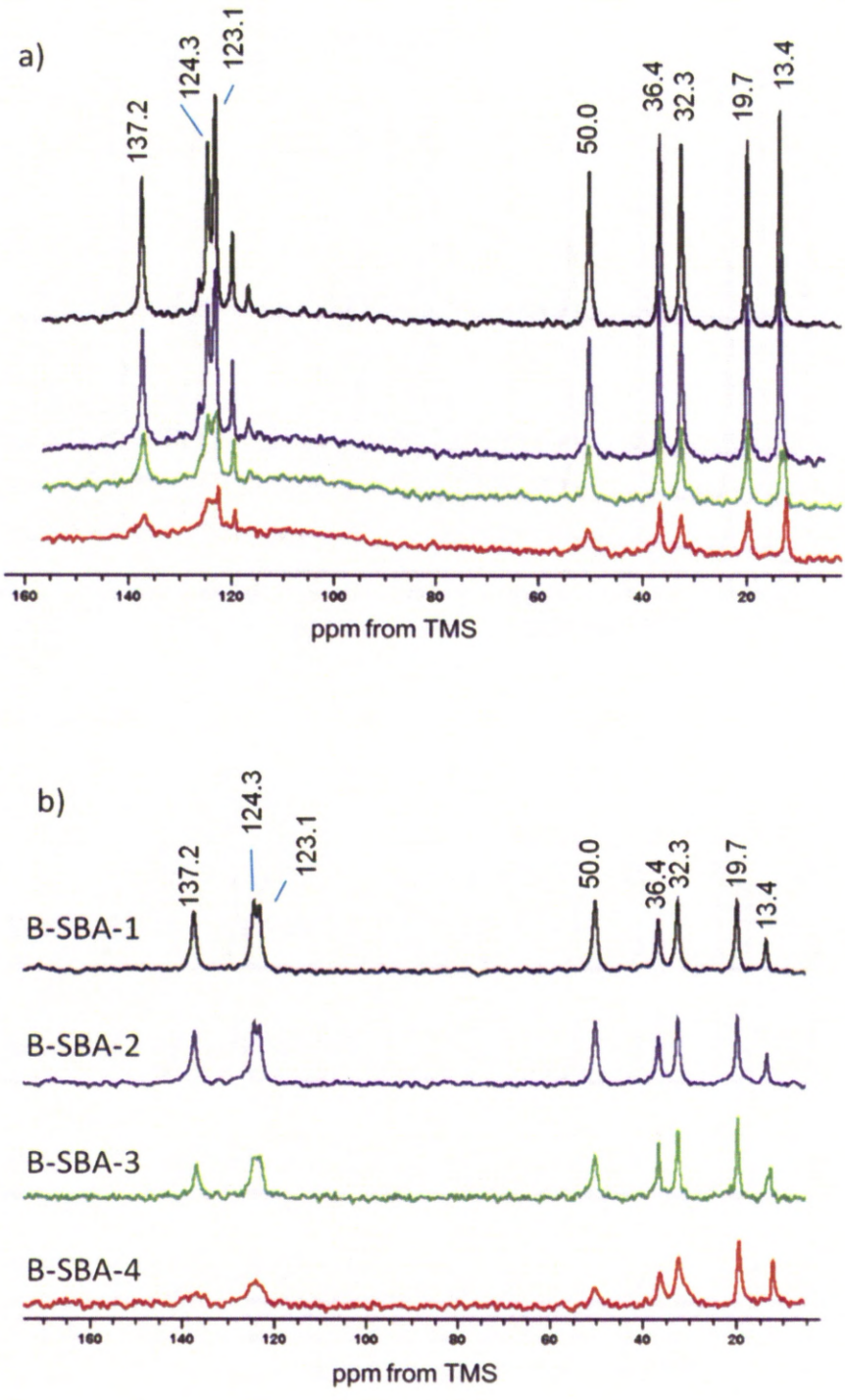

Figure 3.7 a) ^{13}C $\{^{1}H\}$MAS NMR spectra and **b)** ^{1}H–^{13}C CP-MAS NMR spectra for various loadings of [bmim]OTf in SBA-15. The intensities of the resonances in the CP spectra are similar for each loading level. No normalisation was applied. The broad feature observed in the $^{13}C\{^{1}H\}$ MAS NMR spectra is due to background signal from the probe. MAS rate was 10.0 kHz

$^{13}C\{^{1}H\}$ MAS NMR spectra (**Figure 3.7a**) show an increasing intensity with increasing loading of [bmim]OTf. These spectra also display a quartet at *ca.* 120 ppm that is due to coupling to fluorine in the anion. This is not observed in the CP spectra as only carbons bonded to hydrogen are observed. Each resonance has a broad and narrow component, which is ascribed to a surface confined layer and bulk ionic liquid inside the pores respectively. The ratio of these two components has been estimated by deconvolution of the $^{13}C\{^{1}H\}$ MAS NMR spectra for the various loading levels (**Table 3.2**) The half-height peak widths give information about the mobility of the carbons whereas the area under the peak can be intergrated to measure the amount of carbons in a particular environment. However, there are inconsistencies in the deconvolution. This is due to overall resonance broadening as the loading decreases. Exchange will also occur between the bulk RTIL in the centre of the pore and motionally restricted RTIL near the surface. The rate of this exchange is difficult to predict. Also, the method of deconvolution used does not account for the layer nearest the pore wall, the bilayer and subsequent layers until bulk IL is achieved. To model this more accurately a distribution of peaks would be required and although we can gain an insight to how much "bulk" and "surface confined" IL is present, deconvolution data are inconclusive.

Table 3.2 Peak widths (FWHM) and areas of deconvoluted ^{13}C {^{1}H} MAS NMR spectra

Sample		narrow	broad	narrow	broad
	Peak/ppm	Area	Area	FWHM/Hz	FWHM/Hz
B-SBA-1	137.2	129.2	112.3	264.3	1042.8
B-SBA-2		124.4	110.2	287.1	965.6
B-SBA-3		70.5	210.7	303.2	827.7
B-SBA-4		70.9	414.6	525.6	70.9
B-SBA-1	50.0	85.8	142.3	198.9	622.0
B-SBA-2		127.9	116.9	266.5	1039.7
B-SBA-3		191.0	128.7	430.5	1534.6
B-SBA-4		95.7	228.6	440.0	2106.2
B-SBA-1	36.4	105.8	129.0	175.9	550.3
B-SBA-2		131.6	113.3	200.2	683.8
B-SBA-3		125.9	182.1	207.0	679.8
B-SBA-4		190.7	82.3	362.3	943.4
B-SBA-1	19.7	83.3	140.2	163.4	459.3
B-SBA-2		105.6	139.8	188.0	552.3
B-SBA-3		79.3	179.1	194.2	530.4
B-SBA-4		123.5	121.9	333.6	693.7
B-SBA-1	13.4*	98.7	134.3	158.3	421.9
B-SBA-2		103.0	142.5	154.1	433.1
B-SBA-4		111.9	104.4	214.8	421.0

**For B-SBA-3 the peak at 13.4 ppm is split hence no values are given for comparison*

Figure 3.8 shows deconvolution of peaks for imidazole ring C(2), C(8) located on the butyl chain and C(10) methyl carbons at varying loadings.

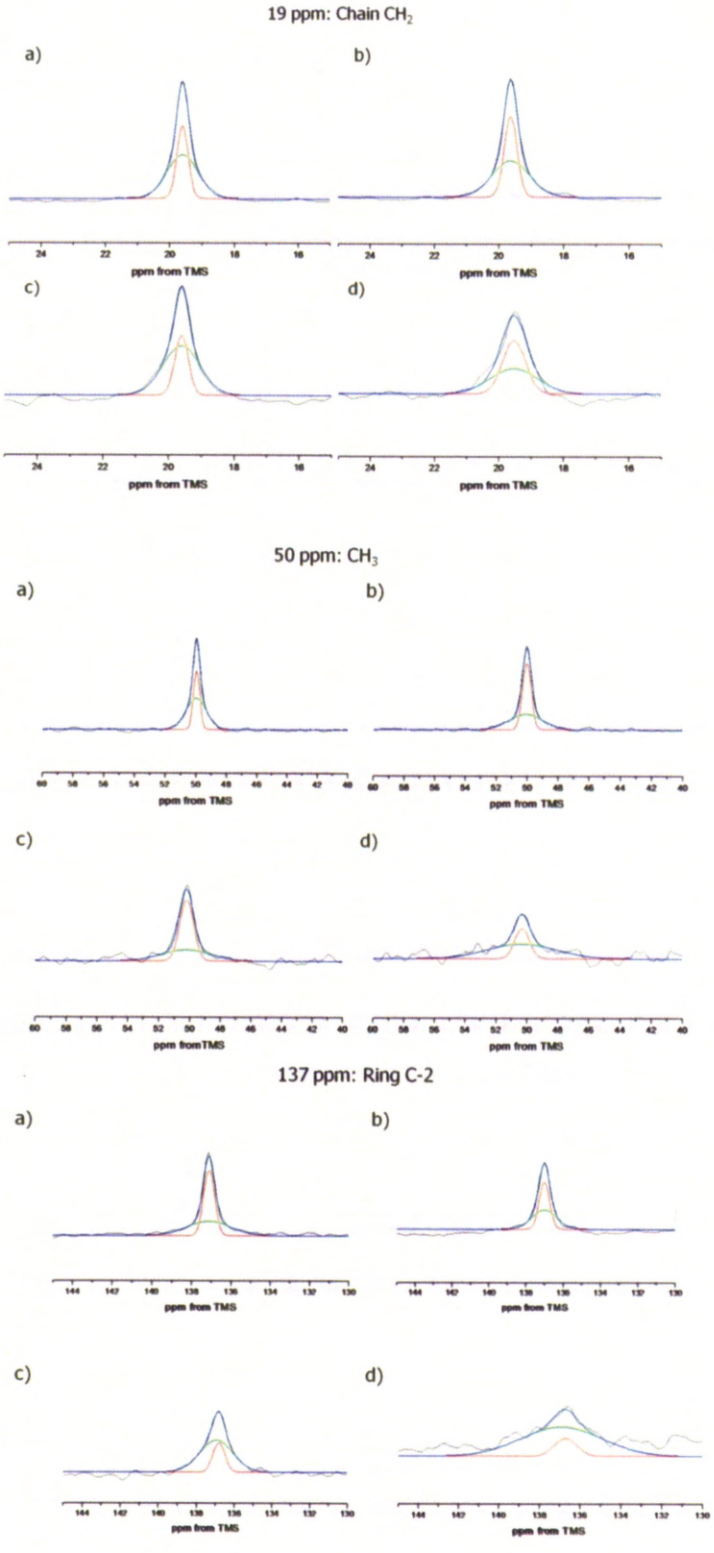

Figure 3.8 Deconvolution of broad and narrow components of chain CH_2 peak at 19.7 ppm, CH_3 at 50 ppm and Ring C-2 at 137 ppm for a) B-SBA-1, b) B-SBA-2, c) B-SBA-3 and d) B-SBA-4.

Comparison of $^{13}C\{^{1}H\}$ MAS NMR spectra with $^{1}H–^{13}C$ CP-MAS NMR spectra reveals differences that can be ascribed to the presence of a surface confined and bulk [bmim]OTf. Thus, neat [bmim]OTf does not give a CP signal since dipolar couplings are averaged in liquids, whereas, a substantial intensity is observed in the $^{1}H–^{13}C$ CP-MAS NMR spectra for [bmim]OTf encapsulated in SBA-15 (**Figure 3.7b).** This indicates strong dipole-dipole interactions are present, consistent with the existence of confined [bmim]OTf. The intensities of the peaks in the $^{1}H–^{13}C$ CP-MAS NMR spectra do not change with loading of [bmim]OTf, consistent with the view that only a surface confined layer of [bmim]OTf in the mesopores of SBA-15 is responsible for the CP-MAS spectra.

^{1}H-^{13}C CP-MAS kinetics studies provide further detail of the mobility of the $[bmim]^{+}$ cation (**Table 3.3, Figure 3.9)**. In both B-SBA-2 and B-SBA-4, the [bmim]OTf is motionally restricted compared to neat ionic liquid and magnetization can be transferred efficiently through the induced dipolar interactions. The rate of magnetization transfer depends on the strength of the ^{1}H-^{13}C dipolar couplings and has been assessed using the classical I-S in preference to the I-I*S model (described in **Section 2.5.2.4**) due to more accurate fitting of the curves (**Table 3.3**).

Table 3.3 ^{1}H–^{13}C CP kinetics parameters for B-SBA-2 and B-SBA-4

^{13}C Site / ppm	T_{IS} / ms	$T_{1\rho}^{H}$ / ms	$T_{1\rho}^{C}$ / ms	R^2
B-SBA-2				
137.2 C(2) (ring N-CH-N)	1.62±0.15	9.78±0.87	8.77±0.46	0.9899
124.3 C(4) (ring N-CH)	1.84±0.19	11.58±1.29	10.97±0.48	0.9878
123.1 C(5) (ring N-CH)	1.58±0.14	12.41±1.14	10.76±0.56	0.9905
50.0 C(10) (CH_3)	1.57±0.14	8.55±0.71	9.23±0.45	0.9896
36.4 C(6) (chain N-CH_2)	2.40±0.24		23.63±1.13	0.9947
32.3 C(7) (chain CH_2)	2.73±0.22	12.59±1.21	14.20±0.76	0.9964
19.7 C(8) (chain CH_2)	2.96±0.33	20.28±3.55	17.72±7.40	0.9944
13.4 C(9) (chain CH_3)	4.92±0.30		51.16±9.48	0.9940
B-SBA-4				
137.2 C(2) (ring N-CH-N)	0.17±0.06	2.63±0.74	2.38±0.70	0.8871
124.3 C(4) (ring N-CH)	0.31±0.06	3.20±0.46	4.57±0.61	0.9541
123.1 C(5) (ring N-CH)	//	//	4.77±0.72	//
50.0 C(10) (CH_3)	0.21±0.06	2.85±0.73	3.40±0.37	0.8681
36.4 C(6) (chain N-CH_2)	0.91±0.15	6.41±0.93	12.22±1.30	0.9504
32.3 C(7) (chain CH_2)	0.50±0.08	4.86±0.58	6.74±0.35	0.9608
19.7 C(8) (chain CH_2)	1.42±0.27	3.88±0.64	7.92±1.04	0.9777
13.4 C(9) (chain CH_3)	3.80±2.21	10.06±8.24	17.89±6.10	0.9910

Comparing different carbon sites within B-SBA-2, the fastest CP build-up times are for carbons in the imidazolium ring (C(2), C(4) and C(5)). The longest CP build-up time is observed for the terminal methyl carbon of the butyl chain (C(9)). This is expected as the CH_3 of the butyl chain is more mobile than the imidazolium ring. The $T_{1\rho}^H$ relaxation times for the imidazolium ring protons are short, consistent with the trend observed for CP build up and also the ^1H T_1 relaxation times. B-SBA-2 shows no $T_{1\rho}^H$ relaxation in the time scale of the acquisition for C(9) (13.4 ppm) due to the significant flexibility of this group in comparison to the imidazolium ring protons.

B-SBA-4 shows the same trend in CP build-up times as B-SBA-2 with ring carbons being fast and the terminal CH_3 on the butyl chain being slow. This is due to their respective molecular mobilities. The $T_{1\rho}^H$ times also follow the same trend as for B-SBA-2. However both the CP build-up time and $T_{1\rho}^H$ are faster for B-SBA-4. These data fit with the idea of both a surface confined layer and bulk IL being present in B-SBA-2 as the CP kinetics curves are governed majorly by the surface confined layer. However, according to the deconvolution of the corresponding $^{13}C\{^1H\}$ MAS NMR spectrum, there is a significant contribution from bulk IL. In B-SBA-4 the ratio of bulk to surface confined layer is smaller indicating that the increase in both CP build-up and $T_{1\rho}^H$ times occur predominantly from the surface confined layer. The differences in CP build-up and $T_{1\rho}^H$ for B-SBA-2 and B-SBA-4 could also be due to the affects that the bulk has on the surface confined layer and the exchange between them. Clearly, there will be interactions between [bmim]OTf in both the surface confined layer and bulk, which will inhibit their mobility, particularly in a system where the pores are flooded. At decreasing loading however, the CP kinetics will be dependent on the ratio of bulk to surface confined layer, the "free space" (when both bulk, surface confined layer and porosity is observed) and the interactions between them. From this we can conclude that with decreasing loading there is a gradual change from bulk and surface confined ionic liquid to purely surface confined ionic liquid.

$T_{1\rho}^C$ motions are on a kHz scale (*e.g.* slow rotation of the molecule) and such relaxation occurs *via* chemical shift anisotropy, quadrupolar interactions and dipolar interactions, similarly to T_1 relaxation. $T_{1\rho}^C$ relaxation times were also collected to directly observe the slower carbon motions at varying loadings (**Table 3.3**).

a)

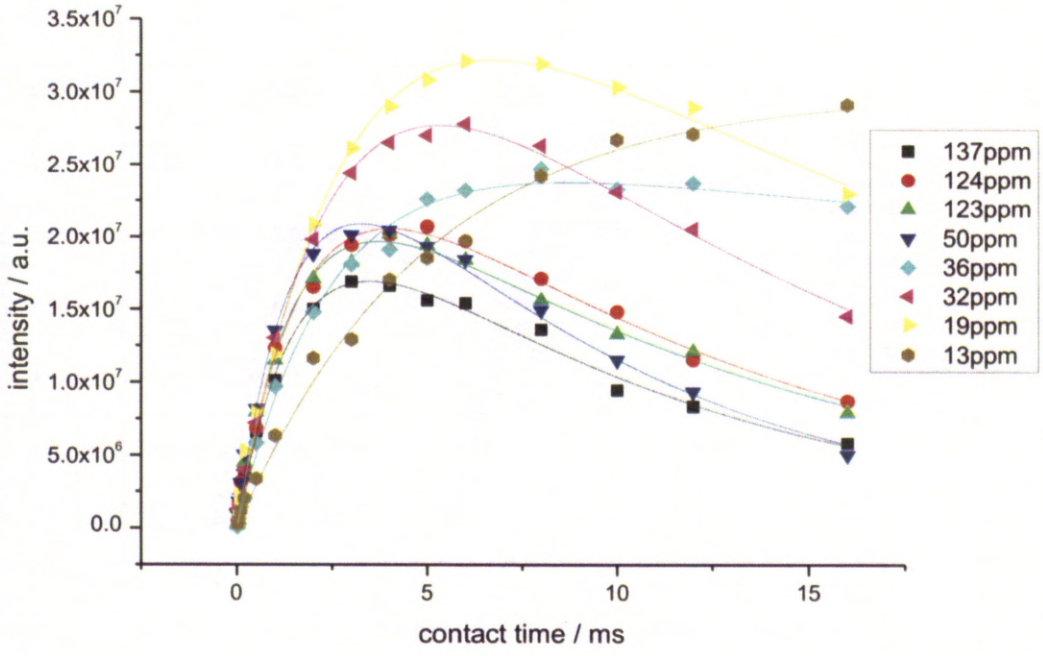

b)

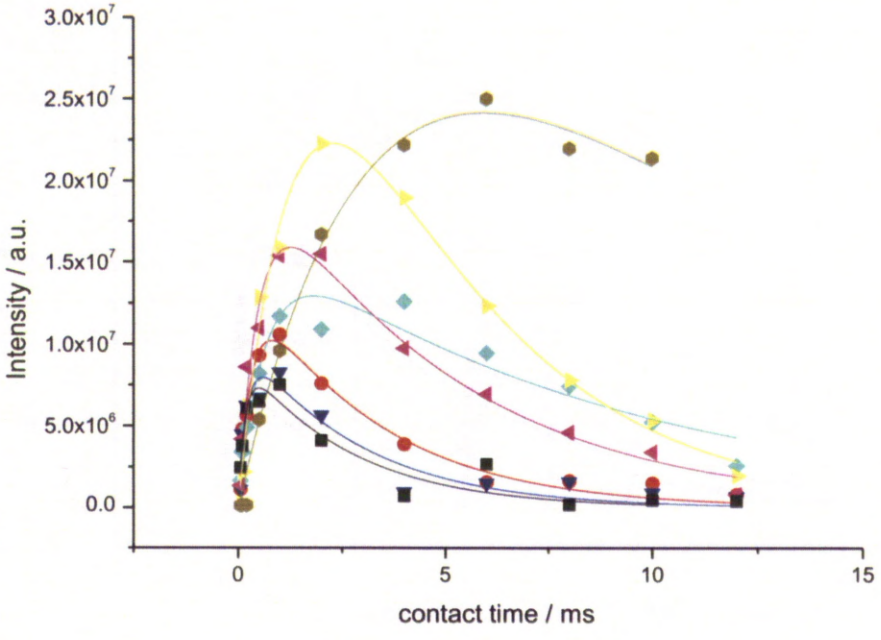

Figure 3.9 ^{1}H–^{13}C CP-MAS dynamics curves for **a)** B-SBA-2 and **b)** B-SBA-4

The shortest $T_{1\rho}^C$ is for C(2) in the imidazolium ring at both high and low loading. C(4) and C(5) have similar $T_{1\rho}^C$ relaxation times, slightly longer than C(2) but greater than C(10) and greater than butyl chain carbons for all loadings. This indicates a restricted internal motion for the ring carbons, as would be expected, but also for C(10), indicating this group may be closely interacting with the surface of the pore wall. C(7) and C(8) have the next longest $T_{1\rho}^C$ relaxation time, followed by C(6) and C(9). We would expect C(6) to have a shorter relaxation time than the neighboring C(7) as it is attached to the imidazole ring, although this could also be due to these two groups interacting with the pore surface. The difference between the values for C(6) and, C(7) and C(8) are not significant in comparison to the terminal C(9) which has the greatest molecular motion. The rotation and translational motions for the terminal C(9) will also be greater as shown in their contribution to the T_1 relaxation time.

Although the trend for the carbons in the $[bmim]^+$ cation is the same for both loadings, overall, the $T_{1\rho}^C$ relaxation times are significantly shorter for B-SBA-4. This is consistent with the surface confined layer being the dominant contributor to the relaxation time where as in B-SBA-2 we are observing the bulk as the dominate contributor, which overall, is more mobile.

A consistent picture emerges from these ^1H, ^{13}C NMR and relaxation studies of SBA-15 encapsulated [bmim]OTf with varying loadings; a surface confined layer and a bulk are present in samples with higher loading, and a surface confined layer is present at lower loadings.

3.4.2.3 ^1H–^{29}Si CP-MAS and HETCOR NMR

The ^1H-^{29}Si CP-MAS NMR spectrum of SBA-15 displays three resonances at -92.1, -101.1 and -111.8 ppm corresponding to Q^2 ($SiO_2(OH)_2$), Q^3 (SiO_3OH) and Q^4 (SiO_4) sites respectively. The relative intensities of the Q sites reveal the degree of condensation of silica in the framework (**Table 3.4**). The degree of condensation in SBA-15 was measured by deconvolution of the ^1H-^{29}Si CP-MAS NMR spectrum recorded with a CP contact time of 10.0 ms, which contained the most intense resonances (**Figure 3.10**).

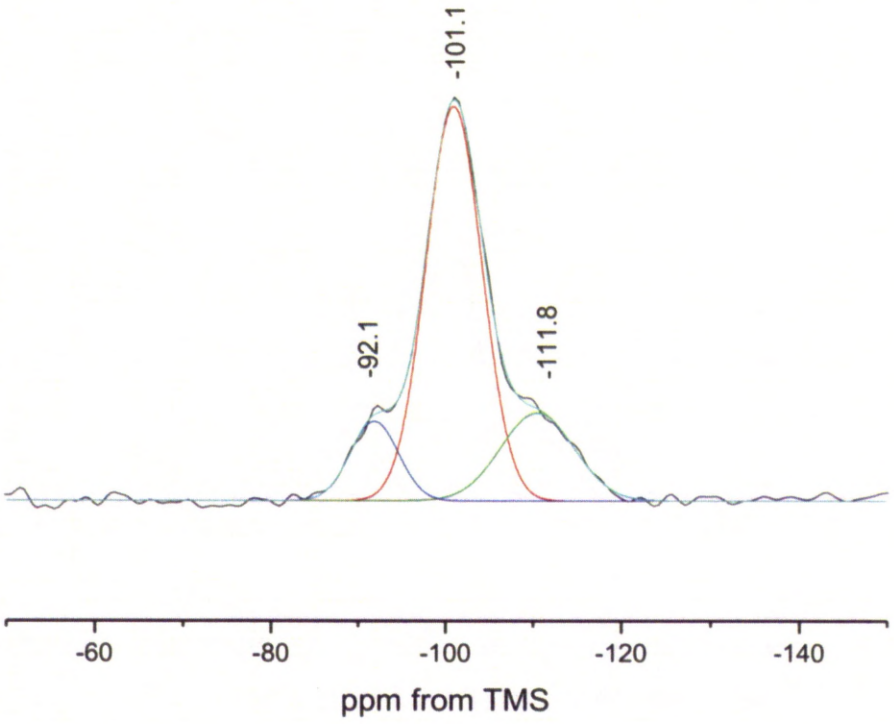

Figure 3.10 Deconvoluted ^{1}H-^{29}Si CP-MAS NMR spectrum of SBA-15 (line broadening of 80.0 Hz was used)

Table 3.4 Degrees of condensation for parent SBA-15

Chemical Shift / ppm	Area / a.u.	FWHM /ppm	Q^2+Q^3 / Q^4
SBA-15			3.98
-92.1	10.9	6.33	
-101.1	7.32	7.39	
-111.	4.58	9.83	

The ^{1}H MAS NMR spectrum of SBA-15 (**Figure 3.11**) shows resonances at 1.49, 1.96 and 2.19 ppm corresponding to surface Si–OH groups as well as a broad resonance at 3.92 ppm corresponding to water. In SBA-15 there are three possible SiOH groups; single, hydrogen bonded and geminal[285]. Geminal Si-OH groups are rare in comparison to single and hydrogen bonded Si-OH and usually appears at 1.96 ppm as an upfield shoulder on the resonance at 2.19 ppm. The resonances at 1.49 and 2.19 ppm can be assigned to single and hydrogen bonded SiOH respectively.[286-290]

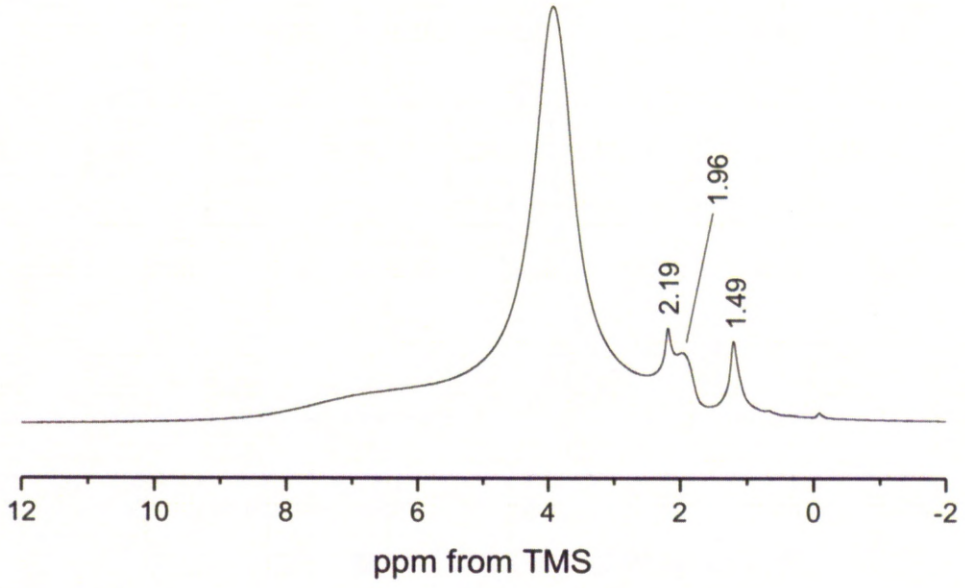

Figure 3.11 ^{1}H MAS NMR spectrum of parent SBA-15 (MAS = 10 kHz)

In order to investigate the orientation of the ionic liquid with respect to the pore wall, we have undertaken ^{1}H-^{29}Si heteronuclear correlation experiments to observe protons on the ionic liquid that interact with the silicon in the pore wall. The HETCOR experiment correlates ^{29}Si resonances from SBA-15 to ^{1}H sites from $[bmim]^{+}$ that are in close proximity to each other.

The ^{1}H-^{29}Si correlation maps for B-SBA-2 and B-SBA-4 are shown in **Figure 3.12**. Q^2 sites are observed at -93.3 and Q^3 sites at -101.8 ppm in the ^{1}H-^{29}Si CP MAS NMR spectrum (*t2*). Resonances in the ^{1}H MAS NMR spectrum (*t1*) are assigned to the proton sites in $[bmim]^{+}$ (see **Figure 3.3**). Cross peaks are observed between Q^3 Si site and protons bonded to C(6), C(7), C(8) and C(10) at a contact time of 2.0 ms.

Cross peaks are observed at *ca.* 1.09 and 4.17 ppm in the ^{1}H dimension. ^{1}H resonances assignable to surface –OH groups on SBA-15 do not occur at these frequencies, so we can therefore assume that these cross peaks are between the SBA-15 support and [bmim]OTf. Cross peaks can also be observed for Si and surface hydroxyl groups in SBA-15 and give rise to the greater intensity of the cross peak centred at *ca.* 1.09 ppm. This indicates that the butyl chain is in close contact with the pore wall and the imidazolium ring protrudes towards the centre of the

pore. The cross peak for N-CH_3 indicates that this group is also close in space to the pore wall. However, this may be an effect of alternating orientations of the cation with respect to the pore wall or a constrained orientation of the $[bmim]^+$ cation in which the N-CH_3 and the butyl chain are both in contact with the surface of the pore wall.

a)

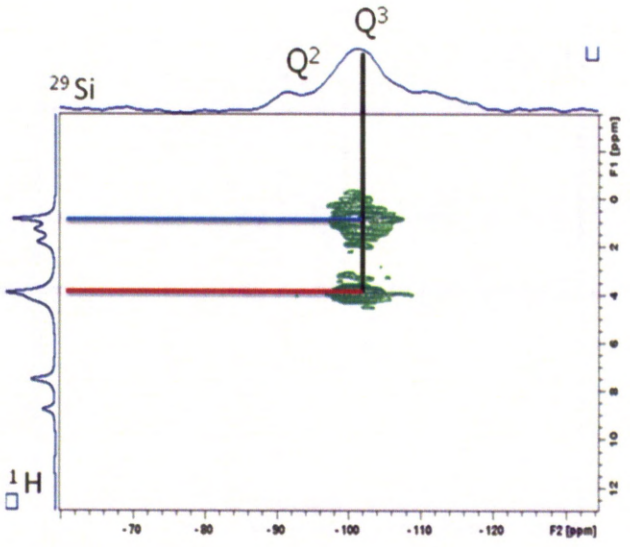

b)

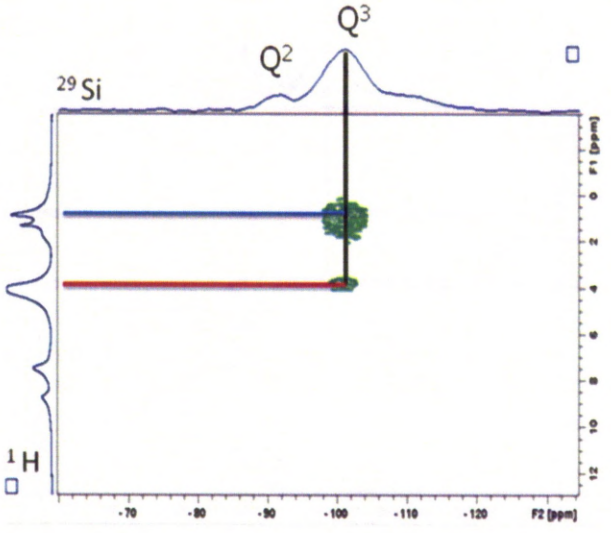

Figure 3.12 ^1H-^{29}Si HETCOR NMR Spectra for **a)** B-SBA-2 and **b)** B-SBA-4 at a contact time of 2.0 ms

Confirmation that the magnetization transfer occurs between the $[bmim]^+$ protons and the Si in the pore wall as well as the surface hydroxyl groups was obtained from ^1H-^{29}Si CP kinetics measurements on both the parent SBA-15 and the [bmim]OTf loaded SBA-15 (**Figure 3.13, Table 3.5**). Comparison of the parent SBA-15 (**Figure 3.13a**) to the [bmim]OTf loaded SBA-15 (**Figure 3.13 b and c**) shows a difference in the CP-build up and relaxation, particularly for Q^3. This indicates that magnetization is transferred from the $[bmim]^+$ protons to the Si in the pore walls.

a)

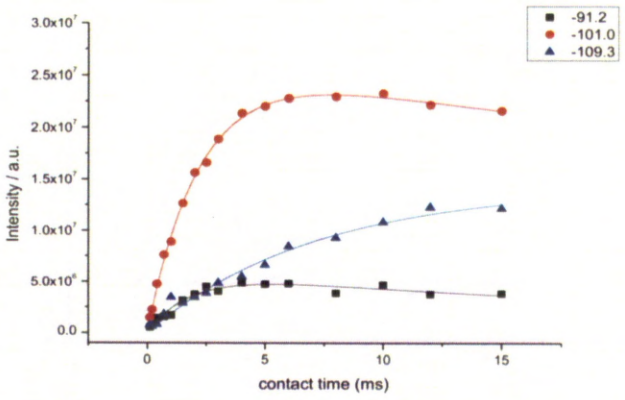

b)

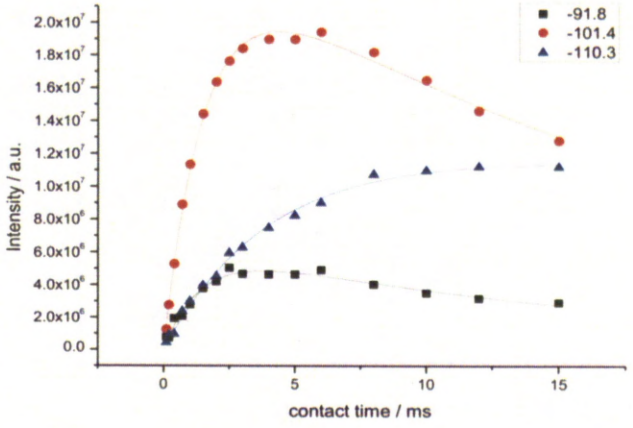

c)

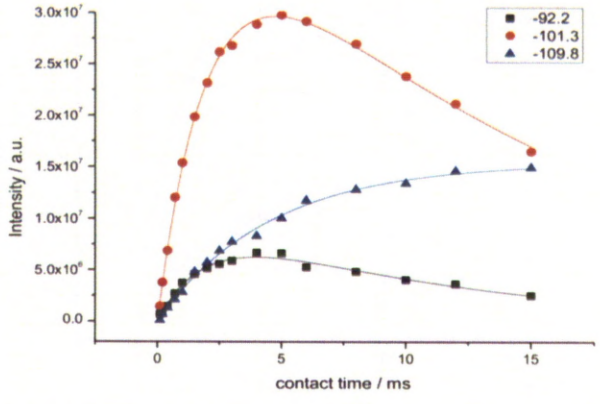

Figure 3.13 ^{1}H-^{29}Si CP kinetics curves for **a)** parent SBA-15, **b)** B-SBA-2 and **c)** B-SBA-4

Table 3.5 ^{1}H-^{29}Si CP kinetics

^{29}Si Site / ppm	T_{IS} / ms	$T_{1\rho}{}^{H}$ / ms	R^2
SBA-15			
-91.2 Q^2	1.80±0.35	30.0±12.1	0.9391
-101.0 Q^3	2.16±0.10	72.9±16.0	0.9977
-109.3 Q^{4*}	7.22±0.90		0.9790
B-SBA-2			
-91.8 Q^2	1.40±0.16	17.1±2.70	0.9649
-101.4 Q^3	1.52±0.06	22.6±1.40	0.9969
-110.3 Q^{4*}	3.93±0.56		0.9946
B-SBA-4			
-92.2 Q^2	3.77±0.76	9.70±1.40	0.9736
-101.3 Q^3	3.00±0.22	14.0±4.80	0.9977
-109.8 Q^{4*}	4.50±0.20		0.9959

**no $T_{1\rho}{}^{H}$ relaxation was detected for Q^4 units*

The results of the ^{1}H-^{29}Si correlation experiments and ^{1}H T_1 relaxation measurements are mutually consistent and provide evidence for the presence of a surface confined, motionally restricted, layer of RTIL at low loadings. At higher loadings (B-SBA-1 and B-SBA-2) the presence of a bulk, more mobile, RTIL environment is observed by comparison of the $^{13}C\{^{1}H\}$ MAS NMR experiments which display a narrow and broad component for each resonance. These data are also in support of the conclusions made from the correlation experiments.

3.4.3 Interaction between OTf⁻ anion and pore surface

The ^{19}F MAS NMR displays a single resonance at -79.6 ppm attributed to CF_3 in the anion. The mobility of the anion has been studied using ^{19}F T_1 relaxation measurements. **Figure 3.14** shows ^{19}F T_1 relaxation times as a function of loading of [bmim]OTf in SBA-15 and **Figure 3.15** show T_1 relaxation time as a function of temperature. As the loading of [bmim]OTf in SBA-15 decreases (**Figure 3.15**), the T_1 relaxation times get shorter, as observed for the ^1H relaxation times. In contrast to the ^1H T_1 relaxation measurements in which a minimum is present for B-SBA-2 and B-SBA-4 (**Figure 3.6**), the T_1 minimum for ^{19}F is not in the temperature range studied for B-SBA-2. However, a minimum is observed for B-SBA-4. This indicates the ^{19}F containing anion is in a different motional regime that is affected by the loading level, in comparison to the ^1H containing cation. As SBA-15 was synthesized using a non-ionic surfactant, P123, in strongly acidic conditions the surface of the pores will be slightly positively charged even after removal of the template by calcination. This is because it is below the isoelectric point of silica (pH ≈ 2)[291] at which point the oxygen of the Si-OH becomes protonated. For this reason we can expect the OTf anion to be attracted to the surface hydroxyl groups.

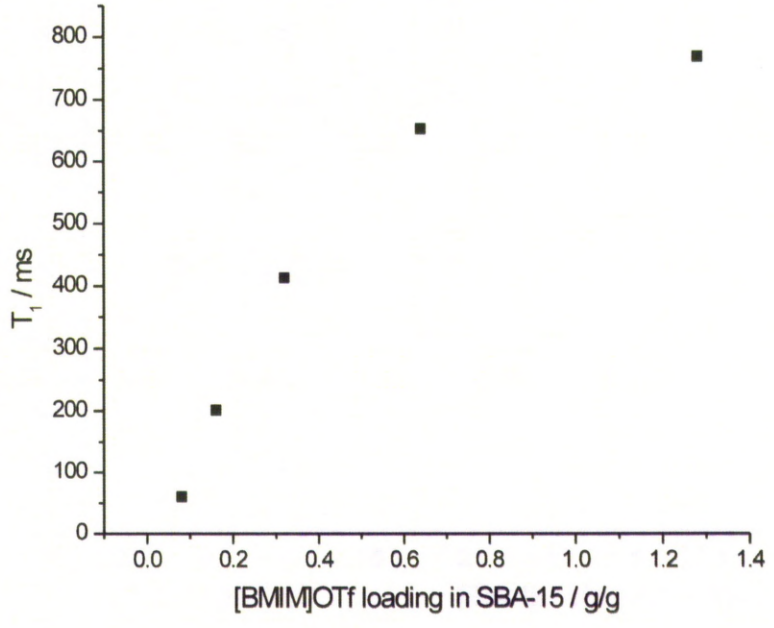

Figure 3.14 ^{19}F T_1 relaxation times plotted as a function of loading

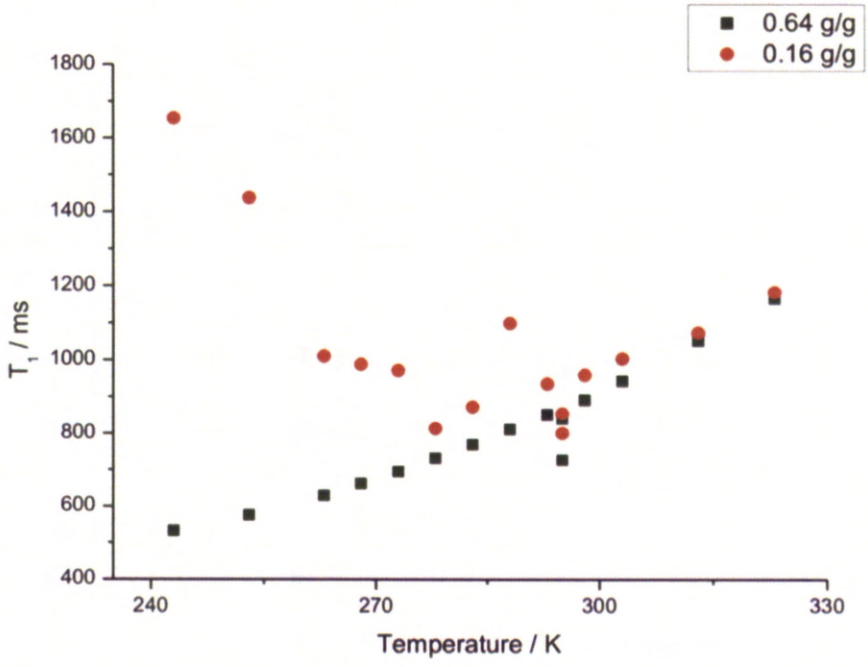

Figure 3.15 ^{19}F T_1 relaxation time as a function of temperature for high and low loading levels of [bmim]OTf (circles = 0.16 g/g (B-SBA-4) and squares = 0.64 g/g (B-SBA-2))

3.4.4 Computational Modelling of interactions between [bmim]OTf and SBA-15 mesopore surface

In order to further demonstrate the interactions between [bmim]OTf and the pore wall of SBA-15, computational modelling has been compared with experimental results to give a clear description of these systems.

Initially, a unit cell of the standard model of amorphous silica provided in Materials Studio was redefined into a super cell to make it large enough for a hole to be cut with a pore width equal to that determined experimentally by N_2 gas sorption isotherms. The terminal groups were functionalised with hydrogen atoms to create the surface hydroxyl groups. Before the [bmim]OTf ion pairs were added to the silica pore, the molecule was fully geometry minimised using the DMol3 module with GGA-BLYP functional and DND basis set. The number of [bmim]OTf

ion pairs added into the pore was equivalent to each level of loading (1381 molecules per cell for B-SBA-1, 691 for B-SBA-2, 345 for B-SBA-3, 173 for B-SBA-4 and 86 for B-SBA-5). Loading was performed using a Monte-Carlo approach (**Figure 3.16**).[292] This method of loading allows the [bmim]OTf molecules to position themselves in the pore in a favourable orientation. The first [bmim]OTf ion pairs to be loaded form surface confined layer until a point at which the surface is saturated (**Figure 3.16a**). Upon loading with increasing amounts of [bmim]OTf, a bulk-like environment forms in the centre of the pore (**Figure 3.16b**). This fits well with the conclusions made from analysis of the experimental data.

a)

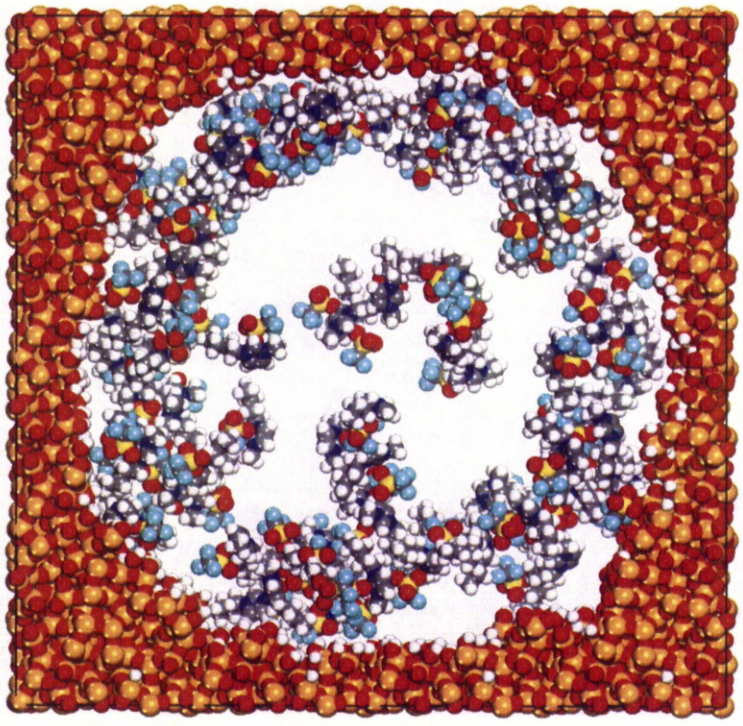

b)

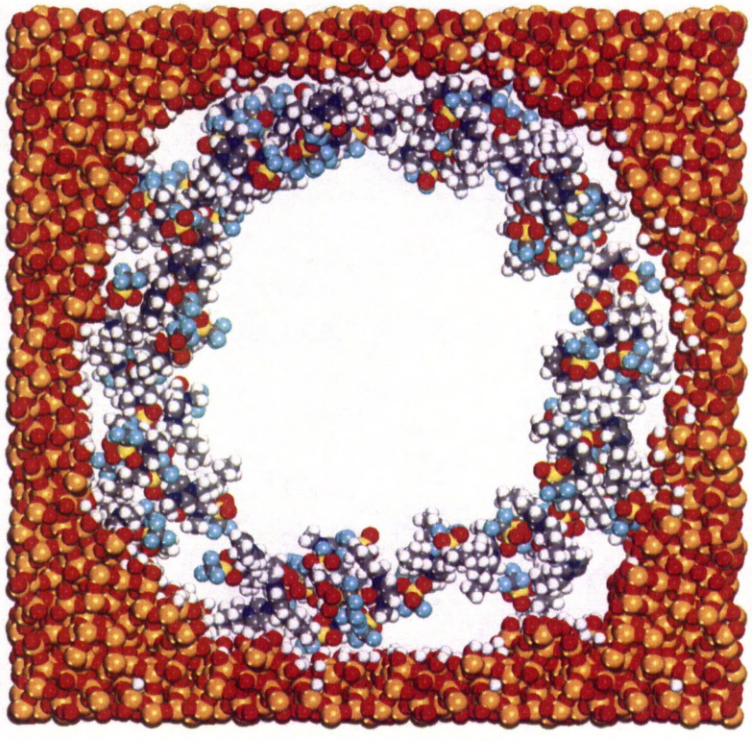

3.16 Molecular model of a single mesopore containing **a)** 1381 (ion pairs) molecules of [bmim]OTf per cell (B-SBA-1) and **b)** 173 [bmim]OTf molecules per cell (B-SBA-4)

In order to test the experimental conclusions concerning the orientation of [bmim]OTf with respect to the pore wall from the ^{1}H-^{29}Si HETCOR spectra, one [bmim]OTf ion pair was placed on the surface of amorphous silica.

The amorphous silica slab was created from a standard amorphous silica model available in Materials Studio 5.0. This was then cut and functionalised with hydroxyl end groups (**Figures 3.17a** and **b**). The Van der Waals surface area (**Figures 3.17c** and **d**) shows the morphology of the surface and cavities in the wall of the silica representative of micropores in the pore walls of SBA-15. To predict the possibility of [bmim]OTf entering these microporous cavities, a Connolly surface area was applied[293] (**Figures 3.17e** and **f**) with a limit of 1.82 Å, the kinetic radius of N_2 and 3.5 Å for the [bmim]OTf ion pair, which corresponds to the maximum diameter of the molecule, measured across the CF_3 group in the anion (**Figure 3.19**). The Connolly surface area shows the whole free volume that can be access by the probe molecule. This can include pores that do not have a surface opening, contained in the backbone of the silica. In this system, the Connolly surface areas show a reduction in the area accessible to substrates in comparison with the Van der Waals surface, and confirms that N_2 can penetrate the micropores (**Figure 3.17e**), whereas [bmim]OTf cannot (**Figure 3.17f**).

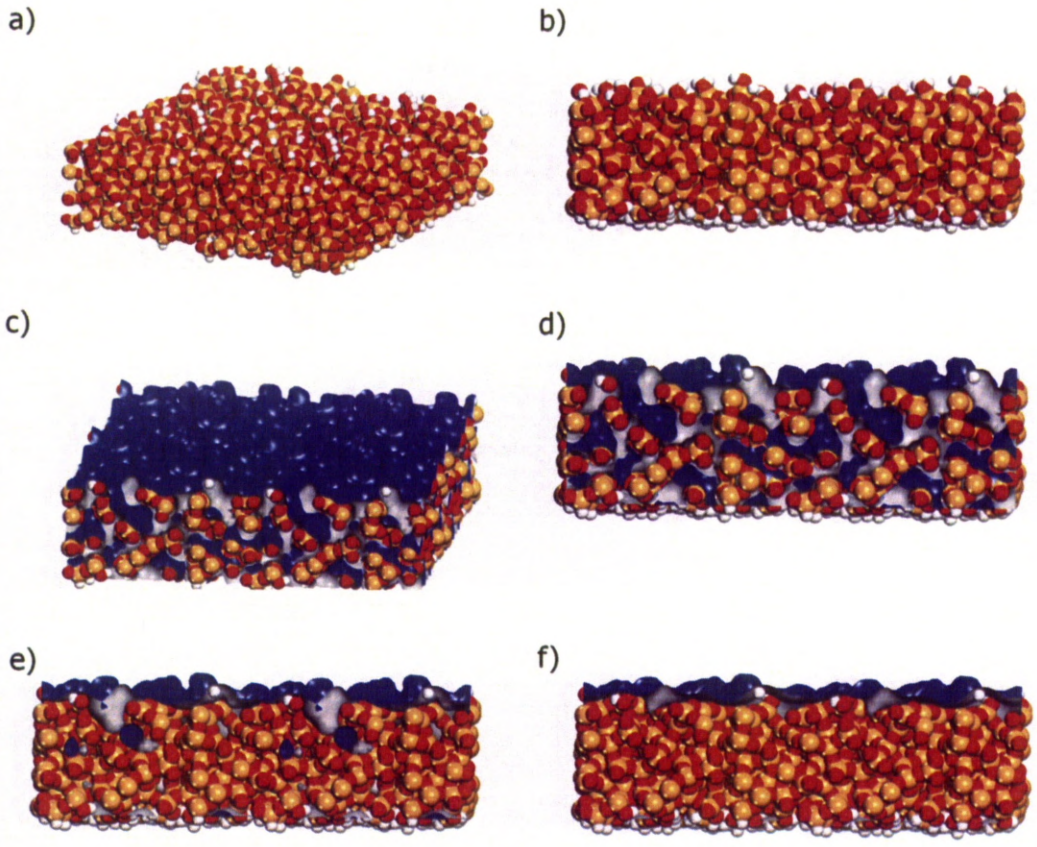

Figure 3.17 a) and b) Model of silica surface, c) and d) silica with Van der Waals surface and e) and f) silica with Connolly surface for N_2 and [bmim]OTf respectively

The solvent accessible surface area was used to investigate the possible locations of [bmim]OTf on the silica surface. This is the surface area that can be penetrated by the sorbate, *i.e.* pores that have an opening on the surface so that sorbates can enter. **Figure 3.18** shows a possible orientation for [bmim]OTf with respect to the surface. In this orientation the $[bmim]^+$ is situated between two surface hydroxyls with OTf^- sitting in the cavity created by the surface hydroxyls. The average distance between surface hydroxyls is *ca.* 10 Å, a distance comparable to the length of $[bmim]^+$, 9.5 Å (**Figure 3.19**). This seems plausible since H-bonding can occur between CH_3 groups and –OH groups on the silica surface. The protons of the methyl and butyl chain are in closest contact with the surface with distances between Si and C**H**$_3$ and C(9)**H**$_2$ measuring *ca.* 5.0 Å and 5.7 Å

respectively (**Figure 3.19**). The distance from Si to C(6)$\mathbf{H}_2$ and imidazolium ring protons is *ca.* 10 Å, which is larger than the distance over which magnetization can be transferred through dipolar couplings that give rise to a cross peak in the ^{1}H-^{29}Si HETCOR spectra. Another explanation for this orientation is an interaction between the anion and the surface. The electrostatic interaction between the ion pairs would still be present and coincidentally allow the cation to sit above the cavity on the silica surface in the orientation show in **Figure 3.19.**

This model is also consistent with the ^{1}H and ^{19}F T_1 relaxation data which describes the cation and anion being in different motional regimes. In the model depicted in **Figure 3.19**, the anion motion is clearly different from that of the cation as it is confined against the surface and between the hydroxyl groups. The anion in the bulk will however be more mobile than cations in the bulk as they are smaller. This explains the absence of a minimum for B-SBA-2 in the ^{19}F T_1 relaxation times *vs* temperature but the presence of a minimum for B-SBA-4. The orientation of the anion and cation with respect to the surface could be a result of the anion interacting strongly with the surface, which in turn dictates the orientation of the cation. Alternatively, this could be due to H-bonding between the methyl end groups and the surface hydroxyls that confines the anion against the surface.

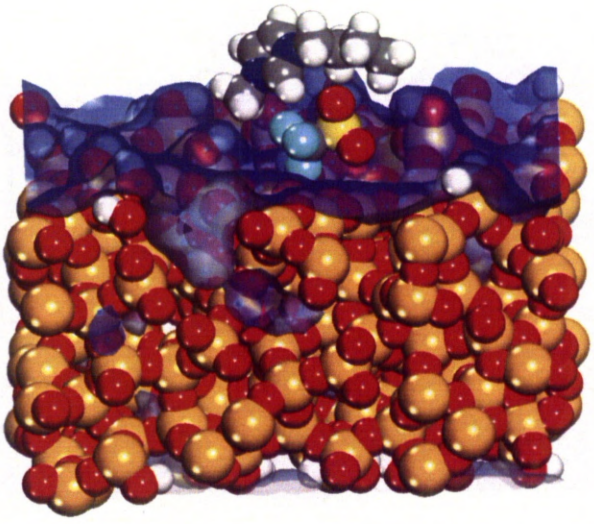

Figure 3.18 Orientation of [bmim]OTf on silica surface predicted by molecular modelling. Blue represents Connolly surface area.

Energy minimisation could not be performed on this system to investigate whether this is a plausible orientation due to the system size. Clearly, the ionic liquid could twist into a different geometry due to its interaction with the surface however this cannot yet be predicted using modelling.

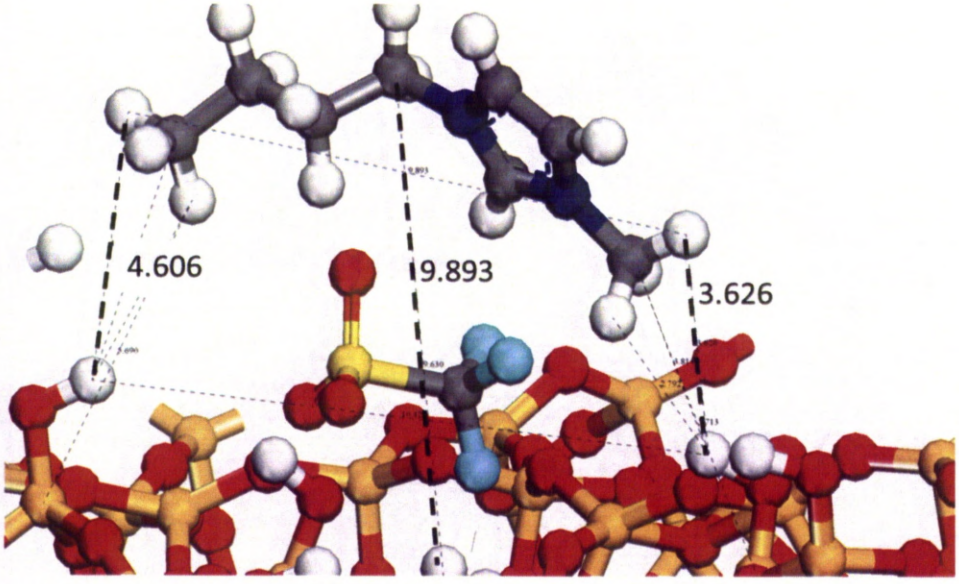

Figure 3.19 Model of [bmim]OTf on silica surface with distances labelled

Another limitation is that due to the system size it is difficult to accurately model the interaction of many ionic liquid ion pairs with the surface as the arrangement shown in **Figure 3.19** would be affected if another ion pair was brought into close proximity.

The results of the modelling are consistent with the experimental data and are collectively in support of a surface confined ionic liquid with orientation depicted in **Figure 3.18**.

3.5 Conclusions and outlook

In summary, this system is potentially useful for applications such as gas storage and catalysis if the position of the anion and cation are such that the guest molecules can interact favourably with the desired component of the ionic liquid. The orientation of the molecule has been characterised both experimentally and computationally and displays the anion in close proximity to the surface while the imidazolium ring of the cation protrudes into the centre of the pore.

By studying ^{1}H line widths and T_1 relaxation times, a surface confined layer and bulk material has been found to exist inside the mesopores of SBA-15. ^{1}H-^{13}C CP dynamics also confirmed the different mobilities of the bulk and surface confined layer.

Further investigations of this system may include a study of gas storage properties of these new SILPs versus neat [bmim]OTf. Initial investigations of this have been performed for CO_2 uptake. **Figure 3.20** shows the uptake of CO_2 into SBA-15, B-SBA-2 and B-SBA-4.

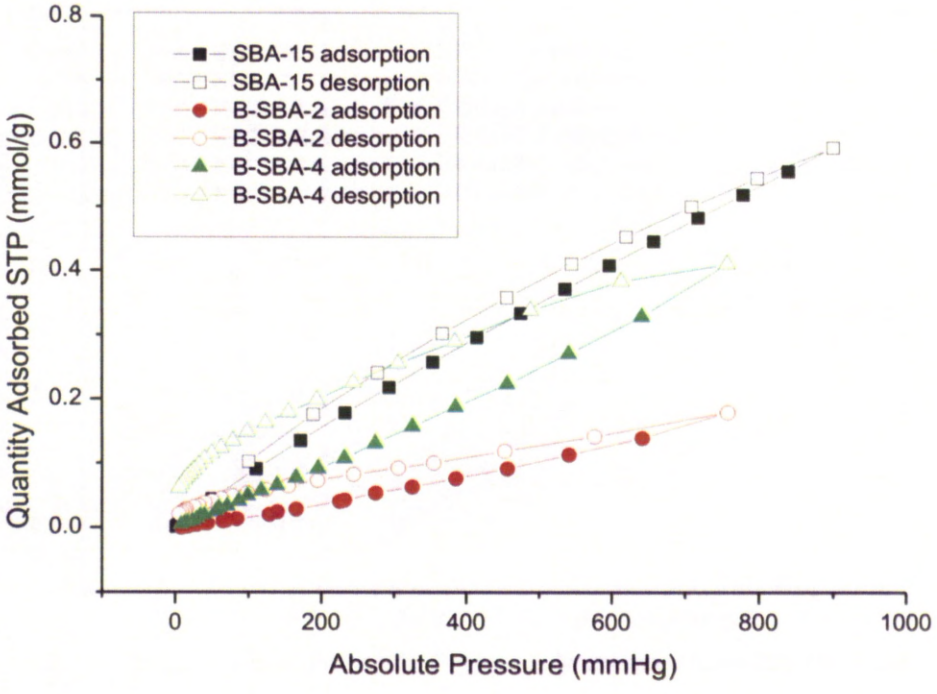

Figure 3.20 Uptake of CO_2 into SBA-15, B-SBA-2 and B-SBA-4

Initial data shows that the loaded SBA-15 have less uptake than SBA-15. However, initial uptake (below 100 mmHg) is faster for [bmim]OTf loaded samples implying that the ionic liquid has a greater affinity for CO_2 than the SBA-15 surface. The surface area of the mesopores decreased with increasing loading as shown in the N_2 isotherms (**Figure 3.2**). It is for this reason the higher loading of

[bmim]OTf has a lower quantity of CO_2 adsorbed as the pore volume is less than B-SBA-4 and SBA-15. Note the change in hysteresis upon encapsulation of [bmim]OTf. The rate of desorption is much less when ionic liquid is present. This can be attributed to mass transfer occurring at a slower rate through the viscous ionic liquid or due to favourable interactions between the ionic liquid and CO_2. From these initial finding it can be said that the presence of ionic liquid increases the affinity for CO_2 and enhances the initial rate of uptake. However, due to ion pairs occupying a fraction of the pore volume, the overall uptake is less than in SBA-15.

Allowing B-SBA-2 and B-SBA-4 systems to be kept at a constant pressure of CO_2 may result in a similar volume of CO_2 to SBA-15. However, further investigation would be required. There are also many other variables to consider such as the effect of temperature on uptake kinetics as this will affect the viscosity and dynamics of the ionic liquid inside the mesopores. Experiments used to probe such systems are described in **Chapter 5** and **Appendix I**.

Chapter 4

NMR Spectroscopy and Powder X-ray Diffraction Studies of 1-Butyl-3-methylimidazolium Methanesulfonate Encapsulated in SBA-15 and MCM-41

4.1 Introduction

In the previous chapter various analytical techniques were used to probe changes in mobility of [bmim]OTf upon encapsulation into SBA-15 and possible orientations that the ionic liquid might adopt when located in a surface confined layer. Although probing the mobility gave us an idea of the changes in phase behaviour, this was limited to interpretation of ^1H T_1 relaxation times with varying temperature. In this chapter [bmim]CH_3SO_3 has been encapsulated into SBA-15 and MCM-41 to further investigate the changes in the properties of confined ionic liquids. [bmim]CH_3SO_3 also provides a contrast to [bmim]OTf as it exists as a solid at room temperature. The two mesoporous hosts were chosen in order to provide a direct comparison of the encapsulated ionic liquids (in SBA-15) and to study the effects of pore size on the behaviour of the RTIL upon confinement (in MCM-41).

As previously described, it is important to distinguish changes in the properties of the ionic liquid upon encapsulation in order to identify possible applications. Many reports suggest that RTILs possess properties of both a solid and a liquid[294] and one can therefore predict that upon encapsulation the RTIL could transform from a liquid to a solid.[49,180] The previous chapter went some way in investigating this phase transformation suggested by Chen and co-workers who have studied the behaviour of a RTIL ([bmim]PF_6) in carbon nanotubes. They report, upon confinement, formation of [bmim]PF_6 crystals possessing a melting point of 473 K; 194 K higher than that of neat [bmim]PF_6.[49] Investigation by PXRD and DSC showed that upon encapsulation, weak interactions are induced by geometric factors leading formation of [bmim]PF_6 crystals. The weak interactions are attributed to a shorter C-H···F distance and give rise to a significantly enhanced melting point.

An unexpectedly high melting point was also described by Golovanov *et al.*[295] in their investigation of 1-methyl-3-propylimidazolium SiF_6 the reason for which was also due to the short C-H···F bond (2.5-2.6 Å in neat [mpim]PF_6 is reduced to 2.2-2.4 Å). Other reports of melting point depression of ionic liquids upon confinement have been reported by Kanakubo *et al.*[296] in their investigation of 1,3-dialkylimidazolium-based ionic liquids confined in controlled-pore glasses (up to 30 K lower than in the bulk). Neouze *et al.*[297] found that upon entrapment of [bmim]NO_3 in metallic silver matrix (in which silver was precipitated around the ionic liquid), the

thermal stability of the ionic liquid composite became much higher than of the neat $BMINO_3$. In addition, Sha *et al.*[175] report a drastic phase transition in simulations of [mmim]Cl confined between graphene walls.

The change in morphology[174] and new crystal structures[49] upon confinement of ionic liquids, as in the work of Chen and co-workers, has previously been described by Mickelson *et al.* for C_{60} confined in boron nitride nanotubes.[298] They suggest that in a confined space, crystal structures combine with quantum mechanical effects to modulate the properties of the material. The morphology of the encapsulated guest (the RTIL in this case) is not only determined by interatomic distance but by a self-imposed surface energy and the external geometrical constraints. [298]

Other studies have been performed on "ionogels". The first example of an ionogel was the physical gelation of ionic liquids occurring by dissolving amide-group-enriched glycolipids.[45] More recent examples of ionogels are ionic liquids confined within a silica matrix.[39,44,257,299-300] These experiments suggest that the ionic liquid behaves partly like a solid and partly like a liquid upon confinement, maintaining the properties of the liquid ionic liquid while having a solid consistency. The emphases of research so far has focussed on application of these composite materials and to date there are few papers that study interactions between ionic liquids and silica.[40,44,170,172,300-302]

Le Bideau *et al.*[40] have investigated the mobility of ionic liquids confined in silica by studying ^{1}H NMR as described in **Section 3.1**. Neouze *et al.* also showed that the phase transitions of confined ionic liquids are heavily affected by confinement by studying change in the appearance of ^{1}H NMR with varying temperature.[44] Taubert *et al.*[170,300] extends the studies of Le Bideau and Neouze by observing the FT-IR spectra and ^{1}H NMR spectra of [emim]OTf in monolithic silica however, all of these studies are limited by the absence of in-depth molecular level investigations of mobility.

The aim of the research described in this chapter is to build on the understanding of these systems by using a variety of analytical techniques. Again we have used ordered mesoporous silicas as the host for the ionic liquid, an approach which is yet to be reported in the literature.

4.2 Experimental

Pluronic surfactant, P-123, tetraethylorthosilicate (TEOS), cetyltrimethylammonium chloride (CTMACl), colloidal silica source, LUDOX-HS-40, sodium chloride, acetic acid and ionic liquid, 1-butyl-3-methylimidazolium methanesulfonate, [bmim]CH_3SO_3, were purchased from Sigma-Aldrich. [bmim]CH_3SO_3 was stored in a dry, nitrogen-filled glove box and was characterized by ^1H and $^{13}C\{^1H\}$ NMR spectroscopy and DSC before use. Dichloromethane was purchased from Fisher Scientific and freshly distilled before use. All preparations were carried out using Schlenk procedures, under N_2.

4.2.1 Synthesis of mesoporous silica hosts: SBA-15 and MCM-41

SBA-15 was synthesized by the surfactant templating method detailed by Li *et al.*[267] as described in **Section 3.2.1.**

MCM-41 was synthesized according to the procedure outlined by Ryoo *et al.*[124,303-304] A solution of $NaOH_{aq}$ (1 M, 46.9 g, 117.3 mmol) and LUDOX HS-40 (14.3 g, 40% wt) were heated to 353 K for 2 hours. This solution was added via a dropping funnel to a polypropylene bottle containing a mixture of NH_{3aq} (0.29 g, 28% wt, 17.02 mmol) and template, hexadecyltrimethylammonium chloride, HTACl, (20.0 g, 25% wt). The resulting solution was stirred vigorously for 1 hour at room temperature then at 370 K for 24 hours. After cooling the mixture to room temperature the pH was changed to 10.2 by addition of acetic acid and the mixture returned to the oven for a further 24 hours. This was repeated three times. The mixture was then cooled to room temperature, filtered and washed with DDI water. The filtered white solid was calcined by heating from room temperature to 773 K over 10 hours and maintaining 773 K for 4 hours. The final composition of the synthesis mixture was: 6 SiO_2 : 2 HTACl : 1.5 Na_2O : 0.15 $(NH_4)_2O$: 250 H_2O

4.2.2 Encapsulation of [bmim]CH_3SO_3 in SBA-15 and MCM-41

4.2.2.1 SBA-15: With solvent

The requisite amount of [bmim]CH_3SO_3 was dissolved in freshly distilled dichloromethane (12.5 ml) and added to the dry SBA-15 (0.25 g). The suspension was refluxed for 2 hours at 313 K following which, a dry white paste remained. In cases where solvent remained after 2 hours, excess was removed using a rotary evaporator. This gave a series of encapsulated samples, BM-SBA-1 (1.12 g/g [bmim]CH_3SO_3 in SBA-15), BM-SBA-2 (0.56 g/g), BM-SBA-3 (0.28 g/g) and BM-SBA-4 (0.14 g/g).

4.2.2.2 SBA-15: Incipient wetness

The requisite amount of [bmim]CH_3SO_3 was inserted into a shortened pipette and heated until it turned to liquid and dripped into a flask containing dry SBA-15 (0.25 g/g) at a rate that mixture remained a solid white powder throughout. The composite mixture was then stirred and heated at 373 K overnight. Two samples were prepared by this method and have been denoted BM-SBA-IW-1 (1.12 g/g [bmim]CH_3SO_3 in SBA-15) and BM-SBA-IW-3 (0.28 g/g).

4.2.2.3 SBA-15: Molten mixing

The requisite amount of [bmim]CH_3SO_3 was added to dry SBA-15 (0.25 g) and heated to 373 K for 12 hours with stirring. Two samples were prepared by this method and have been denoted BM-SBA-S-1 (1.12 g/g [bmim]CH_3SO_3 in SBA-15) and BM-SBA-S-3 (0.28 g/g).

4.2.2.4 MCM-41: With solvent

Calcined MCM-41 was dried in a vacuum oven at 373 K for 20 hours. The requisite amount of [bmim]CH_3SO_3 (0.25 g, 0.13 g 0.06 g and 0.03 g) was then dissolved in dry, degassed dichloromethane (12.5 ml) and added to the dry SBA-15 (0.25 g). The suspension was refluxed for 2 hours at 313 K at which point a dry white paste remained. In cases where solvent remained after 2 hours, a rotary

evaporator was used to remove excess solvent. All synthesis was carried out using Schlenk procedures, under N_2. This gave a series of encapsulated samples, BM-MCM-1 (1.04 g/g [bmim]CH_3SO_3 in SBA-15), BM-MCM-2 (0.52 g/g), BM-MCM-3 (0.26 g/g) and BM-MCM-4 (0.13 g/g).

The molten mixing technique (described for SBA-15 in **Section 4.2.2.3**) was used to load [bmim]CH_3SO_3 into MCM-41 (1.04 g/g). This sample is denoted BM-MCM-S.

4.3 Characterisation conditions

Many of the characterisation methods detailed in this chapter are common to both chapters 3 and 4. In order to avoid repetition, this section will describe characterisation conditions that were not detailed in **Section 3.3**.

4.3.1 Powder X-ray diffraction

Low angle PXRD patterns (**Figures 4.1 and 4.2**) were recorded using conditions described in **Section 3.3.1**.

A PANalytical X'pert pro multi-purpose diffractometer (MPD) in transmission geometry operating with a Cu anode at 40 kV 40 mA was used for high angle analysis. Samples were mounted as loose powder onto transparent Mylar® film and measured using a 96 well plate XYZ HT stage. PXRD patterns were collected in 1 hour scans with a step size of 0.013 degrees 2θ and scan time of 115 s/step over 5–50 degrees 2θ. The incident X-ray beam was conditioned with 0.04 rad Sollar slits and an anti-scatter slit of 1/2 deg. The diffracted beam was passed through 0.04 rad Sollar slits before processing by the PIXcel detector operating in scanning mode.

Variable temperature PXRD patterns were collected in the temperature range 243-393 K on a Bruker D8 3-circle diffractometer with an APEX CCD detector and 1.5 kW graphite monochromated Mo Kα radiation. The detector to crystal distance was 50 mm; 2θ was set to 0°. An exposure time of 600 s per Φ rotation image was used per temperature step. The subsequent 2D diffraction image generated was

integrated using GADDS[305] software package producing a conventional 1D diffraction pattern. Analysis of the data and the subsequent discussion was carried out with the help of Dr. Sam Chong.

4.3.2 Differential scanning calorimetry

DSC measurements were record using the same method described in **Section 3.3.3.** Each sample was heated and cooled in the range of 98 K to 393 K using the following temperature program:

1. Heating from 303 K to 393 K at 5 K/min;
2. Hold for 1 min;
3. Cool from 393 K to 98 K at 5 K/min;
4. Hold for 1 min;
5. Heat from 98 K to 303 K

This sequence was repeated three times. All transition temperatures reported herein for neat ionic liquid were calculated from the third temperature cycle by measuring the onset temperature of the thermal event. Analysis of the encapsulated samples after the first temperature cycle are unreliable due to the thermal history of the sample, which may have caused some leaching of the encapsulated ionic liquid from the pores.

4.3.3 Nitrogen sorption isotherms

Nitrogen sorption isotherms were recorded using the same method described in **Section 3.3.2.**

4.3.4 Solid-State NMR

Solid state NMR spectra were recorded using methods described in **Section 3.3.4.**

4.3.4.1 ^{1}H MAS NMR and T_1 inversion recovery

^{1}H T_1 relaxation times were measured for BM-SBA-1 and BM-SBA-3 over the temperature range 243-363 K using the conventional inversion recovery pulse sequence as described in **Section 2.5.3.2.4, Figure 2.29.** Nineteen different delay times were sampled in the range from 10 μs to 5.0 s. A typical temperature cycle used in these experiments was as follows:

1. Cool from room temperature to 243 K over 30 min
2. Allow to equilibrate for 20 min then record spectra
3. Heat by 10 K, allow to equilibrate for 20 min then record spectra
4. Repeat step 3 until 363 K is reached (in B-SBA-2 and B-SBA-4, the T_1 minimum was observed at *ca.* 293 K. For this reason data points were collected at 5 K intervals around this temperature).
5. After recording spectra at 363 K cool to room temperature overnight
6. Acquire room temperature spectra the following day

The intensities of the resonances as a function of delay time, τ, were fitted according to *eqn. 2.30.*

4.3.4.2 ^{1}H-X Cross Polarisation Magic Angle Spinning (CP-MAS)

CP-MAS NMR experiments were carried out using the method described in **Section 3.4.4.2.**

4.3.5 Data processing

All powder XRD data were processed using PANalytical High Score plus software. Nitrogen adsorption isotherms were analysed using Micromeretics ASAP2020 software. All solid-state NMR spectra were acquired using XWINNMR 3.5 and processed using Bruker TopSpin 2.1 software. CP kinetics curves, relaxation curves and deconvolution of spectra were fitted using Origin8.5 software.

4.4 Results and discussion

PXRD and N_2 gas sorption analysis were used to determine the location of [bmim]CH_3SO_3 with respect to the porous silica host. [bmim]CH_3SO_3 has a known crystal structure,[306] thus PXRD is an invaluable method of monitoring any changes to the unit cell parameters and to suggest any changes to the properties of [bmim]CH_3SO_3 upon encapsulation in a mesoporous silica support. Changes to the properties of [bmim]CH_3SO_3 have also been investigated by using differential scanning calorimetry and NMR spectroscopy.

The characterisation of the interactions between [bmim]CH_3SO_3 and the surface of the porous host is important in understanding the applicability of this system for gas processing or catalysis. A variety of NMR spectroscopic techniques that can monitor changes in the mobility of [bmim]CH_3SO_3 upon encapsulation have been used to understand the relationship between restricted mobility and changes in the properties of [bmim]CH_3SO_3 upon encapsulation.

The rationale for the choice of loading levels of [bmim]CH_3SO_3 into SBA-15 and MCM-41 was based on the respective mesopore volumes, similar to the approach taken for [bmim]OTf encapsulation in SBA-15. The highest loading is calculated to completely fill the mesopores, reducing the loading by half until approximate monolayer coverage was achieved. The size of [bmim]CH_3SO_3 molecules was estimated using its crystal structure given by Baldelli *et al.*[306]

4.4.1 Characterisation of SBA-15 and MCM-41 and incorporation of [bmim]CH_3SO_3 into SBA-15

4.4.1.1 Identifying the location of [bmim]CH_3SO_3 with respect to the mesoporous host

Initially, PXRD was used to characterise the hexagonal ordering of pores expected for SBA-15 and MCM-41. The PXRD for parent SBA-15 (**Figure 4.1**) show typical d_{100}, d_{110} and d_{200} reflections at 81.5, 49.0 and 43.2 Å. The PXRD pattern for parent MCM-41 (**Figure 4.2**) shows typical d_{100}, d_{110} and d_{200} reflections at 38.2, 22.2 and 19.1 Å. Upon loading SBA-15 and MCM-41 with increasing amounts of

[bmim]CH_3SO_3, the d_{100}, d_{110} and d_{200} peaks become less intense indicating [bmim]CH_3SO_3 has entered the mesopores. **Figures 4.1** and **4.2** both show PXRD patterns for solids loaded using dichloromethane solutions of the ionic liquid.

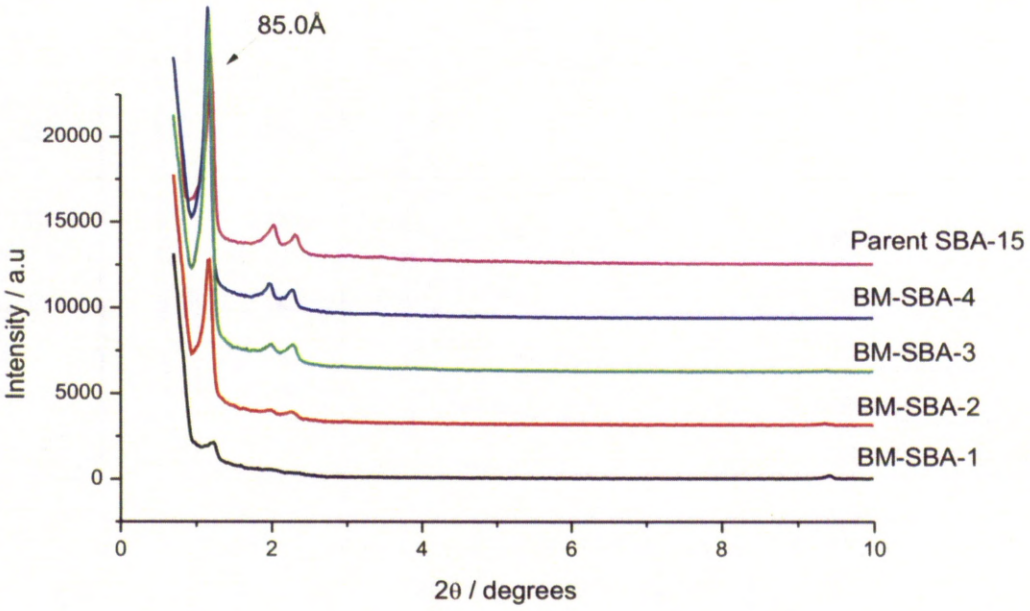

Figure 4.1 PXRD patterns of parent SBA-15 and SBA-15 with varying loading levels of [bmim]CH_3SO_3

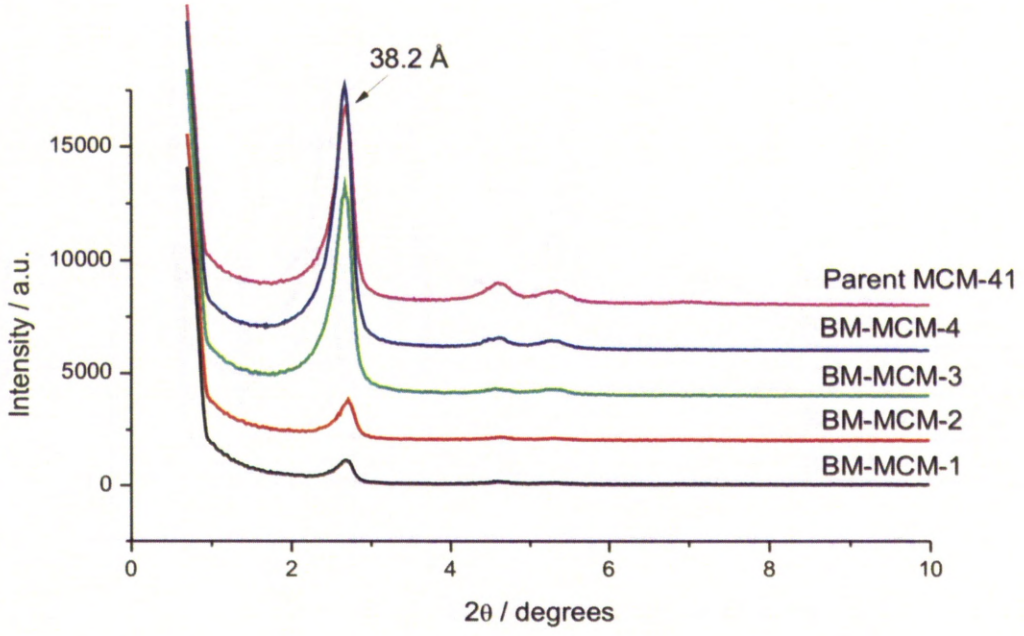

Figure 4.2 PXRD patterns of parent MCM-41 and MCM-41 with varying loading levels of [bmim]CH_3SO_3

Upon closer inspection of the samples BM-SBA-1 to BM-SBA-4, a small peak with a d-spacing of 10.9 Å is observed (**Figure 4.1**). The intensity of this peak increases with increasing loading of [bmim]CH_3SO_3 indicating that it is related to the ionic liquid rather than the SBA-15 support. However, this peak does not appear for samples BM-MCM-1 to BM-MCM-4 (**Figure 4.2**). These observations were further investigated and are discussed in greater detail in **Section 4.4.1.2.**

N_2 adsorption–desorption isotherms and corresponding pore size distributions are shown in **Figure 4.3 and Figure 4.4** for impregnation in SBA-15 and MCM-41 respectively. Textural data are assembled in **Table 4.1** and show that for SBA-15 and MCM-41 loaded samples, the BET surface areas, total pore volumes and pore size decrease as loading of [bmim]CH_3SO_3 increases.

Analogous to the SBA-15 produced for encapsulation of [bmim]OTf, the parent SBA-15 displays a characteristic type IV adsorption/desorption isotherm with a type H1 hysteresis.[307] Consistent with the PXRD, SBA-15 shows a high degree of mesoscopic ordering with the sharpest capillary condensation step on the adsorption branch ($p/p_0 \approx 0.70$).

As the isotherms displayed maintain type IV character and H1 hysteresis for each loading level it can be concluded that the ionic liquid does not block the opening of the pores. As with [bmim]OTf (**Figure 3.2a**) the cation is too large to enter the micropores and upon loading [bmim]CH_3SO_3 prevents N_2 from entering the micropores.

a)

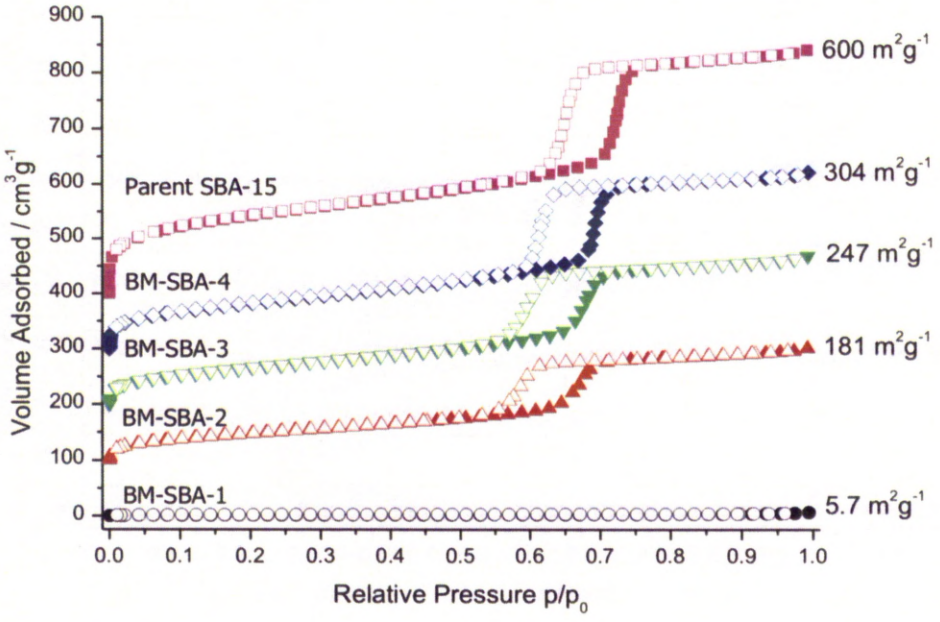

b)

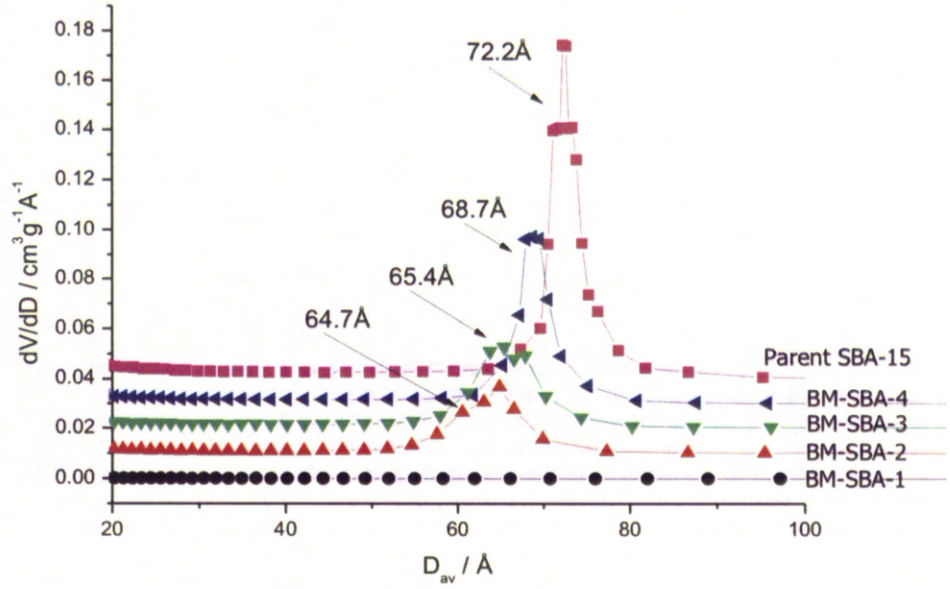

Figure 4.3 Nitrogen adsorption–desorption isotherms of parent SBA-15 and SBA-15 with varying loading levels of [bmim]CH_3SO_3 (each isotherm is offset by 100 cm^{3}g^{-1}). **b)** Pore size distribution plots calculated from the adsorption branch of the N_2 isotherms (each plot is offset by 0.01 cm^{3}g^{-1}Å^{-1})

The N_2 isotherms for MCM-41 are also type IV isotherms with pore size, surface area and volume in agreement with the literature.[124-125] Upon loading with increasing amounts of [bmim]CH_3SO_3 using solvent, the pore size, surface area and pore volume decrease similarly to the loading of SBA-15.

The study by Khodakov *et al.*[280] describing impregnation of varying amounts of aqueous cobalt nitrate into MCM-41 reported a loss of mesoscopic ordering upon impregnation; the type IV isotherm of the parent MCM-41 was lost and a type I isotherm was observed. The isotherms observed for MCM-41 impregnated with [bmim]CH_3SO_3 using solvent maintain type IV shape and no loss of ordering is observed.

a)

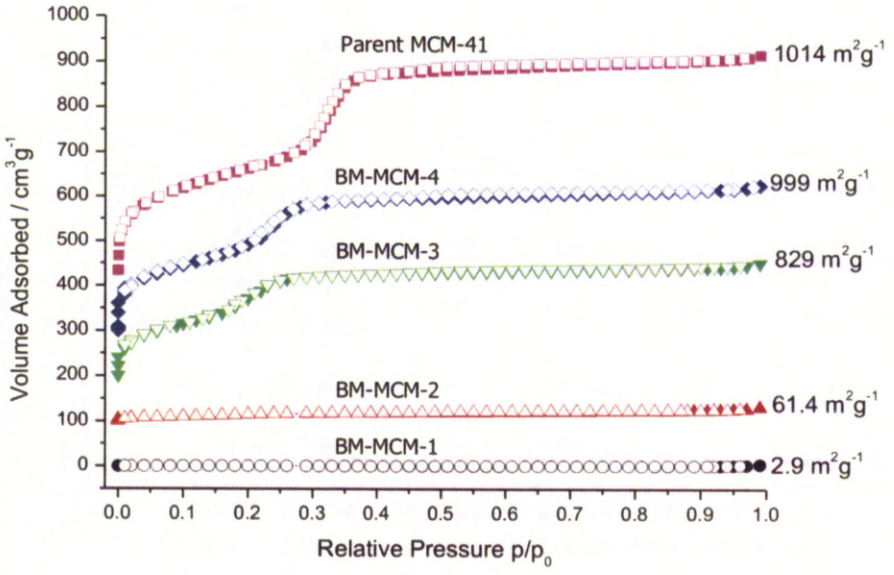

b)

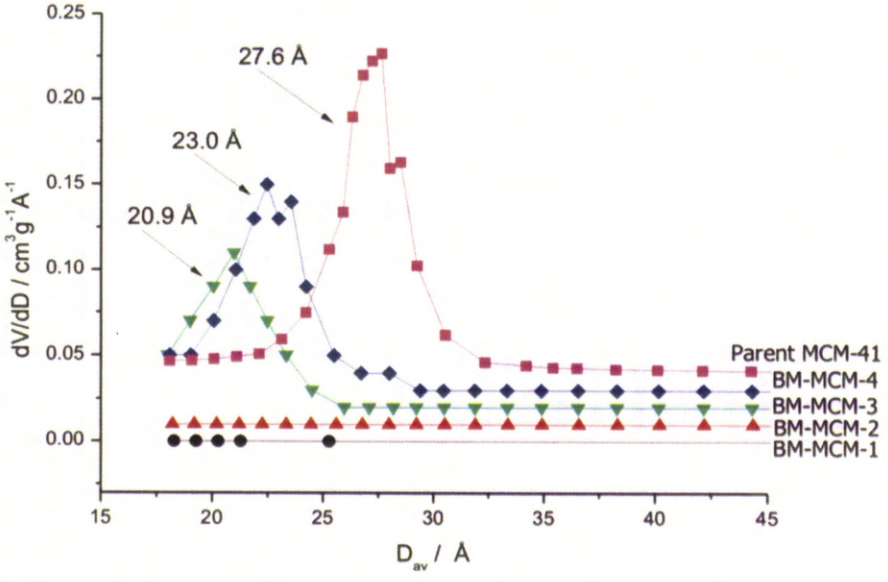

Figure 4.4 a) Nitrogen adsorption–desorption isotherms of parent MCM-41 and MCM-41 with varying loading levels of [bmim]CH_3SO_3 (each isotherm is offset by 100 cm^3g^{-1}). **b)** Pore size distribution plots calculated from the adsorption branch of the N_2 isotherms.

Table 4.1 Textural properties of SBA-15, MCM-41 and [bmim]CH_3SO_3 impregnated SBA-15 and MCM-41[a]

Sample	S_{BET} / m^2g^{-1}	V_{ads} / cm^3g^{-1}	D_{AV}^{ads} / Å	d_{100} / Å	a^b / Å	W / Å
Parent SBA-15	600	0.740	72.2	85.0	98.1	25.9
BM-SBA-4	304	0.488	68.7	88.5	102.2	33.4
BM-SBA-3	247	0.406	65.4	87.4	101	35.6
BM-SBA-2	181	0.304	64.7	85.6	98.8	34.1
BM-SBA-1	5.7	0.008	--	85.6	98.8	--
BM-SBA-1-IW	67.7	0.123	57.8			
BM-SBA-1-S	36.2	0.065	57.8			
BM-SBA-3-IW	299	0.429	64.3	82.0	94.7	30.0
BM-SBA-3-S	296	0.432	64.3	84.7	97.8	33.5
Parent MCM-41	1014	0.822	27.6	38.3	44.2	16.6
BM-MCM-4	999	0.495	23	38.4	44.3	21.3
BM-MCM-3	829	0.381	20.9	38.4	44.3	23.4
BM-MCM-2	61.4	0.043	--	37.9	43.8	--
BM-MCM -1	2.9	0.005	--	38.0	43.9	--

[a]Pore volumes determined at $p/p_0 = 0.9$. W is wall thickness determined from $\bar{a}$ - D_{av}. [b]Unit cell parameter $\bar{a}$ determined from d_{100} values using $\bar{a} = 2d_{100} / \sqrt{3}$.

N_2 isotherms were also recorded for SBA-15 samples impregnated with RTIL using incipient wetness and molten mixing (**Figure 4.5 and 4.6)** and are comparable to BM-SBA-1 and 3.

a)

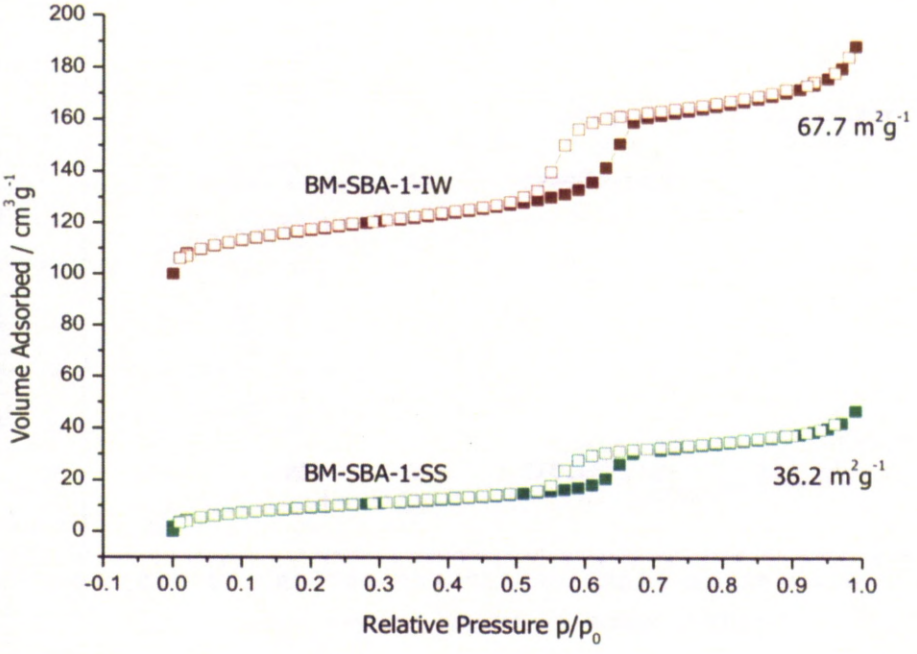

b)

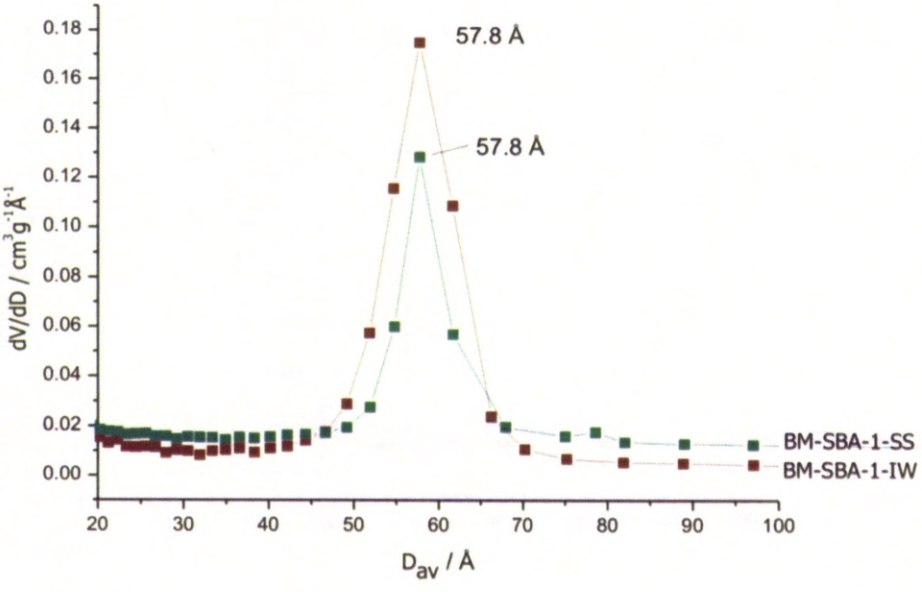

Figure 4.5 a) Nitrogen adsorption–desorption isotherms of BM-SBA-1-IW (brown) and BM-SBA-1-S (green) (each isotherm is offset by 100 cm^3g^{-1}). **b)** Pore size distribution plots calculated from the adsorption branch of the N_2 isotherms (each plot is offset by 0.01 $cm^3g^{-1}Å^{-1}$)

The isotherms of BM-SBA-1-S, BM-SBA-3-S, BM-SBA-1-IW and BM-SBA-3-IW show that [bmim]CH_3SO_3 enters the pores of SBA-15 (**Figures 4.5 and 4.6**). As all isotherms are type IV, we can conclude that the method of loading in SBA-15 does not cause the pore opening to be blocked. The surface area and pore volume of BM-SBA-1-IW and BM-SBA-1-S are larger than for BM-SBA-1 in which the same amount (as confirmed by elemental analysis) of [bmim]CH_3SO_3 was used for the encapsulation. This can be attributed to the liquid form of [bmim]CH_3SO_3 being more viscous than when dissolved in solvent. This causes the diffusion into the pores to be inhibited so that a non-uniform layer of ionic liquid is deposited on the surface of the pores.

a)

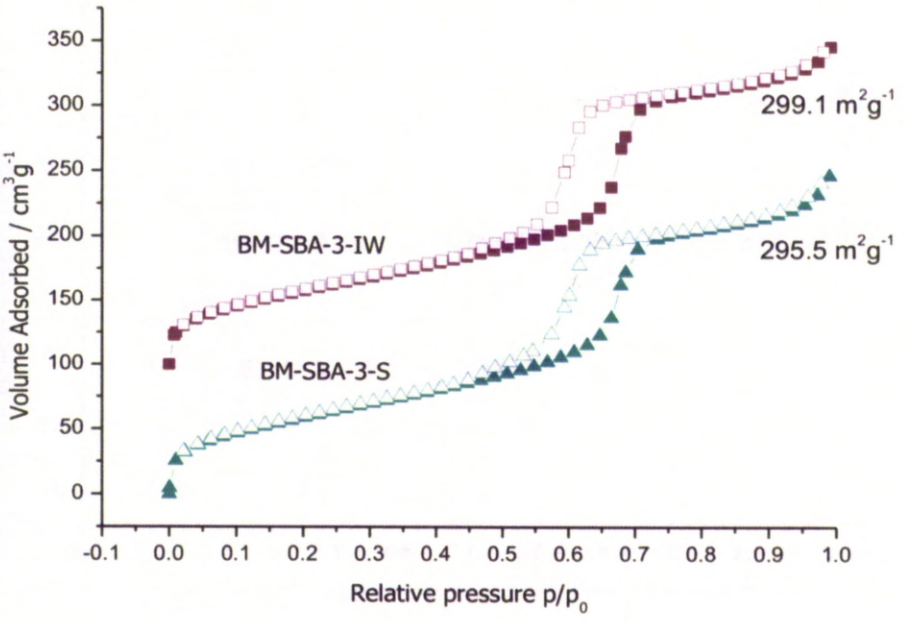

b)

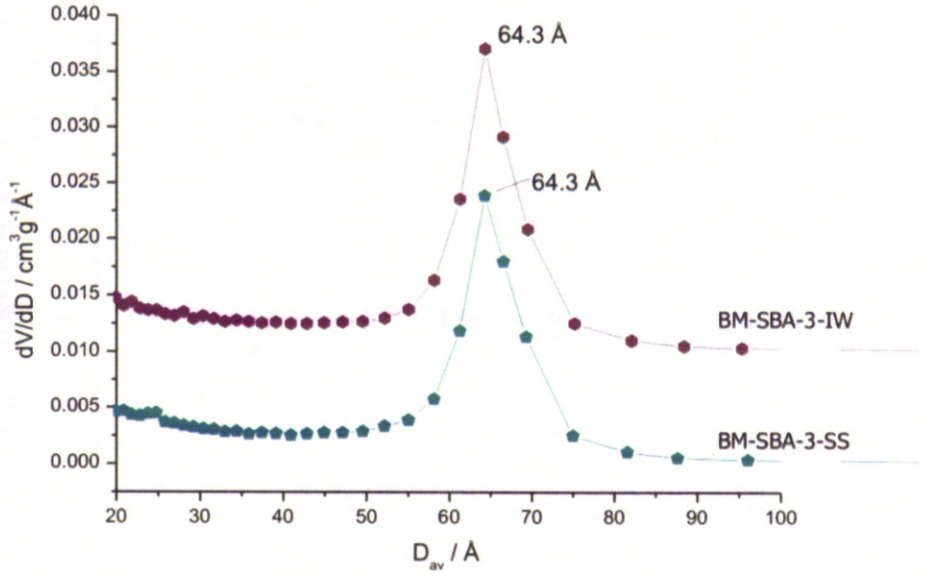

Figure 4.6 a) Nitrogen adsorption–desorption isotherms of BM-SBA-3-IW (purple) and BM-SBA-3-S (cyan) (each isotherm is offset by 100 cm^3g^{-1}). **b)** Pore size distribution plots were calculated from the adsorption branch of the N_2 isotherms (each plot is offset by 0.01 $cm^3g^{-1}Å^{-1}$)

From the combination of low angle PXRD and N_2 sorption isotherms it can be concluded that [bmim]CH_3SO_3 has entered the mesopores of SBA-15 and MCM-41 in all cases. As the same techniques were used for impregnation into SBA-15 it can be said that pore diameter is an important factor in determining the location of the ionic liquid.

In a similar study, Chen *et al.*[174] in their report of $[(CH_3)_3NC_2H_4OH]ZnCl_3$ encapsulated in single walled nanotubes (SWNTs), showed the use of photoluminescence in determining the diameter threshold at which the ionic liquid would enter the pores. For $[(CH_3)_3NC_2H_4OH]ZnCl_3$, they observed a diameter of *ca.* 0.97 nm was required to accommodate the ionic liquid. To test this hypothesis based on the experimental findings, the Van der Waals surface of $[(CH_3)_3NC_2H_4OH]ZnCl_3$ was calculated as a sphere of 0.7 nm in diameter and combined with the Van der Waals radius if the sp^2 –bonded carbon (0.15 nm). From this, they calculated that the smallest tube diameter capable of accommodating $[(CH_3)_3NC_2H_4OH]ZnCl_3$ is approximately 1 nm, consistent with their experimental findings. It is predicted that [bmim]CH_3SO_3 can diffuse into the SBA-15 pore more easily than MCM-41 in samples that were prepared by molten mixing due to the increased pore diameter of SBA-15. The number of ion pairs that are capable of fitting into SBA-15 and MCM-41 are discussed in the next section.

4.4.1.2 Packing dependence of [bmim]CH_3SO_3 on silica host material

The packing arrangement of C_{60} molecules in SWNTs is known to depend on nanotube diameter.[298,308] Chen *et al.*[174] also observed changes in packing arrangement of $[(CH_3)_3NC_2H_4OH]ZnCl_3$ with varying pore diameters. These range from single-chain, double-helix, zigzag tube to random tubular forms and were observed using HRTEM. The morphologies described in Chen's paper displayed structural characteristics not present in the bulk or film form of $[(CH_3)_3NC_2H_4OH]ZnCl_3$.

This study compares two chemically identical hosts. Both SBA-15 and MCM-41 are mesoporous silicas with hexagonally arranged pores that differ only by their pore size and pore connectivities (SBA-15 has hexagonally arranged

mesopores connected by micropores whereas MCM-41 does not contain micropores) to investigate the changes in morphology of [bmim]CH_3SO_3 upon encapsulation. As mentioned in **Section 3.4.1.2** the ion pair is too large to penetrate the micropores of SBA-15 The approach we have chosen to investigate changes in morphology is PXRD and later, NMR spectroscopy.

High angle PXRD patterns are shown in **Figure 4.8** along with the pattern collected for the neat [bmim]CH_3SO_3 used in the synthesis. The intensity of most of the peaks increases with increasing loading level of [bmim]CH_3SO_3 suggesting that the peaks observed are attributable to [bmim]CH_3SO_3. The d-spacings of the peaks from neat [bmim]CH_3SO_3 do not match the peaks from confined [bmim]CH_3SO_3.

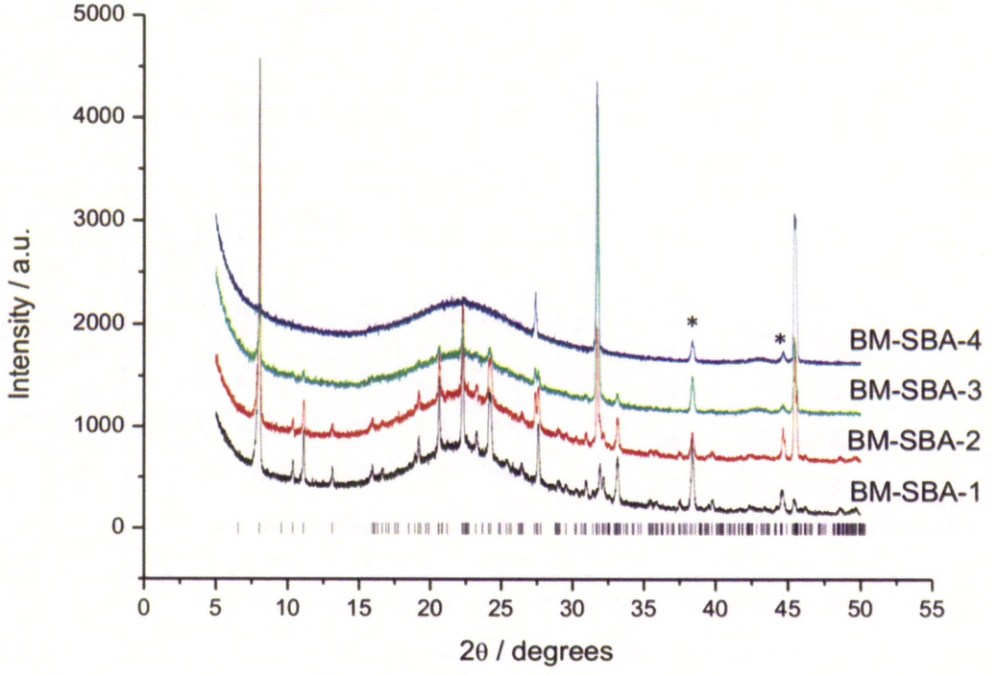

Figure 4.7 High angle PXRD patterns for [bmim]CH_3SO_3 encapsulated in SBA-15 (all peaks are from [bmim]CH_3SO_3 with background signal resulting from SBA-15)

The Le Bail fit (carried out by Dr. Sam Chong) of the neat [bmim]CH_3SO_3 confirms triclinic (P1) crystal symmetry as shown by Baldelli *et al.*[306] Le Bail fitting was applied to PXRD patterns of the ionic liquid composites and show that an orthorhombic phase is present at all loadings with a = 22.0 Å, b = 17.1 Å and c = 5.6 Å (**Table 4.2**). The same unit cell can be used to index the peaks observed

for each loading, with a slightly decreased cell volume at lower loadings *i.e.* the structure of the crystalline phase is not affected by the loading level of [bmim]CH_3SO_3.

The previous chapter described an interaction between CH_3 groups on the cation and –OH groups on the surface of the silica. It is predicted that a smaller unit cell may result from a decreased spacing between surface –OH groups on the surface if the pore has to accommodate more [bmim]CH_3SO_3. As well as agreeing with the work of Chen *et al.*,[174] this hypothesis also fits with the model described by Mickelson *et al.*[298] in their study of C_{60} inside boron nitride nanotubes, as there would be a greater geometric implication resulting in stronger intermolecular interactions as loading is increased. They show that pore diameter applies geometrical constraints and, coupled with the degree of loading, affect the intermolecular interactions governed by the distance between molecules. These factors in turn would affect the stacking configurations of ionic liquid molecules inside the pore as, at large pore diameters, C_{60} behaves as it does in the bulk whereas when loaded into a smaller pore diameter and high loading level, a new stacking configuration is obtained that are unknown for bulk or thin film forms of C_{60}. In this system however, the Le Bail fit is the same for each loading level so it can be concluded that the change in loading and does not have a significant impact on the stacking configuration, it is more likely to be the geometric constraints of the pore.

There is a considerable change in the relative peak intensities upon decreasing the loading level with many reflections not observed at the lowest loading of the ionic liquid (BM-SBA-4). This is consistent with the absence of significant confined bulk crystalline material (represented in **Figure 4.9** in purple and green) within the pores and a preferential orientation of the remaining ionic liquid that is interacting with the pore surface. There does not appear to be a simple correlation between which reflections are lost as the loading is decreased (*i.e.* it is not as straightforward as (00l) losing intensity, whilst (hk0) remains). This has made it difficult to identify what the relationship is.

The peak at 32^0 is attributed to material inside the pores although the intensity of this peak increases with decreasing loading of RTIL. The reason for this is due to the preferred orientation of material on the surface of the pores. There is

relatively less scattering from material orthogonal to the pore walls yet the planes that lie along the axis of the pores dominate the scattering. The absence of some peaks in the diffraction pattern that would be expected for the orthorhombic phase given in **Figure 4.8** could be due to preferential orientation of [bmim]CH_3SO_3 caused by the 2D hexagonal arrangement of mesopores SBA-15.

In order to eliminate solvent effects on the change in crystal symmetry, various methods of loading [bmim]CH_3SO_3 into SBA-15 were investigated. These methods included incipient wetness (BM-SBA-1-IW *etc.*) and by heating [bmim]CH_3SO_3 and SBA-15 together to 373 K (above the melting point of [bmim]CH_3SO_3) with stirring overnight (BM-SBA-1-S etc.). All methods of loading led to products with the same d-spacings in the PXRD pattern (**Figure 4.8**) at all loading levels (BM-SBA-3, BM-SBA-3-IW and BM-SBA-3-S are shown in **Figure 4.9**). From this we can conclude the method of loading does not have an effect on the crystal symmetry for [bmim]CH_3SO_3 in SBA-15.

A change in crystal symmetry upon confinement has been observed previously by Cai *et al.*[309] in their work on SBA-15 encapsulated hexanitrohexaazaisowurtzitane (HNIW). In this study, the confined HNIW gave a diffraction pattern assignable to an unknown polymorph analogous to what is observed in this study. They suggest that, the powder pattern probably implied some preferred orientation of HNIW crystals by torsion of the nitro groups. This is induced by H-bonding and could also reveal the presence of a new polymorph which is only stable under confined conditions.[309]

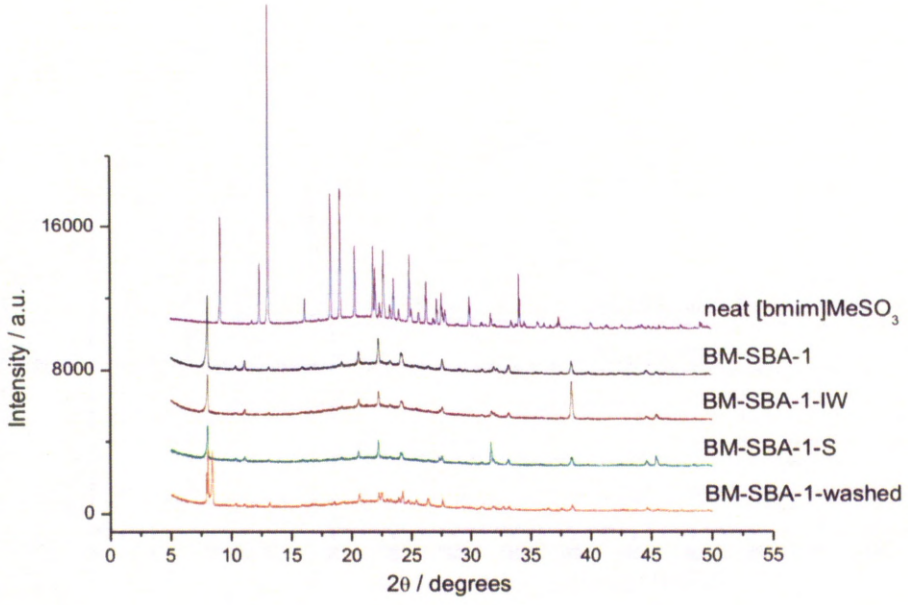

Figure 4.8 PXRD patterns for neat [bmim]CH_3SO_3 and BM-SBA-1 loaded with solvent, via incipient wetness, by solid mixing at 373 K and washed with dichloromethane

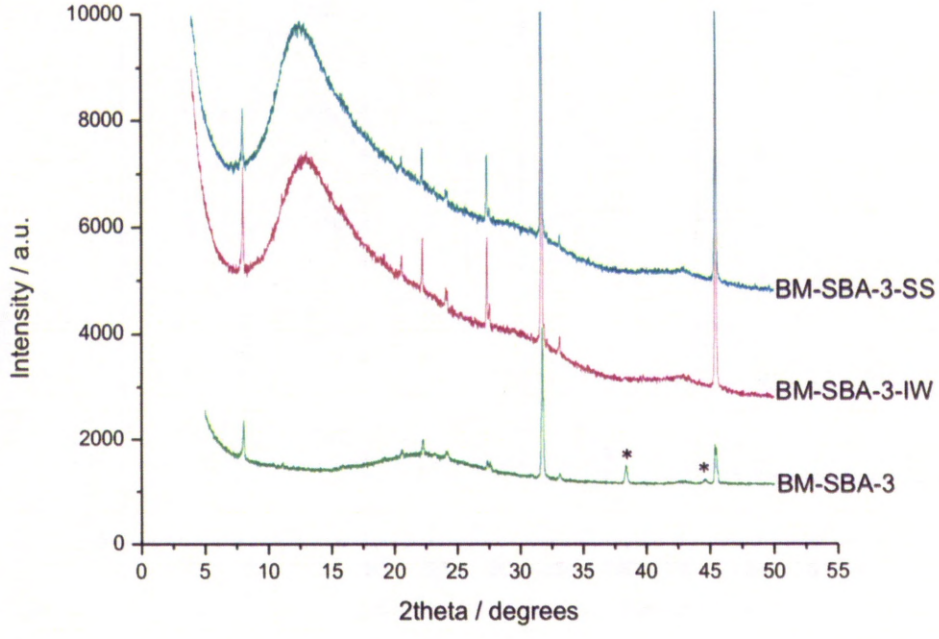

Figure 4.9 PXRD patterns for neat [bmim]CH_3SO_3 and BM-SBA-3 loaded with solvent, by incipient wetness and by solid mixing at 373 K (broad feature on baseline is due to background from mylar films acting as the sample holder).

BM-SBA-1 was washed with dry dichloromethane (same solvent used to load the [bmim]CH_3SO_3) to observe any changes in crystal symmetry and to confirm that the PXRD pattern observed were from [bmim]CH_3SO_3 inside the pores of SBA-15 and not on the external surface. The PXRD pattern for the washed BM-SBA-1 is displayed in **Figure 4.8** and exhibit more peaks than both the neat [bmim]CH_3SO_3 and encapsulated samples as it is not a single phase. Some of the peaks observed correspond to the orthorhombic phase of the encapsulated samples and are likely to be due to [bmim]CH_3SO_3 that has remained inside the pore. The peaks that do not correspond to the orthorhombic phase could be from [bmim]CH_3SO_3 that has leached during washing with DCM. As it is not possible to perform a Le Bail fit of this pattern, it is difficult to index the phases present in this pattern unambiguously.

High angle PXRD patterns were also recorded for BM-MCM-1 to BM-MCM-4 and show no crystalline phase present from [bmim]CH_3SO_3. This could be due to a difference in geometric constraints due to the reduced pore diameter of MCM-41 with respect to SBA-15. As the study by Chen *et al.*[49] suggested for [bmim]PF_6, the change in pore diameter may affect the stacking configuration of [bmim]CH_3SO_3. To eliminate the possibility of not observing a PXRD pattern due to sample size, experiments were run for 12 hours in comparison to the 1 hour scan required for BM-SBA samples and gave no diffraction peaks.

Table 4.2 Summary of lattice parameters for neat [bmim]CH_3SO_3, SBA-15 loaded and MCM-41 loaded [bmim]CH_3SO_3

Sample	Crystal symmetry	Space Group	a / Å	b / Å	c / Å	α / °	β / °	γ/ °
[bmim]$MeSO_3$	Triclinic	P1	7.934	8.480	10.28	103.4	99.57	111.6
BM-SBA-(1-4)	Orthorhombic	$P2_12_12_1$	22.0	17.1	5.60	90	90	90
BM-SBA-IW	Orthorhombic	$P2_12_12_1$	22.0	17.1	5.60	90	90	90
BM-SBA-S	Orthorhombic	$P2_12_12_1$	22.0	17.1	5.60	90	90	90

As mentioned in the previous section, it is possible to estimate the number of ion pairs present in a cross section of a mesopores of SBA-15 and MCM-41. It was postulated that the mesopores in MCM-41 are not large enough for nucleation of a crystal. Furthermore, the ionic liquid may not be able to penetrate far enough

into the pore without the pore becoming blocked, in turn, preventing crystal growth. Using the unit cell parameters calculated for the orthorhombic polymorph of [bmim]CH_3SO_3 from the Le Bail fits (**Table 4.2**) and the pore diameter measured from the pore size distributions (**Table 4.1**) it is estimated that 171 ion pairs are present in a pore cross section of SBA-15 and 25 in a pore cross section of MCM-41 (**Figure 4.10**).

The density of packing of [bmim]CH_3SO_3 in SBA-15 given unit cell parameters can also be estimated by $V = n(n_{non\text{-}H} \times 18)$ where 18 Å^3 is the approximate volume of a non-hydrogen atom. $V_{[bmim]CH3SO3} = 270$ Å^3. The orthorhombic unit cell volume is 2109 Å^3, therefore there are approximately 8 ion pairs per unit cell (2109 Å^3/270 Å^3) giving a packing density of 1.47 g/cm^3. The unit cell volume of [bmim]CH_3SO_3 in the triclinic phase is 601 Å^3. Therefore the density of packing in the neat form is 1.29 g/cm^3. The increase in packing density is to be expected upon confinement and means that the distance between ion pairs will be smaller. This in turn affects the intermolecular forces between ion pairs and will affect their arrangement with respect to each other, giving rise to the observed new polymorph.

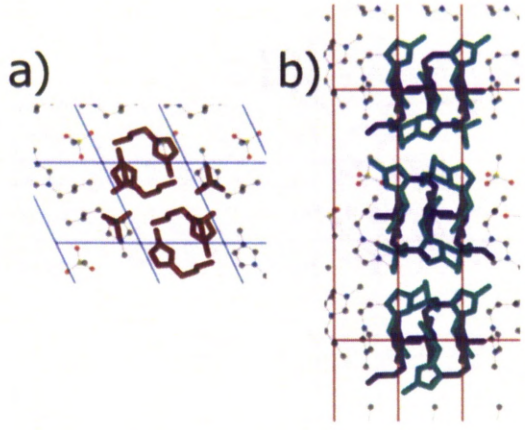

Figure 4.10 a) Representation of triclinic arrangement of ion pairs in neat [bmim]CH_3SO_3 and **b)** proposed orthorhombic arrangement of ion pairs in SBA-15 confined systems.

In summary, there are multiple effects that could cause the change in crystal symmetry upon encapsulation, which in turn affect the properties of [bmim]CH_3SO_3. Sha *et al.*[175] predicted theoretically the formation of solid monolayer [mmim]Cl when confined between two parallel graphite walls. They describe a model system for the

study of H-bonding molecules confined in hydrophobic nanospaces. The investigation was performed using two-dimensional mass-centered radial distribution functions and describes an elevated melting point of the new phase [mmim]Cl.

The work of Chen *et al.*[174] describes the microstructure of the RTIL studied by varying graphite wall distance. Upon the formation of a bilayer of RTIL between the walls, the imidazolium ring forms a strong π–π stacking structure in which each cation is surrounded by the three nearest neighbor anions. The bilayer that is formed is a new phase of [mmim]Cl , different to that of the bulk material.

From the knowledge gained from the literature,[49,174-175,298,309] it is predicted that the inner pore surface of both SBA-15 and MCM-41 provide an interfacial confinement effect in which [bmim]CH_3SO_3 assembles into a contact layer with a preference for orientation. Such an interfacial-induced nucleation, along with the effect of confinement in the mesopores, causes the ion pairs to assemble together when the diameter of the pore is suitable. The formation of cylindrical sheets of [bmim]CH_3SO_3 that arise from this give rise to the PXRD pattern observed for SBA-15 encapsulation. However, MCM-41 does not have a suitable diameter to allow enough repeat units to exist inside the pore, hence the absence of diffraction peaks.

4.4.1.3 Melting behaviour of [bmim]CH_3SO_3 confined in SBA-15

The change in crystal structure in this system is complimentary to the work of Chen *et al.*[49] who observed a different crystal structure for [bmim]PF_6 confined in multiwalled carbon nanotubes (MWNT) to that described by Choudhury *et al.*[278] for neat [bmim]PF_6. In their study, they describe a more stable crystal of [bmim]PF_6 formed inside the MWNT which is then further proven by the elevated melting point (196 K higher than neat [bmim]PF_6) detected by DSC. The study by Choudhury *et al.*[278] describes a crystal structure of [bmim]PF_6 that was formed under *in situ* cryocrystallisation conditions to avoid glass formation of [bmim]PF_6 as under ambient conditions it is difficult to obtain the crystalline phase. The crystallisation of [bmim]PF_6 inside MWNTs happened spontaneously indicating that it is more stable than in the bulk system. Other studies have reported new phases formed upon encapsulation causing elevated melting points.[40,44] Sha *et al.*[49] showed a

liquid-to-solid phase transition of bilayer [mmim]Cl at 425 K in the confined system. The melting point of bulk [mmim]Cl is 399 K. Upon confinement, theoretical calculations suggest a melting point of *ca.* 825 K, which is attributed to the strong $\pi\cdots\pi$ – stacking interactions between imidazolium rings and a strong interaction with the surface of graphite. It is reported that if RTILs fill pores of a solid material and remain in a liquid state (*i.e.* fast dynamics and weak interactions with the walls), then the change in melting point is caused by capillarity which reduces the melting point.[310] In the case of [mmim]Cl confined between graphite walls and in the work of Kanakubo *et al.*[296] in which RTILs are encapsulated between controlled-pore glasses (CPGs), strong RTIL-pore wall interactions always lead to an increase in melting temperature. The modelling carried out by Sha *et al.*[209] describes strong interaction energy between graphite walls and the RTIL causing a sharp increase in melting point. They also suggest that an increased average number of nearest neighbours in the new solid bilayer of ionic liquid leads to a higher melting-point than the bulk material which can be explained by simple mean field theory.*[42,311-314] These observations are also consistent with the increased melting point of [bmim]PF_6 confined in MWNT mentioned earlier.[49]

Variable temperature PXRD and DSC measurements have been used to investigate melting point behaviour of SBA-15 confined [bmim]CH_3SO_3 (**Figures 4.11 and 4.13**). Analyses of ^1H NMR linewidths, ^1H spin-lattice relaxation and variable temperature ^1H-^{13}C CP-MAS NMR have also been used to describe the change in melting point behaviour. A more thorough description of the spectra described in this section is given in the following section however the spectra positioned here have been included to aid the description of melting point behaviour.

The variable temperature XRD patterns (**Figure 4.11**) show peaks that correspond to SBA-15 encapsulated [bmim]CH_3SO_3 phase. The patterns show no loss of peak intensity at temperatures above the melting temperature of neat [bmim]CH_3SO_3 (*ca.* 348 K). As described in the literature, this could be due to strong interactions between the pore surface and [bmim]CH_3SO_3 and geometric constraints, increasing the intermolecular forces between molecules.

---

* The main idea of mean field theory is to focus on one particle and assume that the most important contribution to the interactions of such particle with its neighbouring particles is determined by the mean field due to the neighbouring particles.

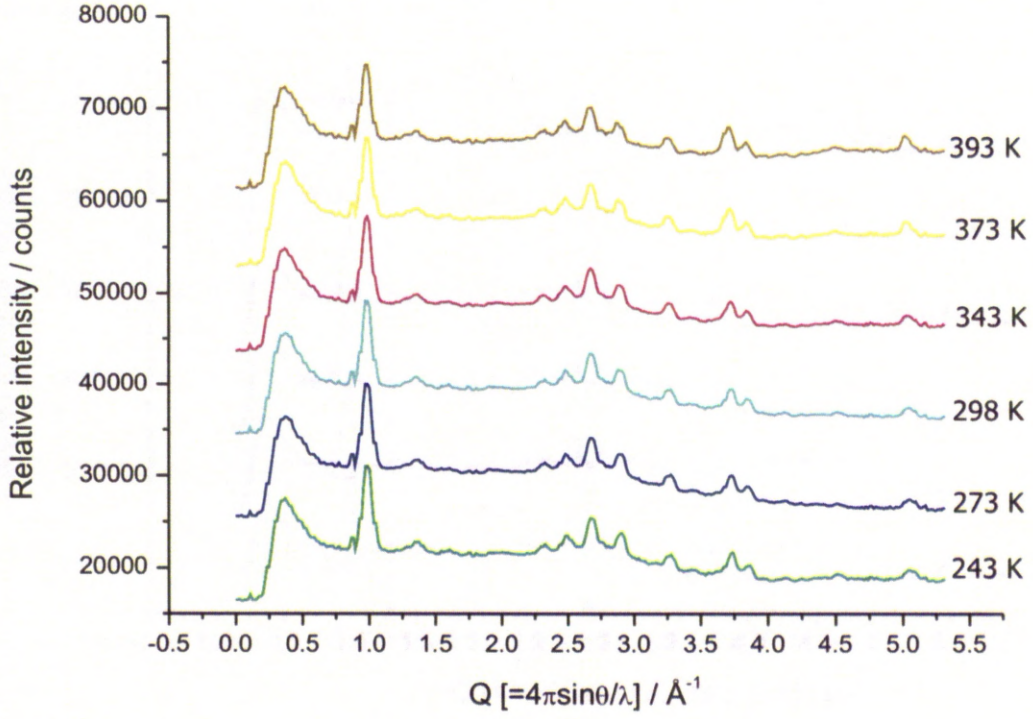

Figure 4.11 Variable temperature PXRD patterns of BM-SBA-1 collected on a single crystal diffractometer.

DSC data were recorded for neat [bmim]CH_3SO_3 (**Figure 4.12**) and BM-SBA-1 (**Figure 4.13**). For neat [bmim]CH_3SO_3 the sample was first heated from 298 to 373 K at a rate of 10 K/min. At this temperature the sample is melted completely and displays a phase transition peak at 348 K. The sample was then cooled to 98 K at a rate of 10 K/min. Upon cooling a peak is observed at 271 K at which point crystallization takes place. The phase transitions observed are characteristic of [bmim]CH_3SO_3 and are in agreement with the literature.[315]

Upon impregnation of [bmim]CH_3SO_3 into SBA-15 the transition temperatures of [bmim]CH_3SO_3 cannot be observed clearly. Initially, it was thought that this may be due to the sensitivity of the instrument however, calculations show that in an 18 mg sample of B-SBA-1, 0.02 mg of [bmim]CH_3SO_3 is present. This amount is on the lower limit of sensitivity of the instrument. This indicates that [bmim]CH_3SO_3 inside

the SBA-15 pores does not make a contribution to the transition observed for the neat [bmim]CH_3SO_3 and results in disappearance of these peaks. This has been previously observed by Waechtler *et al.*[96] and Deng *et al.*[172] in their studies of ionic liquids in mesoporous silica gel. From the absence of this peak we can also assume that there is no ionic liquid outside the pore system of SBA-15 that would behave in the same manner as bulk [bmim]CH_3SO_3.

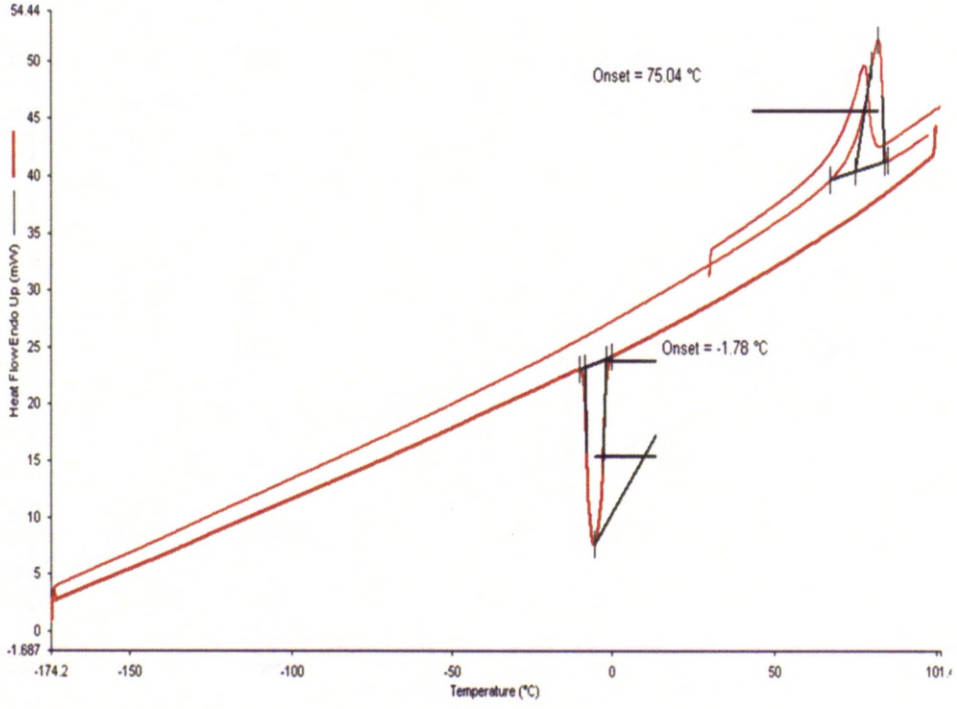

Figure 4.12 DSC thermograph of [bmim]CH_3SO_3

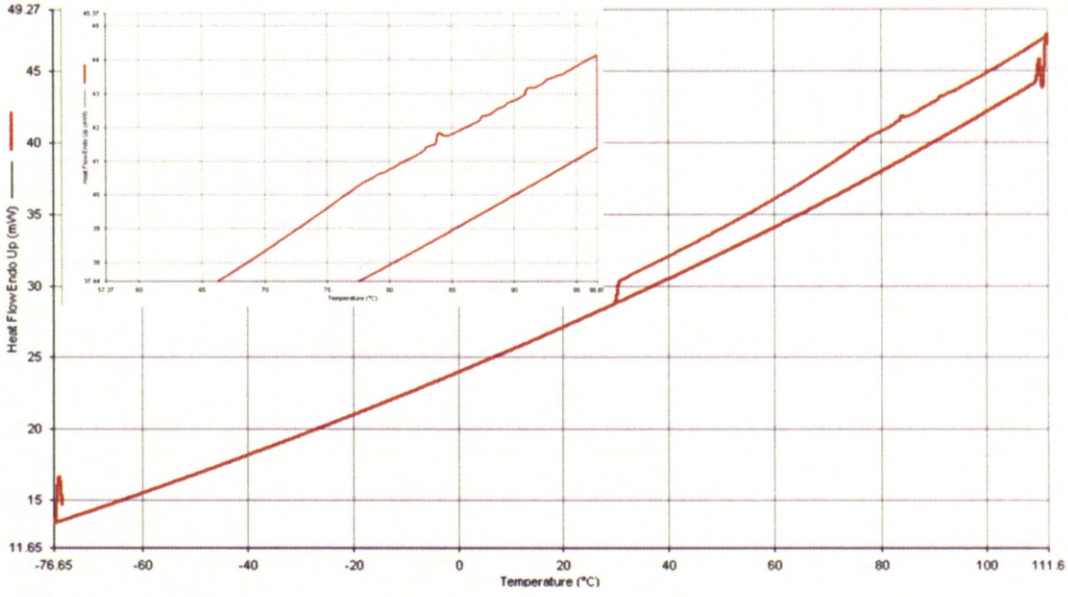

Figure 4.13 DSC thermograph of BM-SBA-1

DSC data are, therefore, in agreement with the PXRD patterns as these too display a different melting point to bulk [bmim]CH_3SO_3.

The DSC thermographs of BM-SBA-1 do not show a melting transition at any point up to 383 K which is the temperature limit of the equipment. The melting point could be predicted using the Gibbs-Thompson equation (*eqn. 4.1*) if the contact angle with the surface and the enthalpy of fusion is known.[316]

$$\Delta T_m = \frac{k_{GT}}{X} \qquad \textit{eqn. 4.1}$$

Where ΔT_m is the melting point depression, k_{GT} is a geometric constant dependant on the ionic liquid, the pore diameter and the wetting nature of the pores and X is a dimension that defines the effective size of the pores.[316]

In an analogous study by Singh *et al.*[312] an imidazolium based cation with a large anion ($OctSO_4$) was confined in a nanoporous silica gel matrix. The characterisation of their system was by DSC and PXRD and shows a decrease in melting point of the ionic liquid by 52 K. Unlike what we have observed, they used PXRD to monitor the glassy nature of SiO_2 with and without ionic liquid. The DSC results on the other hand clearly show a phase transition at the decreased melting

point. They attribute this to a preferential interaction of the anion with –OH groups on the surface of silica and the decreased melting point due to the overall increased size of the ion pair. In comparison to this study, the anion used in this study is relatively small and therefore an increase in melting point is to be expected.

Complementary to the PXRD and DSC data, ^{1}H MAS NMR spectra were acquired at various temperatures for neat [bmim]CH_3SO_3 and BM-SBA-1 and 4 (**Figures 4.14, 4.15** and **4.16**). Resonance assignments for ^{1}H MAS NMR spectra of neat [bmim]CH_3SO_3 and BM-SBA-1 are as follows: δ/ppm 0.76 terminal C(9), 1.19 C(8), 1.78 C(7), 2.60 C(11), 4.17 C(10), 4.32 C(6), and 7.91 N-C(4)-H, N-C(5)-H, 9.43 imidazolium ring N_2-C(2).[244]

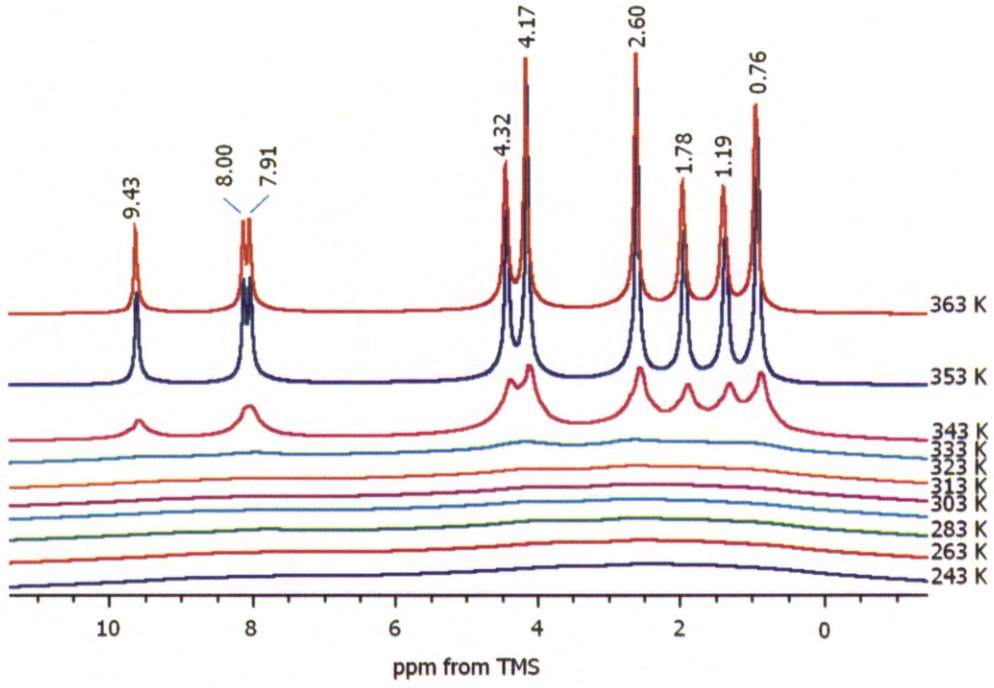

Figure 4.14 ^{1}H MAS NMR spectra of [bmim]CH_3SO_3 with varying temperature

^{1}H MAS NMR spectra for neat [bmim]CH_3SO_3 display broad resonances in the temperature range 243-333 K and distinctly narrower resonances above 343 K, as expected, since melting occurs at 348 K. Comparing the spectra at 343 and 353 K, resonances become increasing narrow after the melting point transition. Narrowing at 343 K, in comparison to the spectra recorded at 333 K, is due to partial melting of the system.

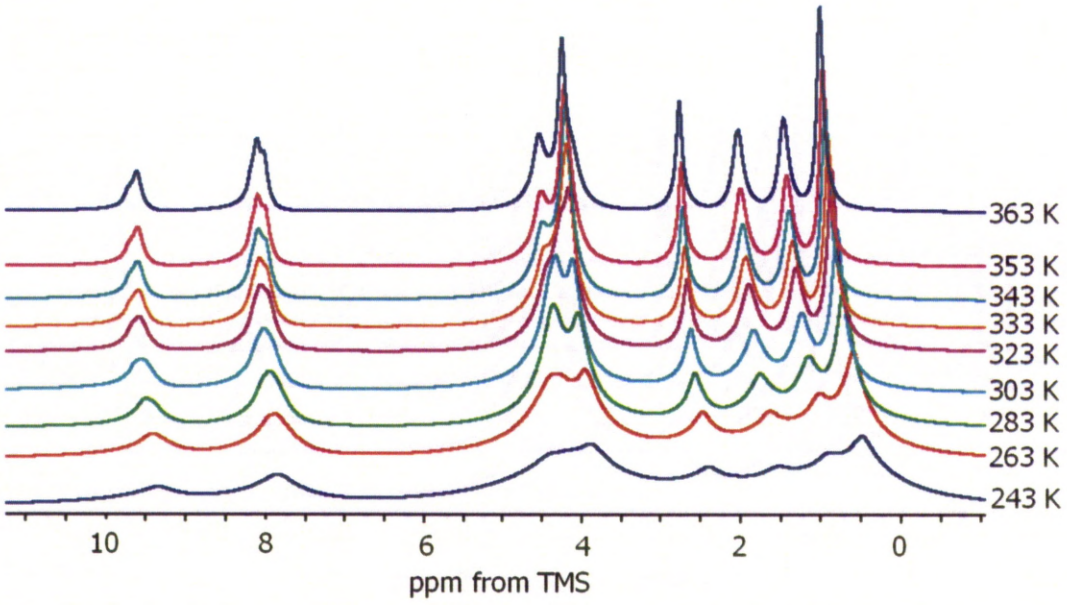

Figure 4.15 ^{1}H MAS NMR spectra of BM-SBA-1 with varying temperature

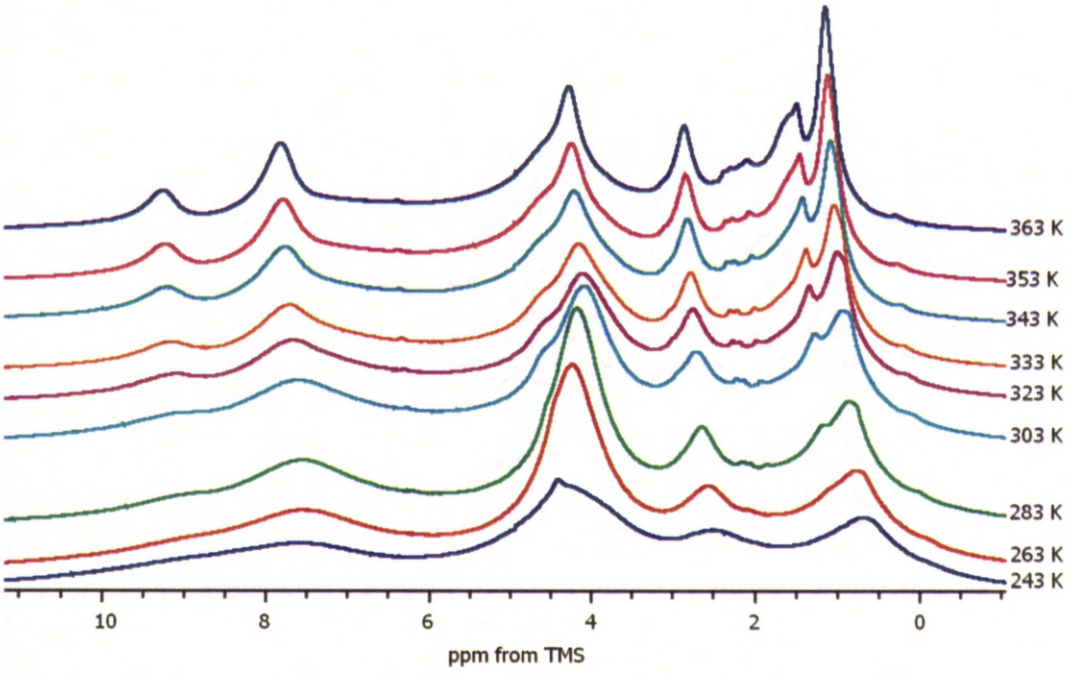

Figure 4.16 ^{1}H MAS NMR spectra of BM-SBA-4 with varying temperature

The ^{1}H MAS NMR spectra for loaded samples BM-SBA-1 and 4 are different compared to neat [bmim]CH_3SO_3. At temperatures below the melting point of neat [bmim]CH_3SO_3 the resonances are narrower than for neat [bmim]CH_3SO_3. The resonances narrow slightly with each increased temperature interval as the ionic

liquid becomes more mobile. However, the distinctive change in linewidth that occurs upon melting (348 K) is not observed for BM-SBA-1. This observation is in support of the lack of a phase transition at the melting point of neat [bmim]CH_3SO_3 upon encapsulation.

In all spectra, for neat and encapsulated RTIL, a slight upfield chemical shift change for all resonances is observed with changing temperature. This is most likely due to increasing temperature. However, it has been previously reported that changes in chemical shift to higher frequencies with increasing temperature is due to aggregation. This could potentially change the strength of the interaction between the cation and the anion, as the distance between them would be altered. Lungwitz *et al.*[317] observed an upfield chemical shift change in the ^1H NMR spectra of [Hmim]Cl on an Areosil300 silica surface with decreasing loading. They attributed this shift to a change in interaction strength of the cation and the anion caused by the hydrogen bonding strength between the anion and the surface. Further discussion of these spectra and corresponding ^1H T_1 relaxation times is given in the next section.

To confirm that confined [bmim]CH_3SO_3 remains solid above the melting point of neat [bmim]CH_3SO_3, ^1H-^{13}C CP-MAS NMR spectra were recorded at room temperature and 353 K (**Figure 4.17**). Resonance assignment is as follows: δ 14.0 C(9), 20.0 C(8), 32.7 C(7), 37.2 (38.3) C(10), 42.1 (41.3) C(11), 50.1 C(6), 123.7 C(4), 124.8 C(5) and 138.0 ppm C(2). The high intensity of the peaks in the CP spectra at 353 K confirms that confined [bmim]CH_3SO_3 remains solid above the melting point of neat [bmim]CH_3SO_3.

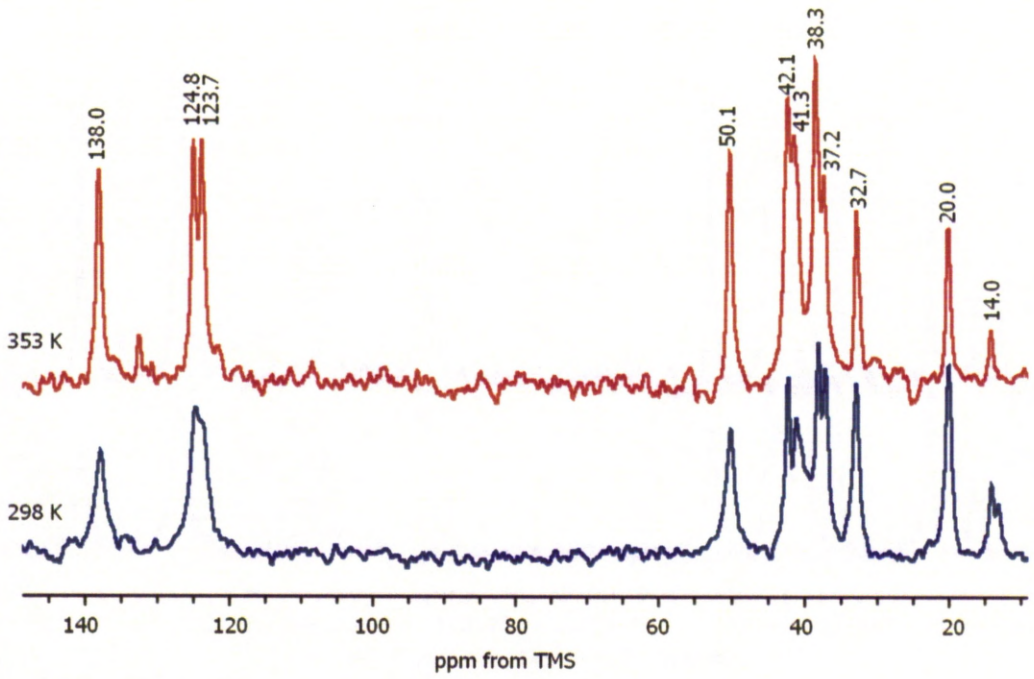

Figure 4.17 ^{1}H-^{13}C CP-MAS NMR spectra of BM-SBA-2 at 298 and 353 K (MAS = 10 kHz)

Another observation that was made from the ^{1}H-^{13}C CP-MAS NMR spectra of BM-SBA-2 was the splitting of peaks at 42.1 and 37.2 ppm corresponding to C(11) (C in anion) and C(10) (N-CH_3 in cation) respectively. **Figure 4.18** displays the ^{1}H-^{13}C CP-MAS NMR spectra of neat [bmim]CH_3SO_3 in which no splitting of these resonances is evident, and BM-SBA-1.

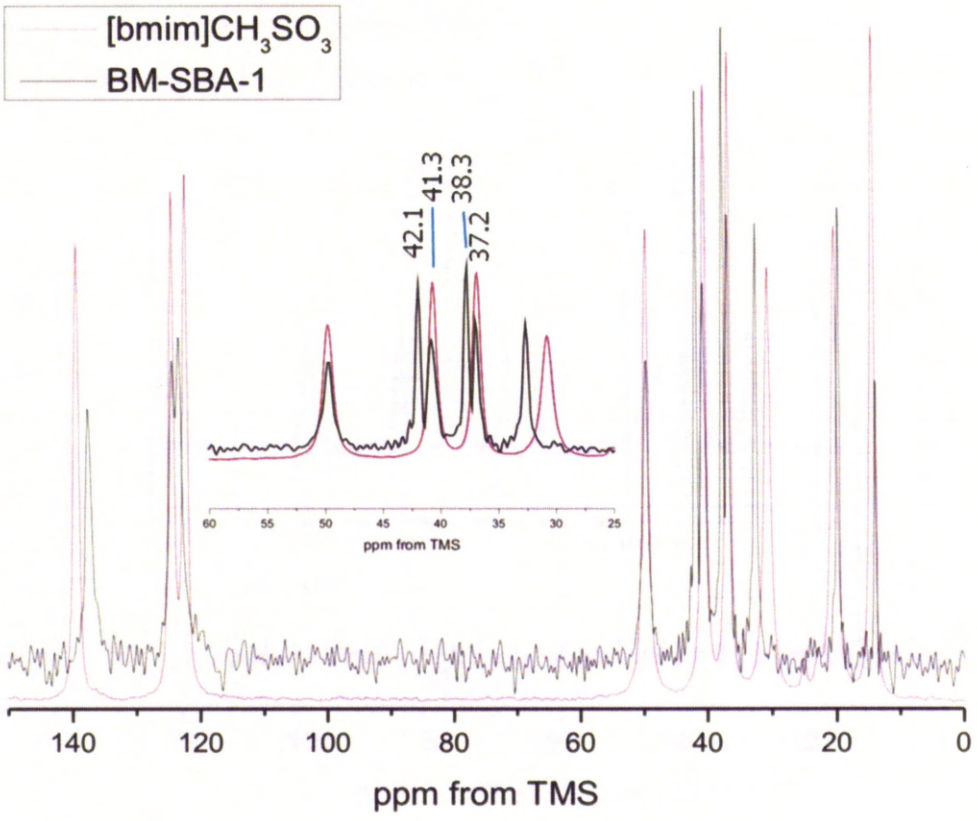

Figure 4.18 ^{1}H-^{13}C CP MAS NMR spectra of neat [bmim]CH_3SO_3 and BM-SBA-1

The ^{1}H-^{13}C CP-MAS NMR spectra shows these peaks at a different relative intensities to the $^{13}C\{^{1}H\}$ MAS NMR spectra that display an abundant environment at 41.3 ppm and a less abundant environment at 42.1 ppm (**Figure 4.18**). The cause of this splitting is difficult to rationalise unambiguously. However, it could be due to a number of reasons that have been investigated and are discussed in **Section 4.4.2.2**. Comparison of the neat and encapsulated spectra in **Figure 4.18** also shows an upfield change in chemical shift for the following resonances: δ 138.0, C(2), 32.7, C(7), 20.0, C(8), 14.0 ppm, C(9). This change is an effect of encapsulation and reorientation of the ion pairs within the pore giving rise to a new crystal structure. This could be due to a change in packing arrangement. The fact that there are no resonances in the spectra of encapsulated RTIL that correspond to the resonances of the neat RTIL spectra indicates that there is no neat [bmim]CH_3SO_3 present in the intercalates.

In summary, SBA-15 confined [bmim]CH_3SO_3 experiences an elevation of melting point in comparison to neat [bmim]CH_3SO_3. This can be attributed to

stronger intermolecular forces between the ion pairs induced upon confinement. The new melting point is yet to be determined as the limits of the instruments available are not suitable to measure this accurately. As mentioned earlier, the Gibbs-Thompson equation can be used to estimate the melting point,[318] however, many of the required parameters (*e.g.* the surface tension at the RTIL-silica interface) are yet to be measured for this system.

4.4.2 Molecular level characterisation of [bmim]CH_3SO_3 confined in SBA-15 using NMR spectroscopy

There are many reports of elevated or depressed melting points and changes in crystal structures as a result of confinement. However, an in-depth characterisation of interactions that cause these effects is rare. This section aims to go some way in displaying techniques that can be used to further understand the interactions that give rise to the changes observed upon confinement.

4.4.2.1 ^{1}H MAS NMR and T_1 relaxation time measurements

^{1}H MAS NMR spectra were acquired for neat [bmim]CH_3SO_3, SBA-15 composites loaded with varying amounts of [bmim]CH_3SO_3 *via* solvent, incipient wetness and molten mixing methods (**Figures 4.19, 4.20 and 4.21** (spectra were recorded at ambient temperature)).

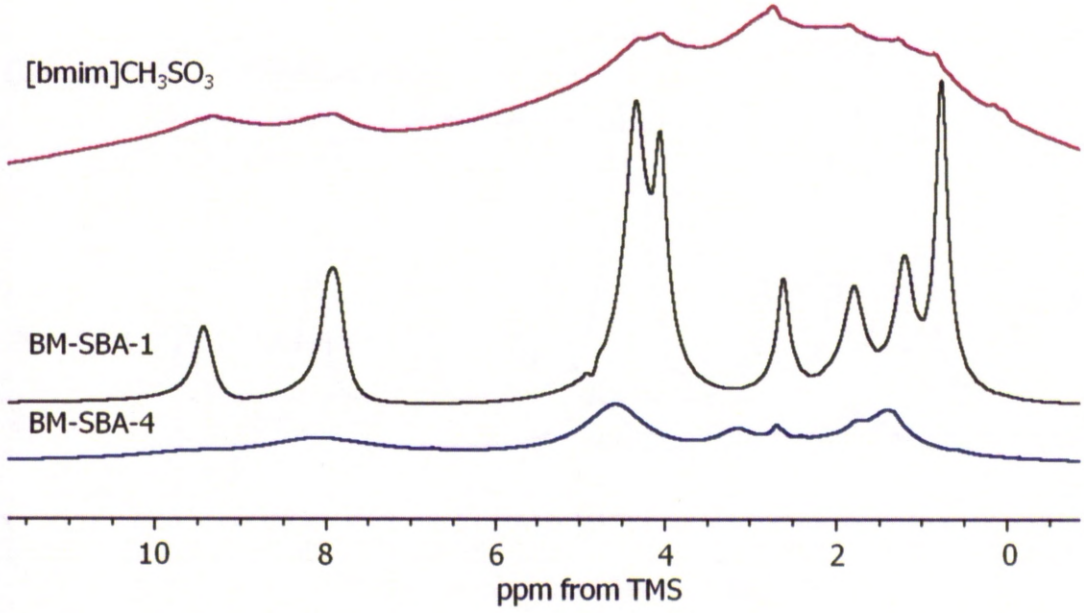

Figure 4.19 ^{1}H MAS NMR spectra of [bmim]CH_3SO_3, BM-SBA-1 and BM-SBA-4 (MAS rate = 10 kHz)

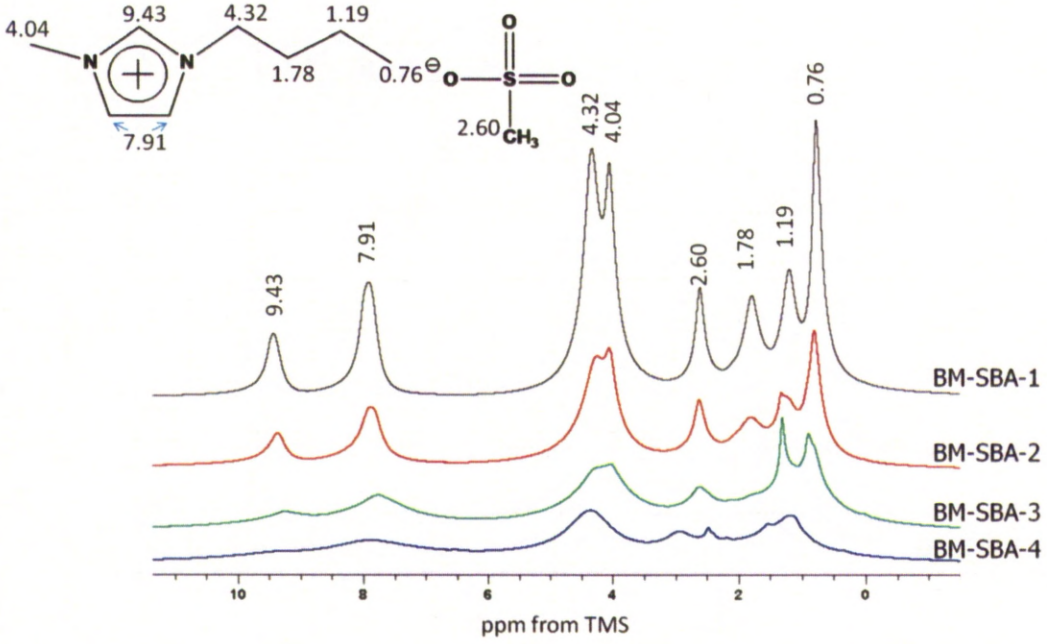

Figure 4.20 ^{1}H MAS NMR spectra of BM-SBA-1, BM-SBA-2, BM-SBA-3 and BM-SBA-4 (MAS rate = 10 kHz)

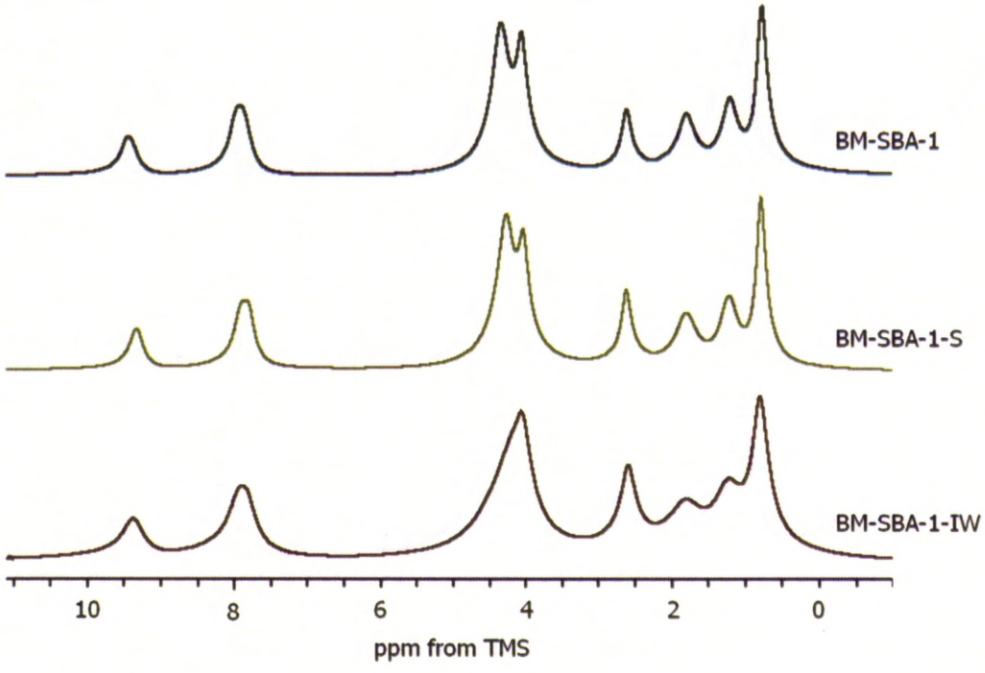

Figure 4.21 ^{1}H MAS NMR spectra of BM-SBA-1, BM-SBA-1-IW and BM-SBA-1-S (MAS rate = 10 kHz)

As clearly shown in **Figure 4.22**, at ambient temperature resonances of confined [bmim]CH_3SO_3 are narrower than in neat [bmim]CH_3SO_3. The reasons for this are not clear, however, this could be due to ^1H-^1H dipolar coupling networks being weakened in confined space or the confined bulk ionic liquid having more rotational freedom. Since the appearance of a spectrum of a solid depends on the strength of different magnetic interactions giving rise to a fluctuating local magnetic field (B_1) (detailed in **Section 2.5.3.2**), the linewidth is not easy to rationalise in terms of one specific parameter. The ^1H MAS NMR spectra of neat [bmim]CH_3SO_3 were recorded at a higher MAS rate (30 kHz) with the aim of reducing dipolar couplings and achieving a more resolved spectrum however this gave no improvement to the resolution (**Figure 4.22**). This indicates that the chemical shift anisotropy Hamiltonian has a negligible effect on the line width in comparison to that of the dipolar Hamiltonian.

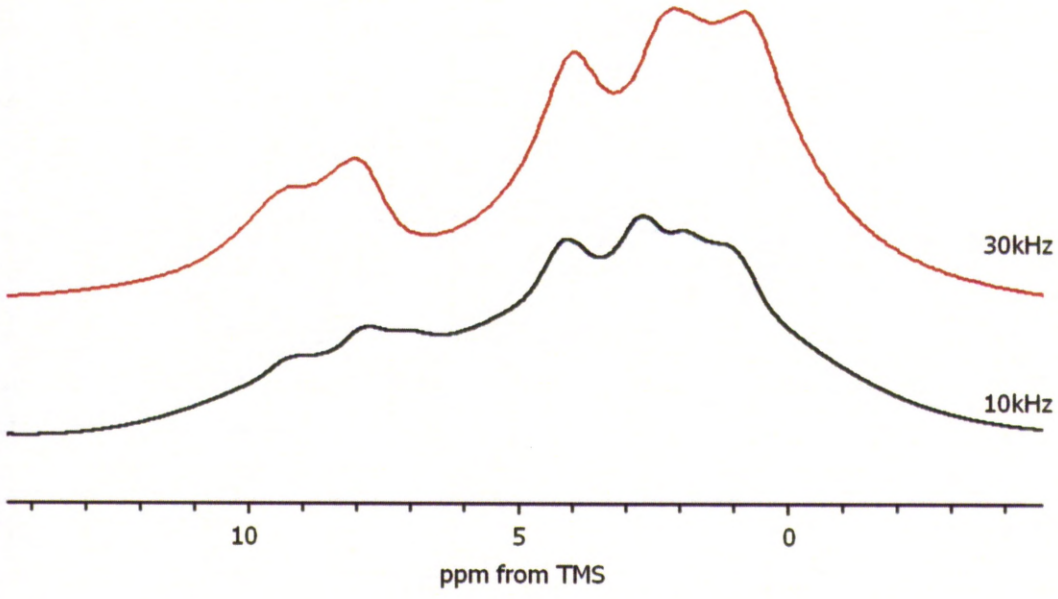

Figure 4.22 ^1H MAS NMR spectra of [bmim]CH_3SO_3 at MAS rate= 10 and 30 kHz

The Hamiltonian for dipolar couplings in a homonuclear system of more than one spin ($\hat{H}^{DD,homo}$) is given by, as previously described in **Section 2.5.1.2.1**:

$$\hat{H}^{DD,homo}(\theta) = d_{jk}(3\hat{I}_{jz}\hat{I}_{kz} - \hat{I}_j.\hat{I}_k) \qquad \textit{eqn. 4.2}$$

Where I_j and I_k are spins with the same gyromagnetic ratio (γ) (*i.e.* two protons) and in which:

$$d_{jk} = -\frac{\mu_0}{4\pi}\frac{\gamma_j\gamma_k\hbar}{r_{jk}^3}\frac{1}{2}(3cos^2\theta - 1) \qquad \textit{eqn. 4.3}$$

Here γ is the gyromagnetic constant for spins j and k, r_{jk} is the distance between the spins, $\mu_0 = 4\pi \times 10^{-7}$ Hm^{-1}, the magnetic constant and $\hbar = 1.055 \times 10^{-34}$ Js.

The geometric term can be averaged by magic angle spinning as $(3cos^2\theta - 1) = 0$ at $\theta = 54.74^0$. The spin diffusion term on the other hand, $(3\hat{I}_{jz}\hat{I}_{kz} - \hat{I}_j.\hat{I}_k)$ and the distance dependence is more difficult to diminish and therefore leads to line broadening.

In the neat ionic liquid, the homonuclear dipolar interaction is stronger than upon encapsulation when there is only a limited number of ion pairs across the width of a pore. Consider a ^1H site in the molecule of neat ionic liquid. The energy from that spin can be transferred to many surrounding spins and spin diffusion is abundant. Now consider the same site of the ionic liquid species encapsulated inside the mesopore. There are now fewer spins within the same pore to which energy can be transferred. The effect of this is to decrease the $(3\hat{I}_{jz}\hat{I}_{kz} - \hat{I}_j.\hat{I}_k)$ term of the homonuclear dipolar Hamiltonian, resulting in narrower lines. Also, within the pore network, it is possible that the distance between ion pairs is less as the density of packing is greater. Therefore, the r^3 term of the equation is increased causing a reduction of the dipolar Hamiltonian and a decreased linewidth, however, without further analysis of the structure by crystallography this is difficult to prove.

The decreased linewidth upon encapsulation is most likely attributed to the disruption of the spin diffusion part of the dipolar Hamiltonian or an increased mobility rather than an increase in crystal symmetry. As the crystal nucleates at the surface of the pores it grows into the centre of the pore yielding needle like crystals orientated along the channel. Depending on the orientation of the ion pairs within the unit cell, this could allow a greater degree of mobility in the form of rotational motion of individual cations than in the neat form allowing a reduction in the

strength of ^{1}H-^{1}H dipolar interactions. The packing arrangement of neat [bmim]CH_3SO_3 is shown in **Figure 4.10.**

As loading level is decreased resonances broaden and are shifted slightly upfield. In this case there will be a wider distribution of orientations of ionic liquid on the surface than in the neat ionic liquid or the encapsulated ionic liquid at higher loadings. The linewidth of each resonance is given with respect to loading level in **Figure 4.23** and shows that the ring protons are broadened significantly in comparison to the protons located on the butyl chain, the methyl group and the anion. Loading into SBA-15 *via* molten mixing and incipient wetness gives similar results to that of BM-SBA-1 in the line width analysis. This would be expected since the PXRD patterns and N_2 sorption isotherms are also similar for these products.

At low loading levels ion pairs that are interacting with the surface are observed. As loading is increased, the lineshape is dominated by confined bulk [bmim]CH_3SO_3 in the channel. The significant change observed for the ring could indicate that this group interacts with the surface more strongly, and other carbon environments protrude towards the centre of the pore.

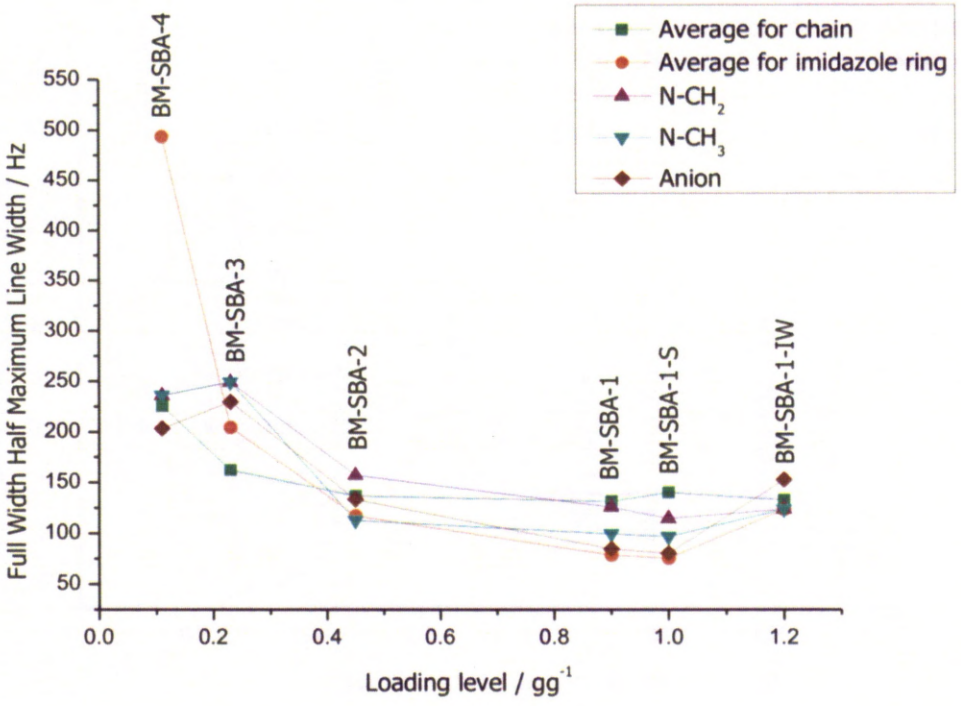

Figure 4.23 ^{1}H linewidths for [bmim]CH_3SO_3 in SBA-15with varying loading levels

As was observed for [bmim]OTf in SBA-15, detailed in the previous chapter, with decreasing loading resonances broaden. **Figure 4.24** shows the line widths of peaks for encapsulated [bmim]CH_3SO_3 (solid ionic liquid, BM-SBA-1) (*ca.* 80 to 130 Hz) are broader than for encapsulated [bmim]OTf (liquid ionic liquid, B-SBA-1)(*ca.* 28 to 40 Hz), as would be expected due to the relative mobilities of solids and liquids. Due to the rates of molecular tumblings in liquids being faster than solids, narrower linewidths are observed at the isotropic chemical shift as their motions are more easily averaged. The differences in chemicals shifts of the resonances assigned to the butyl chain (*ca.* 0.7, 1.2 and 1.8 ppm) in BM-SBA-1 and B-SBA-1 is most probably due to the different anions associated with the cation in each case.

Unlike SBA-15 confined [bmim]OTf samples, the change in linewidths for [bmim]CH_3SO_3 displays a slight decrease for chain, N-methyl and anion protons from BM-SBA-3 to BM-SBA-4. BM-SBA-4 has approximately monolayer coverage and therefore large linewidths are a result of surface restricted ion pairs within the pore space. The ^{1}H linewidths of BM-SBA-3 are determined by that of the surface confined layer and an additional layer creating a surface confined bilayer.

Therefore, it can be interpreted that upon loading an additional layer on top of the surface confined monolayer, mobility of protons environments that protrude into the pore are slightly restricted in the first layer in comparison to the same surface confined layer in which a bilayer is absent (as in BM-SBA-4). As loading increases from monolayer (BM-SBA-4) to bilayer (BM-SBA-3), and then to bulk (BM-SBA-2 and 1), ^{1}H-^{1}H dipolar couplings are disrupted. Chemical shift anisotropy also increases for ion pairs located on the surface of the pore wall. Together, homonuclear dipolar coupling and CSA cause a larger chemical shift distribution for surface confined ionic liquids as observed in the broadening of resonances in the spectra of BM-SBA-4 compared to BM-SBA-1.

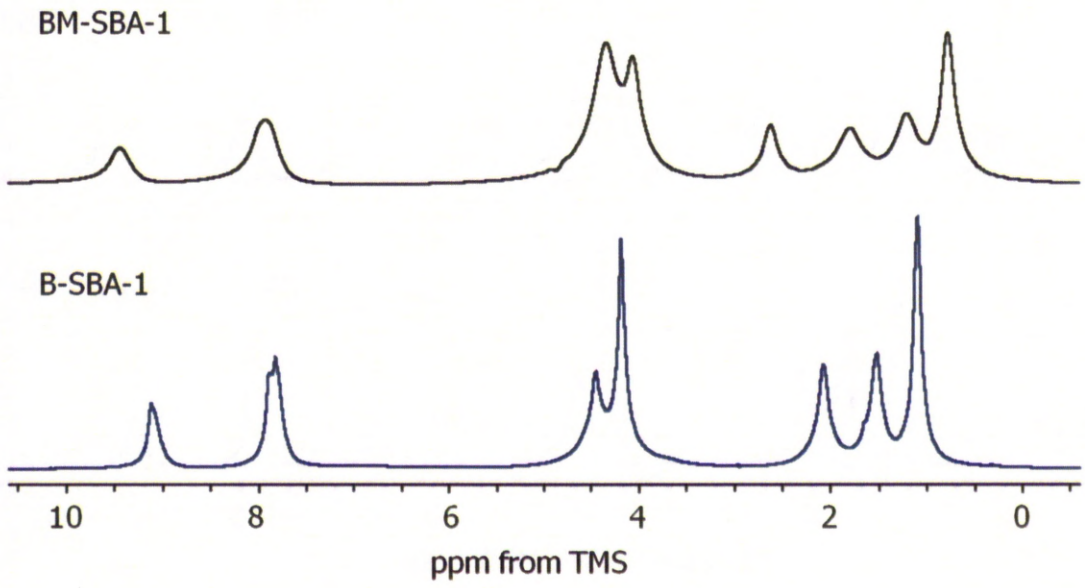

Figure 4.24 ^{1}H MAS NMR spectra of BM-SBA-1 and B-SBA-1 (MAS rate = 10 kHz)

The T_1 relaxation times at ambient temperature for neat [bmim]CH_3SO_3 and the various [bmim]CH_3SO_3 loaded SBA-15 are shown in **Figure 4.25**. Since the ^{1}H MAS NMR spectrum of neat [bmim]CH_3SO_3 is broad, an averaged T_1 value of 1570 ms was measured for all proton environments. Compared with the values given in **Figure 4.25**, this is much longer than the relaxation times measured for

confined [bmim]CH_3SO_3. However, because the dipolar interactions in these systems are different, they cannot be compared directly.

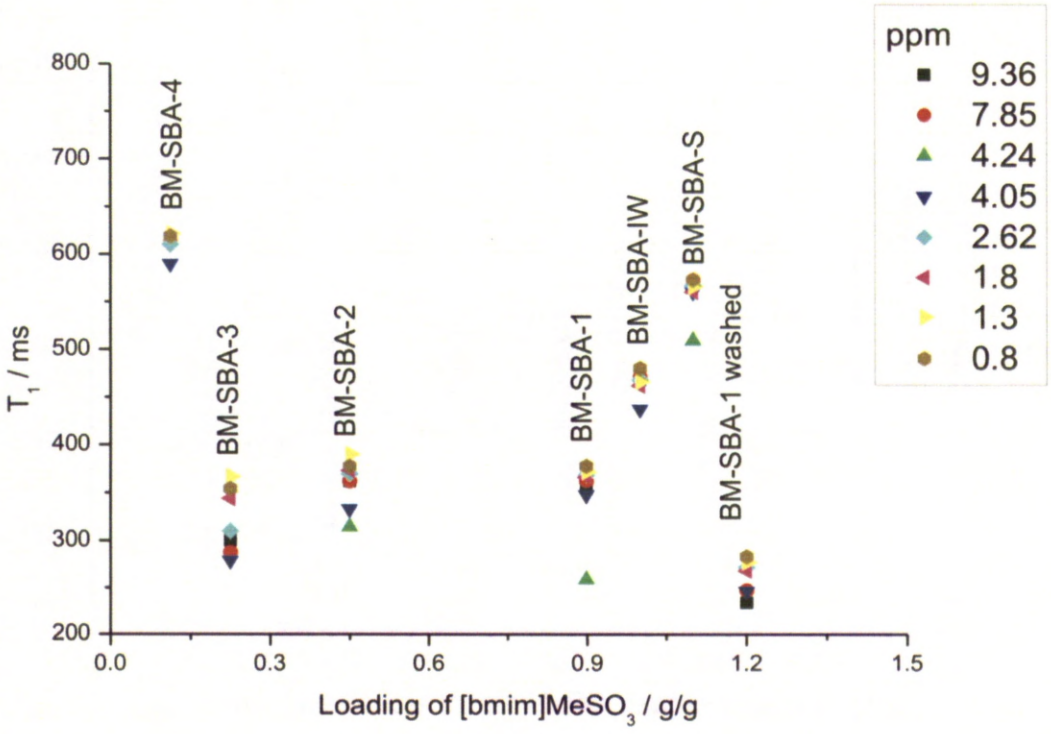

Figure 4.25 ^1H T_1 relaxation times vs loading level for BM-SBA systems

As during the loading of SBA-15 with [bmim]OTf, the T_1 times for the various proton sites are similar upon encapsulation. However, the range of T_1 times is greater for encapsulated [bmim]CH_3SO_3. In the neat form, [bmim]CH_3SO_3 displays restricted mobility compared to [bmim]OTf due to [bmim]CH_3SO_3 being solid at room temperature.

With decreasing loading level a similar trend is observed to that of [bmim]OTf indicating that with decreasing loading there is a decrease in mobility of [bmim]CH_3SO_3. T_1 relaxation times were also measured with varying temperature.

Figures 4.26 and 4.27 show ^1H T_1 relaxation time *vs* temperature for neat [bmim]CH_3SO_3 and loaded [bmim]CH_3SO_3 (BM-SBA-1 and BM-SBA-3) respectively. Spectra (**Figure 4.15**) were recorded by cooling from room temperature to 243 K

and heating at 10 K intervals to 363 K. This heating cycle was chosen in order to probe mobility of ion pairs in the environment they adopt upon impregnation.

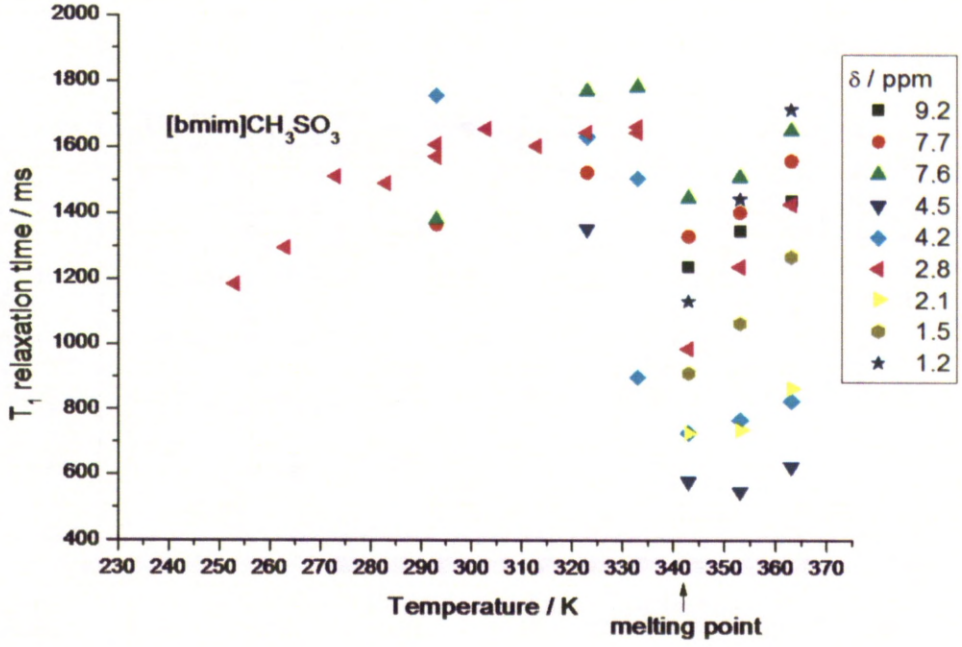

Figure 4.26 ^{1}H T_1 relaxation times *vs* temperature for neat [bmim]CH_3SO_3

The T_1 relaxation times for neat [bmim]CH_3SO_3 become longer with increasing temperature. Below the melting point (348 K), the resolution for the spectrum was not sufficient to measure individual proton sites so an average T_1 time for all environments is displayed in **Figure 4.26**. As temperature increases, T_1 relaxation time also increases as expected for fluid-like mobility.

Above the melting point of the neat [bmim]CH_3SO_3, the resolution of the spectra improved and T_1 times could be measured for each site. The spread of ^{1}H T_1 relaxation times observed at 343 K is close to the melting point observed in the DSC. The increase range in T_1 times and a significant decrease of linewidths happens simultaneously as expected when recording a spectrum of a liquid versus a solid sample, providing further proof of a melting point transition.

So how can a solid have fluid like motion? As previously described, T_1 relaxation is a measure of reorientational motions. In the case of neat [bmim]CH_3SO_3, dipolar coupling is strong however, the ion pairs have fast

reorientational motion. This has previously been observed for amorphous pharmaceuticals.[319-323]

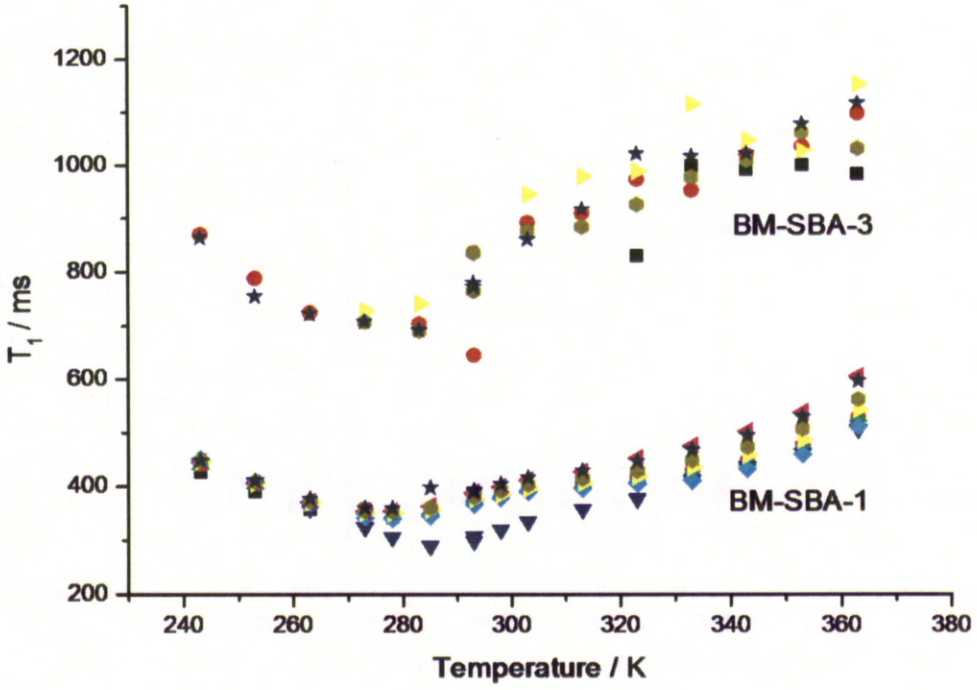

Figure 4.27 ^{1}H T_1 relaxation times *vs* temperature for BM-SBA-1 and BM-SBA-3

Comparing the range of T_1 relaxation times above the melting point of neat [bmim]CH_3SO_3 (**Figure 4.26**), the encapsulated samples show little deviation from the trend observed below the melting point. A distinct change in the range of T_1 relaxation times is not evident indicative of no change in the phase at the melting point of free [bmim]CH_3SO_3 however a slight inflection is observed. These observations are consistent with the PXRD data and DSC thermographs in which the absence of a phase change is also observed.

For SBA-15 encapsulated samples, both curves display a minimum T_1 time at room temperature. This means when recording T_1 relaxation times *vs* loading, we are at an interface between the regions where $1>> \omega_0^2\tau_C^2$ and $1<< \omega_0^2\tau_C^2$, similar to the SBA-15 encapsulated [bmim]OTf samples. These regions correspond respectively to fast and slow reorientational molecular motions respectively.[283]

When comparing the T_1 relaxation times *vs* temperature for the encapsulated (**Figure 4.27**) and free [bmim]CH_3SO_3 (**Figure 4.26**), there are

significant differences in the appearance of the curves. Firstly, the shape of the curve changes upon encapsulation. The resolution of the spectra for the encapsulated samples is improved allowing more accurate measurement of the T_1 times for specific sites. These curves display a minimum that is absent in the plot for neat [bmim]CH_3SO_3.

BM-SBA-1 and BM-SBA-3 follow a similar trend in T_1 relaxation times with changing temperature as in both cases the ionic liquid is encapsulated inside a pore causing motional restriction in comparison to the neat form. The T_1 minimum in both systems is approximately at room temperature. However, overall the T_1 relaxation times for BM-SBA-3 (less [bmim]CH_3SO_3 in the pore) are longer (by *ca.* 400 ms). Most probably this increase in relaxation time observed for BM-SBA-3 is due to surface confined ion pairs being the main contributor to the relaxation time measurement. In BM-SBA-1, in which there is significant confined bulk ionic liquid within the pores, this is the dominant contributor to the relaxation time. As the confined phase interacts less strongly with the pore surface, the reorientational motions increase to give, overall, shorter relaxation times. Both BM-SBA-1 and 3 show a steady increase in T_1 time above room temperature indicating the presence of an increasingly mobile system at higher temperatures without the obvious phase change observed for the neat [bmim]CH_3SO_3.

As observed in SBA-15 loaded [bmim]OTf, at higher temperatures T_1 relaxation times for individual proton environment become increasingly different however the spread of T_1 times is much smaller than that of neat [bmim]CH_3SO_3 at the melting point. This is in support of the idea that confined bulk [bmim]CH_3SO_3 is the dominant phase contributing to the T_1 times measured as if this was not the case we would see a spread of T_1 times.

By way of comparison, T_1 relaxation times were recorded for BM-MCM-1. In this case a minimum is observed at *ca.* 273 K. As in the SBA-15 systems, this indicates that motion is restricted in comparison to [neat [bmim]CH_3SO_3. However, the spread of T_1 times is much larger than in the SBA-15 systems and, at the melting point of the neat ionic liquid, the spread increases. The reasons for this could be that some ionic liquid is contained within the pores of MCM-41, interacting with the support surface and therefore causes a decrease in reorientational motion. The overall increase in the spread of T_1 times could be due to the range of

environments that the ionic liquid is in, *i.e.* surface confined, confined bulk and ionic liquid on the external surface of MCM-41 are contributing to the relaxation time.

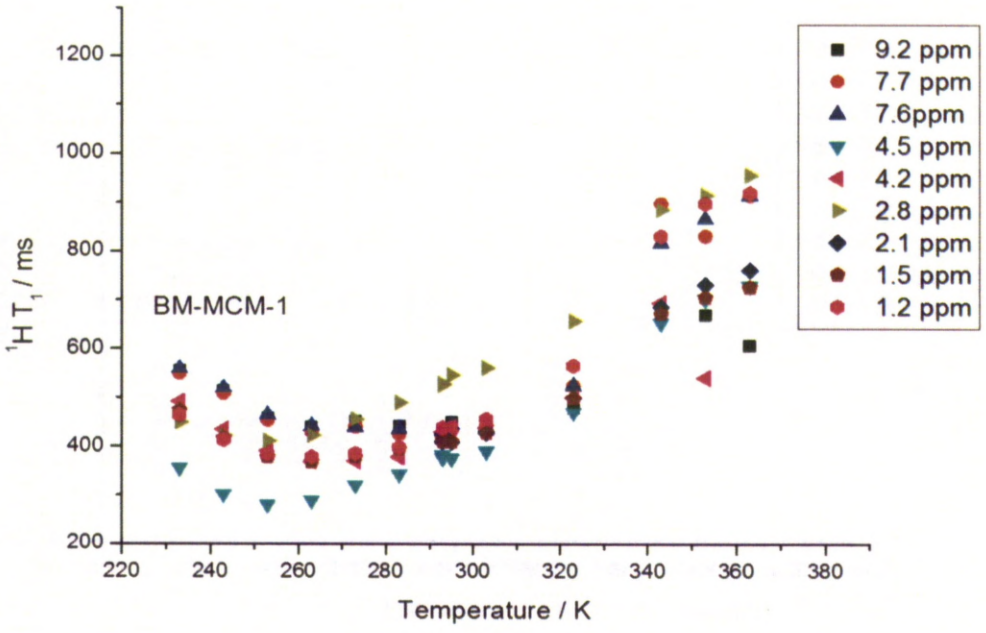

Figure 4.28 ^{1}H T_1 *vs* temperature plot for BM-MCM-1

In summary, ^{1}H line width analysis and T_1 relaxation times suggest that upon encapsulation ^{1}H-^{1}H dipolar couplings are reduced compared to the neat form. The neat ionic liquid displays distinct change in line width and T_1 relaxation times upon melting. The broad lines exhibited by neat [bmim]CH_3SO_3 below the melting point are attributed to strong dipolar couplings and efficient ^{1}H-^{1}H spin diffusion between ion pairs. Upon encapsulation, the symmetry of the system increases and due to the nature of the needle like crystal growth along the mesopores channels. The reduced number of ionic liquid pairs present across the width of the pore causes a disruption of the strong ^{1}H-^{1}H dipolar coupling present in neat [bmim]CH_3SO_3.

Although the melting point of confined [bmim]CH_3SO_3 is elevated, implying stronger interactions between the ion pair and the pore wall, the ion pairs also have increased local mobility giving rise to narrower resonances and lower T_1

relaxation times than neat [bmim]CH_3SO_3. As loading level decrease, T_1 relaxation times become longer. This is because mobility on different timescales is affected differently by encapsulation as the contributing proton environments are located in close proximity to the pore wall. Due to the nature of the strong H-bonding interactions between the silica surface and the ion pair, mobility is decreased.

4.4.2.2 ^{13}C MAS NMR spectra

^{1}H-^{13}C CP-MAS NMR spectra have been shown previously for neat [bmim]CH_3SO_3, BM-SBA-1 and 2 in **Section 4.4.1.3**. **Figures 4.29** and **4.30** display ^{1}H-^{13}C CP-MAS NMR spectra and ^{13}C {^{1}H} MAS NMR spectra for BM-SBA-1 to 4, respectively.

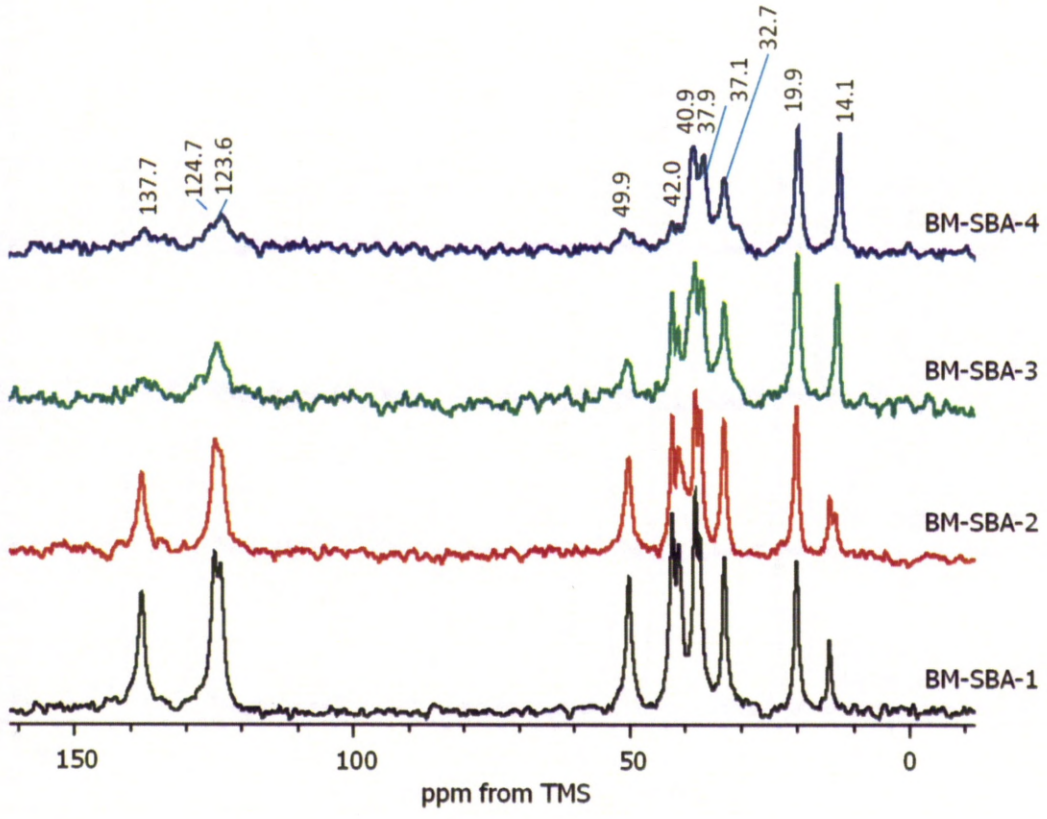

Figure 4.29 ^{1}H-^{13}C CP-MAS NMR spectra of BM-SBA-1, 2, 3 and 4 (MAS = 10 kHz)

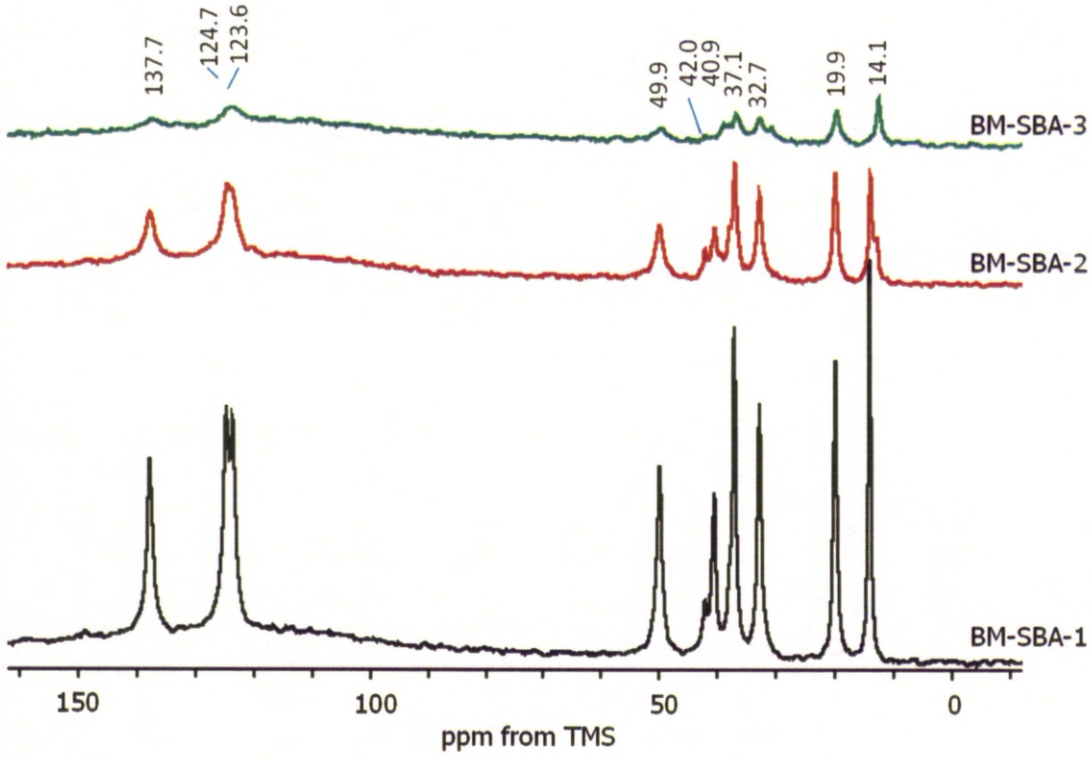

Figure 4.30 ^{13}C {^{1}H} MAS NMR spectra of BM-SBA-1, 2 and 3 (MAS = 10 kHz)

^{1}H-^{13}C CP-MAS NMR spectra of BM-SBA-1 to 4 show a decreasing intensity with decreasing loading of [bmim]CH_3SO_3. In the previous chapter, [bmim]OTf displayed the similar intensities in the CP spectra for all loading levels due to only the surface confined layer being immobile enough to be detectable by CP. The decreasing intensity in this system is to be expected as both surface confined and confined bulk [bmim]CH_3SO_3 are solid. BM-SBA-1 contains resonances attributable to both surface confined layer and confined bulk [bmim]CH_3SO_3. As loading decreases, only the surface confined layer contributes to the observed resonances (BM-SBA-4). **Figure 4.29** and **4.30** show slight changes in chemical shift for a number of sites. The most noticeable is that of the C(9), terminal methyl. The change in chemical shift is most likely due to deviations in the conformation of the aliphatic chain as a consequence of loading level.[242] At low loading (BM-SBA-4), the resonances are attributed to the surface confined layer of ionic liquid. In this case, a lower chemical shift is observed for C(9). This is analogous to the change in chemical shift observed for different conformations of aliphatic chains in organic surfactants used to template aluminophosphate materials.[242] In a trans

conformation, the aliphatic chain is less mobile and observed at *ca.* 33.0 ppm. In gauche conformation the aliphatic chain is more mobile and observed at *ca.* 31.0 ppm. As loading increases, there is an increased contribution to the chemical shift and lineshape from the confined bulk ionic liquid and a shift to a slightly higher chemical shift is observed (as seen is BM-SBA-1, corresponding to a trans dominated effect). The CP spectrum for BM-SBA-2 shows the peak at *ca.* 14.1 ppm to be split. This can be explained by both the surface confined and confined bulk ionic liquid being observed, analogous to both a gauche and trans phase being present in the surfactant templating aluminophosphates. Upon pore flooding, the dominate contribution to the resonance position is from the bulk confined ionic liquid and therefore a single resonance is observed at a chemical shift that corresponds to C(9) in the conformation it is holds in the confined bulk. The intensity of these peaks should also be mentioned. Note that as loading is increased, the intensity of surface confined layer C(9) decreases and the confined bulk C(9) increases however, the peak at *ca.* 14.1 ppm in BM-SBA-1 is not as intense as the peak at *ca.* 13.8 ppm. Since CP depends on ^{1}H-^{13}C dipolar coupling, which is strong for more rigid solids, the intensity of the resonances corresponding to the surface confined layer are expected to be more intense. As shown by ^{1}H T_1 analysis, samples with the lower loading have a stronger contribution from the surface confined layer, which, due to motional restriction, have increased ^{1}H-^{1}H dipolar coupling in comparison to the confined bulk material.

The line shape of both the CP and ^{13}C $\{^{1}H\}$ NMR spectra are similar and, analogous to the SBA-15 confined [bmim]OTf system, contain a broad and narrow component. The reason for this is again due to a more surface confined monolayer and confined bulk. However both these components are observed in the CP spectrum for [bmim]CH_3SO_3 based materials because the ionic liquid in this system is a solid. In the $^{13}C\{^{1}H\}$ MAS NMR spectra, as loading increases, the intensity of the peaks also increases. The spectrum for BM-SBA-1 contains contributions from both a surface confined and the more mobile confined bulk layer whereas in the spectrum for BM-SBA-3, the surface confined layer is predominantly responsible for the observed peaks. The peaks in the spectrum of BM-SBA-3 are also much broader than the peaks in BM-SBA-1. However, a broad and narrow component is observed in the spectrum of material with higher loading of [bmim]CH_3SO_3. The narrow component here is due to the confined bulk [bmim]CH_3SO_3, although, since

this is still solid, the linewidth is still much broader than that observed for the $^{13}C\{^{1}H\}$ MAS NMR spectrum of B-SBA-1.

As mentioned in the previous section, splitting is also observed for the N-methyl C(10) and anion C(11), which is not present in spectra of neat [bmim]CH_3SO_3. This splitting is observed at all loading levels for the SBA-15 system, in both the CP and $\{^{1}H\}$ spectra and for all methods of loading (**Figure 4.31**). As the loading level decreases the intensity of the splitting also changes. This again can be observed more clearly in **Figure 4.32.**

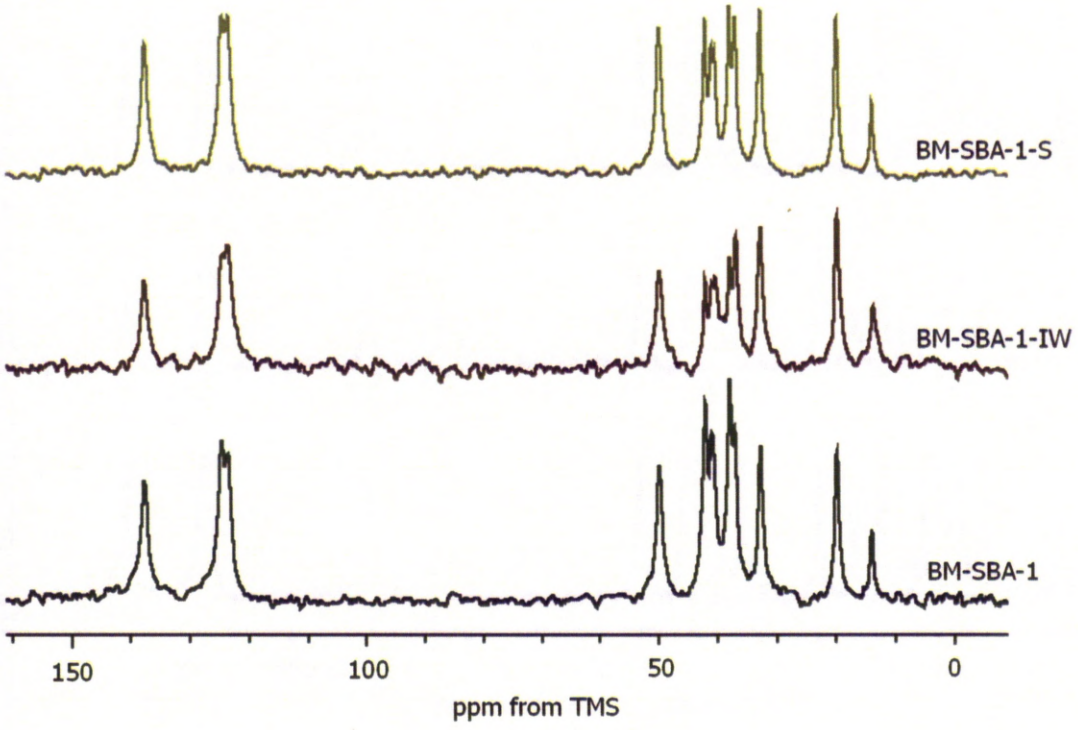

Figure 4.31 ^{1}H-^{13}C CP-MAS NMR spectra of BM-SBA-1, BM-SBA-1-IW and BM-SBA-1-S (MAS = 10 kHz)

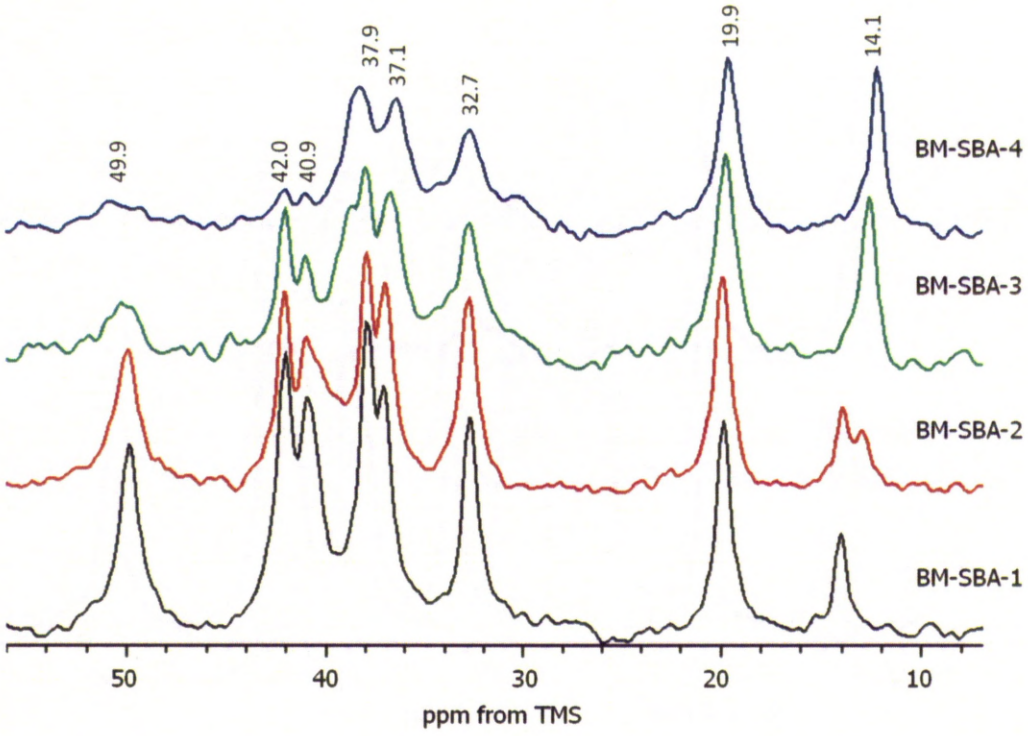

Figure 4.32 ^{1}H-^{13}C CP-MAS NMR spectra of BM-SBA-1, 2, 3 and 4 expanded to show splitting

Resonances corresponding to C(10) and C(11) are split at all loading levels, however, as loading is decreased, a third component moves from *ca.* 41 ppm in BM-SBA-2 to *ca.* 38 ppm in BM-SBA-3 and then broadens the resonance at 37.9 ppm in the spectra of BM-SBA-4.

The origin of this splitting could be due to a number of reasons related to the mobility and orientation of the ion pairs within the mesopores. As described in the interpretation of ^{1}H T_1 relaxation data, the orientation of the ionic liquid with respect to the pore surface could mean that in the monolayer (low loading BM-SBA-4), C(10), C(11) and C(9) have greater mobility as they point into the pore. As loading increases, the amount of confined bulk material increases, which will overall have a greater mobility than ion pairs that are surface confined. This would explain why we see a splitting of resonances at high loading, one for the surface confined bilayers (at a higher chemical shift) and one for confined bulk material (at lower chemical shift). The splitting could also be a result of polymorphic modifications that result in non-equivalent sites from different organisation of ion pairs within the

pores. To further investigate the nature of this splitting, CP dynamics has been used and is detailed in **Section 4.4.2.3**.

It can be observed in the $^{13}C\{^{1}H\}$ MAS NMR that the splitting is less obvious than in the CP spectra. The most intense peaks (42.0 (C(11) anion) and 37.9 ppm (C(10) N-methyl)) in the CP spectra are of very low intensity in the $^{13}C\{^{1}H\}$ NMR spectra. This fits with the hypothesis that this splitting is caused by C(9), C(10) and C(11) present in a bilayer, close to the surface if the pore and a confined bulk layer. Although this does not explain why all other peaks remain unsplit and at the same chemical shift at all loading levels. The other peaks could simply be averaged out and be a characteristic feature of the sample.

The changes in chemical shift of the peaks at *ca.* 41-38 ppm and 14.1 ppm could be due to a different reason. To this end, ^{13}C NMR spectra have been recorded at variable temperature to investigate the possibility of chemical exchange between confined bulk and surface confined layers. This is detailed in **Section 4.4.2.4.**

4.4.2.3 ^{1}H-^{13}C CP dynamics

^{1}H-^{13}C CP dynamics has been used to rationalise the components of the split peaks present for N-methyl C(10) at *ca.* 37 ppm and anion C(11) at *ca.* 41 ppm as well as provide the assessment of local mobility. Variable contact time experiments were recorded for neat [bmim]CH_3SO_3 and BM-SBA-1, which contains both the components predicted to arise from the bilayer (less mobile) and the confined bulk (more mobile) (**Figures 4.33** and **4.34, Tables 4.3** and **4.4**). Here we are investigating motions that are on a kHz time scale such as reorientation of segments and ion pair clusters whereas ^{1}H relaxation investigated the mobility of individual chains within the ion pair.

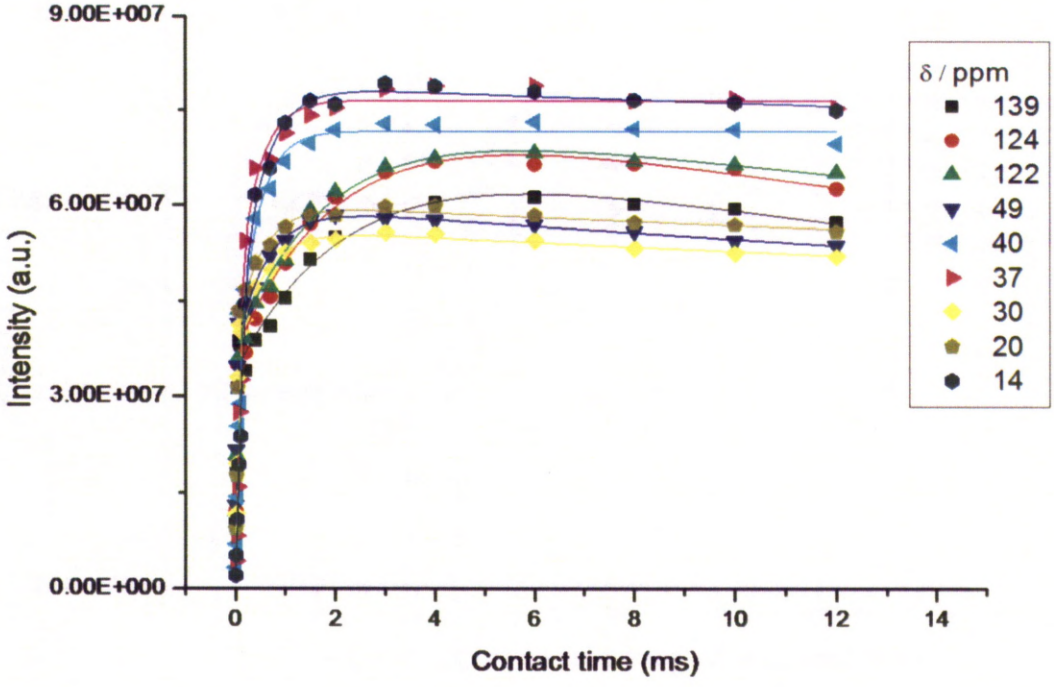

Figure 4.33 ^{1}H-^{13}C CP dynamics curves for neat [bmim]CH_3SO_3

Table 4.3 ^{1}H-^{13}C CP dynamics for [bmim]CH_3SO_3

^{13}C site	ppm	Fitting model	T_{df} / ms	λ	$T_{1\rho}^{H}$ / ms	T_2 / ms	R^2
C(2) ring N-CH-N	137.7	II*S	2.38 ± 0.87	0.533 ± 0.061	>50.0	0.016 ± 0.001	0.979
C(4) ring N-CH	124.7	II*S	2.19 ± 0.79	0.530 ± 0.058	>50.0	0.015 ± 0.001	0.975
C(5) ring N-CH	123.6	II*S	1.95 ± 0.59	0.498 ± 0.046	>50.0	0.015 ± 0.001	0.981
C(6) chain N-CH_2	49.9	II*S	0.610 ± 0.131	0.389 ± 0.024	>50.0	0.015 ± 0.001	0.983
C(11) anion S-CH_3	40.9	II*S	0.395 ± 0.062	0.593 ± 0.073	>50.0	0.0665 ± 0.009	0.995
C(10) N-CH_3	37.1	II*S	0.408 ± 0.095	0.463 ± 0.092	>50.0	0.079 ± 0.010	0.992
C(7) chain CH_2	32.7	II*S	0.545 ± 0.141	0.353 ± 0.028	>50.0	0.017 ± 0.001	0.981
C(8) chain CH_2	19.9	II*S	0.511 ± 0.126	0.340 ± 0.028	>50.0	0.022±0.001	0.987
C(9) chain CH_3	14.1	II*S	0.497 ± 0.074	0.540 ± 0.072	>50.0	0.121 ± 0.014	0.997

The CP dynamics curves for carbons in neat [bmim]CH_3SO_3 have all been fitted using the II*S model (described in **Section 2.5.2.4**). All carbon sites display long relaxation times ($T_{1\rho}^{H}$>50.0 ms) in agreement with the ^{1}H T_1 relaxation times measured for neat [bmim]CH_3SO_3 as they too also display liquid like mobilities. The

similarity in ^{1}H times can be attributed to a uniform ^{1}H-^{1}H dipolar coupling network present in the neat RTIL.

CP build up times reflected in the spin-diffusion time constant (T_{df}) are quite fast as expected for a system that has strong dipolar coupling present however, the relaxation of the spins is long indicating a high mobility. The relaxation times are longer for ring carbons than carbons located in the butyl chain, N-methyl and anion. This is to be expected due to the motional restriction of carbons located in the ring in comparison to the flexible butyl chain.

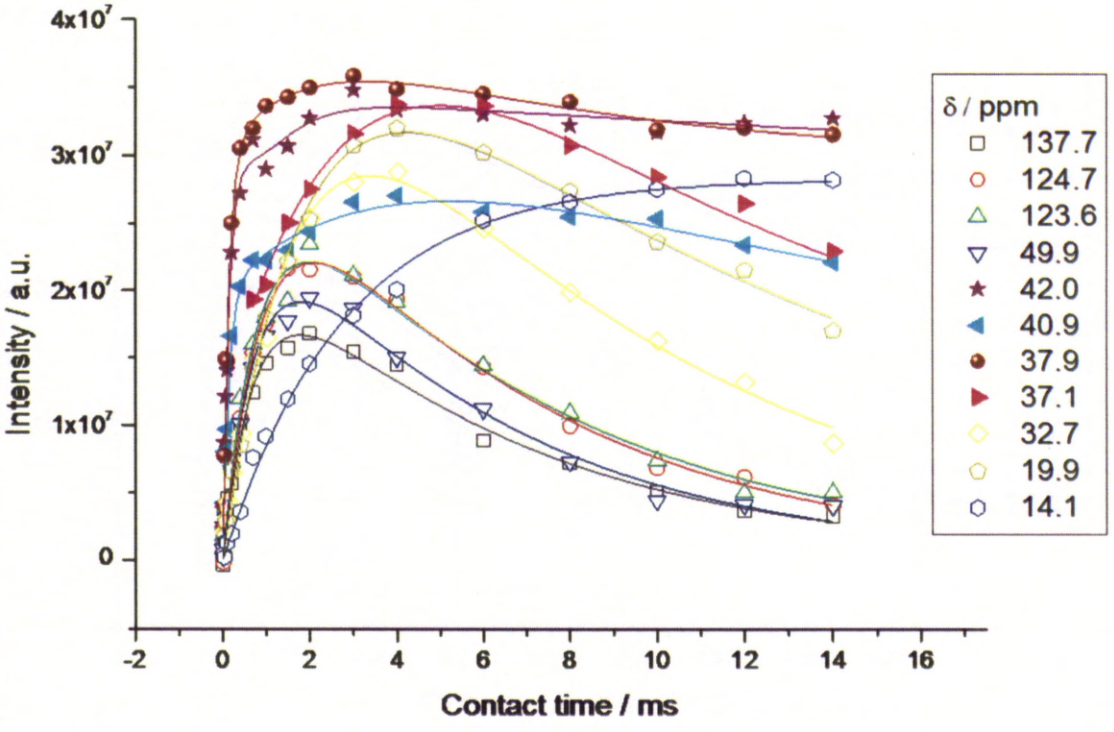

Figure 4.34 ^{1}H-^{13}C CP dynamics curves for BM-SBA-1

Table 4.41H-13C CP dynamics for BM-SBA-1

^{13}C site	ppm	Fitting model	T_{IS} / ms	$T_{1\rho}{}^{H}$ / ms	R^2
ring N-CH-N	137.7	I-S	0.718 ±0.070	6.506 ± 0.521	0.984
ring N-CH	124.7	I-S	0.911 ±0.056	6.525 ± 0.337	0.994
ring N-CH	123.6	I-S	0.808 ±0.088	7.066 ± 0.644	0.974
chain N-CH_2	49.9	I-S	0.762 ±0.073	6.040 ± 0.477	0.982
anion S-CH_3	42.0	Two component IS	0.158 ±0.042	0.503 ±0.042	0.993
			0.755 ±0.043	>50.0	
anion S-CH_3	40.9	Two component IS	0.138 ±0.010	29.09 ±6.39	0.991
			2.529 ±0.356	>50.0	
N-CH_3	37.9	Two component IS	0.147 ±0.062	0.433 ±0.187	0.993
			0.632 ±0.033	>50.0	
N-CH_3	37.1	IS	1.31 ±0.153	26.2 ±5.21	
chain CH_2	32.7	I-S	1.70 ±0.186	8.19 ±0.883	0.984
chain CH_2	19.9	I-S	1.79 ±0.144	13.8 ±1.41	0.993
chain CH_3	14.1	No relaxation	2.82 ±0.107		0.997

In the encapsulated sample BM-SBA-1, the contributions to the observed build up and relaxation times is from the surface confined layer and confined bulk [bmim]CH_3SO_3 inside the pores. Overall, the CP build-up times for BM-SBA-1 are faster for ring carbons than in neat [bmim]CH_3SO_3 and have shorter relaxation times. This can be attributed to restricted motion of these carbon sites. On the other hand, chain carbons have faster CP build-up times in neat [bmim]CH_3SO_3, due to direct ^{1}H-^{13}C transfer, but have long relaxation times. This is due to the chain being more flexible. In addition this effect could be explained by limited number of ionic liquids species contained within the pore causing a reduction in the spin diffusion term and a decrease in ^{1}H-^{1}H dipolar coupling. In the encapsulated

materials, the differences in the relaxation times are more prominent than in neat [bmim]CH_3SO_3 due to the effects of confinement.

The peaks for the anion and N-methyl that display splitting in the ^{13}C MAS NMR spectra in the encapsulated samples show differences in CP dynamics. The peaks for the anion at 42.0 and 40.9 ppm both have a fast and slow component contributing to their dynamics. The build up and relaxation are faster for the peak at 40.9 ppm. The two component fit required for these curves may be due to a surface confined and bulk layer. On the other hand, there could be a difference in conformation of the anion in the surface confined layer (which would give rise to a less mobile species, *i.e.* the peak at 40.9 ppm) and the confined bulk (a more mobile species due to less interaction with the surface, *i.e.* the peak at 42.0 ppm). As the confined bulk layer is more dominant in BM-SBA-1, the ^{13}C $\{^1H\}$ MAS NMR spectrum would show the more mobile site at 42.0 ppm at a greater intensity, which it is not. Therefore, it is interpreted that the surface and bulk ionic liquid contribute to both peaks and the splitting is due to different conformations within the pore.

The splitting of the N-methyl peak at 37.9 and 37.1 ppm follows a similar trend. Both peaks have a fast and slow component, however, looking at the curves, the build-up and relaxation is faster for the peak at 37.1 ppm. The origin of these splittings is difficult to rationalise any further and are most probably due to different, non-equivalent environments being present.

If the splitting is due to a surface confined and confined bulk environment, it may be possible that chemical exchange may take place or that changing the temperature will change the rate of reorientational motion for one environment more than the other. To investigate, ^{13}C CP and $\{^1H\}$ MAS NMR were recorded at different temperatures.

4.4.2.4 ^{13}C MAS NMR with varying temperature

The variable temperature ^{13}C CP and $\{^1H\}$ MAS NMR spectra for BM-SBA-1 are displayed in **Figures 4.35** and **4.36** respectively. The first point to note in this system is that there is a negligible change in chemical shift for all resonances

indicating that no chemical exchange is taking place. With respect to the anion and N-methyl peaks, as temperature increases the peaks do not coalesce, confirming that the environments for these species are not in exchange. However, at 363 K, the $^{13}C\{^{1}H\}$ spectra shows N-methyl peaks at *ca.* 37.5 ppm do broaden to the extent where the upfield peak appears as a shoulder to the peak at 37.1 ppm (**Figure 4.36**). This could be indicative of an approach to melting point, however, as yet the melting point is unknown. Contrary to this observation, the splitting is still present in the CP spectra with no change in relative peak intensities, confirming that the system is not in exchange, nor approaching the melting point of the encapsulated ionic liquid.

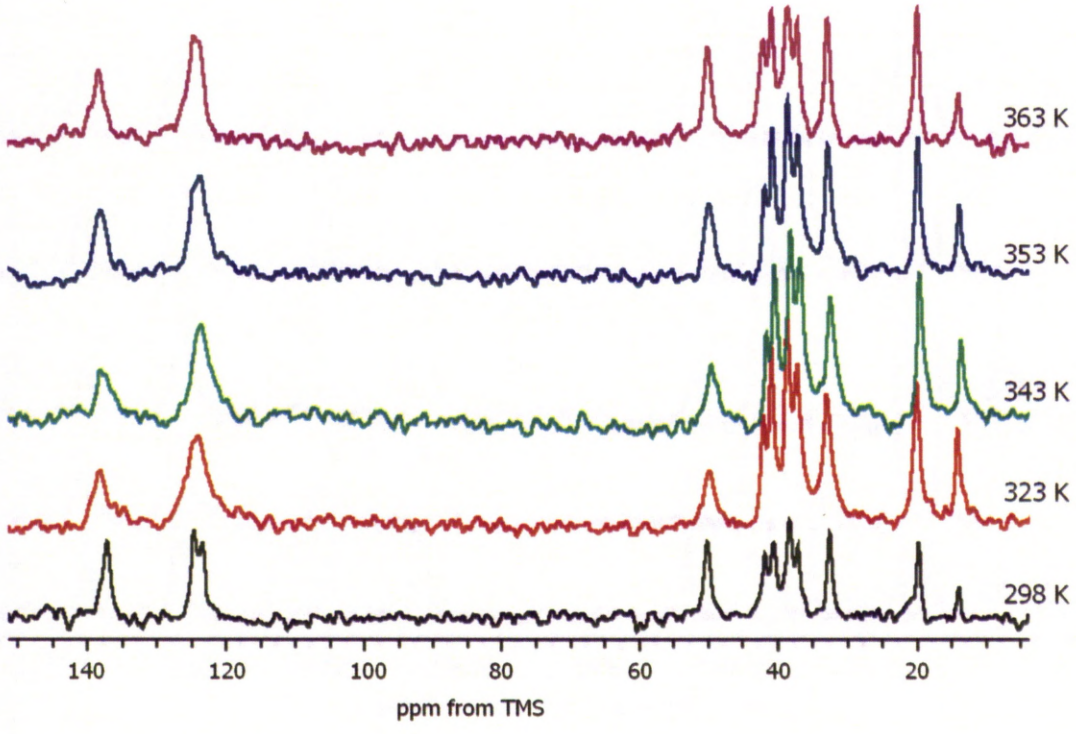

Figure 4.35 ^{1}H-^{13}C CP MAS NMR spectra of BM-SBA-1 with varying temperature

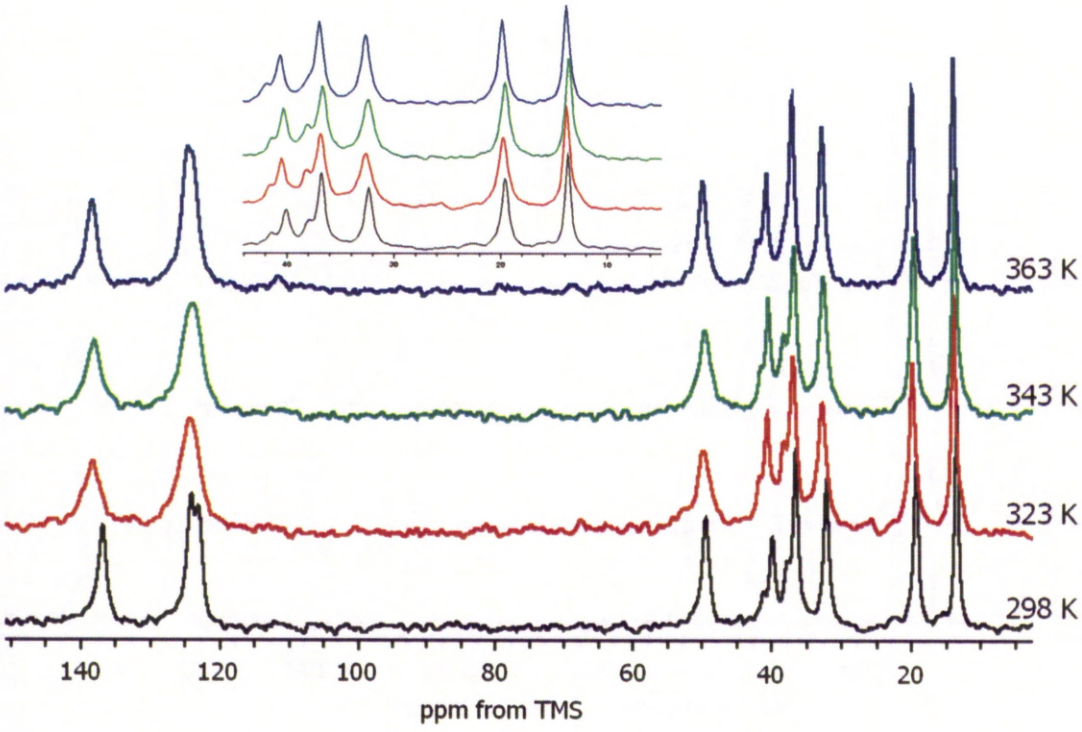

Figure 4.36 ^{13}C {^{1}H} MAS NMR spectra of BM-SBA-1 with varying temperature

The aromatic peaks at *ca.* 137.7 ppm become broader as temperature increases due to the ring becoming more mobile causing C(4) and C(5) to exchange. As temperature increases the resonance coalesce into one peak positioned at a chemical shift in the middle of the two resonances that are observed in the low temperature spectrum. Due to the complexity of this system it is difficult to rationalise this exchange further.

4.4.3 ^{1}H-^{29}Si hetronuclear correlation NMR spectroscopy

^{1}H-^{29}Si HETCOR NMR spectra were recorded for BM-SBA-1 and BM-SBA-4 to identify which proton environment within [bmim]CH_3SO_3 are in close proximity to the pore wall of SBA-15. The spectra shown in **Figures 4.37 a** and **b**, respectively show similar correlations to those of [bmim]OTf encapsulated in SBA-15 and indicate that the butyl chain and N-methyl are again in closest proximity to the pore wall and interact with the surface hydroxyls (indicated by Q^3 site in the ^{29}Si dimension) more strongly.

a)

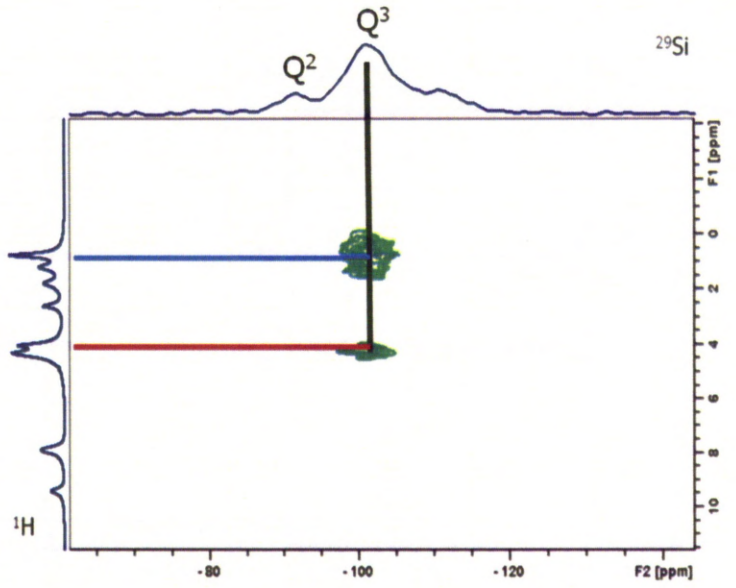

b)

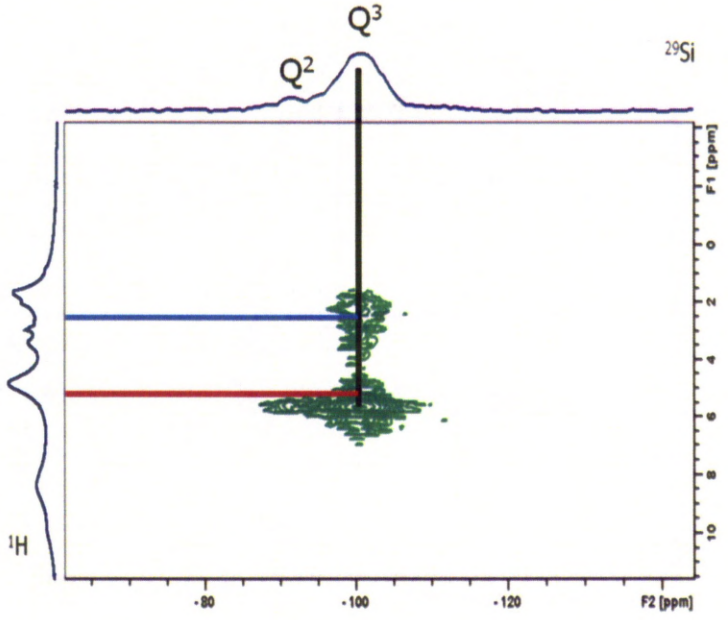

Figure 4.37 ^{1}H-^{29}Si HETCOR of **a**) BM-SBA-1 and **b**) BM-SBA-4 (MAS = 4 kHz)

In combination with the ^{13}C and ^{1}H NMR spectra and the analysis of mobility, it would be expected that the imidazole ring would interact more strongly with the surface. However, it may be that ion pairs next to one another alternate their

orientation to allow the butyl chain to protrude into the pore in one case and the N-methyl of the neighbouring pair to protrude into the pore in the next. Without further analysis this cannot unambiguously be determined.

4.5 Conclusions and outlook

In summary, PXRD of [bmim]CH_3SO_3 loaded into SBA-15 show that there is an increase in long range ordering of [bmim]CH_3SO_3 that can be indexed to an orthorhombic phase. [bmim]CH_3SO_3 present in the mesopores of SBA-15 displays this phase for all loading levels and methods of loading and is induced by surface interaction between the silica pore wall and [bmim]CH_3SO_3. This is evidenced by the loss of some peaks in the PXRD patterns and decreasing pore volume, surface area and size displayed by N_2 isotherms. ^1H MAS NMR is also in support of these observations through the differences in linewidth and T_1 relaxation times of neat and encapsulated [bmim]CH_3SO_3. Therefore nucleation of the orthorhombic phase occurs in the mesopores of SBA-15.

^1H MAS NMR spectra shows an increase in resolution upon loading into SBA-15 compared to that of the neat ionic liquid. Upon decreasing the loading from pore flooding to approximate monolayer coverage, lines broaden similarly to [bmim]OTf. This could be due to a solid and liquid phase being present, however, if this was the case we would observe much narrower resonances in the NMR spectra as well as longer relaxation times in ^{13}C CP kinetics experiments. The PXRD patterns would also not show an increasing intensity of peaks with increasing loading of [bmim]CH_3SO_3. A more likely explanation of line narrowing in the ^1H MAS NMR spectra of BM-SBA- samples is that encapsulation leads to the disruption in ^1H-^1H dipolar coupling network and/or increased mobility.

^1H-^{29}Si HETCOR spectra are similar to those observed for [bmim]OTf loaded SBA-15 and indicate that the butyl chain and N-methyl sites interact more closely with this pore surface. This result however is counterintuitive to the interpretation of amore restricted ring environment indicated by measurement of the CP dynamics. In order to further characterise this system, molecular modelling, analogous to that performed for the [bmim]OTf system could go some way in explaining the orientation of the [bmim]CH_3SO_3 ion pair with respect to the pore wall. The

hypothesis of having alternating ion pairs around the pore surface could also be investigated further by measurement of NOESY NMR spectra to determine the distance between ^{1}H environments. This, however, has been problematic in the past due to different levels of ^{1}H-^{1}H spin diffusion.

The two encapsulated ionic liquid systems described in Chapters 3 and 4 have opened potential for many further investigations. Molecular modelling has provided a useful tool no only to observe the behaviour of IL guests but could also be used to predict new polymorphs, one of which has been identified experimentally for [bmim]CH_3SO_3. Does altering the host material alter the crystal structure of the IL? Does this only happen in silica based hosts? Can the polymorph be observed outside the silica mesopore? What applications do the new physical properties allow? These questions are some of those that I am hopeful will be answered in the future.

Section II

Chapter 5

High Pressure and MAS NMR Studies of Semi-Clathrate Hydrates for Methane Storage

This work has been published in Chemistry of Materials as "Reversible Methane Storage in a Polymer-Supported Semi-Clathrate Hydrate at Ambient Temperature and Pressure" Weixing Wang, Benjamin O. Carter, Christopher L. Bray, John Bacsa, Alexander Steiner, James T.A. Jones, Catherine Cropper, Yaroslav Z. Khimyak, Dave J. Adams and Andrew I. Copper, *Chemistry of Materials*, 2009, 21, 3810-3815

5.1 Introduction to clathrate hydrates

Efficient storage of gases such as hydrogen and methane has become an important challenge for scientists in the development of a hydrogen economy. Storage of gases at ambient temperatures and pressures is desirable in order for transportation and release at the point of delivery to be a low energy process that does not require any complex containment.

Clathrate hydrates are naturally occurring inclusion compounds in which a lattice of water molecules houses molecules of a trapped gas. Clathrate hydrates exist in permafrost formations and under the sea-bed in oceans and contain large amounts of methane (10^{15} to 10^{17} m^3 globally). Naturally occurring clathrate hydrates have also been found to contain other gaseous guests such as H_2S and CO_2. The polyhedral network of water cages are held together by hydrogen bonding and may offer a safe and environmentally friendly method of gas storage. Although clathrates are naturally occurring and have been well studied, there are three main challenges to be addressed before practical applications can be achieved: the relatively low gas storage capacity (particularly in comparison to metal organic frameworks (MOFs) for which uptake of hydrogen can be up to 7.5 %wt);[324] the high pressures required for clathrate formation and stabilization; and the slow kinetics associated with gas enclathration.

Common methods for increasing clathrate formation kinetics include grinding and sieving ice particles to increase the surface area,[325] addition of surfactants,[326] or dispersing the water phase over silica.[327-328] Cooper *et al.* in recent work have shown that it is possible to significantly enhance the rate of uptake of hydrogen by dispersing THF-stabilized clathrates on porous, emulsion-templated polymers.[329] This method was also applied to the storage of methane with little success.

Another approach that was taken by the same group was to disperse a THF-stabilized clathrate on a poly(acrylic acid) sodium salt (PSA).[330] In this investigation, PSA, a swellable polymer used in sanitary products (such as diapers) was used to support the clathrate system and the uptake kinetics of H_2 was measured by high pressure NMR spectroscopy. The effect of clathration on the support material was also monitored by high resolution magic angle spinning NMR spectroscopy (**Appendix I**).

"Dry water", a blend of clathrate hydrate and silica, has been reported by Cooper's group to display better uptake rates of methane into a methane gas hydrate. The "dry water" system is reported to adsorb methane in the absence of mixing. However, droplet destabilization over a number of charge-discharge cycles necessitates re-mixing of the dry water for effective re-use.[331]

As research in the area of gas storage in clathrates continues, the focus of the Cooper group has turned to methane storage in semi-clathrate hydrates. Semi-clathrate hydrates share many of the structural and physical properties of true clathrates. The semi-clathrate hydrates of quaternary ammonium salts such as tetra-n-butylammonium bromide (TBAB), tetra-*n*-butylammonium fluoride (TBAF), and tetra-iso-amylammonium bromide (TiAAB) are stable to temperatures above 273 K allowing transport at ambient temperature with no need for refrigeration.[332-334] The cation of these salts is situated within framework cavities while the anion occupies sites in the hydrogen-bonded framework. Semi-clathrate hydrates of TBAB and TBAF have been shown to trap H_2 in two small, unoccupied lattice cavities.[335-336] These materials are significantly more stable than other H_2 hydrates, with H_2-TBAF hydrates melting at around 302 K.

5.1.1 Characterisation of clathrate systems by NMR spectroscopy

NMR spectroscopy provides a variety of techniques that are useful for characterisation of clathrate structures and intercalated gas molecules. The literature documents a variety of these techniques including: ^{1}H MAS NMR spectroscopy to study the structural transformations of ionic clathrates upon inclusion of co-host molecules (NH_3, THF and $(CH_4)_4NOH$);[337] monitoring changes in chemical shift in ^{13}C NMR spectra of propane molecules encaged in structure II clathrate hydrates;[338] and ^{23}Na, ^{1}H and ^{29}Si NMR spectra to confirm the presence of both sodium and hydrogen in a type I clathrate hydrate.[324]

Neiner *et al.*[324] report a sodium-deficient type I silicon clathrate structure containing two types of polyhedral cavities. Both cavities contain sodium as shown by two resonances in the ^{23}Na MAS NMR spectrum. ^{29}Si MAS NMR is also reported and contains isotropic chemical shifts assigned to three silicon crystallographic sites. ^{1}H MAS NMR spectra was recorded for the system charged with H_2. Unlike previous

work on H_2 storage in type II THF.H_2O clathrate hydrates,[325,330,339] which display two resonances attributed to hydrogen in two small cages, the ^1H MAS NMR spectra for the silicon clathrate is much more complicated. Neiner and co-workers observe sharp and broad resonances. The narrow resonances are consistent with H_2 that can freely rotate, analogous to our work documented in **Appendix I.** The broad resonance is attributed to hydrogen that has more restricted motion and may be interacting with the cages.

In this study, the structure, kinetics, and methane storage behaviour of a polymer-supported TiAAB semiclathrate are reported and show that methane gas can be adsorbed quickly in the absence of mixing and released on demand, albeit with relatively low storage capacities of up to 40 v/v. Solid state NMR techniques were used to observe the tetra-iso-amylammonium (TiAAB) support and presence of methane at various temperatures. By comparison of ^{13}C $\{^1H\}$ MAS NMR and ^1H-^{13}C CP-MAS NMR spectra at varying temperatures, the presence of enclathrated methane is confirmed. The ^1H-^{13}C CP-MAS NMR at ambient temperature show resonances corresponding to the TiAAB support only. By lowering the temperature to 223 K the enclathrated methane peak is observed due to the methane molecules being held in a rigid environment. The amount of methane taken up by the system was quantified by deconvolution of the ^{13}C $\{^1H\}$ MAS NMR spectrum recorded at 263 K.

5.2 Experimental

The methane used was UHP 99.999% grade, BOC Gases, Manchester, U.K. All other reagents and solvents were purchased from Sigma-Aldrich or Pfaltz and Bauer (U.K.) and used as received. The polymer support was prepared as before.[329] Tetra-iso-amylammonium bromide (TiAAB) was prepared as described previously.[340]

5.2.1 Clathrate hydrate formation (synthesis by Dr. B.O. Carter)

5.2.1.1 Clathration kinetics

Stock solutions of tetra-*iso*-amylammonium bromide with a stoichiometric composition of TiAAB·26H_2O and TiAAB·38H_2O were prepared. To carry out the gas uptake kinetic experiments, 20.0 g of a stock solution of TiAAB was loaded into a 68.0 cm^3 high pressure stainless steel cell together with the polyHIPE support (3.4 g). The temperature was controlled by a programmable thermal circulator. The temperature of the compositions in the high pressure cell was measured using a type K thermocouple. The gas pressure was monitored using a high-accuracy gauge pressure transmitter. Both thermocouple and transmitter were connected to a digital universal input panel meter), which communicates with a computer. Prior to experiments, the cell was slowly purged with methane three times at atmospheric pressure to remove any air and then pressurized to the desired pressure at the designated temperature. The temperature (T, K), pressure (P, psi), and time (t, min) were automatically interval-logged using MeterView 3.0 software. Using this setup it was possible to obtain high resolution data (for example, 2 s between individual [T, P, t] points, 120,000 data points in a 2000 min experiment).

5.2.1.2 Balloon release experiment

A 50 mL round-bottomed flask was loaded with TiAAB·26H_2O (40.0 g) semi-clathrate hydrate and polyHIPE (6.8 g). The open flask was pressurized with methane to 9 MPa at 317 K in a 600 cm^3stainless steel pressure vessel. After slowly cooling to 298 K overnight using a water bath, the vessel was vented and the flask

fitted with a balloon, before being immersed in iced water for 5 hours. After warming to room temperature, little gas was released after standing for 4 hours. The flask was then heated to 313 K, at which point all methane was released from the clathrate within 30 minutes.

5.3 Characterisation conditions

5.3.1 Crystallography (Collected by Dr. J. Basca and Dr. A. Steiner)

Crystallographic data were recorded on a Bruker Smart Apex diffractometer (T = 100 K) using Mo Kα radiation (λ = 0.71073 Å, 2θmax = 55°). Structures were refined by full-matrix least squares against F^2 using all data.[341] Powder X-ray diffraction data were collected with Cu $K\alpha_1$ radiation with a Stoe Stadi-P diffractometer in transmission geometry, using a linear position sensitive detector. Data were collected at room temperature, from 2θ = 5–40°, in 0.5° steps at 40 s/step. Samples were prepared by drawing hot (323 K) solutions of TiAAB·38H_2O and TiAAB·26H_2O into 0.5 mm bore capillaries. Each was sealed at both ends with vacuum grease before allowing the semi-clathrate solution to cool to room temperature. The samples were able to crystallize *in situ* without risk of phase transition due to loss of coordinating water.

5.3.2 Powder X-ray diffraction (Collected by Dr. J. Basca)

Powder X-ray diffraction patterns were analyzed using Stoe WinXPow v. 1.10 software. Unit cell parameters for the TiAAB·38H_2O crystal structure were used to index and refine both samples. Peaks not observed in the simulated powder pattern for TiAAB·38H_2O were eliminated before indexing and refining all remaining peak positions. The resulting unit cell parameters for both samples indicate an expected thermal expansion, on account of single-crystal XRD data collection taking place at 100 K.

5.3.3 Differential scanning calorimetry (Collected by Dr. W. Wang)

A methane-loaded TiAAB·38H_2O sample (200 mg) was prepared by cooling from 318 K to 273 K under pressure of methane (8.6 MPa). Using a Q2000 DSC instrument, a 10 mg sample was loaded at 273 K using aluminium sample and reference pans. Data were collected at a heating rate of 0.5 K/min from 272 to 318 K. For the methane-loaded samples, the material was melted at 318 K to release methane before allowing semi-clathrate to reform at 273 K. DSC data collection was then carried out as above for the vacant TiAAB·38H_2O sample.

5.3.4 Solid state NMR

Solid-state NMR spectra were acquired at 9.4 T using a Bruker DSX400 spectrometer equipped with either a 7 mm 1H/X or 4mm 1H/X/Y probeheads. Samples were spun in zirconia rotors under dry nitrogen.

5.3.4.1 Preparation of solid-state NMR samples

For solid-state NMR analysis, the semi-clathrate TiAAB·38H_2O was taken out of the 68.0 cm^3 high pressure stainless steel cell at ambient temperature and loaded immediately into a 7 mm outer diameter rotor. The rotor was fitted with a BN_3 VT cap containing a hole to prevent any pressure build-up in the event of gas loss. The rotor was then placed into a pre-cooled probe at 273 K, spun at an MAS rate of 3.2 kHz, and cooled further to 263 K. After the initial experiments at 263 and 253 K, the rotor was removed from the probe and placed in a fridge at 278 K overnight prior to experiments at 223 K.

5.3.4.2 ^{1}H-^{13}C CP-MAS and ^{13}C {^{1}H} NMR spectra recorded with varying temperature

$^{1}H-^{13}C$ variable temperature (VT) cross-polarization magic angle spinning (CP/MAS) and $^{13}C\{^{1}H\}$ NMR spectra were recorded using the 7 mm probehead at 263, 253, and 223 K. The spectra were acquired at 400.16 MHz and 100.56 MHz for ^{1}H and ^{13}C respectively, at an MAS rate 3.2 kHz. The bearing gas was cooled by passing through a heat exchanger placed in liquid N_2 with the temperature regulation controlled using the standard Bruker heating system. The thermocouple was placed at the bearing gas port inside the probehead stator to obtain the most accurate measurements. In general, the sample was allowed to equilibrate for 30 minutes at each temperature. For the CP experiments, the ^{1}H $\pi/2$ pulse length was of 6.0 μs and the recycle delay was of 8.0 s. Two phase pulse modulation (TPPM) decoupling[269-270] was used during acquisition at an rf field of 47.2 kHz. The CP contact time was 4.0 ms with the Hartmann-Hahn matching condition set using hexamethylbenzene (HMB). $^{13}C\{^{1}H\}$ VT MAS NMR spectra were recorded using a $\pi/3$ ^{13}C pulse length of 2.9 μs and the recycle delay of 20.0 s. TPPM decoupling at an RF field of 47.2 kHz was used during acquisition.

The ambient temperature experiments for the emulsion-templated polymer and TiAAB were recorded using a 4 mm probehead at MAS rates of 3.2 and 10 kHz. The ^{1}H $\pi/2$ pulse length was 3.0 μs and the recycle delay was 8.0 s. TPPM decoupling was used during acquisition with the CP contact time set at 4.0 ms.

5.3.4.3 Dipolar dephasing

^{1}H-^{13}C CP-MAS dipolar dephasing experiments were recorded at a MAS rate of 10 kHz in a similar manner to the CP-MAS NMR. However, a ^{13}C π pulse of 7.8 μs was placed after the CP step with varying delays of 20, 40, 80, 100, 150 and 200 μs on both sides prior to acquisition. All ^{13}C chemical shifts are quoted in ppm with respect to TMS. All NMR data was processed using Bruker Topspin 1.3 software.

5.4 Result and discussion

5.4.1 Formation of the semi-clathrate hydrate system and characterisation by crystallography

Three stable, gas-free polyhydrates of TiAAB have been previously reported and in this study, two compositions were targeted: a 3.7 mol% solution (nominal composition $TiAAB_3$ 26-H_2O) and a 2.6 mol% solution ($TiAAB.38H_2O$). To confirm that these structures had been achieved, single crystals suitable for X-ray structure analysis were obtained for the gas-free semi-clathrate and for CH_4- and Kr-loaded systems. The gas-containing semi-clathrates were grown under gas pressures of 8.6 MPa and found to be sufficiently stable to allow mounting of crystals under ambient (T, P) conditions. The semiclathrate framework was found to be iso-structural to that of $[R_4N]$-X_3 $38H_2O$ (R = iAm, X = F[19] and R = R = nBu, X = Br[20]) and crystallizes in the orthorhombic space group (Pmma). The unit cell contains two 46-hedral cages accommodating the tetraalkyl ammonium ions and six dodecahedral cages that are potential hosts for small molecules.[342] There are two types of dodecahedral cages (labelled A and B in **Figure 5.1**).

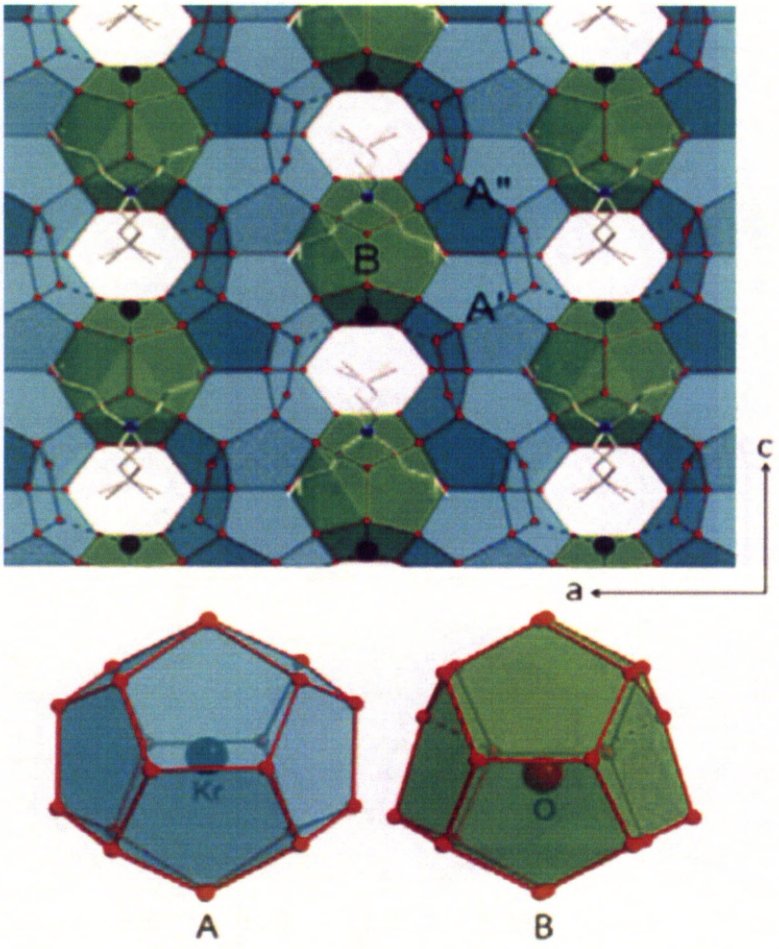

Figure 5.1 Crystal structure of the semi-clathrate TiAAB.38H_2O showing the arrangement of dodecahedral cages. Blue: A-type, Green: B-type. a) A-type cage with CH_4 or Kr guest. b) B-type cage with H_2O guest. The dashed lines indicate the distance between the guest molecule and the framework. In the B-type cage, the distance is 3.2 Å between H_2O and the trigonal nodes of the framework.

The unique cages A′ and A″ (symmetry 2/m) approximate regular dodecahedra and are enclosed exclusively by tetrahedral water molecule nodes. In contrast, the B-type cages (symmetry mm2) are distorted as a result of the presence of two nearly planar trigonal framework nodes (O11). These interact only with water molecules of the B-type cage causing these nodes to protrude inwards as shown more clearly in **Figure 5.2**.

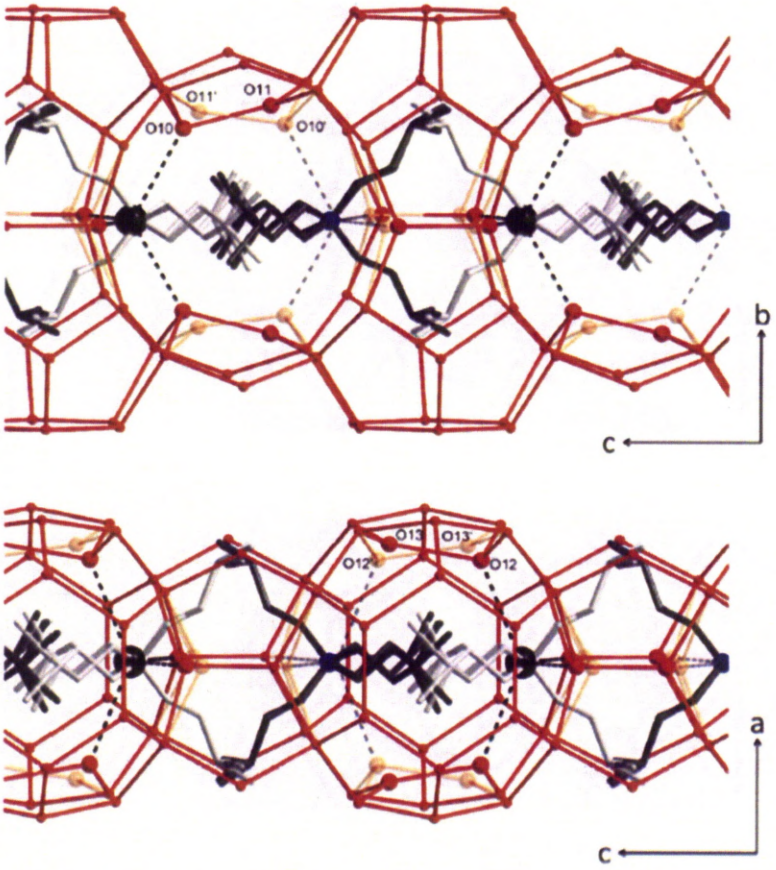

Figure 5.2 Illustration of the disorder along the crystallographic ¼, 0, z -axis. The B-type cage displays distortion due to bonding to water at positions labelled O10 and O11.

The crystal structures show that CH_4 and Kr are accommodated exclusively in A-type cages. Only the crystals that were grown under pressurized atmospheres of CH_4 and Kr exhibit sharp electron density peaks at the centres of A' and A", while no significant electron density was observed in the A-type cages of the gas-free crystals. Upon refinement, as C and Kr gave well-defined atom positions, give occupancy factors that translate into gas uptakes of 0.6 and 0.9 molar equivalents of CH_4 and Kr, respectively.

The centres of the B-type cages of all three compounds exhibit high electron densities. However, these densities do not correlate with the amount of gas-uptake in neighbouring A-type cages. It is thought that the highly distorted geometry of the B-type cages should prohibit the accommodation of Kr or CH_4 since the close proximity of the trigonal node O11 to the central peak position (3.2 Å) is well below

the sum of the Van der Waals radii of O, Kr or CH_4.[343-344] It is thought that the distorted dodecahedra host water molecules, which connect *via* hydrogen bonds to the unsaturated trigonal nodes of the framework.[345-346]

The refinement of O14, the O-atom of the hosted water molecule, gives slightly long but reasonable O-O distances for hydrogen bonding considering its diffuse nature within the structure. The relatively large thermal parameter indicates that the position of O14 is not as well-defined as that of the hosts accommodated in A-cages. The final occupancy factors of O14 refined to 0.23(2) for the gas-free derivative, 0.18(2) for the crystals loaded with CH_4, and 0.48(2) for the crystals loaded with Kr. This variation may simply be a result of different clathration kinetics in different experiments, which are known to be stochastic.[347]

Figure 5.1 also shows the dodecahedral A- and B-type cages together with their guests. Taking the hosted water molecules into account, the overall sum formulas of the three structurally determined systems are $[iAm_4N]Br\ 38.2H_2O$, $[iAm_4N]Br.38.2H_2O{\cdot}0.62CH_4$, and $[iAm_4N]Br.38.5H_2O{\cdot}0.91Kr$, respectively. The crystallography data is summarised in **Table 5.1** below.

Table 5.1 Crystal data and refined occupancy factors of guest atoms

Compound	$[iAm_4N]Br.38.2H_2O$	$[iAm_4N]Br.38.2H_2O$.$0.6CH_4$	$[iAm_4N]Br.38.5H_2O$ .0.9Kr
Chemical formula	$C_{20}H_{120.4}BrNO_{38.2}$	$C_{20.6}H_{122.8}BrNO_{38.2}$	$C_{20}H_{121}BrKr_{0.9}NO_{38.5}$
Formula weight	1067.22	1076.31	1147.51
Space group	*P*mma	*P*mma	*P*mma
a/Å	21.370(4)	21.374(4)	21.397(9)
b/Å	12.766(3)	12.753(2)	12.828(6)
c/Å	11.866(2)	11.904(2)	11.934(5)
V/Å3	3237.2(11)	3244.7(9)	3276(2)
Z	2	2	2
Occupancy factors			
A′-type cage	-	0.33(2) (C)	0.450(3) (Kr)
A″-type cage	-	0.29(2) (C)	0.463(3) (Kr)
B-type cage	0.23(2) (O)	0.18(2) (O)	0.48(2) (O)

5.4.2 Powder X-ray diffraction

Powder X-ray diffraction (PXRD) data show TiAAB.38H_2O is formed preferentially over TiAAB.26H_2O irrespective the water content of the salt solution (**Figure 5.3**).

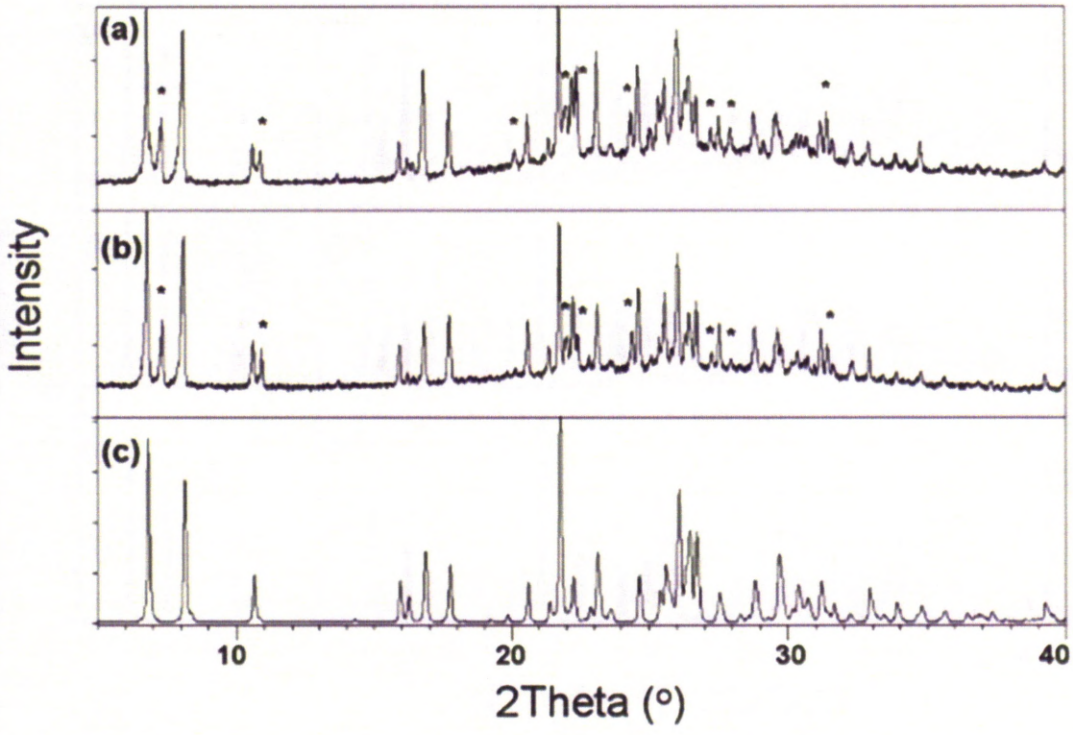

Figure 5.3 PXRD patterns for **a)** TiAAB.38H_2O, **b)** TiAAB.26H_2O and **c)** simulated XRD pattern from single crystal data of TiAAB.38H_2O. Simulated pattern peak positions were corrected to lower 2θ values to take into account the thermal contraction of the unit cell parameters in the single crystal data. Peaks not observed in the simulated powder pattern for TiAAB.38H_2O were eliminated before indexing and refining. All remaining peak positions in **a)** and **b)** and are marked with *.

Comparing the simulated PXRD pattern generated from single-crystal XRD data shows good agreement with the data obtained for both samples. In both cases, extra peaks are apparent (* in **Figure 5.3 a)**and **b)**), that are possibly indicative of a different crystal form. Theoretical PXRD peak positions generated from TBAB.26H_2O crystal parameters26 include a diffraction peak at $2\theta=7.39^0$, in agreement with the additional experimental peak at this 2θ observable in **Figure**

5.3. The extra peaks are therefore ascribed to be consistent with TiAAB.26H_2O hydrate coexisting with the 38H_2O material. This is difficult to rationalise further due to the absence of relative peak intensities or complete crystal data for either TBAB.26H_2O or TiAAB.26H_2O, although, note that Lipkowski *et al.*[348] reported kinetic difficulties in preparing the analogous tetra-iso-amylammonium fluoride (TiAAF.27H_2O), with TiAAF.38H_2O being formed in preference. The data in **Figure 5.3** confirm that the dominant species in both cases is TiAAB.38H_2O. Indexing the PXRD spectra gave cell parameters for the TiAAB.38H_2O feed composition of a = 21.669(6) Å, b = 12.932(3) Å, and c = 12.026(3) Å with a cell volume = 3369.9(11) Å^3 and for the TiAAB.26H_2O feed composition of a = 21.683(10) Å, b = 12.928(5) Å, and c = 12.026(5) Å and a cell volume = 3371.0(18) Å^3. These values are slightly larger than those found from the single crystal data above (**Table 5.1**), which is to be expected considering the higher temperature at which the PXRD data were collected.

5.4.3 Measurement of methane storage capacity and uptake kinetics

Storage of methane within a TiAAB semi-clathrate supported on an ultralow-density, emulsion-templated "polyHIPE" material was also investigated.[329] The interconnected pore structure and very low bulk density allowed the support 20 g of TiAAB solution on 3.4 g of the polymer. **Figure 5.4** shows a P-T plot for the CH_4-TiAAB-H_2O system.

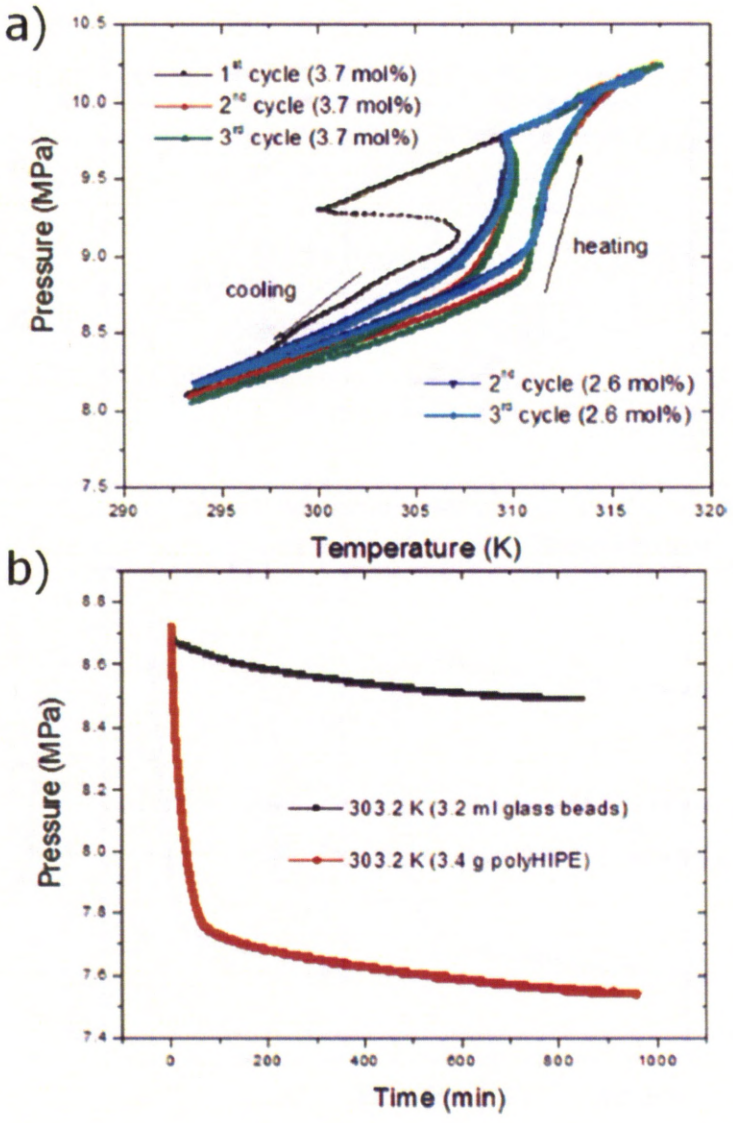

Figure 5.4 a) Pressure vs temperature plot for polymer-supported TiAAB.26H_2O (black, red and green) and TiAAB.38H_2O (blue) (20 g of solution and 3.4 g of support were used) cooling rate = 2 K/h. **b)** Kinetic plot for CH_4 encapsulation in TiAAB.-H_2O semi-clathrate hydrate supported on polyHIPE at 303 K (red) and with "bulk" control experiment glass beads as volumetric filler (the volume of glass beads is equal to that of polyHIPE)(black).

With no support, the P-T relationship for the CH_4 system approximated to the ideal gas law during the heating/cooling cycle (data not shown), *i.e.* very little CH_4 clathrate was formed in the bulk in the absence of mixing. By contrast, clathrate formation and subsequent dissociation occurred in the presence of the polymer support, as evidenced by the significant pressure drop on cooling and the

pressure rise on heating (**Figure 5.4a**). Repeating this cycle, the clathration onset temperature increased by 10 K (310 K versus 300 K in the first cycle). Subsequent cycling then closely follow the second cycle. It is thought that this first "induction cycle" may result from the more uniform distribution of the TiAAB/water system throughout the hydrophobic polymer support, as discussed previously for polymer supported THF-H_2O-H_2 clathrates (see **Appendix I**).[329] However, it may also arise from the clathrate memory effect that has been previously reported for a number of different systems.[347] Data for the 2.6 mol% solution closely followed that for the 3.7 mol% solution, again supporting the preferential formation of TiAAB.38H_2O.

The kinetics of clathration and gas uptake capacity were both greatly enhanced by the presence of the polymer support (**Figure 5.4b**). Again, this effect is reproducible over multiple charge-discharge cycles. The CH_4 capacity derived from the pressure drop, ΔP (1.18 MPa), at 303.2 K was estimated to be 36.8 v/v relative to the amount of TiAAB-H_2O added, as calculated using GasPak v3.41 software. Volumetric release experiments confirmed this capacity. This equates to approximately 80% of the maximum theoretical capacity as calculated for the system based on complete filling of both available A-type cages (blue cages in **Figure 5.1**). The time to reach 90% saturation capacity, t_{90}, was ca. 200 min whereas very little CH_4 uptake was observed in the bulk unmixed system on this time scale (**Figure 5.4b**).

5.4.4 Encapsulation capacity measured by solid-state NMR spectroscopy

The CH_4 encapsulation capacity was also confirmed by ^{13}C MAS NMR. ^{1}H-^{13}C CP-MAS NMR spectra of the supported semi-clathrate show peaks corresponding to the aromatic protons in the polyHIPE support at 127.6 ppm. The peaks at 40.8 and 29.0 ppm are attributed to the aliphatic resonances of the emulsion-templated polymer support (**Figure 5.5**). The spectra were recorded at two MAS rates in order to identify which resonances were spinning sidebands.

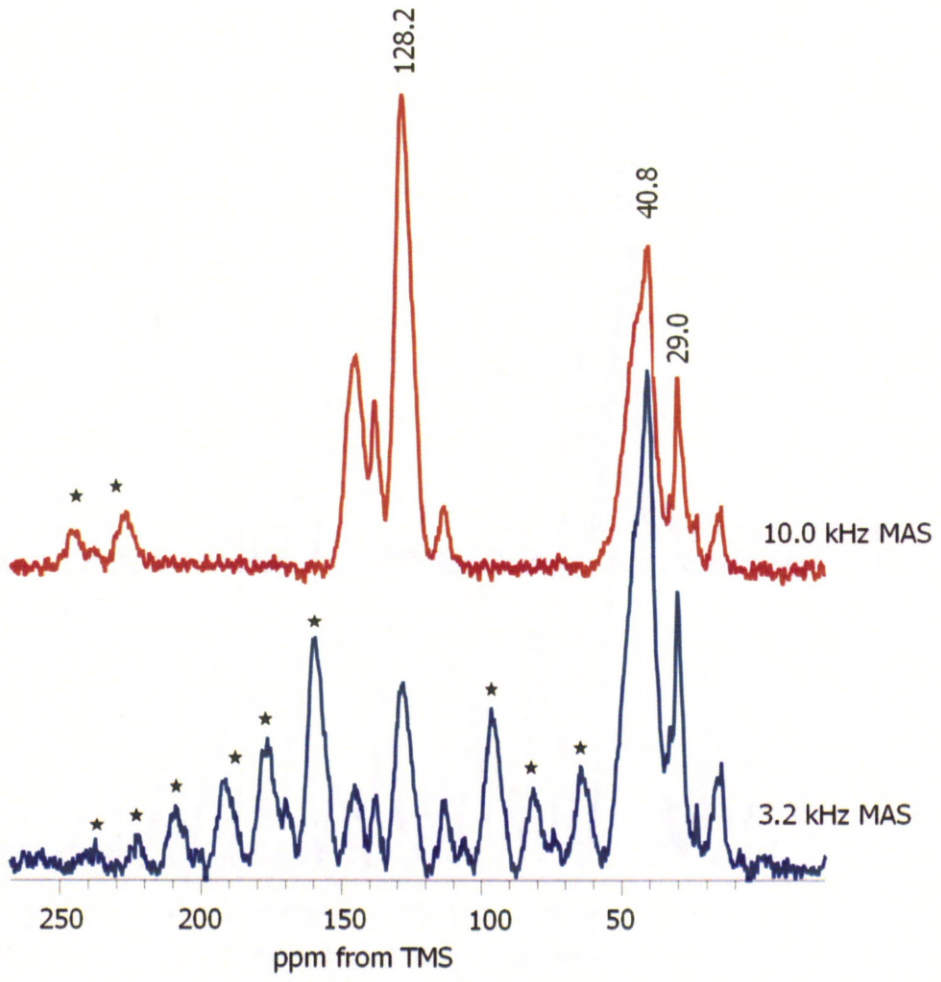

Figure 5.5 ^{1}H-^{13}C CP-MAS NMR spectra of emulsion-templated polystyrene recorded at MAS rates of 3.2 kHz and 10.0 kHz

Both ^{1}H-^{13}C CP-MAS (**Figure 5.7a**) and $^{13}C\{^{1}H\}$MAS NMR (**Figure 5.7b**) spectra show several resonances attributable to TiAAB. A number of peaks are observed for the terminal methyl and methyne sites. This is due to the interactions of the salt with the clathrate framework and their restricted mobility. In order to assign resonances attributable to the template, ^{1}H-^{13}C dipolar dephasing experiments were used (**Figure 5.6**).

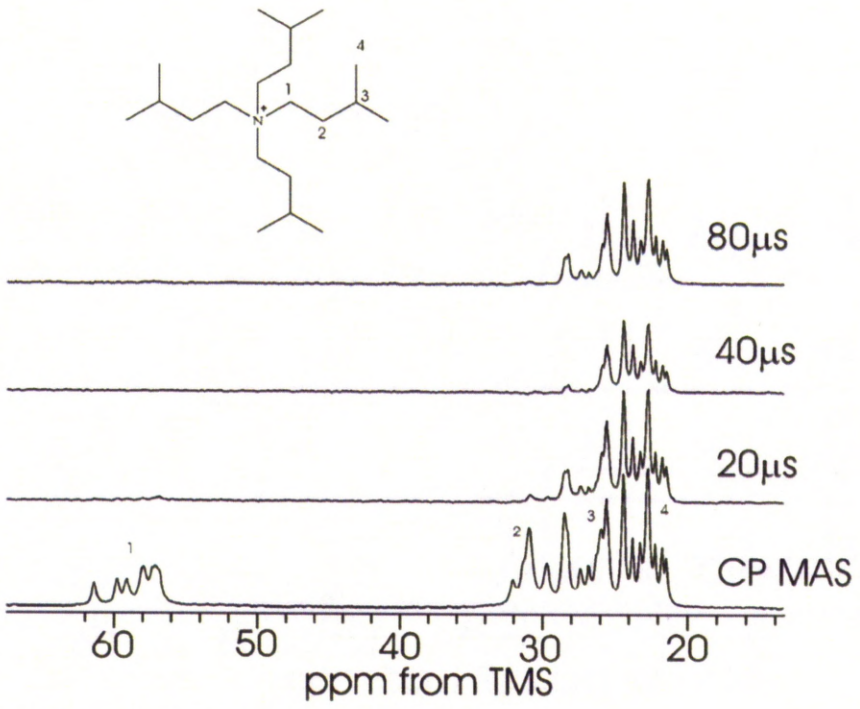

Figure 5.6 ^{1}H-^{13}C CP-MAS and dipolar dephasing spectra (recorded with different dephasing times) of TiAAB. Note the change of the intensities for the resonances corresponding to C(1) and C(2) sites in the structure.

Resonances at *ca.* 57 ppm correspond to -N-CH_2- sites and *ca.* 32 ppm to N-CH_2- **C**H_2-. The two populations for the -N-CH_2- sites indicate the presence of two motionally different environments for the salt. The peak at 56.3 ppm is observed in both the ^{1}H-^{13}C CP-MAS and $^{13}C\{^{1}H\}$ MAS NMR spectra (**Figures 5.7 a)** and **b)**).

CH_4 is observed in all $^{13}C\{^{1}H\}$ MAS NMR spectra but is only observed in the CP spectrum at 223 K. This is because CP relies on dipolar coupling between ^{13}C and ^{1}H to transfer magnetisation to ^{13}C. Dipolar coupling does not exist in gases due to rapid molecular motion. At 223 K, CH_4 has solid like character when enclathrated and therefore has sufficient dipolar coupling for magnetisation to be transferred from ^{1}H to ^{13}C. In the $^{13}C\{^{1}H\}$ MAS NMR spectra, ^{13}C is observed directly and therefore all ^{13}C resonances are observed irrespective of their state.

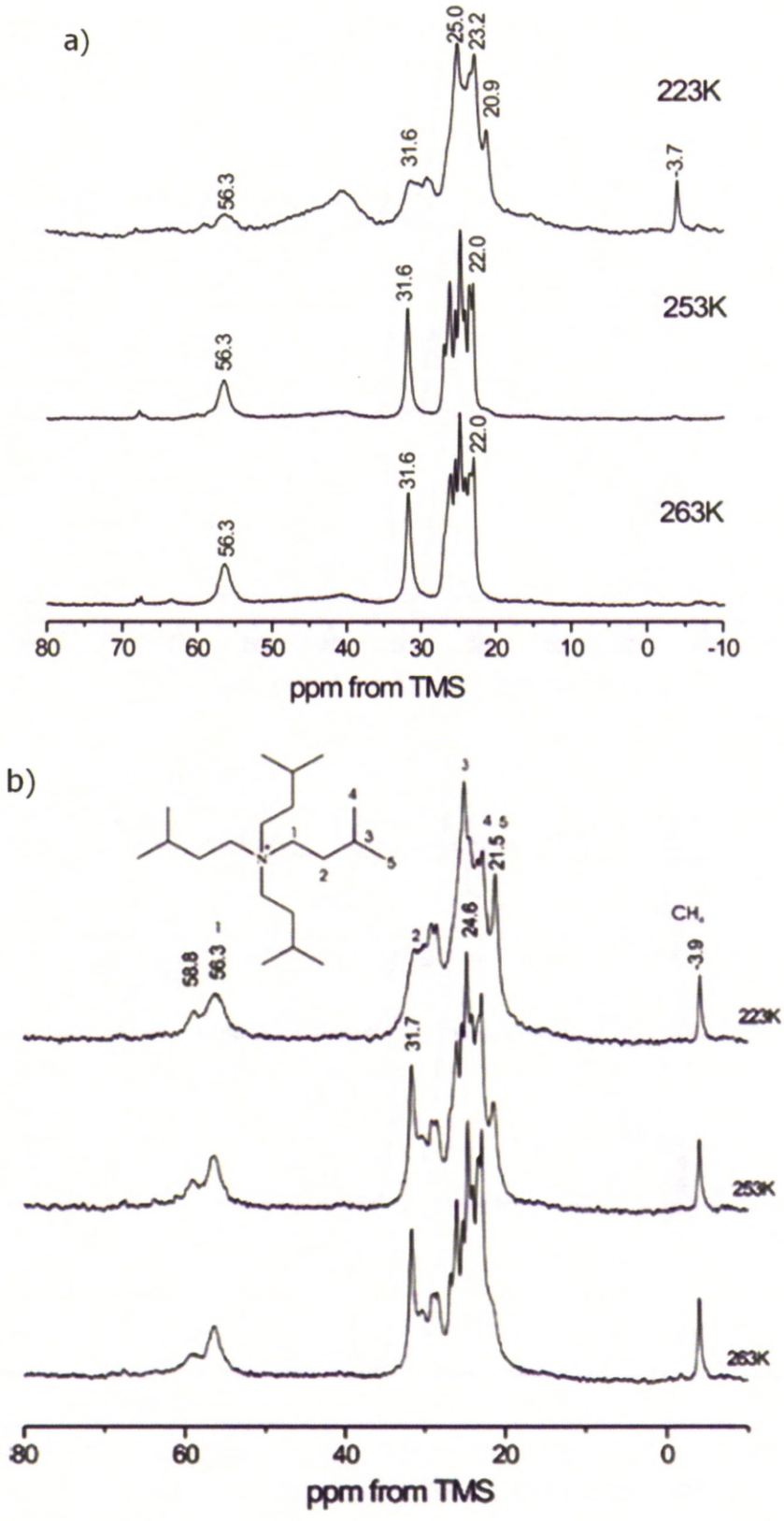

Figure 5.7 a) ^{1}H-^{13}C CP-MAS NMR spectra of H_2O-TiAAB-CH_4 **b**) $^{13}C\{^{1}H\}$ MAS NMR spectra of H_2O-TiAAB-CH_4 semi-clathrate (MAS rate = 3.2 kHz)

The resonance at 58.8 ppm has been observed using ^{1}H-^{13}C CP-MAS experiments only at 223 K, while being present in the $^{13}C\{^{1}H\}$ MAS NMR spectra at all temperatures studied. Most probably the latter environment is due to a disordered salt species with enhanced mobility, hence not registering in the CP spectra at 253 and 263 K.

The ratio between the intensities of the N-CH_2 peak at 56.3 ppm and methane guest peak at -3.7 ppm (spectra measured at 263 K) was determined by deconvoluting these two resonances and was given to be approximately 2.7 suggesting an 81% of the maximum available uptake capacity (as determined from the crystal structure). The ratio between theN-CH_2 resonance at 56.3 ppm and that of methane at 223 K after storage in the fridge overnight (278 K) was found to be approximately 4.2 (56% of the maximum loading). The slightly lower CH_4 occupancy (62%) compared to that estimated from single crystal X-ray could be explained by sample morphology (much smaller polymer-supported domains versus much larger single crystals in X-ray experiments).

5.4.5 Probing the stability of the methane charged semi-clathrate under varying temperature and pressure

A key issue regarding the use of clathrate and semiclathrate hydrates for practical gas storage is the pressure-temperature stability of the material. For many practical applications, the avoidance of cooling, gas overpressure and mechanical mixing would be desirable. The stability of the CH_4-TiAAB-H_2O semi-clathrate hydrate was found to be much higher than the sI methane gas hydrate (**Figure 5.8**).

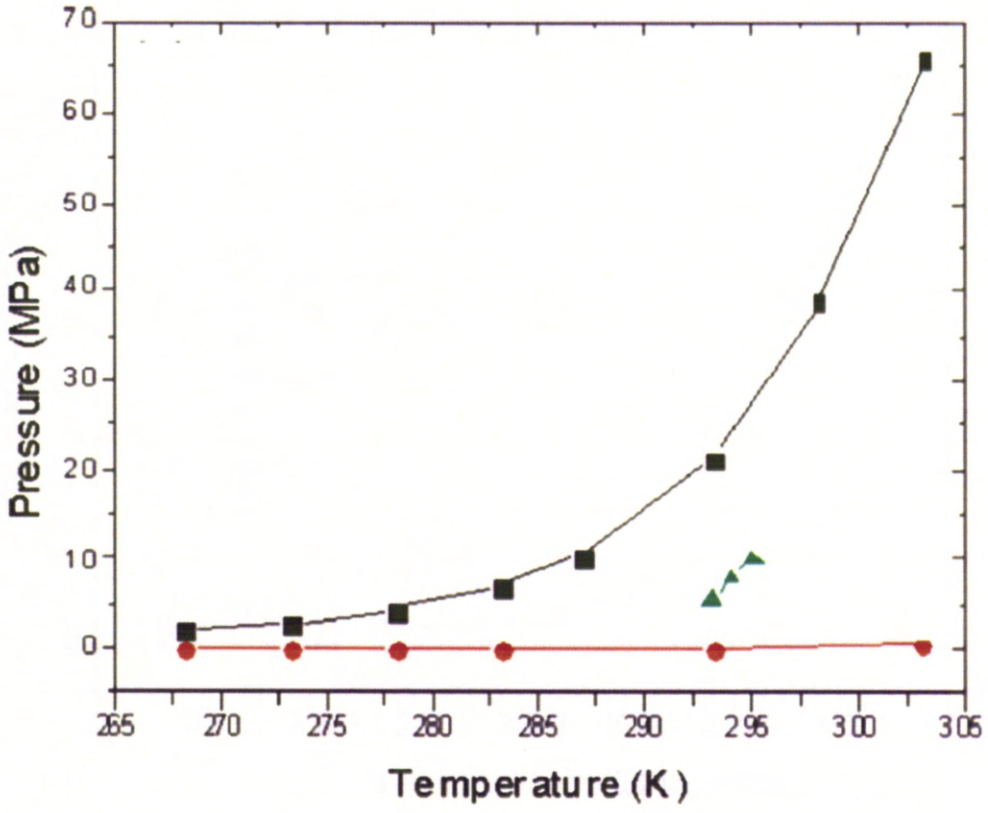

Figure 5.8 Stability ofCH_4-TiAAB-H_2O clathrate hydrate (20 g 3.7 mol% TiAAB solution supported on 3.4 g polymer, red) as compared to sI methane gas hydrate (black) and CH_4-TBAB-H_2Oclathrate hydrate15 (green).

5.4.5.1 Thermal stability of the semi-clathrate system investigated by DSC

To further examine the thermal stability of the CH_4-TiAAB-H_2O clathrate, DSC was used to determine the enthalpies of melting for the TiAAB clathrate hydrate and for the same material containing CH_4 (**Figure 5.9**).

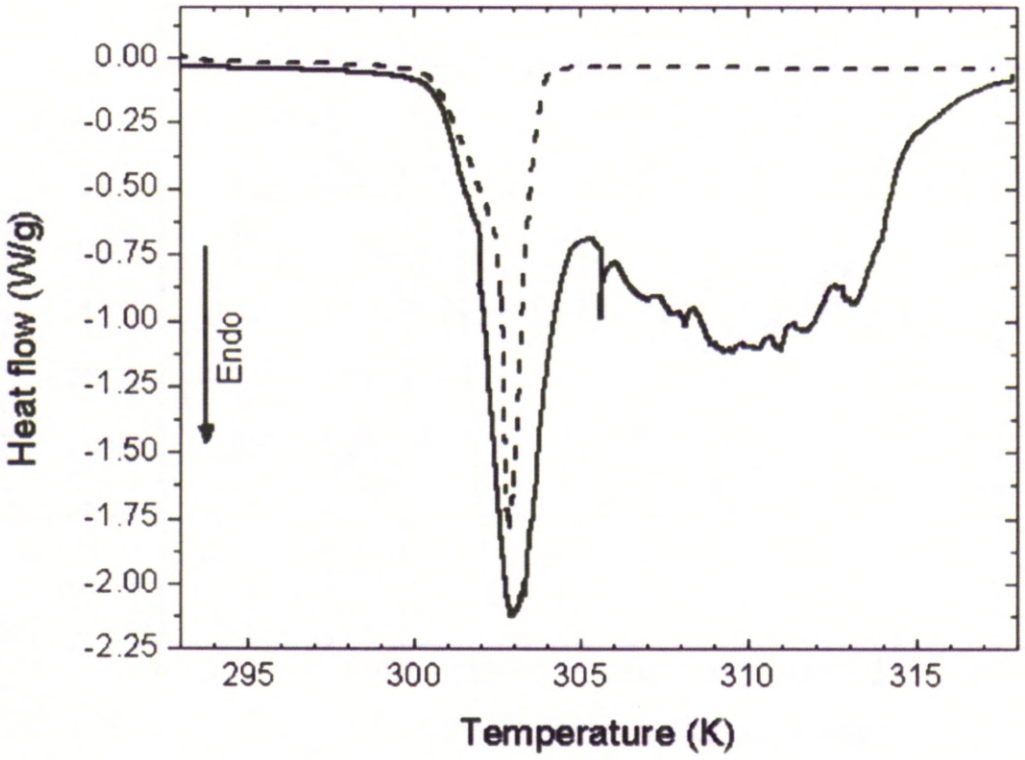

Figure 5.9 Differential scanning calorimetry for TiAAB-H_2O clathrate hydrate (dashed line) and CH_4-TiAAB-H_2O clathrate (solid line)

The neat TiAAB clathrate hydrate melted at approximately 303 K. The CH_4-TiAAB-H_2O also demonstrated a melting point at 303 K, followed by a broad transition centred around 310 K (**Figure 5.9**). These transitions correlate well with the expected melting point of TiAAB clathrate hydrate[349] and also correlate with the temperatures recorded for clathration onset and decomposition at high pressures (**Figure 5.4**). Similar observations have been made in other studies which did not involve TiAAB;[350-351] in those cases, a melting transition for the ice framework was observed followed by a second transition as the methane clathrate melts.[350] These data further illustrate the thermal stability of the CH_4-TiAAB-H_2O hydrate.

5.4.5.2 Thermal stability of the methane charged semi-clathrate measured using a balloon release experiment

CH_4-TiAAB-H_2O was compared with the CH_4-TBAB-H_2O system, used previously to store both CH_4 and H_2.[352-353] CH_4-TiAAB-H_2O semi-clathrate hydrate exhibits enhanced stability over the TBAB system. The iso-amyl chains fill the

available cavity more effectively than butyl chains and hence exert a greater stabilizing effect on the H_2O cages.[334] Indeed, this system retained clathrated CH_4 after several hours at room temperature.

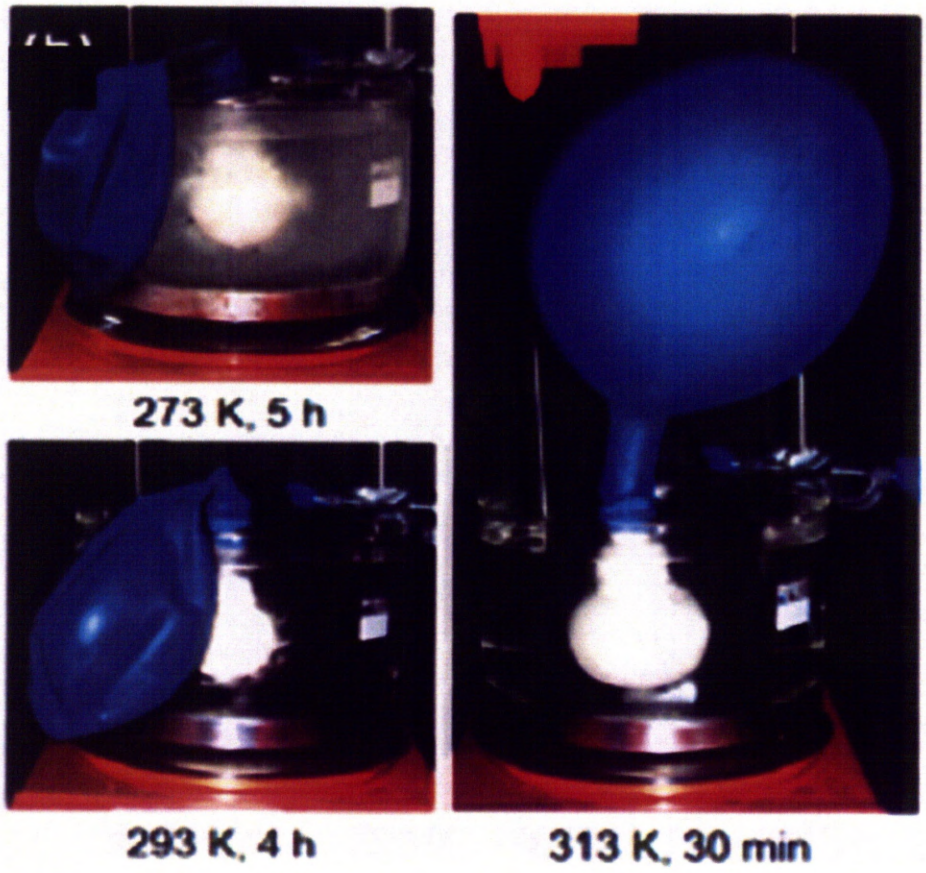

Figure 5.10 Stability of CH_4-TiAAB-H_2O clathrate hydrate supported on polyHIPE. CH_4-TiAAB–H_2O stability at 273 K / 1 bar (5 h; left top), 293 K / 1 bar (4 h; left bottom) and CH_4 dissociation and release at 313 K (right).

Figure 5.10 demonstrates that no CH_4 is evolved after 5 hours at 273 K, as indicated by the deflated balloon. Upon warming to 293 K, virtually no gas is evolved after a further 4 hours. Upon warming to 303 K, the clathrated gas is evolved rapidly, inflating the balloon. This behaviour is in total contrast to CH_4 storage in porous physisorptive materials.[354-356] It is estimated that the H_2O-TiAAB-CH_4 system is around 8 K more stable than comparable TBAB systems,[353] a relatively small difference but important in terms of pushing stabilities above "ambient" temperature. The absence of stirring is also significant: previous studies

with TBAB[353] involved vigorous mechanical mixing under pressure using an impeller. Reversible storage (**Figures 5.4** and **5.8**) using a static, lightweight polymer support with no moving parts may be a much more practical solution for many applications.

5.5 Conclusions and outlook

In summary, emulsion-templated polymer supports have greatly enhanced CH_4 uptake kinetics in semi-clathrate hydrates without introducing complex mixing technologies. These systems show unprecedented thermal stability and can be decomposed upon demand to release the gas. The system is reversible with no degradation in performance over at least 20 charge/discharge cycles. This combines, for the first time, a number of important practical considerations in a single gas storage system. It has also been unambiguously demonstrated that CH_4 and Kr are stored in the dodecahedral cages A′ and A″ which have 2/m symmetry. NMR spectroscopy has been used to confirm the presence and measure the amount of confined CH_4. The ^{13}C MAS NMR spectra gave qualitative estimation of support guest interactions.

The main practical drawback of the system is the relatively low CH_4 capacity with respect to pure methane gas hydrates (35-40 v/v versus 180 v/v). Indeed, this may be insurmountable in the present system since the enhanced stability of the semi-clathrate hydrate arises from the substantial cage filling that occurs.

Ongoing investigation by the Cooper group approaches to combine these promising stability and recyclability advantages with less compromised gas storage capacities. For example, by designing salts which exert equivalent stabilization effects while filling fewer cages. This system also provides a possible "blueprint" for other systems. For example, wholly organic gas clathrates or hydrogel systems[330] dispersed on high pore-volume organic polymer supports.

Overall conclusions and outlook

Two classes of SILP have been prepared. In the first, [bmim]OTf was confined within the mesopores of SBA-15 at varying loadings. In the second, an analogous RTIL, [bmim]CH_3SO_3 was confined within the mesopores of SBA-15 and MCM-41. Various NMR experiments have provided an important insight into the structure and orientation of both confined RTILs.

A new crystal phase that is unique to the intercalated [bmim]CH_3SO_3 in SBA-15 has been identified. This phase is observed both below and above the melting point of neat [bmim]CH_3SO_3. The results of NMR studies are in agreement with this conclusion. Thus, ^1H linewidths and T_1 relaxation times for this material indicate that no phase transition occurs at temperatures around the melting point of neat [bmim]CH_3SO_3. The new crystal phase observed for SBA-15 confined [bmim]CH_3SO_3 is believed to be nucleated by ion pairs interacting with the surface of the pore causing the orientation of the ion pairs to be different from that in the neat form.

For both classes of SILP studied, ^1H linewidths, T_1 relaxation times and ^1H-^{13}C CP dynamics identified the presence of a less mobile surface confined layer at both high and low loadings with a more mobile bulk material emerging in the centre of the mesopores as loading increased. The orientation of the RTILs with respect to the pore surface was probed by ^1H-^{29}Si HETCOR experiments and in both cases showed the butyl chains and N-methyls to interact more closely with the pore surface. Computer modelling of the [bmim]OTf intercalates confirmed the orientation of the cation and predicted that the anion would sit in closest proximity to the pore surface in the cavity created by surface hydroxyls interacting with the terminal methyl groups of the cation (**Figure 6.1**).

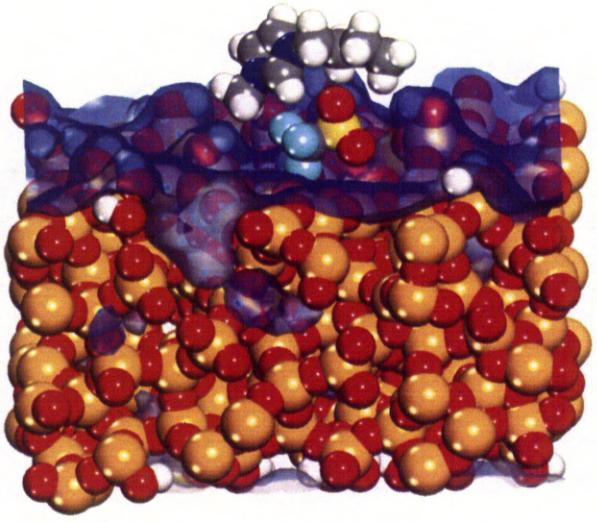

Figure 6.1 Computer modelling of [bmim]OTf on the surface of SBA-15

Preliminary experiments have been performed to investigate the diffusion of [bmim]OTf in SBA-15. These results are promising and indicate that a systematic approach using DOSY NMR in combination with HR-MAS methodology will provide additional insight into the design of new SILP systems.

It is well known that bulk RTILs have a high affinity for CO_2. Initial investigations reveal that the presence of [bmim]OTf at low loading in SBA-15 enhanced the rate of uptake of CO_2 by the material. However, due to the limited space within the pore the overall uptake was lower than for SBA-15 without [bmim]OTf. Further investigations of these SILP systems for CO_2 storage might include loading the CO_2 under pressure or at different temperatures to alter the viscosity of the ionic liquid, in turn, affecting the mass transfer of the gas through the ionic liquid layer. NMR spectroscopy could then be used to investigate the effects of temperature, pressure and identify the interactions between the ionic liquid and the gaseous guest.

This approach has been used in the characterisation of methane incorporated in semi-clathrate hydrates (**Chapter 5**) and hydrogen incorporated

in clathrate hydrates (**Appendix I**). ^{1}H-^{13}C CP-MAS NMR spectroscopy, in combination with dipolar dephasing, has been used both to characterise the semi-clathrate system and to identify the presence of encapsulated methane at low temperature. The encapsulated methane was present at all temperatures in the $^{13}C\{^{1}H\}$ MAS NMR spectra of the semi-clathrate hydrate. The amount of methane intercalated was calculated from the NMR spectra and although found to be low in comparison to some other gas storage systems, there are many advantages to the clathrate approach. These are predominantly their safety, rechargeability and low environmental impact.

Throughout this research NMR spectroscopy has allowed the structure, mobility, and interactions present between intercalates and the host material to be determined.

References

(1) Wasserscheid, P.; Welton, T. *Ionic Liquids in Synthesis*; 2nd Edition ed.; Wiley-VCH, 2008.

(2) Ebbing, D. D., Gammon, S.D. *General Chemistry*; Houghton Mifflin, 2005.

(3) Walden, P. *Bull. Acad. Imper. Sci. (St. Petersburg)* **1914**, 1800.

(4) Plechkova, N. V., Seddon, K. R. *Chem. Soc. Rev.* **2008**, *37*, 123.

(5) Kerton, F. M. *Alternative Solvents for Green Chemistry*; RSC Publishing, 2009.

(6) Lovelock, K. R. J., Villar-Garcia, I. J., Maier, F., Steinruck, H. P., Licence, P. *Chem. Rev.* **2010**, *110*, 5158.

(7) Liu, X., Zhou, F., Liang, Y., Liu, W. *Wear* **2006**, *261*, 1174

(8) Cione, A. M., Mazyar, O. A., Booth, B. D., McCabe, C., Jennings, G. K. *J. Phys. Chem. C* **2009**, *113*, 2384

(9) Li, J., Shen, Y., Zhang,Y., Liu, Y. *Chem. Comm.* **2005**, 360

(10) Bonhote, P., Dias, A. P., Papageorgiou, N., Kalyanasundaram, K., Gratzel, M. *Inorg. Chem.* **1996**, *35*, 1168.

(11) Plechkova, N. V., Seddon, K. R. *Chem. Soc. Rev.* **2007**, *37*, 123.

(12) Adams, D. J., Dyson, P.J., Taverner, S. J. *Chemistry in Alternative Reaction Media*; John Wiley & Sons Ltd.: Chitchester, 2004.

(13) Fredlake, C. P., Crosthwaite, J. M., Hert, D. G., Aki, S. N. V. K., Brennecke, J. F. *J. Chem. Eng. Data* **2004**, *49*, 954.

(14) Davies, C. M., University of Liverpool, 2006.

(15) Atkins, P. W. *Phys. Chem.* W.H. Freeman & Co.: New York, 1994.

(16) Ojovan, M. I. *Entropy* **2008**, *10*, 334.

(17) Holbrey, J. D., Seddon, K.R. *Dalton Trans.* **1999**, 2133.

(18) Ngo, H. L., LeCompte, K., Hargens, L., McEwan, A.B. *Thermochim. Acta* **2000**, *357*, 97.

(19) Huddleston, J. G., Visser, A.E., Reichert, W.M., Willauer, H.G., Broker, G.A., Rogers, R.D. *Green Chem.* **2001**, *3*, 156.

(20) Wasserscheid, P., Keim, W. *Angew. Chem. Int. Ed.* **2000**, *39*, 3772.

(21) Olivier-Bourbigou, H., Magna, L. *J. Mol. Catal. A: Chem.* **2002**, *182-183*, 419.

(22) Chakraborti, A. K., Roy, S.R. *JACS* **2009**, *131*, 6902.

(23) Dominguez de Maria, P. *Angew. Chem. Int. Ed.* **2008**, *47*, 2.

(24) Van Doorslaer, C., Wahlen, J., Mertens, P., Binnemans, K., De Vos, D. *Dalton Trans.* **2010**, *39*, 8377.

(25) Brown, R. A., Pollet, P., McKoon, E., Eckert, C.A., Liotta, C.L., Jessop, P.G. *JACS* **2001**, *123*, 1254.

(26) Alaerts, L., Wahlen, J., Jacobs, P.A., De Vos, D.E. *Chem. Comm.* **2008**, 1727.

(27) Valkenberg, M. H., DeCastro, C., Holderich, W. F. *Green Chem.* **2002**, *4*, 88.

(28) Gordon, C. M. *Appl. Catal., A* **2001**, *222*, 101.

(29) Zhao, D., Wu, M., Kou, Y., Min, E. *Catal. Today* **2002**, *74*, 157.
(30) Dupont, J., de Souza, R.F., Suarez, P.A.Z. *Chem. Rev.* **2002**, *102*, 3667.
(31) Welton, T. *Coord. Chem. Rev.* **2004**, *248*, 2459.
(32) Parvulescu, V. I., Hardacre, C. *Chem. Rev.* **2007**, *107*, 2615.
(33) Han, P., Zhang, H., Qiu, X., Ji, X., Gao, L. *J. Mol. Catal. A: Chem.* **2008**, *295*, 57.
(34) Valkenberg, M. H., DeCastro, C., Holderich, W. F. *Top. Catal.* **2001**, *14*, 1.
(35) Valkenberg, M. H., DeCastro, C., Holderich, W. F. *Appl. Catal., A* **2001**, *215*, 185.
(36) Ciriminna, R., Hesemannm P., Moreau, J. J. E., Carraro, M., Campestrini, S., Pagliaro, M. *Chem.Eur. J.* **2006**, *12*, 5220.
(37) Aksnes, D. W., Gjerdaker, L. *J. Mol. Struct.* **1999**, *475*, 27.
(38) DeCastro, C., Sauvage, E., Valkenberg, M.H., Holderich, W.F. *J. Catal.* **2000**, *196*, 86.
(39) Lunstroot, K., Driesen, K., Nockermann, P., Gorller-Walrand, C., Binnemans, K., Bellayer, S., Le Bideau, J., Vioux, A. *Chem. Mater.* **2006**, *18*, 5711.
(40) Le Bideau, J., Gaveau, P., BEllayer, S., Neouze, M. A., Vioux, A. *Phys. Chem. Chem. Phys.* **2007**, *9*, 5419.
(41) Zhang, L., Zhang, Q., Li, J.H. *J. Electroanal. Chem.* **2007**, *603*, 243.
(42) Neouze, M. A., Le Bideau, J., Leroux, F., Vioux, A. *Chem. Comm.* **2005**, 1082.
(43) Neouze, M. A., Le Bideau, J., Vioux, A. *Prog. Solid State Chem.* **2005**, *33*, 217.
(44) Neouze, M. A., Le Bideau, J., Gaveau, P., Bellayer, S., Vioux, A. *Chem. Mater.* **2006**, *18*, 3931.
(45) Kimizuka, N., Nakashima, T. *Langmuir* **2001**, *17*, 6759.
(46) Bellayer, S., Viau, L., Tebby, Z., Toupance, T., Le Bideau, J., Vioux, A. *Dalton Trans.* **2009**, *8*, 1307.
(47) Kasai, J., Nakagawa, Y., Uchida, S., Yamaguchi, K., Mizuno, N. *Chem. Eur. J.* **2006**, *12*, 4176.
(48) Echelmeyer, T., Meyer, H.W., van Wullen, L. *Chem. Mater.* **2009**, *21*, 2280.
(49) Chen, S., Wu, G., Sha, M., Huang, S. *J. Am. Chem. Soc.* **2007**, *129*, 2416
(50) Gu, Y., Ogawa, C., Kobayashi, J., Mori, Y., Kobayashi, S. *Angew. Chem. Int. Ed.* **2006**, *45*, 7217.
(51) Huang, J., Jiang, T., Gao, H., Han, B., Liu, Z., Wu, W., Chang, Y., Zhao, G. *Angew. Chem. Int. Ed.* **2004**, *43*, 1397.
(52) Mao, S., Liu, Z., Han, B., Huang, J., Sun, Z., Zhang, J., Jiang, T. *Angew. Chem. Int. Ed.* **2006**, *45*, 266.
(53) Mikkola, J. P., Virtnen, P., Karhu, H., Salmi, T., Murzin, D.Y. *Green Chem.* **2006**, *8*, 197.
(54) Mikkola, J. P., Virtnen, P., Kordas, K., Karhu, H., Salmi, T. *Appl. Catal., A* **2007**, *328*, 68.
(55) Virtnen, P., Karhu, H., Kordas, K., Mikkola, J.P. *Chem. Eng. Sci.* **2007**, *62*, 3660.

(56) Riisager, A., Fehrmann, R., Haumann, M., Wasserscheid, P. *Top. Catal.* **2006**, *40*, 91.
(57) Gua, Y., Li, G. *Adv. Synth. Catal.* **2009**, *351*, 817.
(58) Qiao, S. Z., Yu, C.Z., Hu, Q.H., Jin, Y.G., Zhou, X.F., Zhao, X.S., Lu, G. Q. *Microporous Mesoporous Mater.* **2006**, *91*, 59.
(59) Grudzien, R. M., Grabicka, B.E., Jarniec, M. *Colloids Surf., A* **2007**, *300*, 235.
(60) Li, C. M., Yang, H., Shi, X., Liu, R., Yang, Q.H. *Microporous Mesoporous Mater.* **2007**, *98*, 220.
(61) Mouawia, R., Mehdi, A., Reye, C., Corriu, R. *J. Mater. Chem.* **2007**, *19*, 3041.
(62) Wang, X. G., Lin, K.S.K., Chan, J.C.C., Cheng, S.F. *J. Phys. Chem. B* **2005**, *109*, 1763.
(63) Garcia, N., Benito, E., Guzman, J., Tiemblo, P., Morales, V., Garcia, R.A. *Microporous Mesoporous Mater.* **2007**, *106*, 129.
(64) Macquarrie, D. J., Gilbert, B.C., Gilbey, L.J., Caragheorgheopol, A., Savonea, F., Jackson, D.B., Onida, B., Garrone, E., Luque, R., *J. Mater. Chem.* **2005**, *15*, 3946.
(65) Valkenberg, M. H.; deCastro, C.; Holderich, W. F. *Supported Catalysts and Their Applications* **2001**, 242.
(66) Valkenberg, M. H.; deCastro, C.; Holderich, W. F. *Green Chem.* **2002**, *4*, 88.
(67) Valkenberg, M. H.; Holderich, W. F. *Catalysis Reviews-Science and Engineering* **2002**, *44*, 321.
(68) Valkenberg, M. H.; deCastro, C.; Holderich, W. F. *Top. Catal.* **2001**, *14*, 139.
(69) Valkenberg, M. H.; deCastro, C.; Holderich, W. F. *Applied Catalysis a-General* **2001**, *215*, 185.
(70) Valkenberg, M., Hubert ; Sauvage, E.; De Castro-Moreira, C., Paulo; Hoelderich, W., Friedrich 2000; Vol. WO/2001/032308.
(71) Fink, G., Zechlin, J., Przybyla, C., Tesche, B. *Chem. Rev.* **2000**, *100*.
(72) Abbenhuis, H. C. L. *Angew. Chem. Int. Ed.* **1999**, *38*, 1058.
(73) Kahlen, W. *Catal. Lett.* **1998**, *54*, 85.
(74) Schuster, C. H. *Catal. Today* **2000**, *60*, 193.
(75) Bovio, S., Podesta, A., Lenardi, C., Milani, P., *J. Phys. Chem. B* **2009**, *113*, 6600.
(76) Bovio, S., Podesta, A., Milani, P., Ballone, P., Del Popolo, M. G. *J. Phys.: Condens. Matter* **2009**, *21*, 42.
(77) Du, P., Liu, S. N., Wu, P., Cai, C. X. *Electrochim. Acta* **2007**, *52*, 6534.
(78) Leal, J. P., Esperanc, J. M. S. S., da Piedade, M. E. M., Lopes,; J. N. C. Rebelo, L. P. N., Seddon, K. R. *J. Phys. Chem. A* **2007**, *111*, 6176.
(79) Armstrong, J. P., Hurst, C., Jones, R. G., Licence, P., Lovelock,; K. R. J., S., C. J., Villar-Garcia, I. J. *Phys. Chem. Chem. Phys.* **2007**, *9*, 982.
(80) Wang, C., Luo, H., Luo, X., Li, H., Dai, S. *Green Chem.* **2010**, *12*, 2019.
(81) Shi, W., Sorescu, D.C. *J. Phys. Chem. B* **2010**.
(82) Wick, C. D., Chang, T.M., Dang,L.X. *J. Phys. Chem. B* **2010**, *114*, 14965.
(83) Jutz, F., Andanson, J.M., Baiker, A. *Chem. Rev.* **2011**, *111*, 322.
(84) Ravelli, A. L., Mutelet, F., Jaubert, J.N. *J. Phys. Chem. B* **2010**, *114*, 12908.

(85) Kerle, D., Ludwig, R., Geiger, A., Paschek, D. *J. Phys. Chem. B* **2009**, *113* 12727.
(86) Zhang, S., Chen, Y., Li, F., Lu, X., Dai, W., Mori, R. *Catal. Today* **2006**, *115*, 61.
(87) Voss, B. A., Bara, J.E., Gin, D.L., Noble, R.D. *Chem. Mater.* **2009**, *21*, 3027.
(88) Maiti, A. *ChemSusChem* **2009**, *2*, 628.
(89) Shin, E. K., Lee, B.C. *J. Chem. Eng. Data* **2008**, *53*, 2728.
(90) Kohler, F., Roth, D., Kuhlmann, E., Wasserscheid, P., Haumann, M. *Green Chem.* **2010**, *12*, 979.
(91) Cimpeanu, V., Parvulescu, V.I., Amoros, P., Beltran, D., Thompson, J.M., Hardacre, C. *Chem. Eur. J.* **2004**, *10*, 4640.
(92) Paun, C., Stere, C., Coman, S. M., Parvulescu, V. I., Goodrich, P., Hardacre, C. *Catal. Today* **2008**, *131*, 98.
(93) Scott, K., Basov, N., Jachuck, R. J. J., Winterton, N., Cooper, A., Davis, C. *Chem. Eng. Res. Des.* **2005**, *83*, 1.
(94) Yang, H., Han, X., Li, G., Wang, Y. *Green Chem.* **2009**, *11*, 1184.
(95) Kume, Y., Qiao, K., Tomida, D., Yokoyama, C. *Catal. Commun.* **2008**, *9*, 369.
(96) Waechtler, M., Sellin, M., Stark, A., Akcakayiran, D., Findennegg, G., Gruenberg, A., Breitzke, H., Buntkowsky, G. *Phys. Chem. Chem. Phys.* **2010**, *12*.
(97) Gordon, P. G., Brouwer, D. H., Ripmeester, J. A *ChemPhysChem* **2010**, *11*, 260
(98) Trewyn, B. G., Whitman, C. M., Lin, V. S. Y. *Nano Lett.* **2004**, *4*, 2139.
(99) Cooper, E. R., Andrews, C. D., Wheatley, P. S., Webb, P. B., Wormald, P., Morris, R. E. *Nature* **2004**, *430*, 1012
(100) Wang, T., Kaper, H., Antonietti, M., Smarsly, B. *Langmuir* **2007**, *23*, 1489
(101) Yu, X. Y., Liu, C.H., Yang, J.G., Wu, H. H., Peng, H., He, M.Y. *Chin. J. Chem.* **2006**, *24*, 1282.
(102) Zhang, J., Ma, Y., Shi, F., Liu, L., Deng, Y. *Microporous Mesoporous Mater.* **2009**, *119*, 97
(103) Corma, A. *Chem. Rev.* **1995**, *95*, 559.
(104) Walcarius, A., Mercier, L. *J. Mater. Chem.* **2010**, *20*, 4478.
(105) Yuan, Z. Y., Su, B.L. *J. Mater. Chem.* **2006**, *16*, 663.
(106) Liu, L., Ma, T., Yuan, Z. *Petrochemical Technology* **2011**, *40*, 237.
(107) Liu, R., Liao, P., Liu, J., Feng, P. *Langmuir* **2011**, 3095.
(108) Foglia, M. L., Alvarez, G.S., Catalano, P.N., Mebert, A.M., Diaz, L.E., Coradin, T., Desimone, M.F. *Recent Patents on Biotechnology* **2011**, *5*, 54.
(109) Kresge, C. T.; Leonowicz, M. E.; Roth, W. J.; Vartuli, J. C.; Beck, J. S. *Nature* **1992**, *359*, 710.
(110) Jones, M. D. D., M. J.; Hermans, S.; Khimyak, Y. Z.; Johnson, B. F. G.; Thomas, J. M. *Angew. Chem. Int. Ed.* **2002**, *41*, 4726.
(111) Hartmann, M. *Chem. Mater.* **2005**, *17*, 4577.
(112) Xu, J., Luan, Z., He, H., Zhou, W., Kevan, L. *Chem. Mater.* **1998**, *10*, 3690.

(113) Selvam, P.; Bhatia, S. K.; Sonwane, C. G. *Ind. Eng. Chem. Res.* **2001**, *40*, 3237.
(114) Langley, P. J.; Hulliger, J. *Chem. Soc. Rev.* **1999**, *28*, 279.
(115) Lee, J.; Kim, J.; Hyeon, T. *Advanced Materials* **2006**, *18*, 2073.
(116) Zhao, D., Feng, J., Huo, Q., Melosh, N., Fredrickson, G. H., Chmelka, B. F., Stucky, G. D. *Science* **1998**, *279*, 548.
(117) Huo, Q., Leon, R., Petroff, P.M., Stucky, G.D. *Science* **1995**, *268*, 1324.
(118) Zhao, D., Huo, Q., Feng, J., Kim, J., Han, Y., Stucky, G.D. *Chem. Mater.* **1999**, *11*, 2668.
(119) Yu, C., Yu, Y., Zhao, D. *Chem. Comm.* **2000**, *7*, 575.
(120) Shen, S., Li, Y., Zhang, Z., Fan, J., Tu, B., Zhou, W. *Chem Comm.* **2002**, *19*, 2212.
(121) Liu, X., Tian, B., Yu, C., Gao, F., Xie, S., Tu, B., Che, R., Peng, L., Zhao, D. *Angew. Chem. Int. Ed.* **2002**, *41*, 3876.
(122) Fan, J., Yu, C., Gao, F., Lei, J., Tian, B., Wang, C., Luo, Q., Tu, B., Zhou, W., Zhao, D. *Angew. Chem. Int. Ed.* **2003**, *115*, 3254.
(123) Kleitz, F.; Choi, S. H.; Ryoo, R. *Chem. Comm.* **2003**, 2136.
(124) Ryoo, R., Kim, J. M. *J. Chem. Soc., Chem. Comm.* **1995**, 711.
(125) Ryoo, R., Shinae, J. *J. Phys. Chem. B* **1997**, *101*, 317.
(126) Ryoo, R., Kim, J.M., Ko, C.H., Shin, C.H. *J. Phys. Chem. A* **1996**, *100*, 17718.
(127) Chen, F. X.; Song, F. B.; Li, Q. Z. *Microporous Mesoporous Mat.* **1999**, *29*, 305.
(128) Huo, Q. S.; Margolese, D. I.; Stucky, G. D. *Chem. Mat.* **1996**, *8*, 1147.
(129) Khushalani, D.; Kuperman, A.; Coombs, N.; Ozin, G. A. *Chem. Mat.* **1996**, *8*, 2188.
(130) Ryoo, R.; Ko, C. H.; Park, I. S. *Chem. Comm.* **1999**, 1413.
(131) Sizun, C.; Raya, J.; Intasiri, A.; Boos, A.; Elbayed, K. *Microporous Mesoporous Mat.* **2003**, *66*, 27.
(132) Johansson, E. M., Ballem, M.A., Cordoba, J.M., Oden, M. *Langmuir* **3011**, *27*, 4994.
(133) Chen, C. Y., Burkett, S.L., Li, H.L., Davis, M.E. *Microporous Mesoporous Mater.* **1993**, *2*, 27.
(134) Steel, A. C., S. W.; Anderson, M. W. J. *Chem. Comm.* **1994**, 1571.
(135) Huo, Q., Margolese, D., Ciesla, U., Demuth, D., Feng, P., Gier, T., Sieger, P., Firouzi, A., Chmelka, B., Schüth, F., Stucky, G.D. *Chem. Mater.* **1994**, *6*, 1176.
(136) Monnier, A. S., F.; Huo, Q.; Kumar, D.; Margolese, D.; Maxwell, R. S.; Stucky, G. D.; Krishnamurty, M.; Petroff, P.; Firouzi, A.; Janicke, M.; Chmelka, B. F.. *Science* **1993**, *261*, 1299.
(137) Soler-Illia, G., Crepaldi, E. L. Grosso, D. Sanchez, C. *Curr. Opin. Colloid Interface Sci.* **2003**, *8*, 109.
(138) De Paul, S. M., Zwanziger, J. W., Ulrich, R.; Wiesner, U., Spiess, H. W. *JACS* **1999**, *121*, 5727.

(139) Van der Voort, P., Benjelloun, M., Vansant, E. F. *J. Phys. Chem. C* **2002**, *106*, 9027.

(140) Hardacre, C., McMath, S.E.J.,Nieuwenhuyzen, M., Bowron, D.T., Soper, A.K. *J. Phys.: Condens. Matter* **2003**, *15*, S159.

(141) Needham, G. F., Willett, R.D., Franzen, H.F. *J. Phys. Chem.* **1984**, *88*.

(142) Bradley, A. E., Hardacre, C., Holbrey, J.D., Johnston, S., McMath, S.E.J., Nieuwenhuyzen, M., Teat, S.J. *Chem. Mater.* **2002**, *14*, 629.

(143) Bowlas, C. J., Bruce, D.W., Seddon, K.R., *J. Chem. Soc., Chem. Comm.* **1996**, 1625.

(144) Gordon, C. M., Holbrey, J.D., Kennedy, A., Seddon, K.R. *J. Mater. Chem.* **1998**, *8*, 2627.

(145) Hitchcock, P. B., Seddon, K.R., Welton, T. *Dalton Trans.* **1993**, 2639.

(146) Gannon, T. J., Law, G., Watson, P.R., Carmichael, A.J., Seddon, K.R. *Langmuir* **1999**, *15*, 8429.

(147) Law, G., Watson, P.R. *Chem. Phys. Lett.* **2001**, *345*, 1.

(148) Law, G., Watson, P.R., Carmichael, A.J., Seddon, K. R. *Phys. Chem. Chem. Phys.* **2001**, *3*.

(149) Iwahashi, T., Nishi, T., Yamene, H., Miyamae, T., Kani, K., Seki, K., Kim, D., Ouchi, Y. *J. Phys. Chem. C* **2009**, *113*, 19237.

(150) Pensado, A. S., Malfreyt, P., Padua, A.A.H. *J. Phys. Chem. B* **2009**, *113*, 14708.

(151) Bhargava, B. L., Balasubramanian, S. *J. Phys. Chem. B* **2007**, *111*, 4477.

(152) Anaikov, V. P. *Chem. Rev.* **2001**, *111*, 418.

(153) Giernoth, R. *NMR Spectroscopy in Ionic Liquids*, 2009; Vol. 290.

(154) Lin, S. T., Ding, M.F., Chang, C.W., Lue, S.S., *Tetrahedron Lett.* **2004**, *47*, 4293.

(155) Lycka, A., Dolecek, R., Simonek, P., Machacek, V. *Magn. Reson. Chem.* **2006**, *44*, 521.

(156) Brenna, S., Posset, T., Furrer, J., Blumel, J. *Chemistry European Journal* **2006**, *12*, 2880.

(157) Heimer, N. E., Del Sesto, R.E., Carper, W.R. *Magn. Reson. Chem.* **2004**, *42*, 71.

(158) Mele, A., romano, G., Giannone, M., Ragg, e., Fronza, G., Raos, G., Marcon, V. *Angew. Chem. Int. Ed.* **2006**, *45*, 1123.

(159) Antony, J. H., Mertens, D., Dolle, A., Wasserscheid, P., Carper, W.R. *ChemPhysChem* **2003**, *4*, 588.

(160) Heimer, N. E., Wilkes, J.S., Wahlbeck, J., Carper, W.R. *J. Phys. Chem. A* **2006**, *110*, 868.

(161) Carper, W. R., Whalbeck, P.G., Antony, J.H., Mertens, D., Dolle, A., Wasserschied, P. *Anal. Bioanal. Chem.* **2004**, *378*, 1548.

(162) Carper, W. R., Whalbeck, P.G., Dolle, A. *J. Phys. Chem. A* **2004**, *108*, 6096.

(163) Krause, C., Sangoro, J.R., Iacob, C., Kremer, F. *J. Phys. Chem. B* **2009**.

(164) Antony, J. H., Dolle, A., Mertens, D., Wasserscheid, P., Carper, W.R., Wahlbeck, P.G. *J. Phys. Chem. A* **2005**, *109*, 6676.

(165) Hayamizu, K., Tsuzuki, S., Seki, S., Nishikawa, K. *J. Phys. Chem. B* **2008**, *112*, 1189.

(166) Imanari, M., Nakakoshi, M., Seki, H., Nishikawa, K. *Chem. Phys. Lett.* **2008**, *459*, 89.

(167) M. Imanari, H. T., H. Seki, K. Nishikawa and M. Tashiro *Magn. Reson. Chem.* **2009**, *47*, 67.

(168) Jones, J. T. A., Wood, C. D., Dickinson, C., Khimyak, Y. Z. *Chem. Mater.* **2008**, *20*, 3385

(169) Trebosc, J., Wiench, J.W., Huh, S., Lin, V.S.Y., Pruski, M. *Journal American Chemical Society* **2005**, *127*, 3057.

(170) Gobel, R., Hesemann, P., Weber, J., Moller, E., Friedrich, A., Beuermann, S., Taubert, A. *Phys. Chem. Chem. Phys.* **2009**, *11*, 3653.

(171) Liu, Y., Wu, G., Fu, H., Jiang, Z., Chen, S., Sha, M. *Dalton Trans.* **2010**, *39*, 3190.

(172) Zhang, J., Zhang, Q., Li, X., Liu, S., Ma, Y., Shi, F., Deng, Y. *Phys. Chem. Chem. Phys.* **2010**, *12*, 1971.

(173) Safavi, a., Maleki, N., Bagheri, M. *J. Mater. Chem.* **2007**, *17*, 1674.

(174) Chen, S., Kobayashi, K., Miyata, Y., Imazu, N., Saito, T., Kitaura, R., Shinohara, H. *Journal American Chemical Society* **2009**, *131*, 14850.

(175) Sha, M., Wu, G., Liu, Y., Tang, Z., Fang, H. *Journal of Physical Chemistry C* **2009**, *113*, 4618.

(176) Sha, M., Wu, G., Liu, Y., Fang, H., Zhu, G. *Journal of physical chemistry C* **2008**, *112*, 18584.

(177) Matsumoto, K., Endo, T. *Macromolecules* **2008**, *41*, 6981.

(178) Sobota, M., Nikiforidis, I., Hieringer, W., Paape, N., Happel, M., Steinruck, H. P., Gorling, A., Wassercheid, P., Laurin, M., Libuda, J. *Langmuir* **2010**, *26*, 7199.

(179) Kosmulski, M., Szafran, M., Saneluta, C., Marczewska-Boczkowska, K. *J. Colloid Interface Sci.* **2005**, *291*, 214.

(180) Kohler, R., Restolho, J., Krastev, R., Simizu, K., Canongia Lopes, J.N., Saramago, B. *Journal of Physical Chemistry Letters* **2001**, *2*, 1551.

(181) Rivera-Rubero, S., Baldelli, S. *J. Phys. Chem. B* **2006**, *110*, 4756.

(182) Cimatu, K. A., Baldelli, S. *Journal of Physical Chemistry C* **2009**, *113*, 16575.

(183) Hayes, R., Warr, G.G., Atkin, R. *Phys. Chem. Chem. Phys.* **2010**, *12*, 1709.

(184) Liu, Y., Zhang, Y., Wu, G., Hu, J. *Journal American Chemical Society* **2006**, *128*, 7456.

(185) Yokota, Y., Harada, T., Fukui, K. *Chemical Communications (Cambridge)* **2010**, *46*, 8627.

(186) Schafer, T., Di Paolo, R.E., Franco, R., Crespo, J.G. *Chemical Communications (Cambridge)* **2005**, 2594.

(187) Gjikaj, M., Brockner, W., Namyslo, J., Adam, A. *Cryst. Eng.* **2008**, *10*, 103.

(188) Xu, X. H., Hussey, C.L. *Journal of Electrochemical Society* **1992**, *139*, 1295.

(189) Endes, F., Freyland, W. *J. Phys. Chem. B* **1998**, *102*, 10229.

(190) Kluner, R. P., Dolle, A. *J. Phys. Chem. A* **1997**, *101*, 1657.

(191) Antony, J. H., Mertens, D., Breitenstein, T., Dolle, A., Wasserscheid, P., Carper, W.R. *Pure Appl. Chem.* **2004**, *76*, 255.

(192) Hardacre, C., McMath, S.E.J., Holbrey, J.D. *Chemical Communications (Cambridge)* **2001**, 367.

(193) Giernoth, R., Bankmann, D. *Tetrahedron Lett.* **2006**, *47*, 4293.

(194) R. Giernoth, D. B. a. N. S. *Green Chemistry* **2005**, *7*, 279.

(195) Atkins, P. W. *The Elements of Physical Chemistry*; 3rd Edition ed.; Oxford University Press: Oxford, 2003.

(196) Atkins, P. W., De Paula, J. *Physical Chemistry*; 7th Edition ed.; Oxfor University Press: New York, 2002.

(197) Francis Weston Sears, F. W., Zemansky, M.W., Freedman, R.A., Young, H.D., Gaines, J.D. *Sears and Zemansky's University Physics*; 10th edition ed.; Addison Wesley, 1999.

(198) Weller, M. T. *Inorganic Materials Chemistry*; Oxford University Press: Oxford, 1995; Vol. 23.

(199) Nobel Web AB, C., F., Carlson, P. 2001
Vol. 2010.

(200) von Laue, M. *Ann. Physik* **1916**, *50*, 33.

(201) Fletcher, D. A., McMeeking, R.F., Parkin, D. *Journal of Chemical Information and Computer Science*
1996, *36*, 746.

(202) Bragg, W. H., Bragg, W. L. *The Crystalline State*; Macmillan
New York, 1949; Vol. 1.

(203) Hook, J. R., Hall, H. E. *Solid State Physics*; Second Edition ed.; John Wiley & Sons Chitchester, 2003.

(204) Leofanti, G., Padovan, M., Tozzola, G., Venturelli, B. *Catal. Today* **1998**, *41*, 207.

(205) Gregg, S. J., Sing, K.S.W. *Adsorption, surface Area and Porosity*; Academic Press: London, 1982.

(206) Unger, K. K., Roquerol, J., Sing, K.S.W., Kral, H. *Characterisation of Porous Solids*; Elsevier: Amsterdam, 1988.

(207) Roquerol, J., Rodriguez-Rienoso, F., Sing, K.S.W., Unger, K.K. *Characterisation of Porous Solids III*; Elsevier: Amsterdam, 1994.

(208) Rodriguez-Reinoso, F., Roquerol, J., Sing, K.S.W., Kral, H. *Charaterisation of Porous Solids II*; Elsevier: Amsterdam, 1991.

(209) Attard, G., Barnes, C. *Surfaces*; Oxford University Press: Oxford, 2004.

(210) Kaneko, K. *J. Membr. Sci.* **1994**, *96*, 59.

(211) Sing, K. S. W., Everett, D. H., Haul, R. A. W., Moscou, L., Pierotti, R. A., Rouquerol, J., Siemieniewska, T. *Pure Appl. Chem.* **1985**, *57*, 603.

(212) S. Brunauer, L. S. D., W.E. Deming, E. Teller *J. Am. Chem. Soc.* **1940**, *62*, 1723

(213) Brunauer, S. *Physical Adsorption of Gases and Vapours, OUP,*; Oxford University Press, 1944

(214) S. Brunauer, P. H. E., E. Teller *Journal of the American Chemical Society*

1938, *60*, 309.

(215) Lippens, B. C., de Boer, J.H. *J. Catal.* **1965**, *4*, 319.

(216) Barret, E. P., Joyner, L.G., Halenda, P.P. *J. Am. Chem. Soc.* **1953**, *73*, 373.

(217) Davies, G. M., Seaton, N.A. *Carbon* **1998**, *36*, 1473.

(218) Schauer, J., Sikora, A., Pliskova, M., Malis, J., Mazur, P., Paidar, M., Bouzek, K. *J. Membr. Sci.* **2011**, *367*, 332.

(219) Hore, P. J. *Nuclear Magnetic Resonance*; Oxford University Press: Oxford, 2004.

(220) Levitt, M. H. *Spin Dynamics: Basics of Nuclear Magnetic Resonance*; 2nd Edition ed.; WILEY, 2008.

(221) Laws, D. D., Bitter, H-M., L., Jerschow, A. *Angew. Chem. Int. Ed.* **2002**, *41*, 3096.

(222) Scholz, I., Hodgkinson, P., Meier, B.H., Ernst, M. *J. Chem. Phys.* **2009**, *130*, 114510.

(223) Duer, M. J. *Introduction to Solid-State NMR Spectroscopy*; Blackwell Publishing, 2004.

(224) Hatton, B. D., Landskron, K., Hunks, W. J., Bennett, M. R., Shukaris, D., Perovic, D. D., Ozin, G. A. *Mater. Today* **2006**, *9*, 22.

(225) Detken, A., Hardy, E. H., Ernst, M., Meier, B. H. *Chem. Phys. Lett.* **2002**, *356*, 298.

(226) Cobo, M. F., Malinakova, K., Reichert, D., Saalwatchter, K., deAzevedo, E.R. *Phys. Chem. Chem. Phys.* **2009**, *11*, 7036.

(227) van Rossum, B. J., de Groot, C.P., Ladizhansky, V., Vega, S., de Groot, H.J.M. *Journal American Chemical Society* **2000**, *122*, 3465.

(228) Ladizhansky, V., Vega, S. *J. Chem. Phys.* **2000**, *112*, 7158.

(229) Ladizhansky, V., Vinogradov, E., van Rossum, B.-J., de Groot, H.J.M., Vega, S. *J. Chem. Phys.* **2003**, *118*, 5547.

(230) B.-J. van Rossum, B. J., de Groot, C.P., Ladizhansky, V., Vega, S., de Groot, H.J.M. *Journal American Chemical Society* **2000**, *122*, 3465.

(231) Lesage, A., Sakellariou, D., Hediger, S., Eléna, B., Charmont, P., Steuernagel, S., Emsley, L. *J. Magn. Reson., Ser. A* **2003**, *163*, 105.

(232) Hartmann, S. R., Hahn, E.L. *Phys. Rev. A* **1962**, *128*, 2042.

(233) Engelke, F., Kind, T., Michel, D., Pruski, M., Gerstein, B.C. *J. Magn. Reson., Ser. A* **1991**, *95*, 286.

(234) Ambelmann, K., Totsche, K. U., Knicker, H., Kogel-Knabner, I. *Solid State Nucl. Magn. Reson.* **2004**, *25*, 252.

(235) Kaflak, A., Kolodziejski, W. *Magn. Reson. Chem.* **2008**, *46* 335.

(236) Khimyak, Y. Z., Klinowski, J. *Phys. Chem. Chem. Phys.* **2001**, *3*, 616

(237) Khimyak, Y. Z., Klinowski, J. *Phys. Chem. Chem. Phys.* **2001**, *3*, 2544

(238) Xiaoling, W., Shanmin, Z., Xuewen, W. *J. Magn. Reson., Ser. A* **1988**, *77*, 343.

(239) Parker, A. A. *Solid State NMR of Polymers: A review of Molecular Motions and Morphology*, A. A. Parker Consulting and Development, 2004.

(240) Claridge, T. D. W. *High-Resolution NMR Techniques in Organic Chemistry*; 2nd Edition ed.; Elsevier, 2009.

(241) Imanari, M., Uchida, K., Miyano, K., Seki, H., Nishikawa, K. *Phys. Chem. Chem. Phys.* **2010**, *12*, 2959.

(242) Khimyak, Y. Z., Klinowski, J. *Phys. Chem. Chem. Phys.* **2001**, *3*, 616.

(243) Schaefer, J., Stejskal, E. O., Sefcik, M. D., *Macromolecules* **1980**, *13*, 1121.

(244) Xu, W., Wang, L. M., Nieman, R. A., Angell, C. A. *J. Phys. Chem. B* **2003**, *107*, 11749.

(245) Medick, P., Blochowichz, T., Vogel, M., Rossler, E. *J. Non-Cryst. Solids* **2002**, *307-310*, 565.

(246) Dosseh, G., Xia, Y. D., Alba-Simionesco, C. *J. Phys. Chem. B* **2003**, *107*, 6445.

(247) Lusceac, S. A., Koplin, C., Medick, P., Vogel, M., Brodie-Linder, N., LeQuellec, C., Alba-Simionesco, C., Rossler, E. A. *J. Phys. Chem. B* **2004**, *108*, 16601.

(248) Aksnes, D. W.; Gjerdaker, L.; Kimtys, L.; Forland, K. *Phys. Chem. Chem. Phys.* **2003**, *5*, 2680.

(249) Gedat, E.; Schreiber, A.; Albrecht, J.; Emmler, T.; Shenderovich, I.; Findenegg, G. H.; Limbach, H. H.; Buntkowsky, G. *J. Phys. Chem. B* **2002**, *106*, 1977.

(250) Aksnes, D. W., Kimtys, L. *Solid State Nucl. Magn. Reson.* **2004**, *25*, 146.

(251) Masierak, W., Emmler, T., Gedat, E., Schreiber, A., Findenegg, G. H., Buntkowsky, G. *J. Phys. Chem. B* **2004**, *108*, 18890.

(252) Shenderovich, I. G., Buntkowsky, G., Schreiber, A., Gedat, E., Sharif, S., Albrecht, J., Golubev, N. S., Findenegg, G. H., Limbach, H. H. *J. Phys. Chem. B* **2003**, *107*, 11924.

(253) Gedat, E., Schreiber, A., Findenegg, G. H., Shenderovich, I., Limbach, H. H., Buntkowsky, G. *Magn. Reson. Chem.* **2001**, *39*, S149.

(254) Vyalikh, A., Emmler, T., Shenderovich, I., Zeng, Y., Findenegg, G. H., Buntkowsky, G. *Phys. Chem. Chem. Phys.* **2007**, *9*, 2249.

(255) buntkowsky, G., Breitzke, H., Adamezyk, A., Roelofs, F., Emmler, T., Gedat, E., Grunburg, B., Xu, Y., Limbach, H. H., Shenderovich, J., Vyalikh, A., Findenegg, G. H. *Phys. Chem. Chem. Phys.* **2007**, *9*, 4843.

(256) Remsing, R. C., Wildin, J.L., Rapp, A. L., Moyna, G. *J. Phys. Chem. B* **2007**, *111*, 11619.

(257) Petit, D., Korb, J. P., Levitz, P., Le Bideau, J., Brevet, D. *C. R. Chim.* **2010**, *13*, 409.

(258) Canongia Lopes, J. N. A., Pa´dua, A.A.H *J. Phys. Chem. B* **2006**, *110*, 3330.

(259) Chang, T. M., Dang, L.X., Devanathan, R., Dupuis, M. *J. Phys. Chem. A* **2010**, *114*, 12764.

(260) Wang, S., Li, S., Cao, Z., Yan, T. *Journal of Physical Chemistry C.*

(261) Sarkisov, L., Monson, P.A. *Langmuir* **2001**, *17*, 7600.

(262) Sergey M. Melnikov, S. M., Heoltzel, A., Seidel-Morgenstern, A., Tallarek, U. *Anal. Chem. Symp. Ser.* **2011**, *83*, 2569.

(263) Nooruddin, N. S., Wahlbeck, P.G., Carper, W.R. *Tribology Letters* **2009**, *36*, 147.

(264) Mo, Y., Zhao, W., Zhu, M., Bai, M. *Tribology Letters* **2008**, *32*, 143.

(265) Yu, G., Yan, S., Zhou, F., Liu, W., Liang, Y., Yan, S. *Tribology Letters* **2007**, *25*, 197.

(266) Nooruddin, N. S., Wahlbeck, P.G., Carper, W.R. *J. Mol. Struct.* **2007**, *822*, 1.

(267) C. Li, Y. W., Y. Guo, X. Lin, Y. Guo, Z. Zhang, Y. Wang, G. Lu *Chem. Mater.* **2007**, *19*, 173.

(268) E.P. Barret, L. G. J., P.H. Halendar *J. Am. Chem. Soc.* **1951**, *73*, 373.

(269) A. E. Bennett, C. M. R., M. Auger, K. V. Lakshmi and R. G. Griffin *J. Phys. Chem. A* **1995**, *103*, 6951

(270) Hodgkinson, P. *Prog. Nucl. Magn. Reson. Spectrosc.* **2005**, *46*, 197.

(271) Kolodziejski, W., Klinowski, J. *Chem. Rev.* **2002**, *102*, 613.

(272) States, D. J., Haberkorn, R. A., Ruben, D. J. *J. Magn. Reson., Ser. A* **1982**, *48*, 286.

(273) Keeler, J., Neuhaus, D. *Journal of Magnetic Resonance Series A* **1985**, *63*, 454.

(274) Keeler, J. *Understanding NMR Spectroscopy* John Wiley & Sons Ltd., 2005.

(275) Accelrys San Diego, 2005.

(276) Duran, T., Millange, F., Ferey, G., Walton, K.S., Snurr, R.Q. *Journal of Physical Chemistry C* **2007**, *111*, 15350.

(277) Rappe, A. K., Casewit, C.J., Colwell, K.S., Goddard III, W.A., Skiff, W.M. *J. Am. Chem. Soc.* **1992**, *1992*, 10024.

(278) A. R. Choudhury, N. W., A. Steiner, A. I. Cooper and K. A. Johnson *J. Am. Chem. Soc.* **2005**, *127*, 16792.

(279) Wanga, J., Zhenga, S., Liua, J., Xua, Z. *Chem. Eng. J. (Amsterdam, Neth.)* **2010**, *165*, 10.

(280) Khodakov, A. Y., Zholobenko, V.L., Bechara, R., Durand, D. *Microporous Mesoporous Mater.* **2005**, *79*, 29.

(281) Venna, S. R., Carreon, M.A. *Langmuir* **2011**, *27* 2888.

(282) Lin, Y. C.; Chou, H. L.; Sarma, L. S.; Hwang, B. J. *Chem. Eur. J.* **2009**, *15*, 10658.

(283) Bakhmutov, V. I. *Practical NMR Relaxation for Chemists*; WILEY, 2004.

(284) P'Pool, S. J., Klingshirn, M. A., Rogers, R. D., Shaughnessy, K. H. *J. Organomet. Chem.* **2005**, *690*, 3522.

(285) Shi, L., Zou, Y., He, H. *Chem. Lett.* **2001**, 1164.

(286) Zhao, X. S., Lu, G. Q., Whttaker, A. K., Millar, G. J., Zhu, H. Y. *J. Phys. Chem. B* **1997**, *101*, 6525.

(287) Zhao, X. S., Lu, G. Q. *J. Phys. Chem. B* **1998**, *102*, 1556.

(288) Zhao, X. S., Lu, G. D., Hub, X. *Microporous Mesoporous Mater.* **2000**, *41*, 37.

(289) Ghanbari-Siahkali, A., Philippou, A., Dwyer, J., Anderson, M. W. *Appl. Catal., A* **2000**, *192*, 57.

(290) Grunberg, B.; Emmler, T.; Gedat, E.; Shenderovich, J.; Findenegg, G. H.; Limbach, H. H.; Buntkowsky, G. *Chem. Eur. J.* **2004**, *10*, 5689.

(291) Cuia, X., Zinb, W.C., Choc, W. J., Hac, C.S. *Mater. Lett.* **2005**, *59*, 2257.

(292) Trewin, A., Willock, D.J., Cooper, A.I. *Journal of Physical Chemistry C* **2008**, *112*, 20549.

(293) Connolly, M. L. *Science* **1983**, *221*, 4612.

(294) DuPont, J. *Brazilian Chemistry Society* **2004**, *15*, 341.

(295) Golovanov, D. G., Lyssenko, K.A., Antipin, M.Y., Vygodskii, Y.S., Lozinskaya, E.I., Shaplov, A.S. *Cryst. Eng.* **2005**, *7*, 53.

(296) M. Kanakubo, Y. H., K. Minami, T. Aizawa and H. Nanjo *Chem. Commun. (Cambridge, U. K.)* **2006**, 1828.

(297) Neouze, M. A., Litschauer, M. *J. Phys. Chem. B* **2008**, *112*, 16721.

(298) Mickelson, W., Aloni, S., Han, W.Q., Cumings, J., Zettl, A. *Science* **2003**, *300*, 467.

(299) Lunstroot, K., Driesen, K., Nockermann, van Hecke, K., van Meervelt, L., P., Gorller-Walrand, C., Binnemans, K., Bellayer, S., Viau, L., Le Bideau, J., Vioux, A. *Dalton Trans.* **2009**, 298.

(300) Gobel, R., Friedrich, A., Taubert, A. *Dalton Trans.* **2010**, *39*, 603.

(301) Shi, F., Deng, Y. *Spectrochim. Acta* **2005**, *62*, 239.

(302) Zhang, J., Zhang, Q., Shi, F., Zhang, S., Qiao, B., Liu, L., Ma, Y., Deng, Y. *Chem. Phys. Lett.* **2008**, *461*, 229.

(303) Kim, J. M., Kwak, J.H., Jun, S., Ryoo, R. *J. Phys. Chem. A* **1995**, *99*, 16742.

(304) Kruk, M., Jaroniec, M., Kim, J.M., Ryoo, R. *Langmuir* **1999**, *15*, 5279.

(305) Bruker; Bruker.

(306) Santos, C. S., Rivera-Rubero, S., Dibrov, S., Baldelli, S. *Journal of Physical Chemistry C* **2007**, *111*, 7682.

(307) D. Zhao, Q. H., J. Feng, N. Melosh, G. H. Fredrickson, B. F. Chmelka and G. D. Stucky *Science* **1998**, *279*, 548.

(308) Khlobystov, A. N., Britz, D. A., Briggs, G. A. D. *Acc. Chem. Res.* **2005**, *38*, 467.

(309) Cai, H., Yang, R., Yang, G., Huang, H., Nie, F. *Nanotechnology* **2011**, *22*, 1.

(310) Christenson, H. K. *Journal of Physical Condensed Matter* **2001**, *13*

(311) Stanley, H. E. *Mean field theory of magnetic phase transitions: Introduction to phase transitions and critical phenomena*; Oxford University Press, 1971.

(312) Singh, M. P., Singh., R.K., Chandra, S. *J. Phys. Chem. B* **2011**.

(313) Singh, M. P., Singh., R.K., Chandra, S. *ChemPhysChem* **2010**, *11*, 2036.

(314) Hill, T. L. *Statistical Mechanics, Principles and Selected Applications*; McGraw-Hill: New York, 1956.

(315) Blesic, M., Swadzba-Kwasny, M., Belhocine, T., Nimal Gunaratne, N.Q., Canongia Lopes, J.N., Costa gomes, M.F., Padua, A.A.H., Seddon, K.R., Rebelo, L.P.N. *Phys. Chem. Chem. Phys.* **2009**, *11*, 8939.

(316) Webber, J. B. W. *Prog. Nucl. Magn. Reson. Spectrosc.* **2010**, *56*, 78.

(317) Lungwitz, R., Spange, S. *Journal of Physical Chmistry C* **2008**, *112*, 19443.

(318) Beiner, M., Rengarajan, G.T., Pankaj, S., Enke, D., Steinhart, M. *Nano Lett.* **2007**, *7*, 1381.

(319) Apperley, D. C., Forster, A.H., Fournier, R., Harris, R.K., Hodgkinson, P., Lancaster, R.W., Rades, T *Magn. Reson. Chem.* **2005**, *43*, 881.

(320) Voelkel, R. *Angew. Chem. Int. Ed.* **1988**, *27*, 1468.

(321) Schaefer, J., Stejskal, E.O., Buchdahl, R. *Macromolecules* **1977**, *10*, 384.

(322) Schaefer, J., Sefcik, M.D., Stejskal, E.O., McKay, R.A. *Macromolecules* **1984**, *17*, 1118.

(323) Jack, K. S., Whittaker, A.K. *Macromolecules* **1997**, *30*, 3560.

(324) Neiner, D., Okamoto, N.L., Condron, C.L., Ramasses, Q.M., Yu, P., Browning, N.D., Kauzlarich, S.M. *Journal American Chemical Society* **2007**, *129*, 13857.

(325) Strobel, T. A., Taylor, C.J., Hester, K.C., Dec, S.F., Koh, C.A., Miller, K.T., Sloan, E.D. *J. Phys. Chem. B* **2006**, *110*, 17121.

(326) Zhang, J. S., Lee, S., Lee, J.W. *Ind. Eng. Chem. Res.* **2007**, *46*, 6353.

(327) Anderson, R., Chapoy, A., Tohidi, B. *Langmuir* **2007**, *23*, 3440.

(328) Anderson, R., Llamedo, M, Tohidi, B., Burgass, R.W. *J. Phys. Chem. B* **2003**, *107*, 3507.

(329) Su, F., Bray, C. L., Tan, B., Cooper, A. I. *Advanced Materials* **2008**, *20*, 2663.

(330) Su, F., Bray, C. L., Carter, B.O., Overend, G., Cropper, C., Iggo, J.A., Khimyak, Y.Z., Fogg, A.M., Cooper, A.I. *Advanced Materials* **2009**, *21*, 2383.

(331) Wang, W. X., Bray, C.L., Adams, D.J., Cooper, A.I. *Journal American Chemical Society* **2008**, *130*, 11608.

(332) Dyadin, Y. A., Bondaryuk, I. V., Aladko, L. S. *J. Struct. Chem.* **1995**, *36*, 995.

(333) McMullan, R., Jeffrey, G. A. *J. Chem. Phys.* **1959**, *31*, 1231.

(334) Aladko, L. S., Dyadin, Y. A., Rodionova, T. V., Terekhova, I. S. *J. Struct. Chem.* **2002**, *43*, 990.

(335) Chapoy, A., Anderson, R.,Tohidi, B. *Journal American Chemical Society* **2007**, *129*, 746.

(336) Hashimoto, S., Sugahara, T., Moritoki, M., Sato, H., Ohgaki, K. *Chem. Eng. Sci.* **2008**, *63*, 1092.

(337) Shin, K., Choi, S., Cha, J.H., Lee, H. *Journal American Chemical Society* **2008**, *130*, 7180.

(338) Kida, M., Hori, A., Sakagami, H., Takeya, S., Kamata, Y., Takahashi, N., Ebinuma, T., Narita, H. *J. Phys. Chem. A* **2011**, *115*, 643.

(339) Lee, H., Lee, J.W., Kim, D.Y., Park, J., Seo, Y.T., Zeng, H., Moudrakovski, I.L., Ratcliffe, C.I., ripmeester, J.A. *Nature* **2005**, *434*, 743.

(340) Aladko, L. S., Dyadin, Y. A., Mikina, T. V. *Russ. J. Gen. Chem.* **2003**, *73*, 503.

(341) Sheldrick, G. M. *Acta Crystallogr. Sect. A: Found. Crystallogr.* **2008**, *64*, 112.

(342) Jeffrey, G. A. *Incl. Phenom.* **1984**, *1*, 211.

(343) Kobayashi, R., Katz, D.L. *Trans. Am. Inst. Mining Metall. Eng.* **1949**, *186*, 66.

(344) Bondi, A. *J. Phys. Chem. A* **1964**, *68*, 441.

(345) Bonamico, M., McMullan, R.K., Jeffrey, G.A. *J. Chem. Phys.* **1962**, *37*, 2219.

(346) Komarov, V. Y., Rodionova, T.V., Terekhova, I.S., Kuratieva, N.V. *J. Inclusion Phenom. Macrocyclic Chem.* **2007**, *59*, 11.

(347) Sloan, E. D., Koh, C.A. *Clathrate Hydrates of Natural Gases*; 3rd Edition ed.; CRC Press: Boca Raton, 2008.

(348) Lipkowski, J., Suwinska, K., Rodionova, T. V., Udachin, K. A., Dyadin, Y. A. *J. Inclusion Phenom.* **1994**, *17*, 137.

(349) Aladko, L. S., Dyadin, Y. A., Rodionova, T. V., Terekhova, I. S. *J. Mol. Liq.* **2003**, *106*, 229.

(350) Giavarini, C., Maccioni, F., Santarelli, M. L. *J. Therm. Anal. Calorim.* **2006**, *84*, 419.

(351) Giavarini, C., Maccioni, F., Politi, M., Santarelli, M. L. *Energy Fuels* **2007**, *21*, 3284.

(352) Li, D. L., Du, J. W., Fan, S. S., Liang, D. Q., Li, X. S., Huang, N. S. *J. Chem. Eng. Data* **2007**, *52*, 1916.

(353) Arjmandi, M., Chapoy, A., Tohidi, B. J. *J. Chem. Eng. Data* **2007**, *52*, 2153.

(354) Wood, C. D., Tan, B., Trewin, A., Su, F., Rosseinsky, M. J., Bradshaw, D., Sun, Y., Zhou, L., Cooper, A. I. *Advanced Materials* **2008**, *20*, 1916.

(355) Rowsell, J. L. C., Spencer, E. C., Eckert, J., Howard, J. A. K., Yaghi, O. M. *Science* **2005**, *309*, 1350.

(356) Ma, S. Q., Sun, D. F., Simmons, J. M., Collier, C. D., Yuan, D. Q., Zhou, H. C. *Journal American Chemical Society* **2008**, *130*, 1012.

Appendix I

Reversible Hydrogen Storage in Hydrogel Clathrate Hydrates

By *Fabing Su, Christopher L. Bray, Benjamin O. Carter, Gillian Overend, Catherine Cropper, Jonathan A. Iggo, Yaroslav Z. Khimyak, Andrew M. Fogg,* and *Andrew I. Cooper**

The use of clathrate hydrates as potential hydrogen (H_2)-storage materials[1] has attracted considerable attention recently.[2–4] Clathrate hydrates with cage-like, hydrogen-bonded structures comprising mostly water molecules might offer safe and environmentally friendly materials for H_2 storage under moderate conditions. However, there are three challenges to be addressed before practical applications can be achieved: the relatively low H_2-storage capacity; the high pressures required for clathrate formation and stabilization; and the slow kinetics associated with gas enclathration. The work of Florusse et al.[5] has demonstrated that the pressure at which H_2 enclathration occurs can be significantly reduced from 200 to 7 MPa by adding a stabilizer (tetrahydrofuran, THF). Lee et al.[6] reported a H_2-storage capacity around 4 wt% at 12 MPa and 270 K, and the composition of the clathrate hydrates was tuned to optimize gas-storage capacity,[6,7] although subsequent studies suggest lower storage capacities under similar conditions.[8–11] Other clathrates capable of retaining a significant amount of H_2 at moderate pressures and temperatures are being investigated.[12–15]

The extremely slow kinetics of H_2 encapsulation into clathrate hydrate cages,[6,8,16,17] resulting from mass diffusion in a bulk solid phase, may be a generic limitation for the applicability of clathrates in the storage of H_2 and other gases.[2,4] It has been reported that mass diffusion can be enhanced by increasing the surface-to-volume ratio of clathrate hydrates using crushed small ice particles[8,16] or by dispersing the clathrate hydrate on silica-bead supports[6] or on a polymer substrate.[18] However, the use of small ice particles is inconvenient for multiple storage/release cycles, since these revert to bulk water upon melting. Similarly, silica beads have relatively high densities and tend to reduce storage capacities considerably.[19] Thus, improving gas enclathration kinetics and obtaining good rechargeability/recyclability are basic challenges in the development of clathrate hydrates as feasible storage materials for H_2 and other gases. In our previous work,[20] we demonstrated a method that dramatically improved the kinetics and reusability of gas clathrates using an ultralow density, emulsion-templated polymer material as a support. However, the H_2 storage capacity was low under moderate conditions of pressure and temperature, possibly due to the highly hydrophobic nature of the polymer and inefficient wetting of the pore structure. We have also demonstrated that "dry water"[21] is effective in accelerating the formation of methane clathrates,[22] but this approach was unsuccessful for H_2 using THF–H_2O mixtures, because the presence of THF destabilized the dry water inverse foam.

Here, we investigate the possibility of using particulate hydrophilic water-swellable polymer networks as supports for improving the kinetics and recyclability of H_2 enclathration within clathrate hydrates. Superabsorbent polymer networks, such as lightly crosslinked poly(acrylic acid) sodium salt (PSA), are relatively inexpensive and have been used widely in sanitary applications (e.g., in diapers) because of their excellent water-absorption and -retention capabilities. Figure 1 illustrates schematically the clathration process using swollen PSA particles as a H_2-storage medium. The polymer particles are first immersed in a THF–H_2O solution and swell to form a hydrogel at room temperature. Upon cooling below a specific temperature, the THF–H_2O solution within the hydrogel particles forms a clathrate hydrate that can encapsulate H_2. Conversely, upon heating, the clathrate hydrate decomposes, releasing H_2. Because the gels are superabsorbent, only small amounts are required to hold very substantial quantities of aqueous solution – this is the principle behind disposable diapers. The polymer-particle size and its surface chemistry can be easily tailored by synthesis conditions or post-treatment, and thus there is broad potential to optimize interactions between the support and the clathrate hydrate. We have found that it is possible to use hydrogels to enhance the encapsulation of H_2 in terms of kinetics, recyclability, and capacity. After dispersal in THF–H_2O solution (20.0 g), dry PSA particles (1.0 g; Fig. 1b) were transformed into swollen and transparent hydrogel particles (Fig. 1c). The PSA particles readily absorbed all of the solution at this solution-support ratio. This produces a particulate gel material which, unlike ground/sieved ice particles, does not agglomerate or melt to form bulk water upon heating and gas release. Figure 1d shows the morphology of a THF–H_2O hydrogel after five cycles of H_2

[*] Prof. A. I. Cooper, Dr. F. Su, Dr. C. L. Bray, Dr. B. O. Carter, G. Overend, C. Cropper, Dr. J. A. Iggo, Dr. Y. Z. Khimyak, Dr. A. M. Fogg
Department of Chemistry
University of Liverpool
Crown Street, Liverpool L69 7ZD (UK)
E-mail: aicooper@liverpool.ac.uk
Prof. A. I. Cooper, Dr. F. Su, Dr. C. L. Bray, Dr. B. O. Carter
G. Overend, C. Cropper, Dr. J. A. Iggo, Dr. Y. Z. Khimyak,
Dr. A. M. Fogg
Centre for Materials Discovery
University of Liverpool
Crown Street, Liverpool L69 7ZD (UK)

DOI: 10.1002/adma.200803402

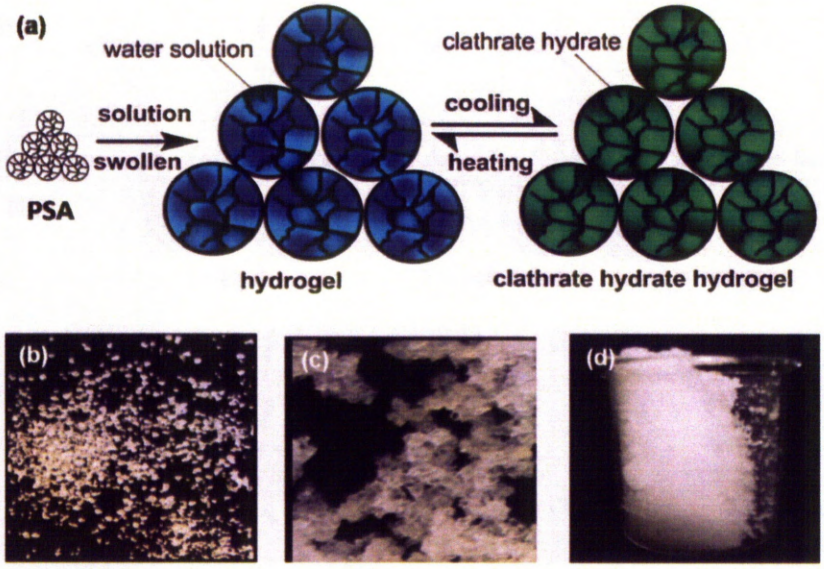

Figure 1. a) Schematic illustration of clathrate hydrate dispersed within gel particles. b) Dry PSA, particle size <1000 μm. c) Fresh THF–H_2O hydrogel particles before exposure to H_2. d) THF–H_2O hydrogel after five cycles of H_2 enclathration and dissociation.

enclathration followed by dissociation, clearly indicating there is no phase separation (no separated water in the bottom of the beaker). Figure 2a shows the kinetic gas uptake curves at 270.0 K for H_2 encapsulation in THF–H_2O clathrate hydrate within PSA hydrogels and, for comparison, in an emulsion-templated polymer.[20] The kinetics of H_2 uptake in bulk, unmixed THF–H_2O solution with an equivalent volume of glass beads is also shown as a control. The amount of H_2 enclathrated was calculated using GASPAK v3.41 software considering nonideality factors with a defined baseline and pressure drops (see Fig. S2, Supporting Information). These uptakes, as calculated by pressure changes, were also confirmed by volumetric gas-release experiments (see Supporting Information). The H_2 uptake shown is normalized to the total mass of both THF–H_2O solution and polymer support used (emulsion-templated polystyrene or PSA). An expansion of the initial uptake kinetics for Figure 2a (<100 min) can be found in Figure S3, in the Supporting Information.

The H_2-uptake kinetics in the bulk control experiment, curve a), are very slow, consistent with our previous results[20] and with the observations of others. The use of an emulsion-templated polymer as a support, curve b), greatly enhances the H_2 uptake kinetics, and the gas uptake levels off after around 150 min.[20] The H_2-enclathration capacity for this system was around 0.15 wt%, low but a significant improvement compared with bulk clathrate shown in curve a) (around 0.016 wt% at 150 min), and consistent with a system where only some of the THF solution wets the pore structure of the emulsion-templated polymer. It should be noted that the maximum equilibrium H_2 uptake in this system might be expected to be around 0.45 wt% under these conditions based on previous studies;[8] as such, 0.15 wt% represents around 33% of this total possible capacity.

Curve c) in Figure 2a shows the kinetic plot for H_2 encapsulation in preformed THF–H_2O clathrate hydrogel hydrate (20.0 g solution) supported in PSA (1.0 g). At 1000 min, the capacity is around 0.25 wt%, compared with 0.15 wt% obtained using the emulsion-templated polymer. The initial uptake is slower than for the porous polymer system, but the final gas capacity is significantly higher (around 56% of total possible capacity under these conditions). This demonstrates the effectiveness of using PSA as a support for H_2 encapsulation with respect to bulk solutions. Curves d–g show the kinetic plots of H_2 encapsulation in preformed THF–H_2O clathrate hydrate with THF–H_2O solution (20.0 g) supported on PSA (3.0 g) for four cycles. The relatively small variability in curves d–g demonstrates the repeatability of the H_2 encapsulation process using this PSA support. At 1000 min, the encapsulated H_2 capacity in curve g) is around 0.29 wt%, which is around two times that obtained using the emulsion-templated polymer, curve b), and around 5.5 times that in the bulk. At around 4000 min, the capacity for bulk hydrate in curve a) is about 0.08 wt%. This uptake is achieved in 6.5 min using PSA (see Fig. S3, Supporting Information), a 600-fold rate increase. The maximum H_2 capacity of around 0.30 wt% in our experiments constitutes 67% of the values reported previously[8] when crushed THF–H_2O clathrate particles (45 or 250 μm) were employed. Previous studies have measured H_2 capacity in hydrates indirectly using Raman

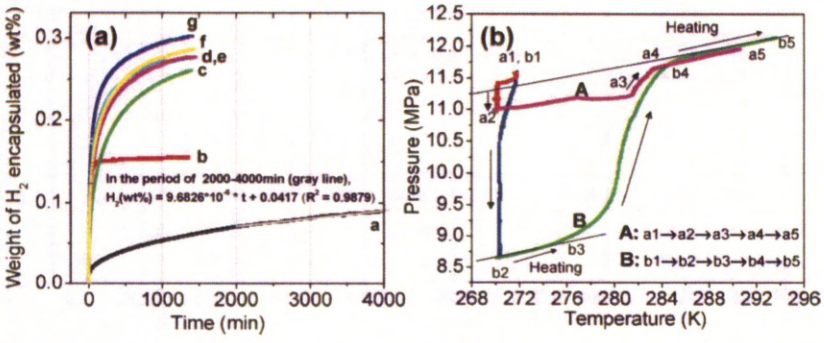

Figure 2. a) Kinetic plots of H_2 encapsulation in preformed THF–H_2O clathrate hydrate at 270.0 K: a) 20.0 g THF–H_2O solution and 3.0 cm^3 glass beads; b) 20.0 g THF–H_2O solution and 3.0 g emulsion-templated polystyrene; c) 20.0 g THF–H_2O solution and 1.0 g PSA; d) 20.0 g THF–H_2O solution and 3.0 g PSA (3rd run); e) 20.0 g THF–H_2O solution and 3.0 g PSA (4th run); f) 20.0 g THF–H_2O solution and 3.0 g PSA (2nd run); and g) 20.0 g THF–H_2O solution and 3.0 g PSA (1st run). b) Pressure–Temperature plot of enclathration and subsequent dissociation for H_2-THF-H_2O system under H_2 pressure with and without PSA: A) 20.0 g of THF–H_2O solution and 3.0 cm^3 of glass beads; B) 20.0 g of THF–H_2O solution and 3.0 g of PSA.

or NMR spectroscopy conducted at low temperatures, and this can lead to discrepancies[6,8,9] in the reported H_2 capacities since these are closely related to factors such as temperature, pressure, composition, and kinetic conditions.[11,23] In this work, volumetric release experiments[8,20] were carried out to further confirm the H_2 capacity as calculated from the observed pressure drop. The amount of H_2 evolved in each case was consistent with the calculated H_2 enclathrated in Figure 2a.

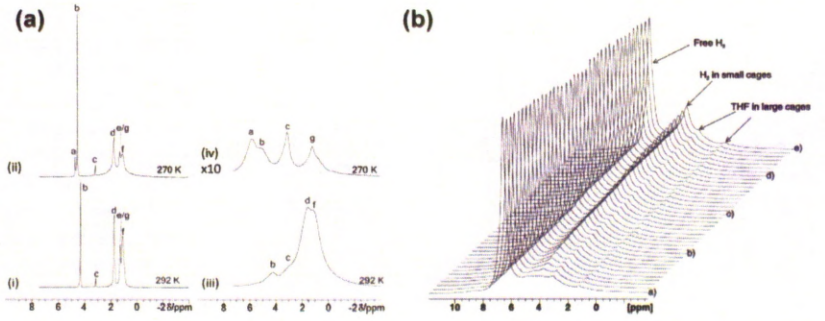

Figure 3. a) ^{1}H NMR spectra of the PSA, D_2O, and THF-d_8 system at 1 bar N_2. i) ^{1}H HR/MAS NMR spectrum at 292.0 K, ii) ^{1}H HR/MAS NMR spectrum at 270.0 K, iii) ^{1}H HP NMR at 292.0 K and iv) ^{1}H HP NMR at 270.0 K spectrum. The resonances can be assigned as follows: a) HDO in small cages; b) disordered HDO; c,g) THF; d–f) PSA (where peak e obscures peak g) in spectra i) and ii) and peaks d) and f) obscure peaks e) and g) in spectrum iii)). HR/MAS recorded at 400.20 MHz, HP NMR at 200.13 MHz. b) ^{1}H HP NMR spectra of the PSA, D_2O, and THF-d_8 systems at 270.0 K recorded using a high-pressure NMR reactor (ref. [22]): a) 0 h, 100 bar H_2, b) 5 h, c) 10 h, d) 15 h, e) 19½ h, 78 bar.

The initial kinetics observed for the PSA system were somewhat slower than for the porous polymer support material, most likely because relatively large PSA particles were used (250–1000 μm before swelling) in comparison with the thin aqueous film that exists in the emulsion-templated polystyrene structure.[20] It is believed that the use of PSA with a smaller particle size could further enhance the kinetics of the H_2 enclathration process significantly, provided that these small gel particles stay discrete and do not agglomerate in the swollen state. It should be noted that the use of PSA as a support introduces much less additional weight compared with other denser support materials such as silica beads,[6,19] improving overall gravimetric storage capacity.

Figure 2b shows the *P–T* plot of H_2 enclathration and subsequent dissociation for the H_2–THF–H_2O system, with and without PSA. Curve A was obtained using 20.0 g of THF–H_2O solution and 3.0 cm^3 of glass beads as "filler". Curve B was obtained with 20.0 g of THF–H_2O solution and 3.0 g of PSA. It can be seen that a pressure drop occurs both in the absence and presence of PSA, indicating that enclathration occurs at 270.0 K (a1 → a2 in curve A, no PSA; b1 → b2 in curve B, PSA present). When the system is heated with a temperature ramp of 1.0 K h^{-1} (a2 → a3 → a4 → a5/b2 → b3 → b4 → b5), a rapid pressure increase is observed, consistent with the dissociation of clathrate and H_2 release (see periods a3 → a4 and b3 → b4). The large difference in pressure change for the two curves further demonstrates the effectiveness of using PSA as a support.

Confirmation of the formation of a THF–H_2O PSA clathrate was obtained by high-resolution magic angle spinning (HR/MAS) and high-pressure (HP) NMR studies.[24] Formation of a clathrate host structure upon cooling to 270.0 K a D_2O/THF-d_8 solution supported in PSA was accompanied by a reaction exotherm (7 °C) and by the appearance of new resonances in the HR/MAS and HP NMR spectra (Fig. 3a). A new resonance shifted downfield from disordered HDO was observed at ~δ_H 4.7–5.8 ppm (Fig. 3aii and iv). The slight difference in chemical shifts is attributed to slight differences in sample temperature and the inherent uncertainty in the shifts of the broad HP NMR lines. The PSA resonances were observed to broaden on freezing (Fig. 3aii and iv) in both the HR/MAS and HP NMR spectra; the PSA resonances become a broad "hump" in the baseline on the HP NMR spectra, consistent with loss of motion for the polymer.

On exposure to 100 bar H_2, a new resonance at δ_H 4.0 ppm was observed (Fig. 3b), which can be assigned to H_2 stored in small clathrate cages by analogy with Lee et al.[6] and Okuchi et al.[19] Similarly, the resonances at δ_H 1.2 and 3.1 ppm may be assigned to THF in large cages. The intensity of the resonance of H_2 in the small cages increased with time (Fig. 3b).

The uptake of hydrogen was found to occur in two phases: an initial uptake, to ~30% saturation, followed simple first-order kinetics, and probably reflects relatively rapid sorption into cages at the surface of the PSA hydrogel particles. Thereafter, uptake of H_2 fits Avrami–Erofe'ev kinetics (Fig. S4, in Supporting Information) with an Avrami exponent of 0.7. Figure S5 in the Supporting Information shows the Sharp–Hancock plot for this phase of H_2 uptake: there is an initial uptake phase, during which nucleation occurs, followed by diffusion-controlled growth. Diffusion-controlled growth typically reduces the Avrami exponent by a factor of two,[25] thus an observed exponent of 0.7 indicates a 1D growth front limited by diffusion.

Other water-swellable polymer networks were also investigated, such as poly(acrylic acid), sodium salt-*graft*-poly(ethylene oxide) (see Fig. S6, Supporting Information), poly(acrylic acid) potassium salt (see Fig. S7, Supporting Information), and poly(isobutylene-*co*-maleic acid) sodium salt (see Fig. S8, Supporting Information). The results showed different enhancements in kinetics and capacity of H_2 enclathration, presumably correlated with the chemistry and particle morphology/particle size of these networks. The physical behavior of PSA particles in different fluids was also investigated (Figs. S9 and S10, Supporting Information). It was found that highly hydrophilic PSA particles are swollen by pure water as well as by the THF–H_2O solution used in these experiments. By contrast, pure THF is only partially absorbed by the same mass of PSA. Initial experiments using tetra-*n*-butylammonium bromide (TBAB) as a coguest[14,20] induced the PSA to coagulate, and this did not form a suitable morphology for enhanced H_2 uptake.

In summary, we have demonstrated for the first time the use of inexpensive hydrogels as supports to significantly improve H_2 enclathration kinetics and capacities in THF–H_2O clathrate hydrate with respect to bulk solutions. This work is of significance in promoting clathrates as a practical means for the storage of H_2 and other gases. The amounts of H_2 stored are well below the

DOE targets for vehicular H_2 storage, but broadly comparable with storage capacities reported for other near-ambient-temperature reversible H_2-storage strategies, such as "spillover" in porous supports.[26] These materials also store significantly more hydrogen than physisorptive polymer supports, which exhibit very low storage capacities at comparable temperatures and pressures.[27] There is clearly a need to design new clathrate phases with much more substantial gas uptakes under moderate conditions. The general approach described here may be of practical utility for a broad range of future systems with more promising H_2 capacities,[28] as well as other gases (methane, for example)[29] which form clathrates with much higher energy density but which nonetheless also suffer from serious issues of kinetics and recyclability.[22] Likewise, hydrogel-based clathrates may represent a scalable and recyclable strategy for CO_2 sequestration or separation, where kinetic issues and mass transport are undoubtedly important factors. The kinetics could no doubt be enhanced significantly by the use of smaller particles, as suggested by the fit with Avrami–Erofe'ev "shrinking core" kinetics. It is interesting to note that the presence of the interconnected PSA network in the gel particles does not significantly disrupt or inhibit the formation of the gas clathrate. This suggests the intriguing possibility of designing new hydrogels where the polymer network itself acts as the costabilizer,[30] thus avoiding the use of a volatile co-stabilizer such as THF.

Experimental

Clathrate Hydrate Formation: A stock solution of THF (5.56 mol%, Aldrich in deionized water; THF · $17H_2O$) was prepared [10]. Similarly, a 2.56 mol% solution of tetra-*n*-butylammonium bromide (TBAB, Fisher) with a stoichiometric composition of TBAB · $38H_2O$ was prepared, as described previously [14]. To carry out the gas uptake kinetic experiments, an amount of the THF · $17H_2O$ stock solution (20.0 g) was homogeneously mixed with PSA (1.0 g or 3.0 g dry mass, Aldrich, lightly crosslinked, 436364-250, 99% <1000 μm particle size) at a given mass ratio, and then loaded into a 60 cm^3 high pressure stainless steel cell (New Ways of Analytics, Lörrach, Germany) [20]. Prior to experiments, the cell was slowly purged with H_2 (UHP 99.999%, BOC Gases, Manchester, UK) three times to remove any air, and was cooled down to a designated temperature (270.0 K). It was then pressurized quickly to the desired pressure. The temperature of the coolant in the circulator bath was controlled by a programmable thermal circulator (HAAKE Phoenix II P2, Thermo Electron Corporation). The temperature of the compositions in the high pressure cell was measured using a Type K thermocouple (Cole–Parmer, −250–400 °C). The gas pressure was monitored using a high-accuracy gauge pressure transmitter (Cole–Parmer, 0–3000 psia). Both thermocouple and transmitter were connected to a digital universal input panel meter (Cole–Parmer), which communicates with a computer. The temperature (T, K), pressure (P, psia), and time (t, min) were automatically interval-logged using MeterView 3.0 software (Cole–Parmer). Using this set up, it was possible to obtain high-resolution data (for example, 2 s between individual points, 90 000 data points in a 1500 min experiment). The apparatus is shown schematically in Figure S1 in the Supporting Information.

Control experiments using 20.0 cm^3 of glass beads plus 3.0 g PSA showed that the system did not leak: no pressure drop occurred over 1200 min. Assuming the true density of the PSA and clathrate hydrates to be approximately 1.0 g cm^{-3}, respectively, the free space volume of the cell (36.9 cm^3) was obtained by subtracting the sum volume of clathrate and support. This was confirmed independently by measuring the free volume with helium gas at 270.0 K. The H_2 enclathration capacity was evaluated approximately using the GASPAK v3.41 software (Horizon Technologies, USA), the pressure drop (ΔP), and the temperature taking into account nonideality factors.

Volumetric release experiments were conducted by venting the reactor rapidly at 270.0 K (the temperature of the kinetic experiments). The vent valve was closed immediately when atmospheric pressure was reached. Subsequent warming released the enclathrated H_2, which was collected and measured by volumetric displacement. Measurements were calibrated to take account of gas expansion in the free space during warming.

High-Resolution Magic-Angle Spinning (HR/MAS) NMR: A mixture of D_2O (GOSS Scientific Instruments Ltd, 0.50 g) and THF-d_8 (0.11 g, Sigma–Aldrich) was added to PSA (0.10 g) in a sample vial under nitrogen, and then transferred to a 4 mm rotor with 50 μL rotor inserts. PSA was dried in a vacuum oven overnight and then washed with fresh D_2O to exchange any strongly bonded water. This was repeated three times. To allow for variable temperature measurements, the ambient gas inlet on the HR/MAS probe was attached to a VT unit and the outlet gas (N_2) from this was then attached to a preheater, which in turn was connected to the bearing gas inlet of the probe. All spectra were acquired on a Bruker AVANCE-II 400 WB spectrometer. Measurements for each sample were taken at 293.0 and 270.0 K. All spectra were acquired at an MAS rate of 4.0 kHz. NMR spectra were referenced to a blank sample containing THF (1.88 and 3.74 ppm in ^{1}H NMR and 25.37 and 67.57 ppm in ^{13}C NMR spectra). All subsequent spectra at room temperature and 270.0 K were referenced to this.

High Pressure (HP) NMR: The samples for HP NMR were prepared under N_2 in a glass liner using standard schlenk techniques. D_2O (5.0 g) and THF-d_8 (1.0455 g) were mixed in a Schlenk tube under N_2 and then syringed rapidly into the liner containing PSA (0.9 g). The injection point was below the PSA, resulting in strong agitation of the PSA bed ensuring that all the PSA was uniformly wetted. The liner was then transferred to the dry high-pressure bubble column [24], and the system pressure tested with N_2. The high-pressure bubble column was then placed in the Bruker AMX 200 magnet, and spectra were acquired at 292.0 K and 270.0 K in the absence and presence of 100 bar H_2 (1 bar = 10^5 Pa). H_2 was added only after the exotherm associated with formation of the clathrate host had been observed and the temperature had returned to 270.0 K. For Figure 3b, typically 200 transients (TD = 16384) were recorded. The Free induction decay (FID) curves were zero filled to 131072 points, and exponentially multiplied, LB = 1 (LB: line broadening), before Fourier transformation.

Acknowledgements

We thank EPSRC (EP/C511794/1, EP/C005643/1, EP/F06229X/1) for financial support. CC and GO thank EPSRC for DTA awards. Supporting Information is available online from Wiley InterScience or from the author.

Received: November 18, 2008
Revised: January 19, 2009
Published online: March 23, 2009

[1] W. L. Mao, H.-K. Mao, A. F. Goncharov, V. V. Struzhkin, Q. Guo, J. Hu, J. Shu, R. J. Hemley, M. Somayazulu, Y. Zhao, *Science* **2002**, *297*, 2247.
[2] Y. H. Hu, E. Ruckenstein, *Angew. Chem. Int. Ed.* **2006**, *45*, 2011.
[3] T. A. Strobel, C. A. Koh, E. D. Sloan, *Fluid Phase Equilib.* **2007**, *261*, 382.
[4] V. V. Struzhkin, B. Militzer, W. L. Mao, H.-K. Mao, R. J. Hemley, *Chem. Rev.* **2007**, *107*, 4133.
[5] L. J. Florusse, C. J. Peters, J. Schoonman, K. C. Hester, C. A. Koh, S. F. Dec, K. N. Marsh, E. D. Sloan, *Science* **2004**, *306*, 469.
[6] H. Lee, J.-W. Lee, D. Y. Kim, J. Park, Y.-T. Seo, H. Zeng, I. L. Moudrakovski, C. I. Ratcliffe, J. A. Ripmeester, *Nature* **2005**, *434*, 743.
[7] D.-Y. Kim, Y. Park, H. Lee, *Catal. Today* **2007**, *120*, 257.

[8] T. A. Strobel, C. J. Taylor, K. C. Hester, S. F. Dec, C. A. Koh, K. T. Miller, E. D. Sloan, *J. Phys. Chem. B* **2006**, *110*, 17121.
[9] R. Anderson, A. Chapoy, B. Tohidi, *Langmuir* **2007**, *23*, 3440.
[10] K. C. Hester, T. A. Strobel, E. D. Sloan, C. A. Koh, A. Huq, A. J. Schultz, *J. Phys. Chem. B* **2006**, *110*, 14024.
[11] K. Katsumasa, K. Koga, H. Tanaka, *J. Chem. Phys.* **2007**, *127*, 044509.
[12] P. Loubeyre, R. Letoullec, J.-P. Pinceaux, *Phys. Rev. Lett.* **1994**, *72*, 1360.
[13] W. L. Mao, H.-K. Mao, *Proc. Natl. Acad. Sci. USA* **2004**, *101*, 708.
[14] A. Chapoy, R. Anderson, B. Tohidi, *J. Am. Chem. Soc.* **2007**, *129*, 746.
[15] T. A. Strobel, K. C. Hester, E. D. Sloan, C. A. Koh, *J. Am. Chem. Soc.* **2007**, *129*, 9544.
[16] K. A. Lokshin, Y. Zhao, *Appl. Phys. Lett.* **2006**, *88*, 131909.
[17] S. Alavi, J. A. Ripmeester, *Angew. Chem. Int. Ed.* **2007**, *46*, 6102.
[18] A. Talyzin, *Int. J. Hydrogen Energy* **2008**, *33*, 111.
[19] T. Okuchi, I. L. Moudrakovski, J. A. Ripmeester, *Appl. Phys. Lett.* **2007**, *91*, 171903.
[20] F. Su, C. L. Bray, B. Tan, A. I. Cooper, *Adv. Mater.* **2008**, *20*, 2663.
[21] B. P. Binks, R. Murakami, *Nat. Mater.* **2006**, *5*, 865.
[22] W. X. Wang, C. L. Bray, D. J. Adams, A. I. Cooper, *J. Am. Chem. Soc.* **2008**, *130*, 11608.
[23] A. Saman, J. A. Ripmeester, D. D. Klug, *J. Chem. Phys.* **2006**, *124*, 204707.
[24] J. A. Iggo, D. Shirley, N. C. Tong, *New J. Chem.* **1998**, *22*, 1043.
[25] U. W. Gedde, in, *Polymer Physics: Crystallization Kinetics*, Chapman and Hall, London **1995**.
[26] a) Y. W. Li, R. T. Yang, *J. Am. Chem. Soc.* **2006**, *128*, 726. b) Y. W. Li, R. T. Yang, *J. Am. Chem. Soc.* **2006**, *128*, 8136.
[27] a) N. B. McKeown, B. Gahnem, K. J. Msayib, P. M. Budd, C. E. Tattershall, K. Mahmood, S. Tan, D. Book, H. W. Langmi, A. Walton, *Angew. Chem. Int. Ed.* **2006**, *45*, 1804. b) J. Y. Lee, C. D. Wood, D. Bradshaw, M. J. Rosseinsky, A. I. Cooper, *Chem. Commun.* **2006**, 2670.
[28] T. A. Strobel, Y. Kim, G. S. Andrews, J. R. Ferrell,, III, C. A. Koh, A. M. Herring, E. D. Sloan, *J. Am. Chem. Soc.* **2008**, *130*, 14975.
[29] E. D. Sloan, *Nature* **2003**, *426*, 353.
[30] a) K. A. Udachin, J. A. Ripmeester, *Angew. Chem. Int. Ed.* **1999**, *38*, 1983. b) I. S. Terekhova, V. L. Bogatyryov, Y. A. Dyadin, *J. Supramol. Chem.* **2002**, *2*, 393. c) I. S. Terekhova, A. Y. Manakov, V. V. Feklistov, Y. A. Dyadin, V. Y. Komarov, D. Y. Naumov, *J. Inclusion Phenom. Macrocyclic Chem.* **2005**, *52*, 207. d) D. V. Soldatov, K. Suwinska, I. S. Terekhova, A. Y. Manakov, *J. Struct. Chem.* **2008**, *49*, 712.

Submitted to ADVANCED MATERIALS

Supporting Information

Reversible Hydrogen Storage in Hydrogel Clathrate Hydrates

Fabing Su, Christopher L. Bray, Benjamin O. Carter, Gillian Overend, Catherine Cropper, Jonathan A. Iggo, Yaroslav Z. Khimyak, Andrew M. Fogg *and* Andrew I. Cooper.

Department of Chemistry and Centre for Materials Discovery, University of Liverpool, Crown Street, Liverpool L69 3BX, United Kingdom.

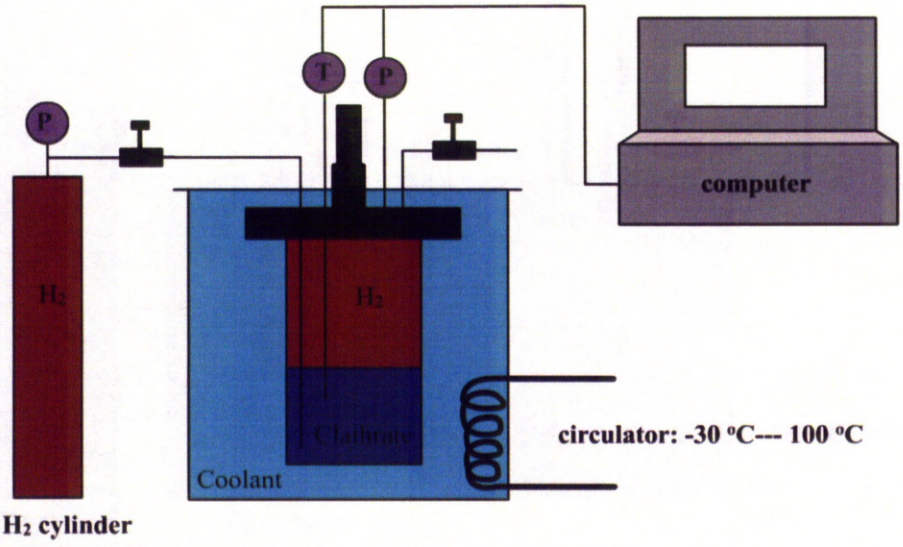

Figure S1. Schematic diagram of the experimental apparatus.

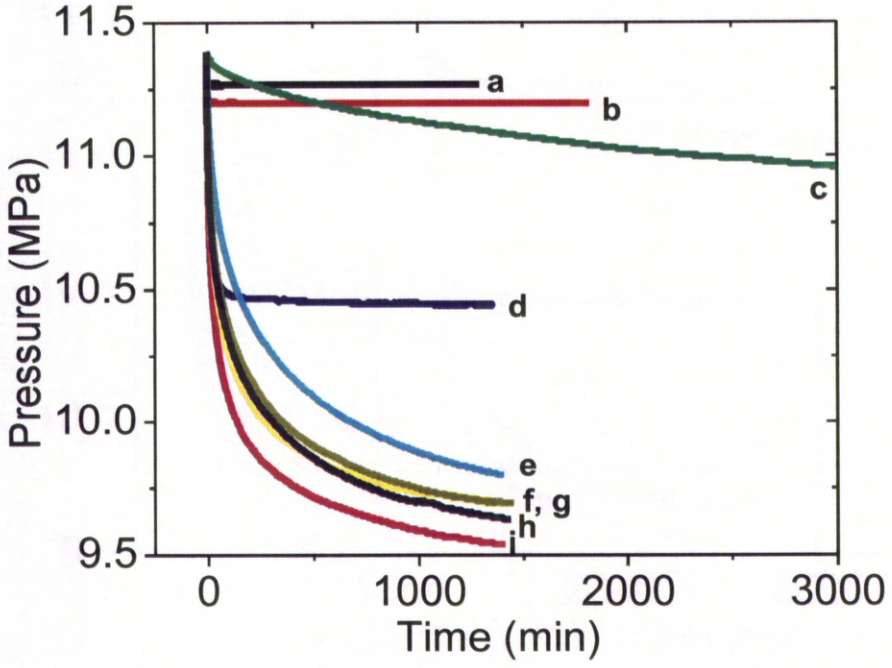

Figure S2. The kinetic plots for H_2 encapsulation in preformed THF-H_2O clathrate hydrate supported with and without PSA at 270.0 K: (a) 20.0 cm^3 glass beads and 3.0 g PSA, no THF solution; (b) 20.0 g pure H_2O and 3.0 g PSA (baseline); (c) 20.0 g THF-H_2O solution plus 3.0 cm^3 glass beads (bulk clathrate); (d) 20.0 g THF-H_2O solution and 3.0 g polyHIPE; (e) 20.0 g THF-H_2O solution and 1.0 g PSA; (f) 20.0 g THF-H_2O solution and 3.0 g PSA (3^{rd} run); (g) 20.0 g THF-H_2O solution and 3.0 g PSA (4^{th} run); (h) 20.0 g THF-H_2O solution and 3.0 g PSA (2^{nd} run); (i) 20.0 g THF-H_2O solution and 3.0 g PSA (1^{st} run).

Curve (a) was obtained with 20-cm^3 glass beads and 3.0 g PSA. No pressure drop at 270.0 K was observed even after 1200 min, suggesting there is no leakage in our experimental system, and that no adsorption of H_2 occurred on PSA. In curve (b), it can be seen that there is no H_2 pressure drop at 270.0 K after 30 min, suggesting that no H_2 encapsulation occurred because there is no clathrate hydrate formed in the absence of THF additive under such conditions. This directly proves the significant role of THF stabilizer in reducing the enclathration pressure (see below), consistent with the results previously reported [1]. This curve also demonstrated there is no leakage in our setup and was employed as our baseline. Curve (c) reveals the kinetic plot obtained in preformed clathrate hydrate with 20.0 g THF-H_2O and 3.0 cm^3 glass beads as a representative of bulk clathrate hydrate. A slow pressure drop with time indicates an amount of H_2 encapsulated in bulk THF-H_2O hydrate. We did not observe the pressure drop when using H_2O instead of THF-H_2O solution (result not shown here), further demonstrating the significance of THF. The description for other curves can be found in the main paper.

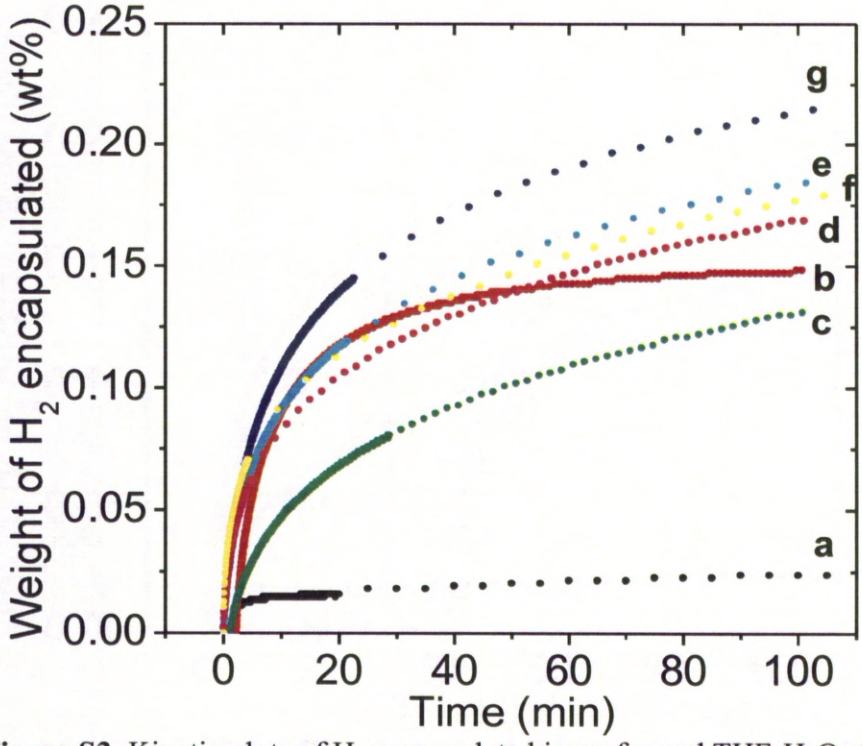

Figure S3. Kinetic plots of H_2 encapsulated in preformed THF-H_2O clathrate hydrate at 270.0 K: (a) 20.0 g THF-H_2O solution, and 3.0 cm^3 glass beads; (b) 20.0 g THF-H_2O solution and 3.0 g polyHIPE (5th run, see previous report [2]); (c) 20.0 g THF-H_2O solution, 1.0 g PSA; (d) 20.0 g THF-H_2O solution and 3.0 g PSA (3rd run); (e) 20.0 g THF-H_2O solution and 3.0 g PSA (4th run); (f) 20.0 g THF-H_2O solution and 3.0 g PSA (2nd run); and (g) 20.0 g THF-H_2O solution and 3.0 g PSA (1st run).

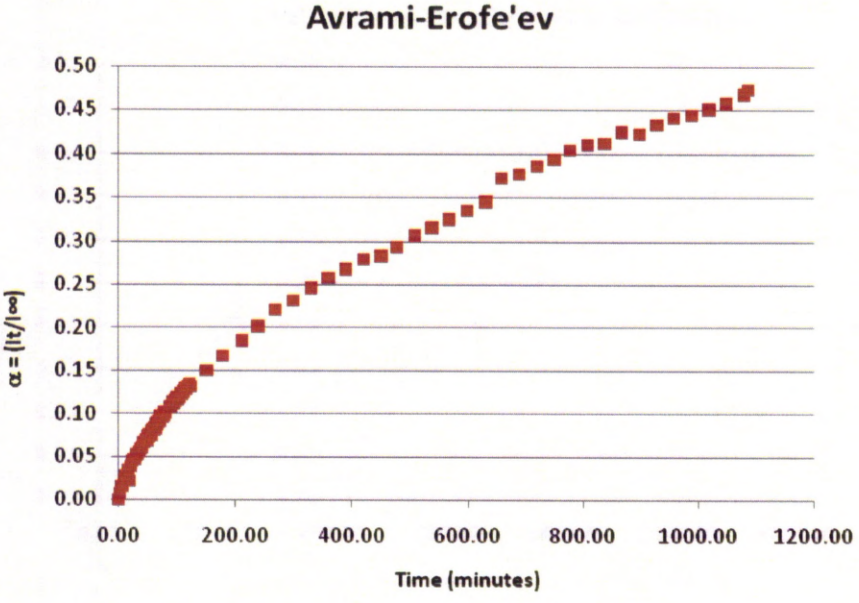

Figure S4. Avrami-Erofe'ev Plot for second growth phase. The ^1H NMR intensity of the H_2 in small cages was fit to a tri-exponential (SPSS, non-linear regression, R^2 = 0.999) from which I∞ was obtained. The Avrami constant was then obtained from a plot of (ln(-ln(1-α))) vs ln(time) (Sharp-Hancock plot) and found to be 0.7.

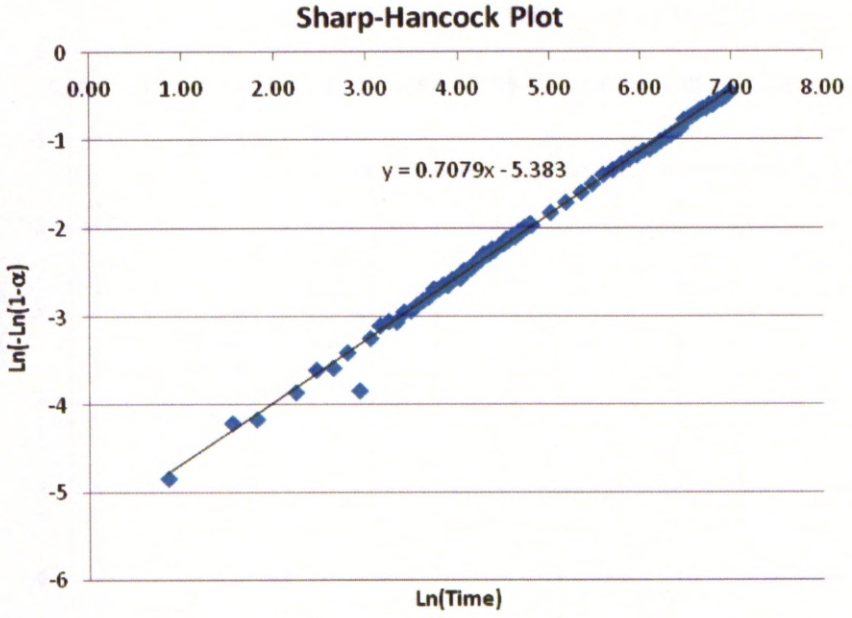

Figure S5. Sharp-Hancock plot of the intensity of the growth of H_2 in cages peak. The gradient of this plot gives an Avrami constant of 0.7. $\alpha = (It/I\infty)$, It = intensity of H_2 in small cages peak at a given time, $I\infty$ = Intensity of H_2 in small cages at the end of reaction when total saturation has been reached.

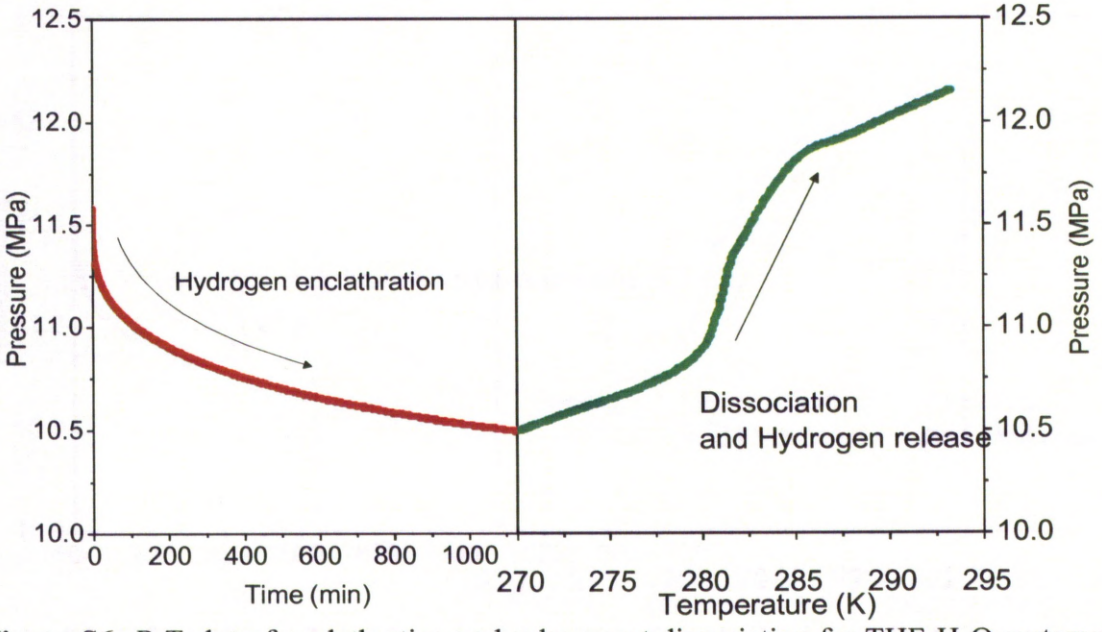

Figure S6. *P-T* plot of enclathration and subsequent dissociation for THF-H_2O system under H_2 pressure with poly(acrylic acid), sodium salt-graft-poly(ethylene oxide), (cross-linked, Aldrich) as the support.

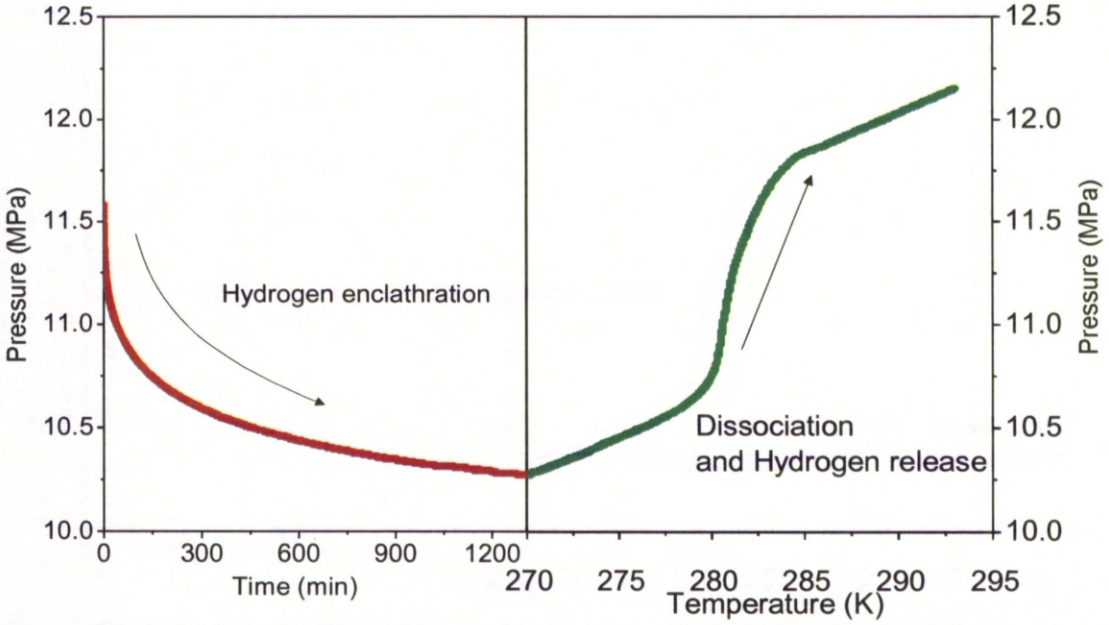

Figure S7. *P-T* plot of enclathration and subsequent dissociation for THF-H_2O system under H_2 pressure with poly(acrylic acid), potassium salt (lightly cross-linked, powder; particle size 99% < 1,000 μm, Aldrich) as the support.

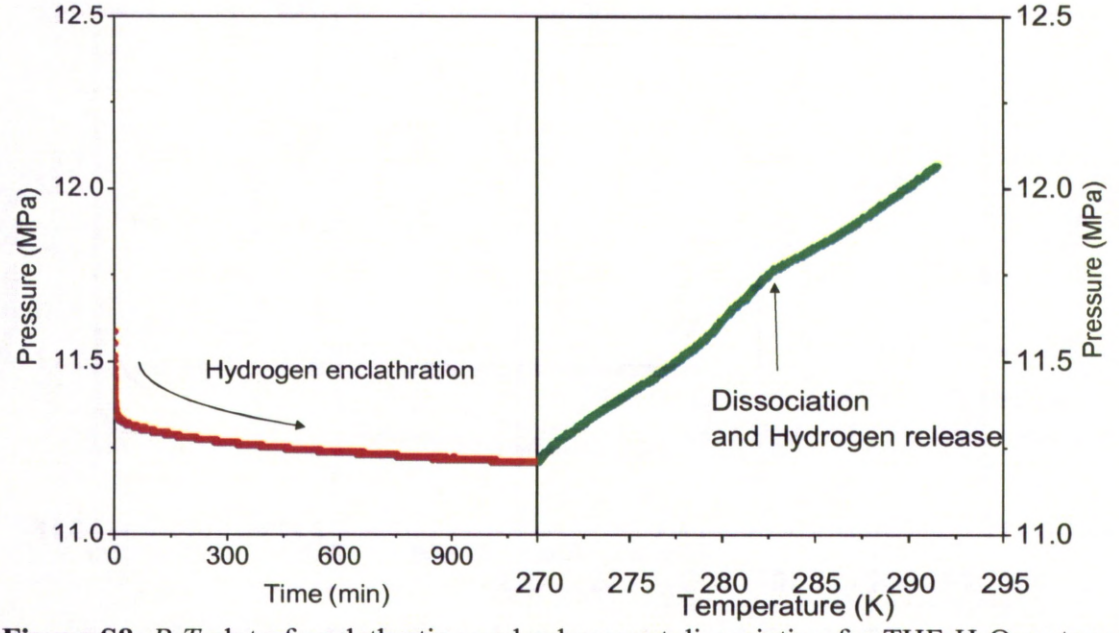

Figure S8. *P-T* plot of enclathration and subsequent dissociation for THF-H_2O system under H_2 pressure with poly(isobutylene-*co*-maleic acid), sodium salt (crosslinked fiber; 24-40 mm diameter, Aldrich) as the support.

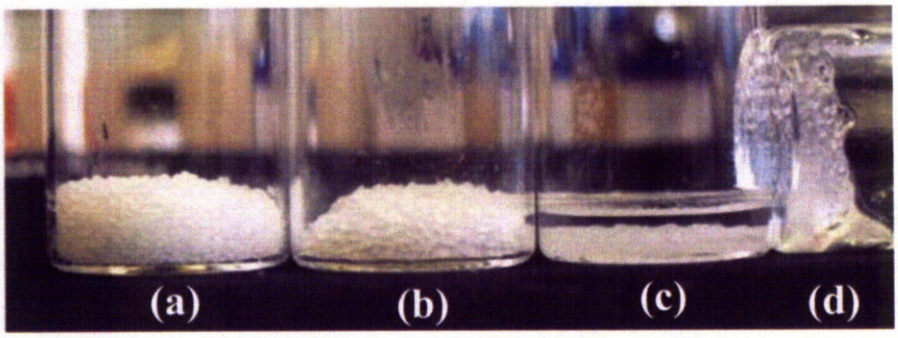

Figure S9. Status of PSA particles in different liquids: (a) PSA in H_2O; (b) PSA in THF-H_2O; (c) PSA in THF; (d) PSA in TBAB-H_2O.

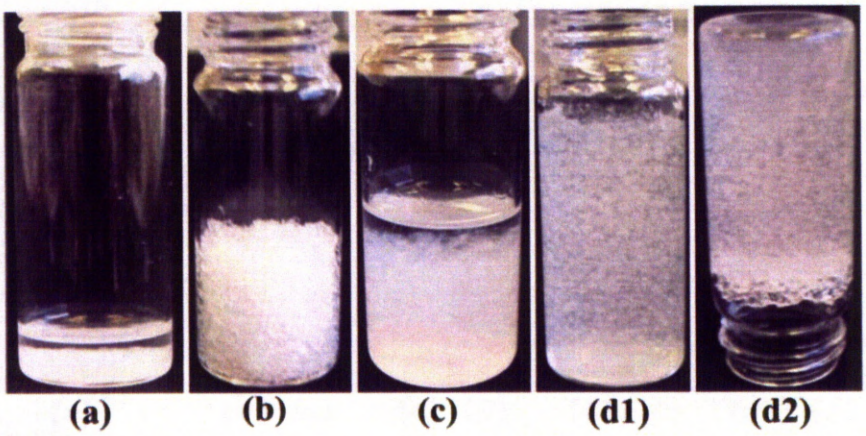

Figure S10. (a) PSA in pure THF; (b) adding H_2O to (a); (c) adding THF to (b); and (d1, d2) adding H_2O to (c). Photographs illustrating the swelling of PSA particles in high (left) and low concentrations of THF (right). Figure S10 (a) shows that PSA is not swollen by pure THF solvent. After addition of H_2O, it can be seen in Figure S10 (b) that PSA is swollen. Upon further addition of THF, the swollen PSA is immersed again in the pure THF, as shown in Figure S10 (c). Adding more H_2O, PSA was largely swollen again and the THF was held within the interstitial voids among PSA particles (Figure S10 (d)).

References

[1] F. Su, C. L. Bray, B. Tan, A. I. Cooper, *Adv. Mater.* **2008,** *20*, 2663.